DISSERTATION

OPTIMIZING REMOTE SENSING DATA FOR ACTUAL CROP EVAPOTRANSPIRATION MAPPING AT DIFFERENT RESOLUTIONS

Submitted by

Edson Costa Filho

Department of Civil and Environmental Engineering

In partial fulfillment of the requirements

For the Degree of Doctor of Philosophy

Colorado State University

Fort Collins, Colorado

Summer 2024

Doctoral Committee:

Advisor: José L. Chávez

Karan Venayagamoorthy
Jeffrey Niemann
Christian Kummerow

ABSTRACT

OPTIMIZING REMOTE SENSING DATA FOR ACTUAL CROP EVAPOTRANSPIRATION MAPPING AT DIFFERENT RESOLUTIONS

This study aimed to advance irrigation water management by developing and evaluating a procedure to improve the multispectral data from sub-optimal remote sensing sensors when using the optimal spectral resolution for a given remote sensing (RS) of crop actual evapotranspiration (ETa) algorithm. Data have been collected at three research sites in Colorado under different irrigation systems, soil textures, and vegetation types. The research site in Greeley (CO) has a five-year dataset (2017-2018 and 2020-2022). The fields in Fort Collins and Rocky Ford (CO) have data from 2020 and 2021.

Three categories of ETa algorithms were evaluated in the study: The reflectance-based crop coefficient (RBCC) with three different models based on the normalized difference vegetation index (NDVI), soil-adjusted vegetation index (SAVI), and fractional vegetation canopy cover (f_c), the one-source simplified surface energy balance (OSEB) based on a surface aerodynamic temperature approach, and the two-source surface energy balance algorithm (TSEB) using two different resistance approaches (parallel and series). All three ETa modeling categories use either just surface reflectance in the visible and invisible light spectrum (e.g., RED, BLUE, GREEN, Near-infrared) or a combination of multispectral and thermal data as inputs to predict crop ETa, alongside local micrometeorological data from nearby agricultural weather stations. A total of six RS of ETa algorithms were evaluated in this study. A total of five RS sensors were evaluated: three spaceborne sensors (e.g., Landsat-8, Sentinel-2, and Planet CubeSat), one proximal device (multispectral radiometer), and an uncrewed aerial vehicle (UAS). The spatial resolution of the RS sensors varied

from 30 m to 0.03 m.

The accuracy assessment of the crop ETa predictions considered a statistical performance analysis using, among several statistical metrics, the mean bias error (MBE) and root mean square error (RMSE), and compared estimated ETa values from all seven RS ETa algorithms with observed ETa values obtained from the Eddy Covariance Energy Balance System (Greeley and Fort Collins sites) and a weighing lysimeter (Rocky Ford). The study was divided into three stages: a) the evaluation of different remote sensing (RS) pixel spatial resolutions (scales) as inputs on the estimation of different types of data needed for estimating ETa in hourly and daily time frames; b) the development of a calibration protocol and standards for the use of different imagery spatial resolutions (scales) in RS of ETa algorithms. The calibration approach involved a novel two-source pixel decomposition approach for partitioning surface reflectance into soil and vegetation using a non-linear, physically based spectral model, machine-learning regression, and a novel spatial light extinction model (k_p); c) the accuracy evaluation of resulting ETa rates from calibrated/standardized data (for each selected RS of ETa algorithms).

Results of stage one of the study indicated that depending on the RS of ETa and RS sensor data (spatial and spectral resolutions), the accuracy (MBE $\pm$ RMSE) of estimated ETa predictions varied. For the NDVI and f_c RBCC ETa algorithms, Sentinel-2 provided the best RS data for predicting daily maize ETa. Errors were 0.21 (5$\%$) $\pm$ 0.78 (18$\%$) mm/d and 0.59 (14$\%$) $\pm$ 1.07 (25$\%$) mm/d, respectively. For the OSEB algorithm, Planet CubeSat gave the best RS data since it provided the smallest error for hourly maize ETa, -0.02 (-3$\%$) $\pm$ 0.07 (13$\%$) mm/h. For the SAVI RBCC model, the MSR data provided the best results since the maize ETa error was -0.13 (-3$\%$) $\pm$ 0.67 (16$\%$) mm/d. For the TSEB in series and parallel, the errors when estimating hourly maize ETa were -0.02 (-3$\%$) $\pm$ 0.07 (11$\%$) mm/h and -0.02 (-4$\%$) $\pm$ 0.09 (14$\%$) mm/h, respectively when using MSR data.

For stage two of the study, the best machine learning regression model for a given RS sensor data and RS of the ETa algorithm depended on the surface reflectance composite (plant or bare soil values). The best machine-learning models for adjusting RS data were the regression tree and the Gaussian Process Regression. Regarding the pixel decomposition approach based on the novel spatial light extinction coefficient model, the novel approach provided reliable predictions of k_p using the different RS sensor data. The error in predicting k_p was -0.01 (-2%) $\pm$ 0.05 (10%) when combining all RS sensor data for the two-year data set at LIRF (years 2018 and 2022).

For stage three of the study, results showed improvements in the accuracy of crop ETa estimation after adjusting the RS data using the proposed calibration protocol. At the Greeley site, regarding the RBCC RS of ETa algorithm, adjusted data from Planet CubeSat had better performance when estimating daily crop ETa since the error was reduced from 21% to 16% for the f_c-input model. For the SAVI-input model, the RS data that performed better was the UAS. Errors were reduced from -0.42 (-11%) $\pm$ 0.76 (20%) mm/d to -0.21 (-5%) $\pm$ 0.41 (11%) mm/d. For the NDVI-input model, the adjusted UAS data performed better when estimating daily maize ETa. The improved accuracy was 0.32 (8%) $\pm$ 0.40 (10%) mm/d. At the Rocky Ford site, for the f_c-input model, adjusted RS optical data from the MSR performed better. Daily maize ETa error was reduced from 17% to 15%. For the SAVI-input model, the RS data that performed better was the Landsat-8, with errors being reduced from -1.84 (-28%) $\pm$ 2.61 (39%) mm/d to -1.14 (-17%) $\pm$ 1.79 (27%) mm/d. The NDVI-based RBCC model had better performance when using adjusted MSR data daily maize ETa.

Regarding the OSEB RS of crop ETa approach, at the Greeley site, the OSEB-adjusted data from UAS performed better. Hourly maize ETa error was reduced from 0.11 (19%) mm/h to 0.07 (13%) mm/h for the OSEB algorithm. For the TSEB parallel algorithm, the RS data that had better performance was the Landsat-8/9 since the error was reduced from 0.19 (34%) mm/h to 0.11 (20%) mm/h. For the TSEB series algorithm, the adjusted UAS data performed better. Daily maize ETa

errors decreased from 0.10 (18%) mm/h to 0.05 (9%) mm/h.

In summary, this study provided an RS calibration approach to support irrigation water management through the development and evaluation of a method for enhancing optical multispectral data sourced from various RS sensors. This study also highlighted the efficacy of machine learning models, like regression tree and Gaussian Process Regression, in adjusting RS data based on surface reflectance composites. Furthermore, a novel pixel decomposition approach utilizing a spatial light extinction model effectively predicted the light extinction coefficient. Overall, this research showcases the potential of RS data adjustments in improving the accuracy of ETa estimates, which is crucial for optimizing irrigation practices in agricultural settings.

ACKNOWLEDGEMENTS

I want to thank, first of all, Jesus, whose endless grace, joy, and inspiration have provided me with the necessary strength and guidance during the triumphs and challenges encountered throughout my doctorate at Colorado State University (CSU). A special thank you goes to my family, whose unwavering love and encouragement have been the foundation upon which this academic achievement stands strong. Also, I want to be grateful to my advisor, José Chávez, for trusting me with such necessary research and for helping me with constructive guidance and resources to the best of his ability. To all those undergraduate and graduate students who worked with me during the data collection campaigns across three different research sites in Colorado from 2017 to 2022, I express my sincere gratitude for helping obtain high-quality data to support my research. I also want to thank the following agencies that provided support for this project: The CSU Agricultural Experiment Station, The United States Department of Agriculture - Agricultural Research Service (USDA-ARS) represented by Huihui Zhang and Kevin Yemoto, The United States Department of Agriculture - National Institute of Food and Agriculture (USDA-NIFA), and Northern Water represented by Jon Altenhofen.

DEDICATION

I would like to dedicate this thesis to my Lord Jesus, family, and scientific community.

TABLE OF CONTENTS

LIST OF TABLES

LIST OF FIGURES

Chapter 1

Introduction

1.1 Climate Change and Agricultural Water Management

The growing threat of climate change, together with expected global population growth in the next 30 years, has created significant concerns about the future of water resources across low to high-income nations (Vermeulen et al., 2012; Wiebe et al., 2019). A Food and Agriculture Organization of the United Nations (FAO) report by Alexandratos et al. (2006), later revised by Alexandratos and Bruinsma (2012), estimated that the global population would be greater than 9 billion people by 2050. An expansion in agricultural production by 60-70% (compared to the total output in 2006) will be required to meet the future global population demands. With climate change rising global temperatures and altering hydrological cycle patterns, seasonal and severe weather will become regular events worldwide. In the context of semi-arid and arid regions, extreme and prolonged drought seasons will have the potential to escalate yield loss due to heatwaves, soil nutrients degradation, and water access disputes (Quiring and Papakryiakou, 2003; MacDonald, 2007; Foley et al., 2011; Godfray et al., 2011; Wang et al., 2014).

Agriculture is the leading water user in the world, withdrawing approximately 70-75% of the freshwater available (Wallace, 2000; Dubois, 2011; Wada et al., 2013) and occupying 12% of the habitable land on the planet, according to the latest FAO land use database (FAO land use, 2019). Rainfed and Irrigated fields are the basis for cropland water use worldwide. Irrigated fields have occupied 18% of the earth's cultivable cropland area while being responsible for about 40% of the global food production (Cai and Rosegrant, 1999; Fereres and Connor, 2004; Siebert and Döll, 2010; Grassini et al., 2011). It is estimated that, by 2050, the global atmosphere will be warmer by 2 to 5 ^oC. The projected rise in temperature has the potential to increase crop water use under

warmer and drier weather conditions (Peterson et al., 1990; Bruinsma, 2009; Troy et al., 2015). The current trends in worldwide water scarcity have added more attention to the international community toward a sustainable approach to cropland production (Brauman et al., 2013; Li et al., 2020).

In the United States of America (USA), climate change and accelerated urban and industrial development can negatively impact the yield and revenue of primary commodities, including row crops such as maize, soybeans, pinto beans, and sorghum. A 2017 report from the United States Department of Agriculture – Agricultural Statistical Service (USDA-NASS) indicated that most whole grains are cultivated in the Midwestern USA and neighboring states (e.g., Kansas, Iowa, Nebraska, Colorado, Wyoming, and Texas). Chung et al. (2014) indicated that a 29% loss in maize yield in the USA would be related to extreme drought events in the next thirty-five years. A reduction in precipitation events in the USA will add more constraints to the water resources available for the agriculture industry during the 21^{st} century (Tubiello et al., 2002; Mote et al., 2005; Lute et al., 2015; Gergel et al., 2017; Marshall et al., 2019).

According to Locascio (2005), 81% of the USA's water use is due to irrigation for farms and landscape facilities, of which 63% of the water supply comes from surface water bodies, and 37% is provided by groundwater extraction. Due to climate variability and food demands, the need to augment irrigation water application has led to a water shortage due to groundwater depletion and streamflow reduction. At the same time, ramping up water allocation costs makes it difficult to improve agricultural water management in the USA and other parts of the globe (Postel, 2003; Perry et al., 2009; Rockström et al., 2012; Momeni et al., 2019). On the environmental side, the overexploitation of water for irrigation has been causing severe damage to groundwater and watershed basins across the USA, which requires action to mitigate the destructive impact of poor water management practices in an agricultural setting (Scanlon et al., 2012; Kustu et al., 2010; Condon

and Maxwell, 2019; Cotterman et al., 2018).

MacDonald and Girvetz (2013) indicated that while the rates of irrigation water application will rise due to climate change in the USA, one way to improve and make agriculture more sustainable is by reducing water losses and supplying the crop water demands based on actual field conditions. Jones (2004) highlighted improving irrigation through enhanced systems or devices that allow for a more controlled water application in the crop root zone that minimizes water losses and increases efficiency (e.g., precision agriculture). Pierce and Nowak (1999) defined precision agriculture as implementing techniques to improve irrigation water management on a spatial-temporal basis. Thus, it is critical to determine the optimal time and amounts to apply water in the root zone to sustain or improve crop yield while conserving soil and water resources. Furthermore, knowing the timely water requirements across the crop growth stages is necessary to determine the timing and amount of water application.

1.2 Irrigation Water Management: The Role of Crop Evapotranspiration

Irrigation water management practices are often based on the soil water balance approach (SWB) for irrigation scheduling (Allen et al., 1998; Wery, 2005; Chávez, 2015; Wu et al., 2017; Costa-Filho et al., 2020). It considers the water entering and leaving the crop root zone to monitor the changes in soil water content over time (Hoffman et al., 2007). A simplified daily SWB budget (Allen et al., 1998) is given by Eq. 1.1 as follows:

$$D_{r,i} = D_{r,i-1} - (P - RO)_i - I_i - CR_i + ET_{a,i} + DP_i \tag{1.1}$$

$D_{r,i}$ is the water depleted in the root zone at the end of day i^{th}; $D_{r,i-1}$ is soil water content at the previous day $(i-1)^{th}$; P_i is the rainfall water depth; RO_i is the surface water runoff; I_i is

the net irrigation water depth; CR_i is the capillary rise from the groundwater storage; $ET_{a,i}$ is the actual crop evapotranspiration; DP_i is the deep percolation (water loss to deeper soil layers). All variables in Eq. 1.1 are given as water depth units (e.g., mm or in, for instance).

In Eq. 1.1, actual crop evapotranspiration (henceforth, ETa) is a critical term for irrigation scheduling since it provides information on the field water losses due to plant transpiration and soil water evaporation. Brutsaert (1982) defines ETa as the rate of water exchanged to the atmosphere by vegetation and shallow soil layers. ETa is a relevant component of the hydrologic cycle since its physical process involves exchanging heat, carbon, and vapor between the plant-soil-atmosphere continuum (Chen et al., 2014; Amatya et al., 2016). At the farm scale, determining accurate ETa rates is essential to improve crop water management and irrigation scheduling and support decision-making approaches for water allocation and optimization of irrigation water management (Gowda et al., 2007; Anderson and French, 2019).

The soil-plant-atmosphere continuum is a complex structure that accounts for different intermittent physical processes that are interconnected and involve but not limited to, environmental biophysics, plant physiology, micrometeorology, physical hydrology, and environmental fluid dynamics (Hopkins, 2009; Arya, 2001; Foken and Napo, 2008; Campbell and Norman, 2012; Patton and Finnigan, 2012; Dingman, 2015). Hence, obtaining ETa data for crop water management demands adequate measuring techniques or modeling approaches that incorporate most physical mechanisms that derive plant transpiration and soil water evaporation.

1.3 Measuring Crop Evapotranspiration: Advantages and Limitations

Measurement techniques have become a straightforward surrogate for determining on-site ETa rates when instrumentation and technical expertise are available for data collection. The most up-

to-date and commendable methods available for directly or indirectly measuring ETa are based on soil mass balance through high precision monolithic weighing lysimeters (Guitjens, 1982; Howell et al., 1991; Yang and Shipping, 2000; Jia et al., 2006; Denich and Bradford, 2010; López-Urrea et al., 2012), above canopy turbulence measurements from a high frequency eddy covariance (henceforth, EC) or optical large aperture scintillometer (LAS) systems (Snyder et al., 1999; Meijninger et al., 2000; Hemakumara et al., 2003; Guo et al., 2004; Sun et al., 2008; Ezzahar et al., 2009; Mkhwanazi et al., 2012; Anapalli et al., 2018; Anapalli et al., 2020), SWB measurements using soil water content sensors (Sass and Horgan, 2006; Shuttleworth, 2008; Sharma et al., 2017; Huang et al., 2021), plant transpiration through sap flow devices (Soegaard and Boegh, 1995; Wilson et al., 2001; Williams et al., 2004; Gong et al., 2007; Zhang et al., 2014; Saitta et al., 2020), and other methods that rely on weather data at different heights above the vegetation such as the aerodynamic profile tower (APT) and Bowen ratio (BR) approaches (Bowen, 1926; Spittlehouse and Black, 1980; Pieri and Fuchs, 1990; Malek et al., 1993; Prueger et al., 1997; Zhang et al., 2007; Qian et al., 2009; de Pinho Sousa et al., 2021).

Although ETa measurements have become reliable for providing measured data from different methods, the temporal and spatial variability in crop water demands at the farm and irrigation district scale makes measuring spatially distributed ETa across cropland fields unrealistic. Soil water content and sap flow sensors provide localized data, which might also prove challenging in obtaining a large spatially measured ETa sample domain for agricultural crop fields due to the need for several sampling locations. Furthermore, techniques such as the EC system, LAS, BR, and APT are representative of their respective 2D heat flux source area or footprint (e.g., an upwind area from which most of the measurements are observed by the instruments) approaches have limitations regarding the local inherent assumptions of surface homogeneity, stationary turbulent conditions, and non-advective conditions (Arya, 2001; Foken and Napo, 2008; Burba, 2013). Thus, these flux-based methods are often used in research studies, where farm management practices are strictly controlled and pre-determined to calibrate or validate ETa modeling approaches (Zhou et

al., 2014; Song et al., 2016; Kustas et al., 2019).

Several papers have compared the accuracy of different measuring ETa techniques that are associated with soil mass balance (e.g., lysimeters) and scalar flux calculation (e.g., EC, LAS, BR, and APT). Typical uncertainty in daily ETa from up-to-date calibrated monolith weighing lysimeters ranges from 0.50% to 2% (Howell et al., 1995; Brown et al., 2021). The next best measurement technique that compares well to lysimeter ETa data is the EC system. The typical uncertainty associated with measurements of ETa (regarding latent heat flux) from an EC unit ranges from 5% to 20% (Weaver, 1990; Hollinger and Richardson, 2005; Mauder et al., 2013).

Studies comparing EC system and lysimeter daily ETa data have indicated a slight underestimation (e.g., 2% - 10%) for grass, maize, cotton, wheat, and vineyards fields in different climate conditions (semi-arid to humid climate) when the lack of surface energy balance closure of the EC fluxes is adjusted (e.g., Chávez et al., 2009a; Ding et al., 2010; Sanchez et al., 2019; Moorhead et al., 2019). The LAS optical approach for indirectly determining latent heat flux and ETa has an overall measurement uncertainty (associated with sensible heat flux) ranging from 10% to 20% (Meijninger and de Bruin., 2000; Kleissl et al., 2008; Solignac et al., 2009). Profile tower techniques (e.g., BR or APT) have more considerable uncertainty when compared to other EC and LAS systems, with typical measurement errors for latent heat flux (or ETa) from 9% up to 40% for daytime data (Sinclair et al., 1975; Halliwell and Rouse, 1989; Perez et al., 1999).

1.4 Modeling Crop Evapotranspiration: Empirical and Physically Based Approaches

Mathematical modeling has become a complementary tool for obtaining evapotranspiration estimates for irrigation scheduling as an alternative to overcome the logistics of spatially measuring ETa. The advancements in the fields of micrometeorology and environmental fluid mechanics

have allowed scientists to investigate the turbulence phenomena of a given passive scalar entity (e.g., temperature, water vapor, for instance) through computational fluid dynamics (CFD) and numerical modeling for more than a century (e.g., Prandtl, 1925; Batchelor, 1949; Daly and Harlow, 1970; Lumley, 1979; Finnigan, 1985; Rogers et al., 1989; Wilson, 1989; Siqueira and Katul, 2002; Cava et al., 2006; Finnigan, 2010; Watanabe et al., 2021).

A passive scalar is an entity present in a fluid flow without interfering with the motion (Warhaft, 2000). However, the use of CFD and numerical modeling has been preferred for research experiments designed to understand turbulence when data collection is not feasible (Katul et al., 2004; Younis et al., 2005; Liu et al., 2021), which is a limiting factor for daily irrigation water management applications. The three-dimensional characteristic of turbulent flows adds complexity to the models based on the turbulent scalar flux budget equation and turbulence closure approaches (Pope, 2001). Thus, practical techniques for estimating ETa created conditions for improving irrigation water management by developing empirical, semi-empirical, and physically-based ETa models.

At about the same time, CFD and turbulence modeling were being studied as empirical formulations based on weather variables (e.g., air temperature, relative humidity, wind speed, solar radiation), geographical location, and reference evaporation from a controlled water body (e.g., pan evaporation). These initial advancements were developed by local calibration for different crops (Thornthwaite, 1948; Blaney and Criddle, 1962; Christiansen, 1968; Hargreaves, 1975). These purely empirical modeling approaches had several assumptions that did not embrace the natural complexity of water vapor transfer in the soil-plant-atmosphere continuum. Such methods might prove challenging to be relevant for daily irrigation water management when changes in local weather conditions throughout the day are concurrent with water vapor exchange in the soil-plant-atmosphere continuum since these empirical ETa models rely on mean values of daily air temperature. Nevertheless, studies have been conducted to assess the validity of simple modeling

schemes when quality data or instrumentation are limiting factors in determining evapotranspiration rates. Some recent studies have reported estimated ETa errors ranging from 20% to 40% for vegetated surfaces such as grass and alfalfa for Blaney and Criddle (1962) and Thornthwaite (1948) improved and calibrated models considering monthly timesteps (Trajkovic et al., 2019; Aschonitis et al., 2021) and daily (Hafeez et al., 2020a; Hafeez et al., 2020b).

A more robust approach to determine daily and hourly crop evapotranspiration was proposed by Monteith (1965), based on Penman (1948), and often referred to as the "1965 Penman-Monteith" equation (PM-65). The PM-65 approach is a physically-based model that involves the concept of the surface energy balance (SEB) coupled with the aerodynamic effects of heat and water vapor transfer favored by the interactions between the wind and the surface (Federer, 1975; Jensen et al., 1990). The initial formulation from Penman (1948) aimed to determine evaporation from water bodies, while Monteith (1965) modified Penman (1948) model to expand its application to vegetated surfaces by introducing surface and aerodynamic resistance terms. Errors in crop evapotranspiration using the PM-65 equation ranged from 10% to 20% compared to respective measured data from the BR method or weighing monolithic lysimeters over short grass and wheat, olive orchards, and maize fields under subtropical, Mediterranean, humid continental climate conditions (Van Zyl and De Jager, 1987; Margonis et al., 2018).

The challenge to applying the PM-65 equation for different vegetated surfaces is the parametrization of the surface resistance (Alves and Pereira, 2000). Some research attempted to determine more sophisticated yet empirically based approaches for estimating the surface resistance based on modifications of the PM-65 equation (Katerji and Perrier, 1983; Pereira et al., 1996; Allen et al., 1998; Todorovic, 1999; Li et al., 2009). Alves and Pereira (2000) argued that a simple but effective approach to modeling surface resistance would use environmental data such as solar radiation, vapor pressure deficit, and temperature to predict surface resistance through an empirical model,

as presented by Jarvis (1976).

The limited transferability of the empirical models for surface resistance regarding different vegetation types under other climate conditions imposes a barrier to applying the PM-65 worldwide. Simpler versions of the PM-65 equation were developed to avoid parameterizing the surface resistance. A famous reformulation of Penman (1948) and Monteith (1965) work is the Priestley-Taylor Formula (Priestley and Taylor, 1972), in which ETa is still related to the SEB concept but with the introduction of a parameter α to simplify the calculations. The range of published values for α varies from 1.15 to 1.50, with 1.26 being the recommended value (as used in Norman et al., 1995; Norman and Kustas, 2000).

Furthermore, the Priestley and Taylor formula tried to represent physically based processes with a numerical parameter, which is insufficient to justify the complexity of water vapor transfer in the soil-plant-atmosphere continuum. There have been attempts to calculate α as a function of the dry air entrainment at the top of the atmospheric boundary layer, surface, and aerodynamic resistances (de Bruin, 1983). Nonetheless, the application of the PM-65 equation has often been applied to standardized surfaces (e.g., clipped grass or alfalfa) of fixed crop height, vegetation structure (e.g., leaf area index or LAI, for instance), and surface resistance, with no water and nutrient deficits. Calculated crop evapotranspiration for standardized surfaces are referred to as reference ET (henceforth, ET_{ref}) and later translated into daily ETa through crop coefficients (Wright, 1981; Allen et al., 1998; Allen, 2000; Allen et al., 2005a; Rawat et al., 2019).

The single crop coefficient method was first introduced by Jensen (1968). It was based on the concept of relating reference and crop evapotranspiration through a proportionality factor, the crop coefficient. The term "single" alludes to the idea of an average coefficient that represents the combined plant transpiration and soil water evaporation. Doorenbos and Pruitt (1977) recommended the Penman (1948) evaporation model to determine ET_{ref}. It was only with the FAO-56 bulletin

(Allen et al., 1998) that the crop coefficient method for crop evapotranspiration considered the PM-65 equation to determine reference evapotranspiration using clipped grass as the vegetation surface (Lecina et al., 2003).

About seven years after the FAO-56 bulletin publication, the American Association of Civil Engineers (ASCE) introduced a standardized version of the PM-65 equation to calculate ET_{ref} using the crop coefficient approach. The ASCE-EWRI (2005) manual provided parameterizations for alfalfa (ET_r) and clipped grass (ET_o) hourly and daily ET_{ref}. The hourly ET_o or ET_r also can be divided into smaller timesteps (e.g., 30 minutes) under daytime and nighttime conditions. The single crop coefficients are dependent on the type of crop being cultivated, the local weather conditions, soil evaporation, and the crop biomass growth stage (Allen et al., 1998). When soil evaporation composes a significant part of the total evapotranspiration (e.g., often the case for row crops during early plant growth stages), the dual crop coefficient approach is recommended (Allen et al., 1998). The dual crop coefficient method is a more sophisticated approach for ETa estimation that partitions the contributions of soil and vegetation to total evapotranspiration.

The single and dual crop coefficient approaches have been widely used in irrigation water management as a standardized tool to estimate ETa. The incorporation of remote sensing spatial data (e.g., on-site, airborne, spaceborne) coupled with remotely sensed ETa models has become essential tools to monitor vegetation growth, crop yield, and quasi-real-time crop water demands (Moran et al., 1989; Hall et al., 1992; Jacob et al., 2002; Seelan et al., 2003; Liaghat and Balasundram, 2010; Liou and Kar, 2014; Khanal et al., 2017; Deng et al., 2018; Awad, 2019; Maes and Steppe, 2019). However, the derivation of crop coefficient curves for different vegetation types was developed for pristine and uniform vegetation conditions. Allen et al. (1998) indicated a method to determine crop coefficients for non-pristine vegetation. Still, the approach is purely empirical, subject to input data uncertainties, and lacks physically-based validation.

Furthermore, the land surface heterogeneity of cropland fields often limits the accuracy of crop coefficient estimates of ETa due to contrasting crop water demands within different varieties of the same crop associated with uncertainties regarding the irrigation uniformity and scheduling practices (Allen et al., 2005; Varmaghani et al., 2021). With the advance of precision agriculture and the relevancy of varying irrigation rates to optimize crop productivity and minimize local and regional environmental disruption, spatially distributed ETa modeling has become attractive to conserve soil and water resources in the past thirty-five years (Mulla, 2013; Bhakta et al., 2019), with RS data being used to capture actual field conditions that deviate from standardized conditions associated to pristine vegetation without lack of water supply (Costa-Filho et al., 2022; Chávez et al., 2024).

1.5 Remote Sensing of Actual Crop Evapotranspiration

Remote sensing is the science of collecting data without having contact with the area of interest or target through measurements of emitted and reflected light within the visible, invisible, and thermal radiation spectrum (Rott, 2000; Schumugge et al., 2002). With the availability of multispectral and thermal spatial data from cameras attached to airborne (e.g., small aircraft, automated aerial vehicles), spaceborne sensors (e.g., satellites), and proximal devices (e.g., handheld radiometers), obtaining land surface information for monitoring crop growth, soil nutrients, and plant water use has become reliable for practical applications in irrigation water management (Pinter Jr et al., 2003; Yang et al., 2005; Liaghat and Balasundram, 2010; Atzberger, 2013; Shanmugapriya et al., 2019).

The different ETa models might be divided into two major approaches: the reflectance-based crop coefficient (RBCC) and the SEB models. The RBCC for daily spatial ETa modeling provides a transpiration crop coefficient (basal) as a function of vegetation indices derived from RED and Near-infrared (NIR) surface reflectance within the shortwave light spectrum, such as the normalized difference vegetation index (NDVI), soil adjusted vegetation index (SAVI), and vegetation

cover (f_c) for a variety of crop types (Heclman et al., 1982; Bausch and Neale, 1987; Neale et al., 1990; Bausch, 1995; Jayanthi et al., 2007; Trout and DeJonge, 2018; Wang et al., 2021).

Some RBCC models for ETa have been developed based on plant transpiration and crop coefficients functions calibrated using lysimeter or SWB ETa data and remote sensing data (e.g., Neale et al., 1990; Bausch, 1995; Trout and DeJonge, 2018). The RBCC modeling approach is empirical and requires multispectral surface reflectance (SR) as the spatial input data for mapping ETa. The RBCC approach has daily ETa estimation errors ranging from 15% to 40% (French et al., 2020; Pereira et al., 2020). Even though the RBCC ETa model approach is very simplistic, it still is a reliable tool for agricultural water management in many nations for a wide range of different crops (Bossie et al., 2009; Kamble et al., 2013; El-Shirberny et al., 2014; Park et al., 2017; Alface et al., 2019; Dingre et al., 2021).

The SEB approach for mapping ETa uses remote sensing SR and thermal data alongside local micrometeorological information to estimate instantaneous ETa at the local time of the remote sensing sensor overpass. Then, instantaneous ETa estimation is extrapolated to daily values through the evaporative fraction or ET_{ref} techniques (as discussed in Chávez et al., 2008). The simplified SEB considers that the control volume (e.g., an infinitely thin soil and vegetation layer) does not store heat. That energy for photosynthesis and plant biological processes are several orders of magnitude smaller than SEB components such as net radiation (R_n), soil heat flux (G), sensible (H), and latent heat (LE) fluxes (Arya, 2001).

The energy required for converting liquid water into water vapor (LE) is determined as the residual term (LE = R_n - G - H). The R_n flux is defined as the energy budget of the shortwave and longwave radiation at the surface level. G is the energy flux density that moves through a layer of soil, and H is the energy flux density transferred between the surface and the atmosphere through

convection (Arya, 2001; Heusinkveld et al., 2004; Foken and Napo, 2008; McShane et al., 2017).

There are two different methods to determine ETa using the SEB approach: the one-source SEB (henceforth, OSEB) considers the combined contributions of soil and vegetation to ETa rates (Lafleur, 1992; Moran et al., 1994; Rim, 2000; Boulet et al., 2012; Tang et al., 2013; Costa-Filho et al., 2021). The two-source SEB (or TSEB) partitions heat fluxes and the ETa in water transpired by the plants and evaporated from the soil (Massman, 1992; Norman et al., 1995; Anderson et al., 1997; Kustas and Norman., 2000; Li et al., 2005; Colaizzi et al., 2012; Kustas et al., 2019).

The OSEB approach relies on the individual modeling of R_n, G, and H fluxes, with H being calculated through a bulk aerodynamic resistance approach in which the air temperature gradient between the sink or source of heat (within canopy temperature) and the reference height above the plants (within the atmospheric inertial sublayer) is associated with a theoretical aerodynamic resistance to heat transfer. Errors related to estimating R_n and G range from 5% to 20% (Bastiaaanssen et al., 1998; Su, 2002; Allen et al., 2007; Costa-Filho et al., 2021). Typical errors associated with modeling scalar fluxes (e.g., H and LE) using the OSEB concept range from 15% to 40% for H and 10% to 30% for LE fluxes (Kustas et al., 1989; Lhomme et al., 2000; Chávez et al., 2005; Zhuang et al., 2016; Costa-Filho et al., 2021).

The more challenging OSEB model variable is the H flux since quantifying the heat transfer between surface and atmosphere is highly influenced by the three-dimensionality of canopy turbulence within and above the plants (Finnigan, 1985). Thus, several different OSEB algorithms have been developed to determine ETa with different approaches for H using remote sensing spatial data and simplifying the temperature gradient through a linear relationship between radiometric surface temperature (T_s) and thermally "cold" (low T_s pixel value) and "hot" (high T_s pixel value) approaches (Bastiaaanssen et al., 1998; Roerink et al., 2000; Su, 2002; Allen et al., 2007; Senay et

al., 2013).

Other H modeling approaches with the OSEB for ETa prediction have attempted to predict the temperature gradient in the bulk aerodynamic model (Chehbouni et al., 1996; Mahrt and Vickers, 2004; Chávez et al., 2005; Matsushima, 2005; Carrasco-Benavides et al., 2017; Costa-Filho et al., 2021). The recent study by Costa-Filho et al. (2021) has shown promising results when predicting maize LE with an overall accuracy of 10%. The OSEB is less computationally intensive than the TSEB approach and requires fewer input variables to map ETa. However, the OSEB method relies on assumptions about the temperature gradient that limit the application of OSEB for different surface types and climate conditions (Gonzalez-Lugo et al., 2009).

The TSEB is an iterative method suitable for remote sensing spatial data and requires SR and thermal data. Developed by Norman et al. (1995), the TSEB model has two different approaches regarding the bulk resistance approach for H associated with the vegetation and soil composites: the parallel TSEB (henceforth, TSEBpar) method considers that the processes that derive the heat transfer between plants, soil, and the air above canopy are independent of each other and can be modeled with two resistances for heat transfer (one for the H flux associated to the plants and another for the H flux related to the soil contribution).

The series TSEB (henceforth, TSEBser) method includes the concept of heat transfer interconnection in the soil-plant-atmosphere continuum through an additional resistance term and a parametrization of the surface aerodynamic temperature (T_o) as a weighted-averaged temperature among soil, plant, and air temperatures with respective resistances as weights. Chehbouni et al. (1996) defined T_o as the within canopy temperature that theoretically could be determined at the source or sink height of heat transfer. Typical errors associated with determining ETa (hourly and daily data) from TSEB algorithm for row crops (e.g., cotton, sorghum, and maize) are within 15% to 20% when compared to measurements of ETa from monolith weighing lysimeters (Chávez et

al., 2009b; Colaizzi et al., 2012; Colaizzi et al., 2014) under advective semi-arid climate conditions.

The SEB algorithms provide estimates of ETa as LE (W/m^2). A simple transformation of units converts instantaneous LE values from W/m^2 to instantaneous ETa in mm/h. Daily SEB ETa values need to be calculated and extrapolated from instantaneous ETa during the time the remote sensing sensor overpasses since remote sensing data are obtained around noon. Several approaches have been used to extrapolate SEB ETa from hourly to daily steps (as described in Chávez et al., 2008) based on daily evaporative fraction self-preservation (Brustaert and Sugita, 1992; Crago, 1996; Crago and Brutsaert, 1996).

However, there is no scientific agreement on the appropriate extrapolation method for daily ETa. Some OSEB and TSEB algorithms use the evaporative fraction ($EF = LE/[R_n - G]$) approach (as in Shuttleworth et al., 1989) as the preferred method to obtain daily ETa from instantaneous SEB ETa (e.g., Bastiaanssen et al., 1998; Roerink et al., 2000; Chávez et al., 2005; Elhaddad and Garcia, 2011; Poblete-Echeverría and Ortega-Farias, 2012; Consoli and Vanella, 2014; French et al., 2015) while others rely on the grass or alfalfa ET_{ref} fraction ($ET_rF = ETa/ET_{ref}$) approach (e.g., Allen et al., 2007; Chávez et al., 2010a; Colaizzi et al., 2014).

Chávez et al. (2008) have indicated that the SEB EF approach may provide more accurate results (5% error) for fields under canopy cover heterogeneity, canopy water stress conditions, and non-advective fields. On the contrary, ET_rF approaches would be recommended for homogeneous, pristine canopy under advective conditions. Furthermore, Chávez et al. (2008) reported that errors due to ET_rF extrapolation methods from grass and alfalfa are within 10% to 15% when estimated daily ETa values (using airborne remote sensing data) are compared to ETa measurements from EC systems.

The TSEB approaches for ETa modeling are often assumed to predict evaporation from soil better, while OSEB models provide reasonable predictions of transpiration from canopies (McShane et al., 2017). However, the TSEB models require the calculation of many input variables and assumptions that might limit the accuracy of ETa estimation compared to precisely calibrated OSEB models (Timmermans et al., 2007; French et al., 2015). Nowadays, with different remote sensing sensors providing images of cropland fields at various spatial resolutions (e.g., pixel size), it is essential to investigate the role of the other spatial resolutions in the RBCC, OSEB, and TSEB models for further refinement and generation of better ETa maps to support sustainable irrigation water management. Understanding the advantages and disadvantages of a given spatial resolution in mapping ETa constitutes the initial step toward defining calibration approaches to enhance multispectral and thermal imagery data quality.

Chapter 2

Literature Review and Study Objectives

2.1 The Spatial and Spectral Resolution Problem in Remote Sensing

Remote sensing technology involves the use of spaceborne (e.g., satellite), airborne (e.g., aircraft, drones, for instance), and proximal (e.g., handheld radiometers, infrared thermometers, or IRT) to obtain spatial and point-based data from the Earth's landscape. Getting near real-time data of an area of interest (AOI) is relevant to support a diverse range of environmental applications such as, but not limited to, water management, weather and climate analysis, flood monitoring, drought assessment, watershed development, forest mapping, and land cover classification (Elachi, 1988; Navalund et al., 2007, Pajares, 2015).

Proximal remote sensing technology has challenging applications in large fields. First, reliable spatial data requires intensive sampling strategies at different locations, which is often unrealistic and impractical due to the direct and indirect costs associated with data collection (e.g., equipment maintenance and technical labor, for instance). Second, systematic errors due to human error when operating sensors and instruments are likely to affect the quality of the data acquired and reduce sample size for further environmental applications (Li et al., 2020). Furthermore, field accessibility is another factor that might limit handheld remote sensing devices. Nonetheless, there have been studies that use handheld remote sensing devices to provide SR and thermal data in cropland fields to optimize crop yield and water management (Wang et al., 2002; Steddom et al., 2005; Reyniers et al., 2006; Gianquinto et al., 2011; Jeong et al., 2018; Hinojosa et al., 2019).

When it comes to obtaining spatial data suitable to any field, RS imagery data acquisition have become a significant asset since the second half of the 20^{th} century (Engel and Weinstein, 1983; Bizzel and Prior, 1985; Hinton, 1996; Johansen et al., 2007; Allam et al., 2019). Regardless of spatial or proximal data, each remote sensing technology has its spatial resolution, often referred to as pixel size or image footprint, and spectral resolution. Townshend (1980) defined imagery spatial resolution as the respective areal dimensions (usually given as a length scale) of a given image's smallest spatial unit data.

The most current spaceborne and airborne remote sensing sensors (e.g., WorldView-3, Advanced Spaceborne Thermal Emission and Reflection or ASTER, Moderate Resolution Imaging Spectroradiometer or MODIS, Landsat, Sentinel-2, Planet CubeSat, Planet RapidEye, Planet SkySat, and unmanned aerial systems or UAS, for instance) have been able to provide SR (e.g., RED, BLUE, GREEN, NIR, shortwave infrared or SWIR bands, for example) and, for some sensors, longwave infrared (LWIR, also referred to thermal radiation) imagery at a wide range of pixel sizes varying from 1000 m to 0.03 m (Johnson et al., 2003; Hansen et al., 2003; Drush et al., 2012; Dube and Mutanga, 2015; Houborg and McCabe, 2018a).

The spectral radiometric resolution is associated with the wavelength range (bandwidth or amplitude) of a given RS band that is sensed by the RS instrumentation. Each satellite, UAS, and proximal radiometer has different optical and thermal filters that allow for a specific range of light to be recorded by the camera or proximal device for a given SR or LWIR band. Some studies have investigated the effects of spectral differences on environmental applications. Rocchini (2007) investigated the effects of spatial and spectral radiometric resolution differences using ASTER, Landsat-7, and Quickbird satellite imagery to map plant species biodiversity in Tuscany, Italy. The conclusions from Rocchini (2007) indicated that spatial resolution was critical to identifying plant species, while the differences in larger spectral resolution bandwidth across the evaluated satellites

had a higher correlation with the biodiversity species richness index.

Pandya et al. (2007) studied the differences in spectral resolution between Indian Remote Sensing satellites (IRS-1A to IRS-1D, IRS-P2 to IRS-P6) for wheat fields in India. They concluded that discrepancies in the spectral resolution of the IRS satellites led to 3 and 4% uncertainty in obtained top-of-the atmosphere reflectance and NDVI, respectively. Skakun et al. (2021) investigated the yield of maize and soybeans in Iowa using WorldView-3, Planet CubeSat, Sentinel-2, and Landsat-8 satellite sensors. They concluded that some spectral resolution bands from Green, Red-Edge, and NIR wavelengths are relevant to characterize crop yield. Furthermore, Skakun et al. (2021) indicated that the explained variability of yield mapping decreases with a pixel size increase.

Different remote sensing sensors have varying bandwidth capabilities to record the brightness levels reflected by a given surface target. The differences in bandwidth from each remote sensing sensor are associated with the multispectral detector radiation sensitivity, cross-sensor data consistency, and signal-to-noise ratio characteristics (Houborg and McCabe, 2016). Trishchenko et al. (2002) indicated that depending on the spaceborne remote sensing system (e.g., AVHRR, MODIS), the surface reflectance in the RED and NIR values vary from -25% to 12% and -2% to 4%, respectively. When comparing surface reflectance from AVHRR and MODIS, differences in RED and NIR bands can be up to 30% to 40%. Vermote et al. (2002) compared BLUE surface reflectance values between MODIS and Landsat-7 and found that BLUE surface reflectance data from MODIS was 7% lower in magnitude compared to its Landsat-7 counterpart.

Furthermore, it is important to acknowledge that the final surface reflectance products uncertainty is also associated with the level of atmospheric corrections applied to the at-sensor brightness data as reflected light travels from the surface and is sensed by a given multispectral detector (Wang et al., 2001). Vermote et al. (2000) indicated the relative error associated with surface reflectance values from MODIS (MOD9) spaceborne sensor in the BLUE (50% - 80%), GREEN (5% - 12%),

RED (10% - 33%), and NIR (3% - 6%) wavelength spectrum could be related to insufficient atmospheric and other environmental corrections to the at-sensor brightness data.

Because remote sensing imagery are often used as input data for a wide range of ecological modeling applications, the accuracy of predicting any pertinent environmental variable will depend on a given model approach response to the characteristics associated with the remote sensing sensor. Hence, spatial resolution in remote sensing applications becomes a never-ending and complex issue that is aggravated when different spectral sensors are considered. Thus, it is imperative to understand the role of an image's spatial and spectral radiometric data on the accuracy of environmental models that use spaceborne, airborne, and proximal sensors as input data. Identifying an optimal remote sensing sensor for ETa mapping might contribute to the adequate use of the best spatial and spectral resolution for a given environmental application.

For ETa mapping, the optimal remote sensing sensor would result in less uncertainty in the prediction of ETa for a given modeling approach. Finding the best remote sensing data characteristics for ETa depends on the reliability of spatial and spectral data from satellite, UAS, or handheld sensors, as well as from information about the spatial and spectral resolution of the data used to calibrate ETa algorithms. A thorough understanding of the underlying factors that contribute to potential differences in ETa model performance across different remote sensing sensors is critical to improving ETa estimated products using algorithms such as the RBCC, OSEB, and TSEB.

The particular problem of spatial scale in remote sensing has been intensively investigated for the past thirty years within a broad range of scientific fields. Turner et al. (1989) studied the impact of different spatial scales on predicting landscape ecological variables associated with the land-vegetation-atmosphere nexus. They indicated that an increase in pixel size decreased the retrieval of information about the number of land cover types. Raffy (1992) analyzed the effect of downscaling the spatial resolution of images on the quality of SR data and provided a generalized

method to reduce errors associated with downscaling images of heterogeneous surfaces. Marceau and Hay (1999) proposed a framework to address the modifiable areal unit problem in remote sensing by studying the effects of dividing a given area into independent sections to characterize a given geographical domain spatially. The works of Kasampalis et al. (2018) and Lechner et al. (2020) reviewed the advantages and disadvantages of using different remote sensing imagery sensors when studying agricultural crop growth modeling and forest ecology management, respectively.

Nonetheless, when investigating the role of spatial scale in estimating ETa, research efforts have only expanded in the past fifteen years. McCabe and Wood (2006) analyzed the role of spatial heterogeneity when predicting watershed ETa using Landsat-5 (30 m), ASTER (90 m), and MODIS (1020 m) satellite sensors using the OSEB approach by Su (2002). Matese et al. (2015), while not addressing the estimation of ETa in an irrigated vineyard field, studied the spatial differences in NDVI across uncrewed aerial vehicles (drone and aircraft at 0.05 m and 0.50 m spatial resolutions, respectively) and satellite sensors (Planet RapidEye at 5 m pixel size). Matese et al. (2015) found that large pixel size imagery is not reliable for the characterization of intra-row vineyard variability for heterogeneous surfaces.

Sharma et al. (2016) studied the impact of Landsat-5 (30 m) and MODIS (500 m) spatial resolution when estimating watershed hourly ETa using several geographical information system (GIS) resampling techniques coupled with the OSEB approach by Su (2002). Sharma et al. (2016) found that aggregated Landsat-5 imagery matching MODIS spatial resolution (500 m) had the smallest root mean square error (RMSE) between the two sensors (0.064 mm/h) and that the OSEB model explained 91% of the variability in measured hourly ETa from a BR system.

Nassar et al. (2020) investigated the accuracy of SEB fluxes using different drone imagery pixel sizes (0.10 m to 0.60 m) in a vineyard field in California using a TSEB model (Norman et

al., 1995). The drone images were aggregated later to generate coarse imagery resolution ranging from 3.6 to 30 m pixel sizes. The findings from Nassar et al. (2020) indicated that R_n and G errors were slightly the same across different remote sensing sensors, while H and LE errors were monotonically related to the remote sensing spatial resolution. Aragon et al. (2021) used Landsat-8 (30 m), Sentinel-2 (10 m), and Planet CubeSat imagery (3 m) to evaluate the accuracy of daily wheat ETa estimation in Saudi Arabia using a modified Priestley-Taylor ETa model (Fischer et al., 2008). Aragon et al. (2021) indicated that differences in the spectral resolution of the spaceborne sensors affected the magnitude of ETa predictions, with Sentinel-2 having the smallest mean value of ETa estimation among the three remote sensing sensors and that fine spatial resolution satellite sensors are recommended for small agricultural fields.

With a wide range of ETa modeling approaches using remote sensing data, there have not been comprehensive studies that evaluate the advantages and disadvantages of a given imagery spatial resolution considering different published ETa modeling approaches. Finally, remote sensing data from spaceborne and airborne sensors are prone to inaccuracy due to attached camera malfunctioning issues, cloud cover effects over the AOI, and other related operational issues (Kelly et al., 2019; Aragon et al., 2020). Thus, there is an opportunity to focus on improving ETa mapping for cropland water use management by adjusting multispectral data for sensors that may fail to deliver consistent and accurate products for a given remote sensing of the ETa algorithm.

2.2 Remote Sensing Methods for Improving Imagery Data

Several studies have attempted to improve the quality of RS imagery data using other sensors as reference (henceforth, imagery fusion). Zhou et al. (1998) developed an approach to merge Landsat and SPOT panchromatic imagery using a wavelet transform function approach (WTFA) for image interpretation. Several studies have investigated the use of WTFA to account for possible image enhancement across multiple spaceborne sensors (Sheng et al., 1992; Wu et al., 2005; Hong

et al., 2009; Cheng et al., 2015; Ma et al., 2019). The WTFA method has several limitations regarding unpredictable changes in the internal coefficients due to input-signal drift (Strang, 1989), poor directionality due to function coefficients not capturing all features in an image (Watson and Ahumada, 1985; Burns et al., 1994); and absence of relevant phase information when merging two different imagery resolutions (Grossman and Morlet, 1984; Grossman et al., 1990). Nonetheless, agricultural management studies have used wavelet transform functions to analyze vegetation index time series and fill missing data in remote sensing images (Martínez and Gilabert, 2009; Kandasamy et al., 2013; Zheng et al., 2020).

As improved versions of the original wavelet transform function, several modified approaches based on the transfer domain method have been investigated in the literature to overcome the limitations of implementing accurate image fusion techniques. A wavelet multi-resolution analysis (WMRA) is an approach that relies on approximating image signals using different spatial resolution sensors and without introducing spectral distortion in the final imagery product (Nunez et al., 1999; Myint, 2010). A bandelet transform function (BTF) is another variation of the WTFA in which an image is decomposed into subsets that, once merged with another spatial resolution imagery, conserve the geometric properties of the original image through a reconstruction process based on bandelet coefficients and inverse function (Le Pennec and Mallat, 2000; Qu et al., 2007).

A curvelet transform function (CuTF) passes a filtering window through an image using smoothed functions to increase image enhancements at a smaller spatial resolution (Starck et al., 2002; Choi et al., 2005; Devulapalli and Krishnan, 2019). A contourlet transform function (CoTF) is a modified CuTF approach that focuses on defining a construction domain of image signal before considering smooth filtering functions (Do and Vertterli, 2005). Even though the list of improved WTFA is extensive, the applicability of such approaches to agricultural fields and, precisely, ETa mapping has its technical challenges. Ha et al. (2013a) argued that these WTFA and modified versions are often used for applications beyond the scope of remote sensing applied to agriculture.

These image fusion techniques are often associated with panchromatic and multispectral image decompression, image visualization, and classification maps. The ending products from WTFA and improved approaches do not provide calibrated SR data, representing a setback to remote sensing environmental modeling (Gao et al., 2006).

Color composition methods have been used in image fusion to combine the visible SR bands (e.g., RED, BLUE, and GREEN) from two different imagery sensors into a secondary enhanced image. This approach is often referred to as intensity-hue-saturation transformation (IHS). It breaks down a multispectral image into hue, saturation, and intensity components in the visible light spectrum. Then, by replacing the intensity image component with a higher resolution image from a different sensor and restructuring it with the original hue and saturation elements, the image fusion process is completed (Pohl and van Genderen, 1998; Tu et al., 2001; Choi, 2006; Jain et al., 2019). For ETa mapping applications, the wavelength bands in the invisible light spectrum (e.g., near-infrared, for instance) are required to calculate vegetation indices that serve as input data for most remotely sensed ETa algorithms (Huete, 1988; Qi et al., 1994; Rondeaux et al., 1996). Thus, the IHS method has limited applicability in mapping ETa.

Another imagery processing method is the Principal Component Analysis (PCA) approach, which is based on the concept of reducing the dimensionality of a given image by merging SR bands into principal components that explain most of the variability for a given spatial domain (Wold et al., 1987; Abdi and Williams, 2010; Bro and Smilde, 2014). The PCA can combine the essential bands in an image based on how much spatial variance they explain (Rao, 1964; Rodarmel and Shan, 2002; Ng, 2017). The first few PCA-generated images are considered to maintain most of the variability in the original image (González-Audícana et al., 2004; Gautam et al., 2007). However, SR and LWIR thermal bands have been used independently to characterize certain element features in an image (Ji et al., 2011; Du et al., 2016; Costa et al., 2020; Raj et al., 2021). Furthermore, PCA values do not provide any physical meaning and have limited applicabil-

ity in modeling (Jolliffe, 1982). Thus, PCA is recommended in scenarios in which remote sensing sensors have several bands (e.g., hyperspectral imagery) that need to be compressed for supervised and unsupervised classification (Farrell and Mersereau, 2005; Sun et al., 2019).

For at least eighteen years, researchers have developed methods that focus on expanding the applicability of image fusion in remote sensing through adaptive image fusion (AIF) approaches (Park and Kang, 2004; Gao et al., 2006; Petrovic and Cootes, 2007; Belgiu and Stein, 2019; Zhang et al., 2020; Wang et al., 2021). AIF approaches have been developed to correct images for geometry distortion and modify imagery spatial resolution without losing the spectral properties of the original image (Ha et al., 2013a).

Three common approaches in the literature for imagery data fusion are the smoothing filter-based intensity modulation (SFIM), the spatial and temporal adaptive reflectance fusion model (STARFM), and the Enhanced STARFM (ESTARFM), developed by Liu (2000), Gao et al. (2006), and Zhu et al. (2010), respectively. Using the STARFM, Li et al. (2017) evaluated the accuracy of estimating LE for different surface types (e.g., maize, orchard, bare soil, wetlands) in irrigated areas in China using combined MODIS (250 m) and ASTER (90 m) spatial resolution with an OSEB model (Su, 2002). Compared to EC measurements of ETa, the normalized errors when predicting H and LE over large maize fields were 47% and 9%, respectively. Cammalleri et al. (2014) evaluated STARFM image fusion performance to estimate daily ETa for cotton, maize, and soybeans in Texas and Nebraska when using Landsat-5 (30 m) and MODIS (250 m) and a TSEB approach. The normalized mean absolute error (NMAE) for cotton, maize, and soybeans ETa estimation was 28%.

Even though there are recent studies that have applied AIF approaches to surface heat fluxes and daily ETa mapping in the literature (Ma et al., 2018; Yi et al., 2018; Xu et al., 2019), the underlying assumptions and intrinsic details of the AIF approaches might be violated depending on the local characteristics of a given agricultural field setting. The STARFM and ESTARFM approaches

use a filtering window mechanism to apply weights on neighboring surface reflectance pixel data from low-resolution imagery by assuming field homogeneity (similar canopy biomass conditions) during the satellite overpass (Gao et al., 2006). However, agricultural fields (row crops, mainly) are prone to show biomass heterogeneity and spatially varying crop water demands due to multiple factors such as soil heterogeneity properties (i.e., texture, organic matter, salinity levels), canopy physiology characteristics, soil water redistribution in the root zone, and local microclimate constrains (Moore et al., 1993; Famiglietti et al., 1998; Hupet and Vanclooster, 2002; Williams et al., 2003; Brocca et al., 2007).

Furthermore, the STARFM and ESTARFM theoretical development to generate SR images of satellite sensors during the respective overpass time window. This is, MODIS data (daily temporal resolution) is used as a surrogate to generate consistent spectral resolution of finer remote sensing sensors rather than improving the spectral resolution of the satellite data being temporally and spatially interpolated for days without imagery. The SFIM method relies on the idea of fusing two temporally coinciding imagery sensors (Liu, 2000).

Besides image fusion approaches, there have been studies to adjust the spatial resolution of a given remote sensing imagery sensor using ancillary multispectral and thermal data. These methods rely on the concepts of upscaling or downscaling the pixel size of an image (Han et al., 2013b; Raj et al., 2013). An upscaled or aggregated remote sensing image has a larger (or coarser) pixel size than the original image. A downscaled image has a smaller (or finer) spatial resolution than its counterpart.

Upscaling an image in remote sensing is often referred to as pixel aggregation (Bian and Butler, 1999; He et al., 2002; Carrasco et al., 2019). Standard image aggregation methods are based on imagery resampling techniques such as simple averaging, nearest neighbor, bilinear, and cubic convolution (Gurjar and Padmanabhan, 2005; Ershadi et al., 2013; Porwal and Katiyar, 2014). Down-

scaling methods for remote sensing imagery adjustment have more straightforward approaches based on pixel resampling techniques (Zheng et al., 2017; Wang et al., 2020) or more sophisticated methods that consider other remote sensing sensors at finer spatial resolution for both SR and LWIR thermal bands (e.g., Kustas et al., 2003; Norman et al., 2003; Trishchenko et al. 2006; Agam et al., 2007; Boucher, 2009). The resampling techniques for either upscaling or downscaling remote sensing images rely on a kernel filtering window passing through a set of pixels and adjusting the values of neighboring pixels at the desired spatial resolution (Schläpfer et al., 2001; Baboo and Devi, 2010; Lyons et al., 2018). Thus, resampling methods do not necessarily improve the accuracy of given remote sensing imagery since changing the spatial resolution of an image using its pixel data generates a new image that often preserves the descriptive statistics of the original image at the expense of only modifying the spatial resolution.

The downscaling methods that incorporate external fine spatial resolution imagery are commonly applied in agricultural studies to thermal image sharpening using multispectral data from fine spatial resolution sensors (Kustas et al., 2003; Agam et al., 2007; Jing-xua et al., 2010; Ha et al., 2010; Faraji et al., 2021). Some downscaling methods have attempted to sharpen multispectral images using auxiliary fine-resolution sensors across various scientific applications (Trishenko et al., 2006; Hilker et al., 2009).

However, these methods are limited to least square regression approaches that are not data-driven and insightful to understanding the role of spatial resolution on ETa mapping. Current research addressing downscaling methods is only applicable to a prescribed set of remote sensing imagery sensors. The sharpening of SR and LWIR thermal images, using pixel disaggregation approaches, is evaluated within the imagery sensor that is selected in the studies and does not identify the optimal spatial and spectral resolution for ETa mapping, which constitutes an evident gap in the current literature.

2.3 Machine Learning, Crop Evapotranspiration, and Remote Sensing Applications

Naga and Murphy (2015) define machine learning (ML) as a set of algorithms based on computer technology that have the purpose of simulating humanity's thinking capacity to learn from external datasets. ML techniques in science have been relevant to advanced modeling and data analysis for the past twenty years (Jordan and Mitchell, 2015). Also, ML has been an appropriate tool for prediction and self-calibration models (Zhong et al., 2021). In micrometeorology, hydrology, and remote sensing studies, ML algorithms are justified due to the large amount of data generated through weather, remote sensing imagery, and surface energy flux sensors. ML algorithms for prediction and calibration purposes are categorized in different regression models (Maulud and Abdulazeez, 2020).

Ordinary ML regression approaches applied in environmental remote sensing studies are the following: Linear regression models (Maxwell et al., 2018, Han et al., 2019); regression trees (Lobel et al., 2005; Homer et al., 2012; Elmahdy and Mohamed, 2021); support vector machines or SVM (Ahmad et al., 2010; Mohajane et al., 2021); Gaussian process regression or GPR (Pasolli et al., 2010; Hultquist et al., 2014; Pipia et al., 2021); ensemble trees such as random forests (Pal, 2005; Avand and Moradi, 2021; Costache et al., 2021). These ML regression approaches are trained to make predictions by learning from the data in the training phase. Once a given ML model has known the intrinsic aspects of different data variables, prediction is made at higher accuracy when compared to fitting empirical equations using least-of-square regression or other curve-fitting techniques (Mair et al., 2000; Granata, 2019).

Recent studies have used ML to estimate ETa or ET_{ref} for various vegetation types under different climate conditions in hydrology and agricultural water management studies. Shrestha and

Shukla (2015) applied an SVM model to estimate pepper ETa and crop coefficients using lysimeter data in Florida, USA. Tang et al. (2018) employed SVM to model rainfed maize ETa. Mohamadi and Mehdizadeh (2020) used an SVM regression to predict grass ET_{ref} using micrometeorological data as predictors from three standardized weather station sites in semi-arid regions of Iran.

Wen et al. (2015) and Chia et al. (2020) applied SVM to predict grass ET_{ref} using limited micrometeorological data in China. Granata (2019) modeled ETa using a regression tree approach with data from a strawberry farm in Florida, USA. Macek et al. (2018) predicted grass ET_{ref} with a regression tree using data from twelve weather stations in Slovenia. Granata et al. (2020) studied the application of a combined regression tree and random forest ML to estimate wetland evapotranspiration in Florida, USA. Carter and Liang (2019) evaluated ten ML approaches to estimate terrestrial ETa from remote sensing data. Karsabi (2018) used GPR to forecast daily grass ET_{ref} in Iran. A recent study by Sattari et al. (2021) attempted an evaluation of monthly ET_{ref} using kernel-based and deep-learning methods.

Regarding the application of ML in remotely sensed ETa, few recent studies have shown progress in providing approaches to adjust the spatial resolution for estimating ETa. Xu et al. (2018) tested different ML approaches for upscaling ETa from local to large scale (e.g., watershed). Houborg and McCabe (2018b) developed an enhancement method to improve the quality of the Planet CubeSat SR data images using an image fusion approach based on ML regression by combining data from Landsat and MODIS for crop water management. Aragon et al. (2021) applied Houborg and McCabe (2018b) ML approach to adjust the spectral data of Planet CubeSat imagery to estimate ETa in an irrigated center pivot wheat field in Saudi Arabia.

However, these few recent studies are not comprehensive. They do not provide evidence to justify the choice of a given ML in the context of the ETa mapping using remote sensing. Surface heterogeneity conditions in agricultural fields have not yet been considered in the literature when

performing image fusion with ML techniques. The pixels of SR and LWIR thermal images from row crop fields are mixed signatures from the simultaneous exposed soil and vegetation during the remote sensing sensor overpass time. The current ML methods for remote sensing image fusion consider the mixed pixel data (original pixel) when adjusting a given sensor's spatial resolution, spectral, and thermal information.

Even though adjusting a given image using the actual pixel values is scientifically justifiable (Houborg and McCabe, 2018b), the singular characteristics of row crop fields regarding surface heterogeneity, canopy structure development, and water stress conditions due to climate change limit the applicability of such holistic approaches to a wide range of real case scenarios. Attempts to incorporate the concepts of pixel decomposition or spectral unmixing approaches (Byonocore et al., 1981; Keshava and Mustard, 2002; Yang et al., 2007; Yang et al., 2017; Kaur et al., 2019) into ML regression for image fusion have not been found in the literature.

The idea of combining spectral unmixing or pixel decomposition methods applied to remote sensing images has been used mainly for image feature classification (Gong et al., 1994; Van Der Meer, 1995; Hu et al., 1999; Goodman and Ustin, 2007; Villa et al., 2010; Martin and Plaza, 2011; Wang et al., 2016). These studies have facilitated the detection of different elements in each imagery pixel to quantify certain features of interest in remote sensing image classification rather than partitioning the SR values of soil and vegetation signals on a pixel-by-pixel basis (Quintano et al., 2012). Regarding surface mixed pixels with only soil and vegetation, Behrens et al. (2005) presented a simple empirical equation to partition soil and vegetation using a linear interpolation approach and f_c for agricultural fields in Germany with different soil textures. However, Behrens et al. (2005) do not provide enough scientific validation to justify the use of their proposed model for SR data decomposition in an agricultural setting.

Goudriaan and van Laar (1994) provided a physically-based model for partitioning the SR data into soil and vegetation based on a non-linear radiative transfer model that accounts for the upward and downward light fluxes above and within the plant canopy structure (e.g., leaves, stems, and other related elements). The non-linear spectral unmixing model is based on the radiation attenuation theory that relates the fraction of light transmitted through the vegetation as an exponential function of leaf area index (LAI) and the light extinction coefficient (k_p).

The LAI variable is the area occupied by plant leaves per unit area of the ground surface. The parameter k_p is associated with the canopy structure, the position of the sun relative to the ground surface, and multispectral leaf response (Price, 1992; Choudhury et al., 1994; Baret et al., 1995; Price and Bausch, 1995). Furthermore, the k_p parameter, a critical term to determine the partitioning of a mixed pixel into soil and vegetation composites, is a function of the solar zenith angle and leaf angle distribution (Campbell, 1986; Campbell, 1990; Goudriaan and van Laar, 1994; Campbell and Norman, 2012). With most remote sensing imagery acquisition around local solar noon for most ETa mapping applications (e.g., 10 am to 2 pm), the solar zenith angle for a given location is approximately the same throughout most of the crop growing season. Regarding leaf angle distribution, the underlying assumption is that, for most canopies, the leaf angle distribution is approximately equivalent to an ideal spherical leaf and remains nearly the same for a given crop throughout its growing season (Garrigues et al., 2008; Campbell and Norman, 2012).

However, the natural heterogeneity of vegetated surfaces also plays a role in determining the effectiveness with which light is reflected, transmitted, absorbed, and intercepted by plants (Drouet et al., 1999; Zhang et al., 2005). De Costa and Dennett (1992) have indicated that under varying conditions of soil moisture (a surrogate for changing biomass conditions), the light extinction coefficient depends on the differences in spatial-temporal canopy structure (e.g., LAI) and might be subject to variability within cropland fields.

A few studies have attempted to investigate k_p and remote sensing data to account for spatial canopy variability. Recent studies by Lai et al. (2012) and Tan et al. (2020) indicated that k_p and NDVI have a strong and linear negative correlation for regional and local scales, respectively. However, relating k_p to a given vegetation index is a purely empirical approach that limits the range of applicability for different crops and remote sensing sensors. Also, the inherited non-linear nature of light transmission, absorption, and scattering within a surface requires more sophisticated approaches to describe the canopy structure in agricultural fields. Thus, it is essential to adequately address k_p modeling using a more robust approach that accounts for spatial variability in row crop fields before partitioning soil and vegetation surface reflectance data.

Thus, there is an evident need for extensive research on the best ML approaches to adjust the spatial and spectral radiometric data of remote sensing images for a given ETa algorithm that incorporates a robust pixel decomposition method. The thorough development of a multidisciplinary calibration approach for SR data fusion towards ETa mapping has not been extensively investigated up to this day.

2.4 Research Hypothesis and Problem Statement

This study hypothesizes that the accuracy of crop ETa mapping products is significantly influenced by the source and type of RS imagery utilized, including spaceborne, airborne, and proximal sensors, as well as variations in RS sensor types and methods of imagery post-processing. It is expected that different RS of crop ETa algorithms, such as RBCC, OSEB, or TSEB, will demonstrate variable sensitivities to these factors. By identifying the optimal spectral and spatial resolutions that provide the most accurate predictions of crop ETa, this study aims to help support sustainable irrigation water management in cropland settings.

Moreover, the complex nature of the data involved in managing irrigation spatially requires the use of reliable data-driven computational approaches such as ML models. The study also acknowledges the extensive capabilities of RS sensors, which vary widely in their spatial, spectral, and temporal resolutions and provide continuous data critical for effective irrigation water management. A key challenge identified is determining which sensors are optimally adequate for specific RS of ETa algorithms. Furthermore, even when an optimal remote sensing sensor is identified as optimal in terms of spectral and spatial resolutions, it may not align with the temporal resolution required by water users, who need consistent data to support daily or weekly irrigation scheduling decisions.

In scenarios where the optimal remote sensing sensor is unavailable, the use of sub-optimal imagery or point-based data could be necessary. This research is essential to bridge the scientific gap in approaches to enhance the quality of RS multispectral data by focusing on identifying the most appropriate remote sensing sensor for a given ETa algorithm and enhancing the quality of sub-optimal data. There is a significant gap in studies that analyze the relationship between the performance of specific ETa algorithms and the spatial and spectral resolutions of remote sensing sensors. Additionally, the literature on the application of ML techniques for image enhancement in the context of agricultural water management often overlooks the distinct contributions of soil and vegetation in mixed pixels, particularly prevalent in row crop fields.

This study focuses on an innovative approach that combines advanced ML regression techniques with an optimized surface reflectance decomposition model. This novel approach, which has not been published, aims to provide scientific contributions to the fields of remote sensing, hydrology, and sustainable agricultural water management, thereby addressing a critical gap in the existing scientific literature.

The main three scientific contributions (novelty) of this study:

a) A comprehensive evaluation of how specific RS of ETa algorithms perform relative to various RS sensors. The novelty relies on identifying the most effective algorithm-sensor combinations for accurate crop ETa predictions in agricultural settings.

b) A novel semi-empirical approach to model the k_p parameter that contributes to the decomposition of surface reflectance data into distinct soil and vegetation components. The novelty of the k_p model relies on the ability to determine spatial predictions of how vegetated surfaces intercept light.

c) A novel methodology to enhance the quality of sub-optimal RS data, enabling its use in generating accurate crop ETa maps. This approach addresses the common challenge of data variability due to non-ideal RS sensor multispectral data availability.

2.5 Study Objectives

2.5.1 Overall Goal

This study's overall goal focused on supporting sustainable irrigation water management practices due to growing concerns about water scarcity related to climate change. Thus, the overall idea was to identify the best RS imagery and data to estimate hourly and daily crop ETa. The study compared three different ETa algorithms to determine which provides the most reliable data under varying agricultural conditions. Furthermore, the study focused on developing and validating an RS data calibration approach to enhance the quality of RS surface reflectance data from the RS sensors that initially did not provide accurate predictions of crop ETa. The calibration protocol for RS surface reflectance data could enable a more precise mapping of crop water usage in terms of crop ETa. Ultimately, this study aimed to provide a comprehensive evaluation that could serve as the basis for future applications in agricultural settings to optimize water usage, enhance crop yield, and contribute to the broader goals of sustainable irrigation scheduling.

2.5.2 Specific Goals

To better support irrigation water management with enhanced RS data quality products, the specific goals of this study are the following:

a) Evaluate the impact of different spatial and spectral resolutions provided by spaceborne, airborne, and proximal remote sensing sensors on the errors encountered when estimating hourly and daily ETa. This evaluation can help understand how pixel size and data resolution affect the accuracy of ETa predictions, thereby guiding the selection of appropriate RS data in irrigation water management applications.

b) Identify the optimal remote sensing spectral and spatial data that yields the most accurate ETa predictions for specific algorithms among various remote sensing sensors, including Landsat-8 (30 m), Sentinel-2 (10 m), Planet CubeSat (3 m), handheld radiometer (1 m), and UAS (0.03 m). The focus is on comparing the effectiveness of different RS sensors and their settings to determine the best ones for predicting crop ETa in a semi-arid climate condition.

c) Improve the quality of the RS surface reflectance data for irrigation water management applications using a novel approach based on spectral decomposition, machine learning, and spatial vegetation architecture modeling. This novel approach for enhancing the quality of the RS data for crop ETa modeling and irrigation scheduling focuses on providing more reliable ETa data to help support sustainable agricultural water management decisions at the local scale (e.g., cropland fields).

d) Evaluate the performance of the optimized RS products for ETa mapping using a multi-year independent dataset from row crop fields in Colorado. This independent performance evaluation of crop ETa models focuses on validating the practical applicability and effectiveness of the developed methodologies in irrigated cropland field settings.

Chapter 3

Materials and Methods

3.1 The Two-Source Pixel Decomposition Algorithm

The light attenuation within the canopy with non-horizontal leaves is modeled using a decaying exponential function based on the Beer-Lambert spectroscopy law, as indicated by Eq. 3.1 below (Anderson, 1966; Larcher, 1983; Marshall and Warring, 1986; Vose et al., 1995):

$$\phi_{down} = \phi_o \cdot exp(-k_p \cdot LAI) \tag{3.1}$$

where ϕ_{down} is the downward short-wave irradiance (light flux) within the canopy (W/m^2); ϕ_o is the downward short-wave irradiance above the canopy (W/m^2); k_p is the light attenuation coefficient (dimensionless); LAI is given in m^2/m^2.

For the case scenario of leaves that are not black and horizontal, there will be a radiation contribution to the ϕ_{down} flux characterized as an upward light flux (ϕ_{up}) from the canopy (Goudriaan and van Laar, 1994). Thus, the exact solution for the downward and upward light fluxes is given as the sum of two non-linear exponential functions and indicated by Eqs. 3.2 and 3.3, respectively (Goudriaan and van Laar, 1994):

$$\begin{aligned}\phi_{down} = &\left[\frac{\phi_o}{1+\eta \cdot exp(-2k_p \cdot LAI)}\right] exp(-k_p \cdot LAI) + \\ &\left[\frac{\phi_o \cdot \eta \cdot exp(-2k_p \cdot LAI)}{1+\eta \cdot exp(-2k_p \cdot LAI)}\right] exp(k_p \cdot LAI)\end{aligned} \tag{3.2}$$

$$\phi_{up} = \left[\frac{\phi_o \cdot SR_c}{1 + \eta \cdot exp(-2k_p \cdot LAI)}\right] exp(-k_p \cdot LAI) + \left[\frac{\phi_o \cdot \eta \cdot exp(-2k_p \cdot LAI)}{SR_c + SR_c \cdot \eta \cdot exp(-2k_p \cdot LAI)}\right] exp(k_p \cdot LAI) \tag{3.3}$$

$$\eta = \frac{SR_c - SR_{soil}}{SR_{soil} - \frac{1}{SR_c}} \tag{3.4}$$

where SR_c and SR_{soil} are the vegetation and soil reflectance of a given multispectral band (dimensionless), respectively. Eq. 3.4 presents the η parameter that is associated with the difference between SR_c and SR_{soil}.

The SR of a mixed surface (vegetation and soil combined) is then calculated as the ratio between the total upward fluxes from soil and vegetation and the downward light flux above the canopy and indicated by Eq. 3.5 as follows (Goudriaan and van Laar, 1994):

$$SR = \frac{\left[\frac{\phi_o \cdot SR_c}{1 + \eta \cdot exp(-2k_p \cdot LAI)}\right] + \left[\frac{\phi_o \cdot \eta \cdot exp(-2k_p \cdot LAI)}{SR_c + SR_c \cdot \eta \cdot exp(-2k_p \cdot LAI)}\right]}{\phi_o} \tag{3.5}$$

where SR is the surface reflectance of mixed surface (dimensionless). After some algebraic manipulation, the final expression for SR of a mixed pixel is given by Eq. 3.6:

$$SR = \frac{SR_c + \frac{\eta \cdot exp(-2k_p \cdot LAI)}{SR_c}}{1 + \eta \cdot exp(-2k_p \cdot LAI)} \tag{3.6}$$

The multispectral data from spaceborne, airborne, and proximal remote sensing sensors provide SR (e.g., RED, GREEN, BLUE, and NIR) to calculate the vegetation indices (e.g., NDVI, OSAVI, for instance) used to estimate LAI in the literature (e.g., Anderson et al., 2004; Hasegawa et al., 2006; Chávez et al., 2009b; Hasegawa et al., 2010). Thus, the only unknowns in Eq. 3.6 are

k_p, SR_c, and SR_{soil}. The multispectral decomposed values of SR are SR_c and SR_{soil}.

The spectral unmixing theory assumes the SR of a given mixed pixel is composed of the individual contribution of land surface features (henceforth, endmembers) associated with a weighting factor that accounts for the percentual area occupied by each endmember (Graetz and Gentle, 1982; Hu et al., 1999; Gilabert et al., 2000; Keshava and Mustard, 2002; Xiao and Moody, 2005; Sprintsin et al., 2007). Thus, for a cropland pixel that has only two endmembers (soil and vegetation), the spectral unmixing model is given by Eq. 3.7, as follows:

$$SR \cong SR_c \cdot f_c + SR_{soil} \cdot (1 - f_c) \tag{3.7}$$

The $SR_c - SR_{soil}$ difference in Eqs. 3.4 and 3.6 might be calculated when the derivative of SR with respect to f_c is introduced in the SR decomposition model. In Eq. 3.7, SR could be also described as a function of two linear terms ($SR = f(c, s) = c + s$) regarding vegetation ($c(f_c) = SR_c \cdot f_c$) and soil ($s(f_c) = SR_{soil} - SR_{soil} \cdot f_c$) contributions to the reflected light of a given band. The c and s functions have f_c as the primary variable. Using the mathematical notation of a function of two variables gives the following algebraic equation for SR, as follows (Eq. 3.8):

$$f(c, s) = c(f_c) + s(f_c) \tag{3.8}$$

Using chain rule, the derivative of SR with respect to f_c is given as follows (Eq. 3.9):

$$\frac{dSR}{df_c} = \frac{\partial f(c, s)}{\partial c} \cdot \frac{dc}{df_c} + \frac{\partial f(c, s)}{\partial s} \cdot \frac{ds}{df_c} \tag{3.9}$$

Since Eq. 3.8 is given as the sum of two functions, the partial derivatives in Eq. 3.9 are given as follows (Eq. 3.10):

$$\frac{\partial f(c,s)}{\partial c} = \frac{\partial f(c,s)}{\partial s} = 1 \tag{3.10}$$

The ordinary derivatives $\frac{dc}{df_c}$ and $\frac{ds}{df_c}$ are given by Eqs. 3.11 and 3.12, respectively:

$$\frac{dc}{df_c} = SR_c \tag{3.11}$$

$$\frac{ds}{df_c} = -SR_s \tag{3.12}$$

Thus, Substituting Eqs. 3.10, 3.11, and 3.12 into Eq. 3.9, SR_c is calculated as indicated below (Eq. 3.13):

$$SR_c = SR_{soil} + \frac{dSR}{df_c} \tag{3.13}$$

The remote sensing sensors measure the SR data, while f_c can be calculated using vegetation indices derived from the RED and NIR surface reflectance bands. In Eq. 3.13, another unknown term is introduced as the first derivative of SR with respect to f_c. In this study, dSR/df_c of a given SR band will be determined for each imagery pixel or point-based multispectral data considering a modified linear interpolation approach based on Long and Singh (2012) surface albedo decomposition. Thus, this study suggests the following procedure to calculate dSR/df_c for every pixel of a given SR imagery band:

a) Using a multispectral image or point-based data for a given remote sensing sensor, calculated f_c and SR data will be divided into f_c intervals. Minimum (SR_{min}) and maximum (SR_{max}) values of SR will be recorded for each f_c interval and their associated f_c values. Each f_c interval will provide two pair of points given as (SR_{min},f_c) and (SR_{max},f_c).

b) Using the Median Absolute Deviation Approach ($MADA$) for excluding outliers (as described by Leys et al., 2013), SR data will be filtered for extreme values to avoid introducing systematic bias into $(dSR/df_c)_{min}$ and $(dSR/df_c)_{max}$ calculation. This is a modification from the original Long and Singh (2012) approach that considers using the standard deviation approach for filtering data.

c) For a given SR band, the pair of points (SR_{min}, f_c) will be linearly regressed to obtain $(dSR/df_c)_{min}$ for when f_c is at the minimum value ($f_{c,min}$) identified in the image or point-based dataset. Similarly, the pair of points (SR_{max}, f_c) will be linearly regressed to provide $(dSR/df_c)_{max}$ for when f_c is at the maximum value ($f_{c,max}$).

d) With $(dSR/df_c)_{min}$ and $(dSR/df_c)_{max}$ values at $f_{c,min}$ and $f_{c,max}$, dSR/df_c will be linearly interpolated for every pixel or ground-based SR data for the remaining values of calculated f_c in a given remote sensing image.

In this study, the f_c modeling approach from Norman et al. (1995) was chosen for the two-source pixel decomposition approach and is indicated by Eq. 3.14:

$$f_c^{[N]} = 1 - exp(-0.5 \cdot CF \cdot LAI) \tag{3.14}$$

where CF is the clumping factor (dimensionless). The superscript "N" indicates the Norman et al. (1995) f_c model. The calculation of CF depends on the green fraction of LAI and fractional soil cover (f_s), as indicated by Kustas and Norman (2000) and Anderson et al. (2005). The CF parameter is calculated as shown by Eqs. 3.15 to 3.18:

$$f_{c,o} = 1 - exp(-0.5 \cdot LAI) \tag{3.15}$$

$$LAI_L = \frac{LAI}{f_{c,o}} \tag{3.16}$$

$$f_s = 1 + f_{c,o} \cdot exp(-0.50 \cdot LAI_L) - f_{c,o} \tag{3.17}$$

$$CF = -ln\left(\frac{f_s}{0.5 \cdot LAI}\right) \tag{3.18}$$

where $f_{c,o}$ is the initial guess of f_c (dimensionless); LAI_L is the local LAI (m^2/m^2); f_s is the ground cover occupied by bare soil (dimensionless); CF is the vegetation clumping factor.

These two f_c models are chosen because they have been either recommended or used to provide f_c input data for the RBCC, OSEB, and TSEB remote sensing of ETa algorithms investigated in this study (e.g., Norman et al., 1995; Kustas and Norman, 2000; Colaizzi et al., 2012; Kullberg et al., 2017; Costa-Filho et al., 2020; Costa-Filho et al., 2021). Norman et al. (1995) f_c approach is an exponential model that accounts for the clustering of leaves (clumping factor) within the canopy architecture based on the fraction of green LAI. Johnson and Trout (2012) f_c model is a linear regression function that uses NDVI as a predictor and was calibrated for several crops (e.g., maize, wheat, cotton, alfalfa, barley, onions, and others) in a semi-arid climate in California, USA, using RED and NIR surface reflectance data from Landsat-5 (30 m).

When combining Eqs. 3.6 and 3.13 and rearranging the remaining algebraic terms, one gets the following equation (Eq. 3.19) with two unknown variables (k_p and SR_{soil}):

$$exp(-2k_p \cdot LAI) = \left(\frac{SR_{soil} - SR}{\frac{dSR}{df_c}} + 1\right)\left(\frac{SR_{soil}^2 + SR_{soil} \cdot \frac{dSR}{df_c} - 1}{SR \cdot SR_{soil} + SR \cdot \frac{dSR}{df_c} - 1}\right) \tag{3.19}$$

The idea here is to solve Eq. 3.19 iteratively for SR_{soil}, then use the SR_{soil} to determine SR_c from Eq. 3.13. However, the k_p parameter must be previously known. Modeling k_p directly from

multispectral data has limited applicability due to k_p being associated with the Photosynthetically Active Radiation (PAR) light spectrum. In this study, k_p will be initially assumed to scale like an equivalent extinction coefficient derived from vegetation indices (henceforth, k_v), such that (Eq. 3.20):

$$k_p \simeq \zeta \cdot k_v \tag{3.20}$$

where ζ is a scaling constant factor between k_p and k_v. Baret et al. (1995) showed that k_p and k_v could be scaled by a constant when deriving semi-empirical calibrated functions for determining the fractional light transmittance from partitioned vegetation indices into soil and vegetation components. In this study, k_p values from on-site measurements of ϕ_{down}, ϕ_{up}, and LAI was calculated from Eq. 3.1. Then, k_p and k_v values were linearly regressed. The k_v variable is determined from a non-linear vegetation index decomposition model based on the modified Beer-Lambert law and indicated by Eq. 3.21 as follows (Hatfield et al., 1985; Clevers, 1989; Baret and Guyot, 1991; Richardson et al., 1992; Gutman and Ignatov, 1998):

$$VI = VI_c + (VI_{soil} - VI_c) \cdot exp(-k_v \cdot LAI) \tag{3.21}$$

where VI stands for a vegetation index (e.g., NDVI, SAVI, for instance); VI_c and VI_{soil}, are the VI values for bare soil ($f_c = 0$) and fully vegetated ($f_c = 1$) surfaces, respectively; k_v is the dimensionless parameter equivalent to an extinction coefficient (Baret and Guyot, 1991).

The main issue with Eq. 3.21 is determining VI_{soil} and VI_c for every pixel in an image or point-based multispectral data from a radiometer. VI_{soil} and VI_c are functions of the unknown variables SR_s and SR_c, which imposes a critical limitation to directly obtaining VI_s and VI_c for a given imagery pixel or point-based measurement. Also, Baret and Guyot (1991) indicate that VI_{soil} is a function of soil texture, roughness, and moisture conditions of the shallow soil layer. Hence, this study proposes to indirectly determine VI_{soil} and VI_c using VI data for a given day of

imagery or ground-based multispectral data. The VI variable in this study was NDVI. The choice for NDVI as the VI was due to NDVI being a strong predictor for f_c (e.g., Verstraete and Pinty, 1991; Gillies and Carlson, 1995; Wittich et al., 1997; Gutman and Iganov, 1998; Qi et al., 2000; Zeng et al., 2000; Jiang et al., 2006; Montandon and Small, 2008; Johnson and Trout, 2012; Song et al., 2017). NDVI is calculated as follows (Eq. 3.22):

$$\text{NDVI} = \frac{NIR - Red}{NIR + Red} \tag{3.22}$$

where NIR and RED are the Near-infrared and Red surface reflectance data from a given remote sensing sensor, respectively.

Rewriting Eq. 3.22 using NDVI as VI gives the following mathematical expression for a mixed NDVI value of soil and vegetation composites (Eq. 3.23):

$$\text{NDVI} = \text{NDVI}_c + (\text{NDVI}_{soil} - \text{NDVI}_c) \cdot exp(-k_v \cdot LAI) \tag{3.23}$$

The $\text{NDVI}_{soil} - \text{NDVI}_c$ difference term in Eq. 3.23 is related to f_c through a unique semi-empirical and quadratic function of NDVI, as indicated by Eq. 3.24 (Gillies and Carlson, 1995; Gillies et al., 1997; Carlson and Ripley, 1997; Gutman and Ignatov, 1998; Brunsell and Gillies, 2002):

$$f_c = \left(\frac{\text{NDVI} - \text{NDVI}_{soil}}{\text{NDVI}_c - \text{NDVI}_{soil}} \right)^2 \tag{3.24}$$

where NDVI_{soil} and NDVI_c are the NDVI for bare soil and fully vegetated conditions, respectively.

Rearranging Eq. 3.24 provides an expression for NDVI as function of f_c, NDVI_c, and NDVI_{soil} (Eq. 3.25):

$$\text{NDVI} = \sqrt{f_c} \cdot \text{NDVI}_c + (1 - \sqrt{f_c}) \cdot \text{NDVI}_{soil} \tag{3.25}$$

In Eq. 3.25, the only unknown variables are NDVI_{soil} and NDVI_c since NDVI and f_c are calculated from the multispectral data of a given remote sensing sensor. Thus, using the chain rule (similarly to the Eq. 3.9) when differentiating Eq. 3.25 with respect to f_c, the following equation for the $\text{NDVI}_c - \text{NDVI}_{soil}$ difference is given as follows (Eq. 3.26):

$$\text{NDVI}_c - \text{NDVI}_{soil} = 2 \cdot \sqrt{f_c} \cdot \frac{d}{df_c}(\text{NDVI}) \tag{3.26}$$

Substituting Eq. 3.26 into Eq. 3.25 gives the following models for calculating NDVI_{soil} and NDVI_c, as indicated by Eqs. 3.27 and 3.28, respectively:

$$\text{NDVI}_{soil} = \text{NDVI} - 2 \cdot f_c \cdot \frac{d}{df_c}(\text{NDVI}) \tag{3.27}$$

$$\text{NDVI}_c = \text{NDVI} + 2 \cdot \left(\sqrt{f_c} - f_c \right) \cdot \frac{d}{df_c}(\text{NDVI}) \tag{3.28}$$

In Eqs. 3.27 and 3.28, it is imperative to determine $d(\text{NDVI})/df_c$. In this study, the same procedure proposed to calculate dSR/df_c was considered to obtain $d(\text{NDVI})/df_c$ for each pixel or point-based data from each remote sensing sensor in the study.

After NDVI_{soil} and NDVI_c are calculated from Eqs. 3.27 and 3.28, respectively, k_v is then obtained by solving Eq. 3.23 as follows (Eq. 3.29):

$$k_v = -ln \left[\left(\frac{\text{NDVI} - \text{NDVI}_c}{\text{NDVI}_{soil} - \text{NDVI}_c} \right) \frac{1}{LAI} \right] \tag{3.29}$$

Eq. 3.29 provides a non-iterative approach for k_v that relies on determining NDVI_c and NDVI_{soil}, since NDVI and LAI are known from the SR data. Also, k_v from Eq. 3.29 gives an alternative approach to calculate k_p for every imagery pixel or point-based data, given a valid mathematical relationship between k_p and k_v. Thus, the novel model for k_p, in its full form, is given by Eq. 3.30:

$$k_p = \beta_o + \beta_1 \cdot \left(\frac{1}{LAI}\right) \cdot ln\left[\left(\frac{\text{NDVI} - \text{NDVI}_c}{\text{NDVI}_{soil} - \text{NDVI}_c}\right)\right] \tag{3.30}$$

where β_o and β_1 are linear regression coefficients when statistically relating k_p and k_v.

For the SR decomposition approach, LAI was retrieved from each remote sensing sensor using the empirical model calibrated for row crops by Chávez et al. (2009b) and indicated below (Eq. 3.31):

$$LAI = 0.263 \cdot exp(3.813 \cdot OSAVI) \tag{3.31}$$

where OSAVI is the Optimized Soil Adjusted Vegetation Index (Rondeaux et al., 1996). OSAVI is an adjusted VI to minimize soil background effects in the reflectance data through an optimized adjustment factor set to 0.16 (Rondeaux et al., 1996) and calculated as follows (Eq. 3.32):

$$OSAVI = \left(\frac{NIR - Red}{NIR + Red + 0.16}\right) \cdot 1.16 \tag{3.32}$$

The LAI model (Eq. 3.31) from Chávez et al. (2009b) has been calibrated for row crops such as sorghum and maize and has been applied in recent SEB ETa studies (Chávez et al., 2010b; Chávez et al., 2012; Costa-Filho et al., 2020; Costa-Filho et al., 2021). Figure 3.1 summarizes the proposed SR data decomposition approach in this research project.

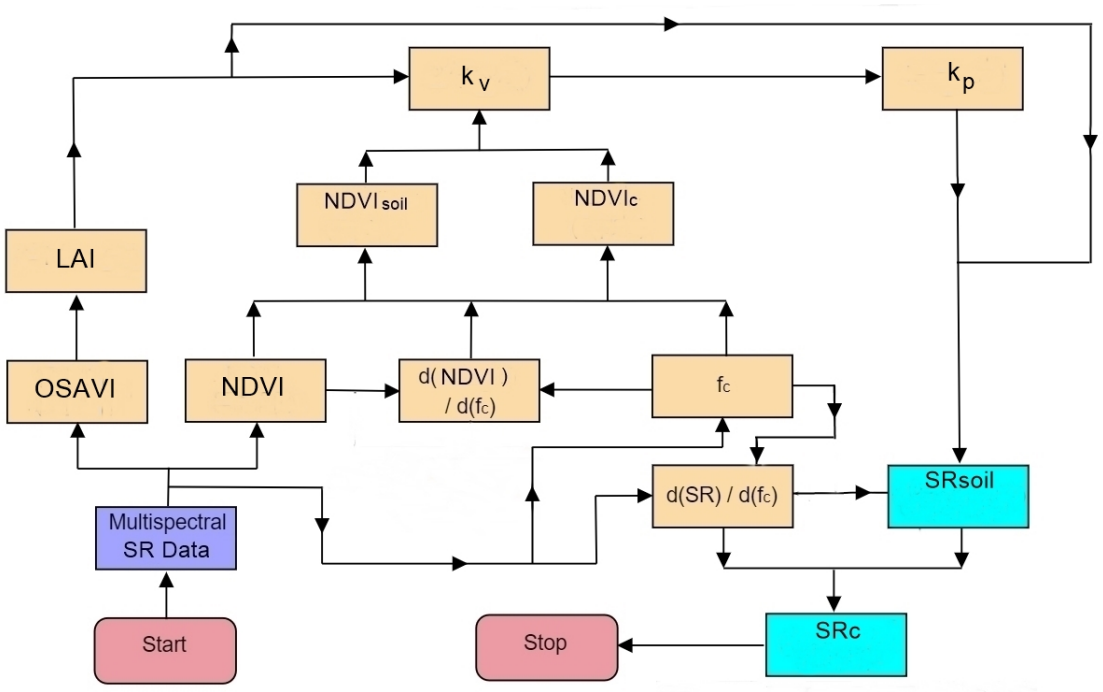

Figure 3.1: A flow chart summarizing the proposed approach for decomposing SR data. The purple, orange, and blue boxes are the input, intermediate, and final products for a given surface reflectance band, respectively.

3.2 Machine-Learning Regression for Imagery Data Fusion

The ML regression algorithms were evaluated to determine the best models to improve the accuracy of the sub-optimal remote sensing sensors. The training data for calibrating the ML regression models were selected using the following criteria: Coinciding days when the optimal and sub-optimal remote sensing sensors have data; if there were not enough coinciding days between the optimal imagery and a given sub-optimal sensor, a $\pm$ 1-day window were considered for days without irrigation or precipitation events to obtain data under similar canopy and microclimate conditions. For a short timespan ($\leq$ 24 hours), the assumption that multispectral surface properties for a given remote sensing sensor do not change significantly during clear-sky days, no registered wetting events (e.g., rainfall or irrigation), and the same vegetation type is valid. Allowing for a flexible timeframe when no coinciding data is available has been previously done by Houborg and

McCabe (2018b) when fusing Planet CubeSat and Landsat-8 imagery using a regression tree ML approach.

The following five ML regression approaches were evaluated to define the best ML model during the training phase for a given remote sensing sensor and ETa algorithm: Linear regression model (ordinary least squares); regression tree (fine tree); SVM (fine Gaussian kernel); GPR (exponential kernel); and random forest (bagged tree). The ML regression technique that provided the best goodness-of-fit (e.g., smallest regressed ML RMSE) was considered the best ML approach to adjust a given multispectral data for a given remote sensing of ETa model. In the end, the adjusted SR data values are restored to a mixed pixel format (soil and vegetation combined) through Eq. 3.6. Figure 3.2 summarizes the proposed SR data decomposition and ML spectral adjustment approach in this study.

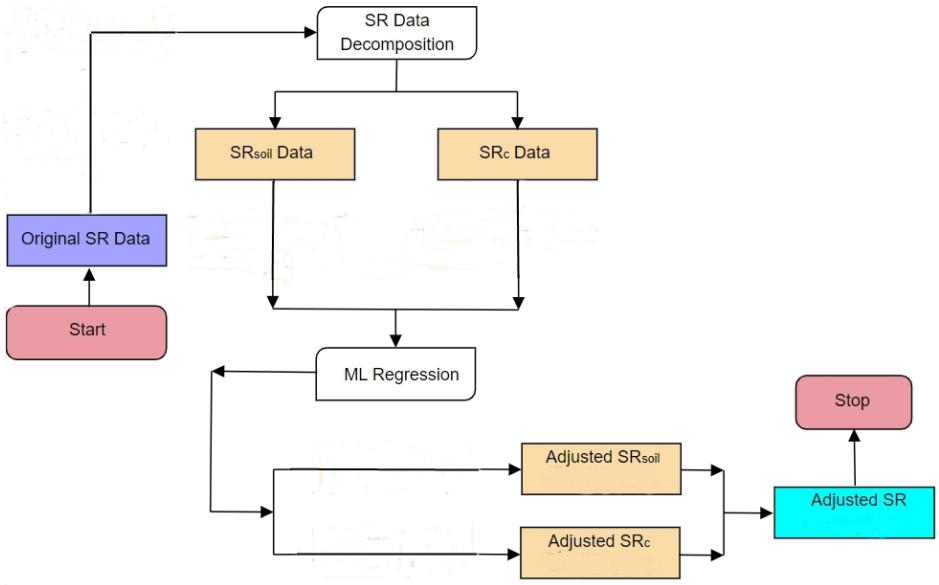

Figure 3.2: Flow chart summarizing the proposed ML spatial and spectral data adjustment approach. The purple box is the input data. The orange boxes are the intermediate outputs. The rounded diagonal rectangles are algorithms used in the proposed approach. The blue rectangle is the final SR adjusted product.

3.2.1 Linear Regression Model (Ordinary Least Squares)

Linear regression is a statistical modeling technique often used to estimate a dependent variable using a set of independent predictors. Ordinary Least Squares (OLS) is an approach within linear regression that aims to minimize the sum of squared deviations between the observed and predicted values of the dependent variable. This technique requires that both the dependent and independent variables are linearly related (Helsel and Hirsch, 1992).

In mathematical terms, a general linear regression model is represented by Eq. 3.33 below:

$$Y_{[q,1]} = \zeta_{[q,1]} X_{[q,m+1]} + \delta_{[q,1]} \tag{3.33}$$

where $\delta_{[q,1]}$, $\zeta_{[q,1]}$, $Y_{[q,1]}$, and $X_{[q,m+1]}$ are the residual, partial coefficient, response variable, and predictor variable matrices, respectively, in which the first index is the number of rows and the second index refers to the number of columns. The number of data points and predictor variables are indicated by subscripts q and m ($q > m$), respectively. The coefficients are determined during the model training process to minimize the overall prediction error.

Linear regression in machine-learning applications focuses on optimizing the derivation of the partial coefficient matrix values that minimize the sum of squared errors between predicted and observed values of a given dependent variable. This partial coefficient optimization is often achieved through iterations using optimization algorithms, such as the OLS (Yan and Su, 2009), based on the model's performance regarding the training datasets used for the machine-learning data assimilation process (Hope, 2020).

The linear OLS is a curve-fitting technique that fits a line through a given dataset by minimizing the distance between the data points and the fitted curve. For a simple linear regression case scenario, in which there is only one independent variable X to predict the dependent variable

Y, the OLS provides estimated values of the slope and intercept parameters of the linear model through an optimization approach based on a linear system of equations given by Eqs. 3.34 and 3.35 below (Malud and Abdulazeez, 2020):

$$\frac{\partial}{\partial \zeta_o} \sum_{i=1}^{n} [y_i - (\zeta_o + \zeta_1 x_1)]^2 = 0 \tag{3.34}$$

$$\frac{\partial}{\partial \zeta_1} \sum_{i=1}^{n} [y_i - (\zeta_o + \zeta_1 x_1)]^2 = 0 \tag{3.35}$$

The solutions of the linear system of equations composed by Eqs. 3.34 and 3.35 are the estimated regression coefficients (Ott and Longnecker, 2015) indicated by Eqs. 3.36 and 3.37 as follows:

$$z_1 = \left[\sum_{i=1}^{n} (y_1 - \bar{y})(x_i - \bar{x}) \right] \cdot \left[\sum_{i=1}^{n} (x_i - \bar{x})^2 \right]^{-1} \tag{3.36}$$

$$z_o = \bar{y} - z_1 \bar{x} \tag{3.37}$$

where z_o and z_1 are the intercepts and the slope estimates of the linear model, respectively.

3.2.2 Regression Tree and Random Forest (Ensemble Tree)

Regression trees are techniques for recursively partitioning a given dataset into smaller groups to find more homogeneous clusters at each iteration (Yang et al., 2017). The regression tree for model prediction divides a given dataset of dependent and independent variables into nodes (often called "leaves") based on the values of a specific explanatory variable (Naghibi et al., 2016; Latif, 2021). The main goal is to predict the dependent variable values using the input data as they move along the tree "leaf" structure. The prediction values of a variable of interest are determined by the mean of the terminal node (the final node without further splits) where the unit ends up (Loh, 2011).

In a single regression tree model, the training data values are partitioned into groups to generate the nodes. Each tree branch division is contingent upon the values of a specific variable, determined by designated splitting criteria. Thus, when the tree algorithm structure is fully created, the estimated dependent variable is calculated by following the tree path from the root node down to the corresponding terminal node. This tree path is oriented by the observed values associated with the variables employed in the splitting decisions. The ultimate predicted response value is straightforwardly derived as the mean of the responses within the pertinent terminal node, encapsulating the aggregate behavior represented by the chosen pathway (Gromping, 2009; Coulston et al., 2016).

Similarly to the OLS approach, the regression tree algorithm focuses on minimizing the sum of squared errors between observed and predicted values of the dependent variable within terminal nodes. The process of partitioning the dataset into sub-groups is an iterative strategy that creates a structure that resembles a tree. At each node or "leaf," the regression tree algorithm selects the feature and corresponding threshold values that optimally divide the data. This iterative process persists until a cut-off value is met, which is often the maximum depth for the tree or the minimum number of samples in a leaf node (Torgo, 1997; Steinberg and Colla, 2009; Belitz and Stackelberg, 2021).

A Random Forest (Figure 3.3) is, by definition, an ensemble regression tree algorithm of multiple random decision trees derived from a given dataset, as introduced by Breiman (2001). A random forest regression comprises a substantial number of individual trees. Each tree is created from a different sample of rows, and at each node, a different sample of features is selected for splitting. Each of the trees makes its prediction. The final values are averaged in the end. Through independent and random data points, each tree branch is generated, with the upcoming division branches being created from sub-groups within the original training data set. Since the creation of a large number of trees is often a random process due to the variability within the original and

subsets of the training dataset, each regression tree often provides different predicted values of a given dependent variable (Gromping, 2009).

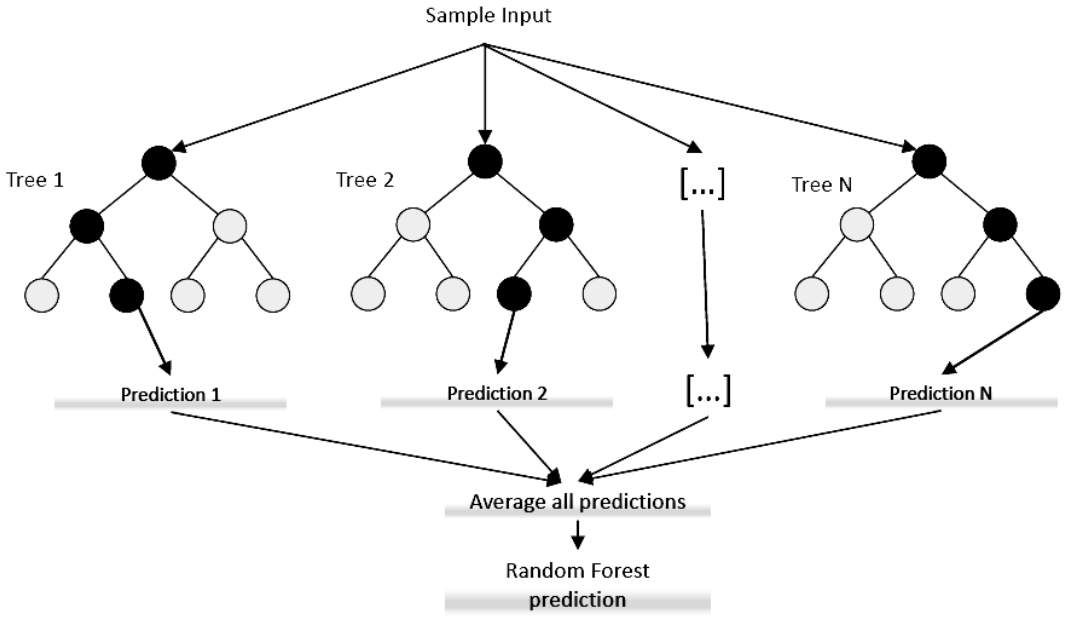

Figure 3.3: Random forest regression layout (Segura et al., 2022). Multiple regression trees are generated, and the average of the predictions is the estimated value of the random forest for a given response variable.

3.2.3 Support Vector Machine with a Gaussian Kernel

The SVM machine-learning algorithms are often used in a wide range of applications that include data classification (Bhavsar and Panchal, 2012) and prediction of any variables of interest (Zendehboudi et al., 2018). When used for model prediction, SVM techniques focus on estimating continuous variables from a given input data group (Noble, 2006; Deka, 2014). SVM model predictions are based on the hyperplane concept, which represents the relationship between the dependent and independent variables considered for a given model. With the use of a Gaussian kernel, the SVM machine-learning algorithm is able to capture non-linearity patterns that might be

present in a given dataset (Ben-Hur et al., 2008; Salcedo-Sanz et al., 2014).

The mathematical formulation of an SVM algorithm for prediction is based on the determination of a model that deviates from the observed and dependent variable by a fixed threshold and with the lowest model parameter values to minimize prediction errors (Scholkopf et al., 1997). That is, an SVM algorithm defines a margin of tolerance to reduce prediction error by individualizing the hyperplane (boundary lines), which maximizes the margin of tolerance and allows part of the error to be accepted in the predictions (Figure 3.4).

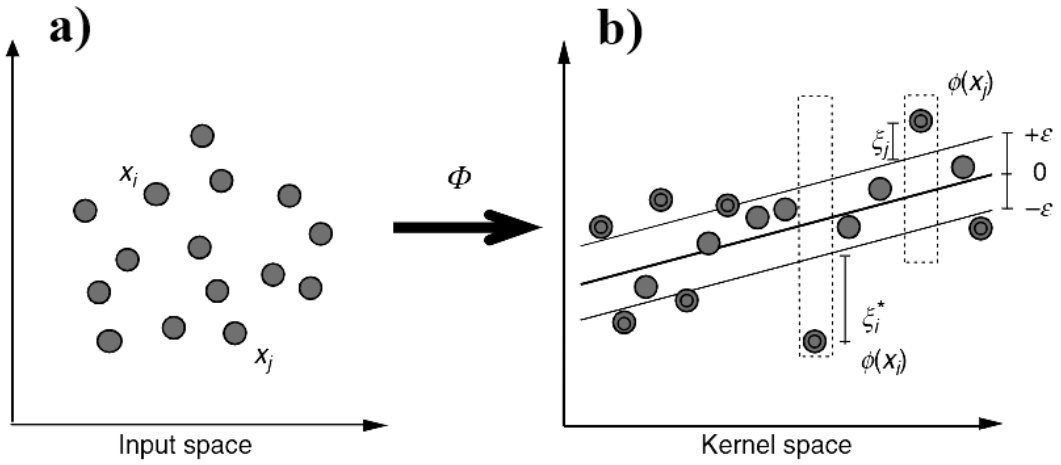

Figure 3.4: The SVM regression approach highlighting the margin of tolerance (ϵ), the non-negative parameters ξ_i and ξ_i^*, and the transformation function ϕ (Salcedo-Sanz et al., 2014).

The SVM for regression is based on the following model criteria, given by Eq. 3.38 as follows (as described by Salcedo-Sanz et al., 2014):

$$min\left[\frac{1}{2}||w||^2 + C\sum_{i=1}^{n}\left(\xi_i + \xi_i^*\right)\right] \tag{3.38}$$

with respect to w and to ξ_i^* and constrained to the following algebraic relationships (Eqs. 3.39 and 3.40):

$$y_i - \left(\langle \phi(x_i), w \rangle + b \right) \leq \epsilon + \xi_i \ \ , \ \ \xi_i \geq 0 \tag{3.39}$$

$$\left(\langle \phi(x_i), w \rangle + b \right) - y_i \leq \epsilon + \xi_i^* \ \ , \ \ \xi_i^* \geq 0 \tag{3.40}$$

where ξ_i and ξ_i^* are auxiliary data points for training samples that have estimation errors larger than the margin of tolerance (ϵ); w and b are linear classified parameters in $\Re^N$; C is the regulation error parameter which controls the trade-off between achieving a small training error and maintaining a wide ϵ; and the pair of points x_i, y_i, is the training data set, with i = 1, 2, 3, ..., n.

For an SVM regression with a given kernel function, the machine-learning data assimilation algorithm determines the regression coefficients that minimize the following function indicated by Eq. 3.41 as follows (Cortes and Vapnik, 1995; Vapnik, 1999):

$$L(\alpha) = \frac{1}{2} \sum_{i=1}^{n} \sum_{j=1}^{n} (\alpha_i - \alpha_i^*)(\alpha_j - \alpha_j^*) G(x_i, y_i) + \epsilon \sum_{i=1}^{n} (\alpha_i + \alpha_i^*) \\ - \sum_{i=1}^{n} y_i (\alpha_i + \alpha_i^*) \ \ , \ \ \text{with} \sum_{i=1}^{n} (\alpha_n - \alpha_n^*) = 0 \tag{3.41}$$

where α_i, α_j, α_i^*, α_j^*, α_n, and α_n^* are non-negative multipliers for each pair of points x_i, y_i; $G(x_i, y_i)$ is the kernel function, and $L(\alpha)$ is the distance between observed value y and ϵ. The values of α_n and α_n^* are between 0 and C.

After the regression coefficients are calculated, the SVM function used for prediction is given by Eq. 3.42 as follows (Cortes and Vapnik, 1995; Vapnik, 1999):

$$f(x) = \sum_{i=1}^{n} (\alpha_n - \alpha_n^*) \cdot G(x_n, x) + b \tag{3.42}$$

where $f(x)$ is the predicted value of the SVM kernel regression model for any given input x data value.

A kernel is a mathematical function that provides some insight into the similarity between data points in the SVM hyperplane space, and it is given by Eq. 3.43 below (Vapnik, 1999):

$$G(x_i, x_j) = \langle \phi(x_i), \phi(x_j) \rangle \tag{3.43}$$

where $\phi(x)$ is a transformation function that translates the original data points in an x-y cartesian frame to a high-dimensional space (kernel space).

Any given kernel function assigns higher weights to nearby points and lower weights to those farther away, which enables the SVM machine-learning algorithm to identify any pertinent local relationships in the data. In other words, the Gaussian kernel determines the influence of each data point on the respective estimated value of the dependent variable and emphasizes those data points that are more relevant (Chapelle et al., 2008; Mammone et al., 2009; Kausar et al., 2011).

The Gaussian kernel function is a non-linear exponential model indicated by Eq. 3.44 below:

$$G(x_i, y_j) = exp\bigg(- ||x_i - x_j||^2 \bigg) \tag{3.44}$$

3.2.4 Gaussian Process Regression with an Exponential Kernel

The GPR machine-learning algorithms are non-parametric models based on probabilistic (bayesian) theory that use kernel functions to derive the probabilities associated with estimating specific parameters to obtain predictions of any variable of interest. Through the introduction of input data

adjusted from a Gaussian process and explicit basis functions, a GPR prediction algorithm is able to determine the best set of values that are representative of estimating a given outcome based on the independent variable data (Seeger, 2004; William and Rasmussen, 2006; Rasmussen and Nickisch, 2010).

A Gaussian process consists of a set of random variables that have a joint Gaussian distribution. It does not have rigid parameters since it is not limited by a $Y = f(x_i, y_i)$ functional form. It's derived from the Bayesian linear regression model. The Gaussian process can be characterized by a mean function and a covariance function, with systematic prediction errors assumed to follow a normal distribution. In mathematical terms, the mean function $m(x)$ and the covariance function $k(x, x_j)$ of a given model $f(x)$ are given as indicated by Eqs. 3.45 and 3.46 as follows (Rasmussen and Nickisch, 2010):

$$m(x) = E\Big(f(x)\Big) \tag{3.45}$$

$$k(x, x_j) = Cov\Big[f(x), f(x_j)\Big] = E\Big[f(x) - m(x)f(x_j) - m(x_j)\Big] \tag{3.46}$$

where $E(f(x))$ is the mean function, $Cov[f(x), f(x_j)]$ is the covariance function, and $f(x)$ is a assumed to be a Gaussian process.

In vector notation, a GPR model is given by Eq. 3.47 below (Williams and Rasmussen, 2006):

$$P(y|f, X) \sim N(y|H\beta + f, \sigma^2 I) \tag{3.47}$$

where X, y are the training data points; H is a set of basis functions responsible for adjusting the original data vector in $\Re^d$ to a new vector data in $\Re^p$; f is the Gaussian process function; β is a p-by-1 vector of Bayesian coefficients; σ^2 is the variance; I is the identify matrix. The notation $P() \sim N()$ indicates that the probability function is normally distributed.

In Eq. 3.47, the terms X, y, H, and f are n-by-1 vectors indicated by Eqs. 3.48 to 3.51, respectively (Seeger, 2004):

$$X = \begin{pmatrix} x_1^T \\ x_2^T \\ \vdots \\ x_n^T \end{pmatrix} \tag{3.48}$$

$$y = \begin{pmatrix} y_1^T \\ y_2^T \\ \vdots \\ y_n^T \end{pmatrix} \tag{3.49}$$

$$H = \begin{pmatrix} h(x_1^T) \\ h(x_2^T) \\ \vdots \\ h(x_n^T) \end{pmatrix} \tag{3.50}$$

$$f = \begin{pmatrix} f(x_1) \\ f(x_2) \\ \vdots \\ f(x_n) \end{pmatrix} \tag{3.51}$$

The covariance function $K(x, x_j)$ is defined as a set of kernel parameters or hyperparameters (θ) based on the joint probability distribution in the GPR algorithm, as indicated by Eqs. 3.52 and 3.53 below (Seeger, 2004):

$$P(f|X) \sim N[f|0, K(X, X)] \tag{3.52}$$

$$K(X,X) = \begin{pmatrix} k(x_1,x_1) & k(x_1,x_2) & \dots & k(x_1,x_n) \\ k(x_2,x_1) & k(x_2,x_2) & \dots & k(x_2,x_n) \\ \vdots & \vdots & \vdots & \vdots \\ k(x_n,x_1) & k(x_n,x_2) & \dots & k(x_n,x_n) \end{pmatrix} \tag{3.53}$$

To estimate the GPR model parameters σ^2, θ, and β, it is necessary to maximize the likelihood $P(y|X)$ as indicated by Eqs. 3.54 and 3.55 as follows (Williams and Rasmussen, 2006):

$$\hat{\beta}, \hat{\theta}, \hat{\sigma}^2 = \text{arg max } logP(y|X,\beta,\theta,\sigma^2) \tag{3.54}$$

$$logP(y|X,\beta,\theta,\sigma^2) = -\frac{1}{2}(y-H\beta)^T[K(X,X|\theta)+\sigma^2 I_n]^{-1}(y-H\beta) - \frac{n}{2}log(2\pi) - \frac{1}{2}log|K(X,X|\theta)+\sigma^2 I_n| \tag{3.55}$$

where H is the vector of explicit basis functions; $K(X,X|\theta)$ is the covariance function matrix; $\hat{\beta}$, $\hat{\theta}$, $\hat{\sigma}^2$ are the respective estimates of β, θ, and σ^2.

When using GPR for the prediction of a given dependent variable, it is necessary to determine the probability density function $P(y_{\text{pred}}|y,X,x_{\text{pred}})$, which is calculated as indicated by Eq. 3.56 as follows (Williams and Rasmussen, 2006):

$$P(y_{\text{pred}}|y,X,x_{\text{pred}}) = \frac{P(y_{\text{pred}},y|X,x_{\text{pred}})}{P(y|X,x_{\text{pred}})} \tag{3.56}$$

Thus, the GPR model prediction for a new dataset that encompasses data points that were not used during the training phase (x_{new}, y_{new}) is given by Eq. 3.57 as follows (Seeger, 2004):

$$E(y_{\text{new}}|y,X,x_{\text{new}},\beta,\theta,\sigma^2) = h(x_{\text{new}})^T\beta + K(x_{\text{new}}^T,X|\theta)\Big(K(X,X|\theta)+\sigma^2 I_n\Big)^{-1}(y-H\beta) \tag{3.57}$$

3.3 The Reflectance-based Crop Coefficient Approach (RBCC)

The RBCC model is based on the notion of ETa being determined as the product of a given crop coefficient and a standardized ET_{ref} (e.g., alfalfa or clipped grass) as indicated by Eq. 3.58:

$$ET_a = K_{cb} \cdot ET_{ref} \tag{3.58}$$

where ET_a is daily crop evapotranspiration (mm/d); K_{cb} is the basal crop coefficient of a given vegetation (dimensionless); ET_{ref} is the daily reference evapotranspiration from either alfalfa (ET_r) or clipped grass (ET_o) standardized surfaces (mm/d).

The RBCC ETa model assumes that the crop coefficients and remotely sensed vegetation indices are linearly correlated (Bausch and Neale, 1987). Thus, Eqs. 3.59 and 3.60 give the RBCC ETa generic formulation:

$$ET_d^{[RFL]} = K_{cr} \cdot ET_{ref} \tag{3.59}$$

$$K_{cr} = a_1 \cdot VI + a_2 \tag{3.60}$$

where $ET_d^{[RFL]}$ is the RBCC daily actual crop evapotranspiration (mm/d); K_{cr} is the reflectance-based crop coefficient (dimensionless); VI is the vegetation index from remote sensing; a_1 and a_2 are the slope and intercept of the K_{cr} model, respectively. The superscript "RFL" in Eq. 3.59 refers to surface reflectance.

3.3.1 NDVI-based RBCC Algorithm

The Neale et al. (1990) RBCC ETa model was calibrated using daily maize ETa from weighing lysimeters and multispectral data from a handheld EXOTECH radiometer with a 1 m footprint and

similar spectral data to Landsat-5. Neale et al. (1990) calibrated their K_{cr} model using data from a maize field under surface (furrow) irrigation, as indicated by Eqs. 3.61 and 3.62 below:

$$ET_{ad}^{[Ne]} = K_{cr}^{[Ne]} \cdot ET_{rd} \tag{3.61}$$

$$K_{cr}^{[Ne]} = 1.181 \cdot \text{NDVI} - 0.026 \tag{3.62}$$

where $ET_{ad}^{[Ne]}$ is the Neale et al. (1990) RBCC model for daily maize ETa (mm/d); ET_{rd} is the daily alfalfa-based reference evapotranspiration (mm/d); $K_{cr}^{[Ne]}$ is the Neale et al. (1990) maize crop coefficient model (dimensionless); The superscript "$[Ne]$" refers to the Neale et al. (1990) ETa model.

3.3.2 SAVI-based RBCC Algorithm

Bausch (1995) model developed a crop coefficient curve using SAVI data derived from the same EXOTECH handheld radiometer mounted on a boom (5-m footprint), with a similar Landsat-5 spectral response, by linearly interpolating K_{cb} values from the bare soil ($\approx$ 0.15) to effective maize canopy cover ($\approx$ 0.93). Huete (1988) developed SAVI as an adjusted vegetation index to minimize soil background effects through a soil background attenuation factor set to 0.50, as commonly used in several previous studies (e.g., Huete, 1988; Gilabert et al., 2002; Glenn et al., 2010; Ren et al., 2018; Carpintero et al., 2020). Bausch (1995) also set the SAVI adjustment factor to 0.50 when calibrating its K_{cr} model. The RBCC ETa model from Bausch (1995) was developed using data from maize fields under center-pivot sprinkler irrigation and indicated by Eqs. 3.63 and 3.64 below:

$$ET_{ad}^{[B]} = K_{cr}^{[B]} \cdot ET_{rd} \tag{3.63}$$

$$K_{cr}^{[B]} = 1.416 \cdot SAVI + 0.017 \tag{3.64}$$

where $ET_{ad}^{[B]}$ is the Bausch (1995) RBCC model for daily maize ETa (mm/d); $K_{cr}^{[B]}$ is the Bausch (1995) maize crop coefficient model (dimensionless); The superscript "$[B]$" refers to the Bausch (1995) ETa model.

The SAVI variable (Huete, 1988) is calculated as follows (Eq. 3.65):

$$SAVI = \frac{NIR - Red}{NIR + Red + L} \cdot (1 + L) \tag{3.65}$$

where L is the soil-background adjustment factor, set to be equal to 0.50 (Huete, 1988).

3.3.3 f_c-based RBCC Algorithm

Trout and DeJonge (2018) model derived their K_{cr} model using f_c values calculated from a digital multispectral camera, 6 m above ground surface (AGS). Trout and DeJonge (2018) model was calibrated using measured ETa from a SWB approach (Eq. 1.1) during a six-year data collection period. Trout and DeJonge (2018) developed their calibrated K_{cr} model in a surface drip irrigated field, as indicated by Eqs. 3.66 and 3.67 below:

$$ET_{ad}^{[T]} = K_{cr}^{[T]} \cdot ET_{rd} \tag{3.66}$$

$$K_{cr}^{[T]} = 1.10 \cdot f_c + 0.17 \tag{3.67}$$

where $ET_{ad}^{[T]}$ is the Johnson and DeJonge (2018) RBCC model for daily maize ETa (mm/d); $K_{cr}^{[T]}$ is the Trout and DeJonge (2018) maize crop coefficient model (dimensionless); The superscript "$[T]$" refers to the Trout and DeJonge (2018) maize ETa model.

Johnson and Trout (2012) f_c model was used in the Trout and DeJonge (2018) RBCC model since it has been used in other publications (e.g., Kullberg et al. 2017), as indicated by Eq. 3.68:

$$f_c^{[T]} = \begin{cases} 1.26 \cdot \text{NDVI} - 0.18 & \text{, NDVI} > 0.15 \\ 0 & \text{, otherwise} \end{cases} \tag{3.68}$$

3.4 One-Source Surface Energy Balance Approach (OSEB)

The OSEB model is a complex method to derive estimates of ETa using remote sensing and micrometeorological data. The simplified SEB is given by Eq. 3.69 as follows (Tanner, 1960):

$$LE = R_n - G - H \tag{3.69}$$

where all terms on Eq. 3.69 are given in W/m^2.

The R_n flux (Eq. 3.70) is calculated using the common net radiation budget model (Monteith and Szeicz, 1961) as follows:

$$R_n = (1 - \alpha_s) \cdot R_s + \epsilon_s \cdot \epsilon_a \cdot \sigma \cdot T_{ak}^4 - \epsilon_s \cdot \sigma \cdot T_{sk}^4 \tag{3.70}$$

where α_s is surface albedo (dimensionless); R_s stands for shortwave incoming solar radiation (W/m^2); ϵ_a is the air emissivity (dimensionless); ϵ_s is the surface thermal emissivity (dimensionless); σ is the Stefan-Boltzmann constant ($5.67 \cdot 10^{-8}\ W/m^2/K^4$). T_{aK} and T_{sK} are air and nadir surface temperatures (K), respectively.

In this study, the surface albedo was calculated based on Brest and Goward (1987) linear multivariate model that relates α_s to RED and NIR surface reflectance bands. Air emissivity has been calculated for clear-sky conditions using Brutsaert (1975) nonlinear model that relates ϵ_a to vapor pressure (e_a, mb) and T_{aK}. Surface thermal emissivity has been determined using Brunsell and

Gillies (2002) model that linearly interpolates ϵ_s from bare soil to full canopy cover conditions based on NDVI values. The values of ϵ_s for bare soil and full-cover vegetation are approximately 0.93 and 0.98, respectively (Caselles et al., 2011; Campbell and Wynne, 2011; Lillesand et al., 2015).

Several different empirical models in the literature estimate the G flux using remote sensing data (e.g., Choudhury et al., 1987; Jackson et al., 1987; Kustas and Daughtry, 1990; Bastiaanssen et al., 1998; Su, 2002; Chávez et al., 2005). In this study, G was estimated using the Su (2002) model since it is a widely used approach in many SEB studies that deal with remote sensing images for ETa modeling at different spatial scales (e.g., Mcabe and Wood, 2006; Verstraeten et al., 2008; Tang et al., 2010). The Su (2002) G model interpolates the G/R_n ratio between bare soil to effective canopy cover conditions using f_c as a weighting factor as follows (Eq. 3.71):

$$\frac{G}{R_n} = \Gamma_c + (1 - f_c)(\Gamma_s - \Gamma_c) \tag{3.71}$$

where Γ_c and Γ_s are the G/R_n ratios for full canopy and bare soil conditions equal to 0.05 (Kustas and Daughtry, 1990) and 0.315 (Monteith, 1973), respectively.

The OSEB model for ETa relies on the single-source bulk aerodynamic resistance approach for H given by Eq. 3.72 (as in Thom, 1972):

$$H = \rho_a \cdot C_{pa} \cdot \left(\frac{T_o - T_a}{r_{ah}} \right) \tag{3.72}$$

where ρ_a is the air density (kg/m^3), C_{pa} is the specific heat of the air ($J/kg/K$), and r_{ah} is the bulk aerodynamic resistance to surface heat transfer (s/m), T_o and T_a are the surface aerodynamic and air temperatures (K), respectively.

The air parameters ρ_a and C_{pa} are calculated as indicated by Eqs. 3.73 to 3.74, respectively (as used in Ham, 2005):

$$\rho_a = \left(\frac{P}{R_d T_a}\right)\left(1 - \frac{0.378 \cdot e_a}{P}\right) \tag{3.73}$$

$$C_{pa} = 1004.7 \cdot \left(1 + \frac{0.522 \cdot e_a}{P}\right) \tag{3.74}$$

where P is the local atmospheric pressure (Pa); e_a is actual vapor pressure (Pa); R_d is the gas constant for dry air ($\approx$ 287.04 $J/kg/K$).

There are several approaches for estimating the temperature difference $T_o - T_a$ or T_o itself in Eq. 3.72 (e.g., Bastiaanssen et al., 1998; Roerink et al., 2000; Su, 2002; Marht and Vickers, 2004; Chávez et al., 2005; Allen et al., 2007; Senay et al., 2007; Senay, 2018; Costa-Filho et al., 2021). This study chose the approach from Costa-Filho et al. (2021) since it has been locally calibrated using maize field data from Colorado with promising results in minimizing the uncertainty regarding T_o estimation. This T_o modeling approach does not require subjective decision-making of "hot" (high) and "cold" (low) surface temperature thresholds to determine the temperature difference in Eq. 3.72 (for more details, see Bastiaanssen et al., 1998; Roerink et al., 2000; Su, 2002; Allen et al., 2007).

The r_{ah} term has been adjusted for atmospheric stability using the Monin-Obukhov stability theory (Monin and Obukhov, 1954) and correction functions (Paulson, 1970; Webb, 1970; Businger et al., 1971; Verma, 1989). More details about r_{ah} calculations are extensively detailed in Appendix A. The OSEB approach for H based on T_o modeling was developed using SR and thermal data from a handheld MSR radiometer (Cropscan, Rochester, MN), a proximal remote sensing sensor with similar spectral resolution as Landsat-5 and sampling area equivalent to a 1-m diameter. Figure 3.5 summarizes the OSEB algorithm. The T_o optimized model for maize sensible heat flux is given as follows (Eq. 3.75):

$$T_o = \begin{cases} -8.742 \cdot f_c + 0.571 \cdot T_a + 0.529 \cdot T_s + 0.806 \cdot r_p + 3.295, & 0.85 \leq LAI \leq 1.50 \\ -9.168 \cdot f_c + 0.485 \cdot T_a + 0.575 \cdot T_s - 0.160 \cdot r_p + 6.491, & 1.50 < LAI \leq 2.50 \\ 4.708 \cdot f_c + 0.350 \cdot T_a + 0.580 \cdot T_s + 0.086 \cdot r_p, & 2.50 < LAI \leq 3.50 \\ -1.912 \cdot f_c + 0.443 \cdot T_a + 0.509 \cdot T_s + 0.115 \cdot r_p + 5.014, & 3.50 < LAI \leq 5.00 \end{cases} \quad (3.75)$$

where T_a is the local air temperature (^oC); T_s is the local nadir-looking surface temperature (^oC); r_p is the turbulent-mixing row resistance (s/m). More details on how to calculate r_p are provided in Appendix A.

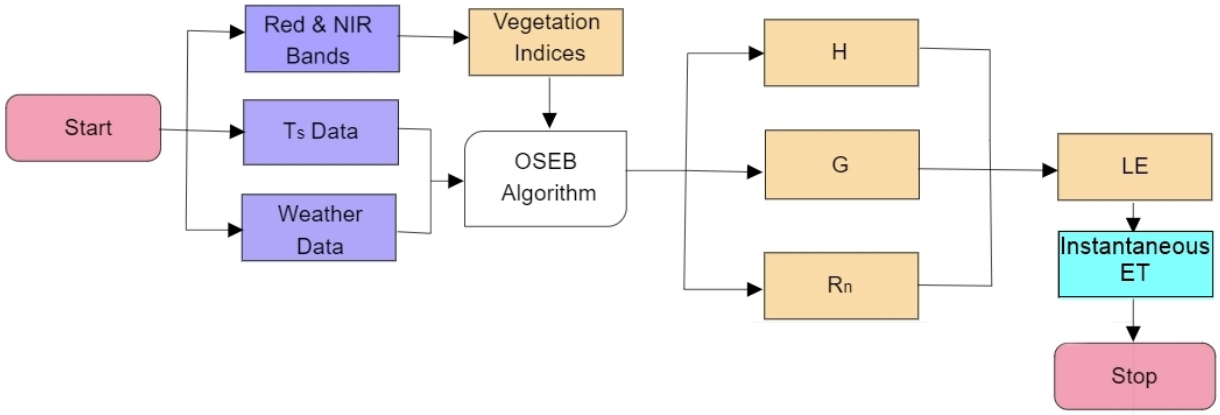

Figure 3.5: A simplified OSEB algorithm flowchart to estimate instantaneous ETa from remote sensing data. The purple boxes indicate inputs. The rounded diagonal corner rectangle is the ETa algorithm. The orange boxes are the intermediate outputs. The rounded diagonal rectangle is the ETa algorithm. The blue rectangle is the final ETa product.

3.5 Two-Source Surface Energy Balance Approaches (TSEB)

The TSEB approach was developed and validated by Kustas et al. (1995) using a radiometer (1^o FOV) attached to a helicopter (airborne sensor). The flight altitude was 300 m AGS, which provided a sampling area equivalent to a 5-m diameter. The TSEB partitions the simplified SEB model (Eq. 3.61) into vegetation and soil components as follows (Eqs. 3.76 to 3.79):

$$LE = LE_c + LE_{soil} \tag{3.76}$$

$$LE_c = Rn_c - H_c \tag{3.77}$$

$$LE_{soil} = Rn_{soil} - G - H_{soil} \tag{3.78}$$

$$G^{[N]} = 0.35 \cdot Rn_{soil} \tag{3.79}$$

where the subscripts "soil" and "c" refer to the soil and canopy layers, respectively. All terms in Eqs. 3.76 to 3.79 are given in W/m^2. The $G^{[N]}$ model is the soil heat flux approach recommended by Norman et al. (1995) as a fraction of the net radiation from the soil layer during midday conditions coinciding with most spaceborne remote sensing sensors overpass time.

Eqs give the partitioning of R_n. 3.80 and 3.81 (Norman and Kustas, 2000):

$$Rn_{soil} = R_{s,soil} + L_{n,soil} \tag{3.80}$$

$$Rn_c = R_{s,c} + L_{n,c} \tag{3.81}$$

where $R_{s,soil}$ and $L_{n,soil}$ are the short-wave and long-wave incoming and outgoing radiation from the soil layer (W/m^2); $R_{s,c}$ and $L_{n,c}$ are the short-wave and long-wave incoming and outgoing radiation from the vegetation layer (W/m^2).

The Rn_c and Rn_{soil} terms in Eqs. 3.80 and 3.81 are calculated following the approaches by Norman et al. (1995), Kustas and Norman (2000), and Colaizzi et al. (2012) and indicated by Eqs. 3.82 and 3.118, respectively:

$$\begin{aligned} Rn_c = (1 - \Omega_{solar})(1 - \alpha_c)R_s + exp(-0.95LAI)L_{sky} + \\ [1 - exp(-0.95LAI)]\epsilon_c \sigma T_{cK}^4 - \epsilon_{soil}\sigma T_{soilK}^4 \end{aligned} \tag{3.82}$$

$$Rn_{soil} = \Omega_{solar}(1 - \alpha_{soil})R_s + [1 - exp(-0.95LAI)]\cdot \\ [\epsilon_a \sigma T_{aK}^4 + \epsilon_{soil}\sigma T_{soilK}^4 - 2\epsilon_c \sigma T_{cK}^4] \tag{3.83}$$

where Ω_{solar} is the solar atmospheric transmittance (dimensionless); α_c and α_{soil} are the canopy and bare soil albedo (dimensionless), respectively; ϵ_c is the canopy thermal emissivity (dimensionless); ϵ_{soil} is the bare soil thermal emissivity (dimensionless); T_{cK} is the canopy temperature (K); T_{soilK} is the soil temperature (K); T_{aK} is the air temperature (K). L_{sky} is the long-wave radiation from the sky (W/m^2).

The α_c and α_{soil} were calculated following the approaches by Costa-Filho et al. (2020) and Post et al. (2000), respectively. Costa-Filho et al. (2020) calibrated an exponential model that relates maize albedo and green LAI for a semi-arid climate region. Post et al. (2000) developed a multivariate model that relates α_{soil} and the visible surface reflectance bands of the light spectrum (RED, GREEN, and BLUE). The Ω_{solar} variable was calculated using the non-linear model from Norman and Jarvis (1975), in which the Ω_{solar} is a function of LAI, surface absorptivity factor (Norman, 1989; Gates, 2012), light extinction coefficient (Campbell and Norman, 1998), and the fraction of incident Photosynthetically Active Radiation or PAR (Goudriaan, 1977; Nikolov and Zeller, 1992; Spokas and Forcella, 2006).

The partition of T_s considers f_c as the weighting factor to quantify the contribution of vegetation and soil composites towards the thermal characteristics on a pixel-by-pixel basis (Norman et al., 1995) as follows (Eq. 3.84):

$$T_s K \cong \left[f_c^{[N]} \cdot T_c K^4 + (1 - f_c^{[N]}) T_{soilK}^4 \right]^{1/4} \tag{3.84}$$

where $f_c^{[N]}$ is the TSEB fractional vegetation model, with the superscript "N" indicating the model proposed by Norman et al. (1995). The $f_c^{[N]}$ model in the TSEB approaches. More details are found in Norman et al. (1995) and Norman and Kustas (2000). Figure 3.6 summarizes the TSEB

algorithm.

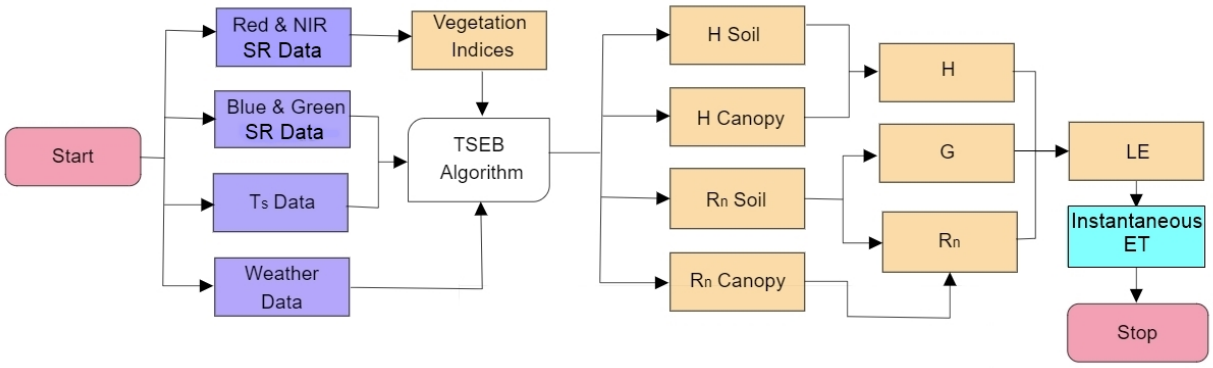

Figure 3.6: A simplified TSEB algorithm flowchart to obtain instantaneous ETa from remote sensing data. The purple boxes indicate inputs. The rounded diagonal corner rectangle is the TSEB ETa algorithm. The orange boxes are the intermediate outputs. The blue rectangle is the final ETa product.

3.5.1 Parallel Resistance TSEB Algorithm

When partitioning H, TSEBpar, and TSEBser have different approaches based on their assumptions regarding the interconnection between heat and water vapor transfer mechanisms. For the TSEBpar, since heat and water vapor exchanges between the surface and atmosphere are considered independent processes, the partition of H is given as follows (Eqs. 3.85 to 3.87):

$$H^{[par]} = H_c^{[par]} + H_{soil}^{[par]} \tag{3.85}$$

$$H_c^{[par]} = \rho_a \cdot C_{pa} \cdot \left(\frac{T_c - T_a}{r_{ah}} \right) \tag{3.86}$$

$$H_{soil}^{[par]} = \rho_a \cdot C_{pa} \cdot \left(\frac{T_{soil} - T_a}{r_{ah} + r_{soil}} \right) \tag{3.87}$$

where T_c and T_{soil} are given in K; r_{soil} is the soil resistance to heat transfer (s/m). ρ_a and C_{pa} are the air density (kg/m^3) and the heat capacity of air ($J/kg/K$), respectively; r_{ah} is also given in s/m. The superscript "par" refers to the parallel TSEB model. More details on how to calculate

r_{soil} are given in Appendix B.

For the TSEBpar algorithm, the initial assumption regarding the initial value for LE_c was based on the original work from Norman et al. (1995) and indicated by Eq. 3.119 as follows:

$$LE_{c,i} = \left[1.30 f_g \left(\frac{\Delta}{\Delta + \gamma}\right)\right][Rn_c + Rn_{soil} - (Rn_c + Rn_{soil}) \cdot exp(0.90 \cdot ln(1 - f_c^{[N]}))] \quad (3.88)$$

where $LE_{c,i}$ is the initial guess value for iterating T_{cK} and T_{soilK} (W/m^2) and f_g is the green fraction of LAI (dimensionless), calculated as indicated by Norman et al. (1995).

3.5.2 Series Resistance TSEB Algorithm

For the TSEBser, the exchanges of heat and water vapor between the surface and the atmosphere are considered co-dependent processes, which gives the following partitioning models for H (Eqs. 3.89 and 3.90):

$$H^{[ser]} = \rho_a \cdot C_{pa} \cdot \left(\frac{T_o^{[ser]} - T_a}{r_{ah}}\right) \quad (3.89)$$

$$T_o^{[ser]} = \frac{\dfrac{T_a}{r_{ah}} + \dfrac{T_{soil}}{r_{soil}} + \dfrac{T_c}{r_x}}{\dfrac{1}{r_{ah}} + \dfrac{1}{r_{soil}} + \dfrac{1}{r_x}} \quad (3.90)$$

where $T_o^{[ser]}$ is the weighted aerodynamic surface temperature derived for the TSEBser algorithm (K); r_x is the total boundary layer resistance (s/m). The superscript "ser" refers to the series TSEB model. More details about the r_x calculations are found in Appendix B.

For the TSEBser algorithm, the modified approach by Colaizzi et al. (2012) has been considered to estimate T_c during the first iterative process. Colaizzi et al. (2012) proposed a modified PM-65 model for an initial T_c guess instead of the Priestley and Taylor LE_c model (Priestley and Taylor, 1972) for the TSEBpar approach, as suggested by Norman et al. (1995). Colaizzi et al. (2012) have indicated that the Priestley-Taylor model for LE_c might underestimate total LE from the TSEBser approach for large vapor pressure deficit (VPD) conditions during warm, cloud-free, and advective days. Thus, this study considered both the TSEBpar and TSEBser with different initial LE_c and T_c models to include updated sub-models from the existing literature. The modified PM approach for an initial T_c value is indicated by Eq. 3.120 (Jackson et al., 1981; Colaizzi et al., 2012):

$$T_{c,O} = T_a + \frac{Rn_c \cdot r_{ah} \cdot \gamma(1 + r_c/r_{ah})}{\rho_a \cdot C_{pa}[\Delta + \gamma(1 + r_c/r_{ah})]} - \frac{e_s - e_a}{\Delta + \gamma(1 + r_c/r_{ah})} \tag{3.91}$$

where $T_{c,O}$ is the initial guess for canopy temperature (K); γ is the psychometric constant ($kPa/^oC$); r_c is the bulk canopy resistance (s/m); Δ is the slope of the saturation vapor pressure curve ($kPa/^oC$); e_s and e_a are the saturated and actual vapor pressures in kPa, respectively. The calculation of r_c is described in Appendix B.

3.5.3 SEB Model Extrapolation: From Hourly to Daily Crop ETa

The LE is converted from W/m^2 to hourly ETa (mm/h) using Eq. 3.121 as follows:

$$ET_{ah} = C_f \cdot d_f \cdot \frac{LE}{\lambda_v \cdot \rho_w} \tag{3.92}$$

where ET_{ah} is the hourly instantaneous actual crop ETa (mm/h); d_f is a time scale factor in seconds (e.g., 1 h = 3,600 s); λ_v is the latent heat of water vaporization (J/kg); ρ_w is the water density

(kg/m^3); C_f is a length scale factor (e.g., 1,000 mm/1 m).

Eqs. 3.122 and 3.123 indicate the SEB and ET_{rF} approaches, respectively:

$$EF_i = \frac{LE_i}{R_{ni} - G_i} \cong EF_d \tag{3.93}$$

$$ETrF_i = \frac{ET_{ai}}{ET_{ref}} \cong ETrF_d \tag{3.94}$$

where EF is the evaporative fraction from the SEB results (dimensionless); $ETrF_i$ is the grass (ET_o) or alfalfa (ET_r) evaporative fraction approach (dimensionless). The subscripts "i" and "d" stand for instantaneous and daily timesteps, respectively.

When the EF or $ETrF$ are determined, daily ETa from the SEB is calculated by Eqs. 3.124 or 3.125, respectively:

$$ET_a^{[S]} = EF_i \cdot (R_n - G)_d \cdot \left(\frac{86,400}{\lambda_v \rho_w}\right) \tag{3.95}$$

$$ET_a^{[R]} = ETrF \cdot ET_{ref} \tag{3.96}$$

where $ET_a^{[S]}$ and $ET_a^{[R]}$ are the actual daily ETa (mm/d) from the SEB and $ETrF$ approaches, respectively; $(R_n - G)_d$ is the daily averaged available energy (W/m^2); λ_v and ρ_w are the latent heat of vaporization (J/kg) and density of water (kg/m^3), respectively.

The grass-based evaporative fraction approach was chosen in this study due to the following reasons:

a) Heat advection is a relevant environmental factor in most agricultural fields located in the USA semi-arid regions when dry and warm air from external areas flows above cooler irrigated fields (Figuerola and Berliner, 2005; Kutikoff et al., 2019).

b) The SEB evaporative fraction extrapolation method relies on daily R_n and G values (Chávez et al., 2008; Consoli and Vanella, 2014). Measuring on-site R_n and G might not be an easy task for farmers or agricultural stakeholders with limited access to proper training and skilled labor resources outside scientific research institutions. Furthermore, estimating daily R_n and G using approaches such as the FAO-56 bulletin or the ASCE modified PM-65 equation (Allen et al., 1998; Allen, 2000; ASCE-EWRI, 2005) introduces another level of uncertainty in ETa estimation due to underlying assumptions regarding daily G (Gavilán et al., 2007; Chávez et al., 2008).

c) Some published studies in the literature use the evaporative fraction from either grass (ET_o) or alfalfa (ET_r) data to estimate daily ETa from remote sensing OSEB and TSEB models (Trezza et al., 2013; Colaizzi et al., 2014; Zhao et al., 2020). Slight underestimation ($< 5\%$) has been reported when evaluating the performance of the ASCE-EWRI (2005) hourly ET_o in Nebraska, a semi-arid climate condition similar to Colorado (Irmak et al., 2008).

d) Chávez et al. (2008) have indicated that, when using grass ET_o instead of alfalfa ET_r data in the $ETrF$ extrapolation method, better performance of daily ETa products is achieved for row crops such as maize and soybeans.

3.6 Research Sites and Instrumentation

3.6.1 Limited Irrigation Research Farm (LIRF)

The LIRF facility is a research farm managed by the United States Department of Agriculture—Agricultural Research Service (USDA-ARS) in Greeley, Colorado, USA (Figure 3.7). The local climate is described as subtropical steppe with cold semi-arid trends (Peel et al., 2007). Located at latitude N 40.4463^o, longitude W 104.6371^o, and elevation of 1432 m, the facility has two rectangular-shaped irrigated maize fields that supported the extensive data collection campaign in 2017, 2018, 2020, 2021, and 2022 from July to September. The field dimensions are 190 m × 110

m, and the sub-surface drip was the irrigation system in each field. The drip irrigation emitters were 0.30 m apart, buried 0.23 m deep at a 0.76 m distance between rows.

The experimental design and data collection stations at LIRF for the years 2020 and 2021 are shown in Figure 3.8. Each of the maize fields had the same irrigation system, a subsurface drip irrigation setup, which had the drip laterals buried at a depth of 0.23 m and emitters spaced every 0.30 m. The maize rows had a North-South orientation and were spaced 0.76 m apart. The distance between adjacent maize plants was 0.17 m. The planting density for maize remained consistent at 87,500 plants per hectare during both years. In 2020, the selected maize variety was NK9227-5222A (Syngenta Inc., Basel, Switzerland), known for its drought tolerance. Planting took place on May 6, 2020, and the harvest occurred on October 13 and 14, 2020. In 2021, there was a change in maize varieties with the introduction of other drought-tolerant maize options: P9998Q and P0157AMXT (Pioneer Hi-Bred International, Inc., Johnston, Iowa, USA), along with CH 194-49 DG (Channel Bio Corporation, Saint Louis, Missouri, USA). Planting for this year was carried out on May 13, 2021, and the harvest took place on October 11 and 12, 2021. Fields W and E, each comprising approximately 83% of their respective plots, were planted with the maize variety P0157AMXT, as indicated in Figure 3.9.

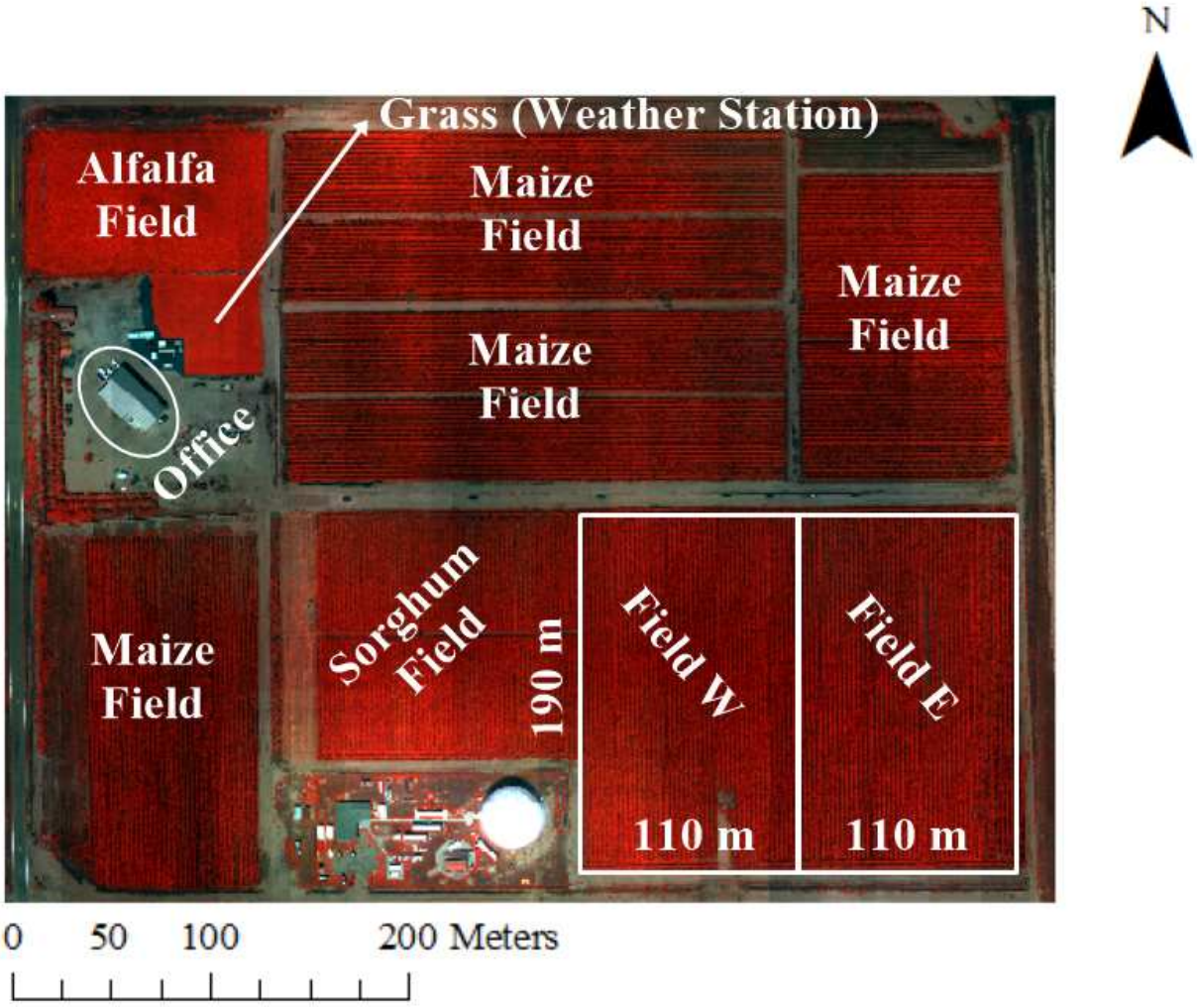

Figure 3.7: False-color image of the LIRF research site. The study maize fields were Fields W and E. Areas in red are vegetated surfaces.

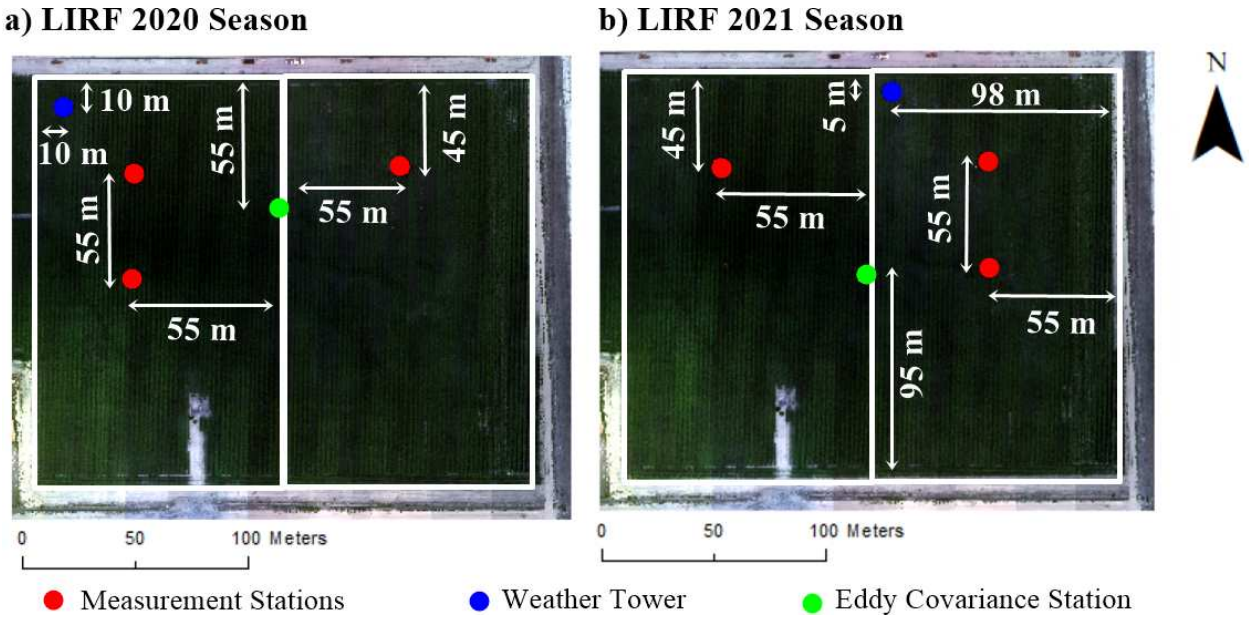

Figure 3.8: The LIRF facility in Greeley, CO. A weather tower was installed at the non-water stress field to calculate BR ETa data. Soil water content sensors were installed at the measurement stations (red circles) to measure ETa through the SWB approach. An EC energy balance system was installed between the two maize fields.

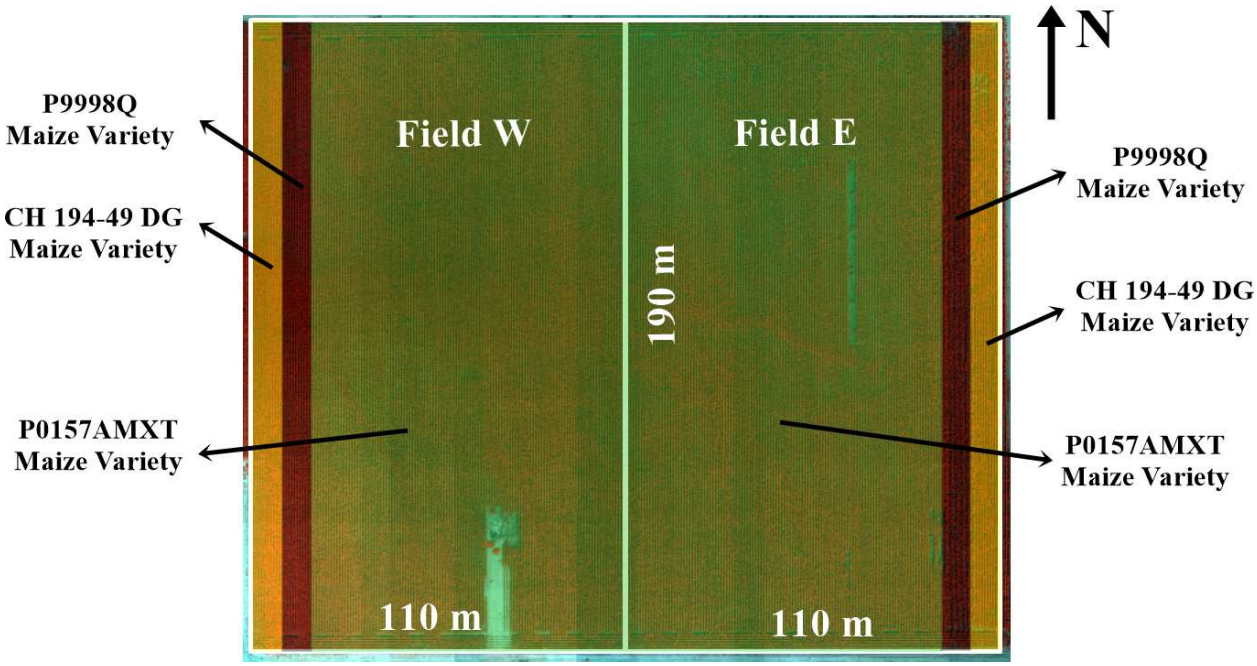

Figure 3.9: Plant variety map at LIRF (Fields W and E) in 2021. Most of the area was occupied by the P0157AMXT maize variety.

For each respective data collection season, each field was subjected to different irrigation water management strategies. In 2020, the West Field, hereafter referred to as Field W, was fully irrigated. In this context, "fully irrigated" represents the conditions in which frequent irrigation events were scheduled to maintain soil moisture in the crop (maize) root zone at non-water stress levels. Conversely, the East Field, designated as Field E, was managed as a deficit-irrigated field, resulting in water stress conditions throughout the growing season. In 2021, the irrigation water management practices were switched between these treatment plots. Field W was transformed into the deficit-irrigated field, while Field E became the fully irrigated plot. A summary of the soil wetting events, which include irrigation and rainfall, for the years 2017 to 2022, is provided in Table 3.1. The water-deficit irrigation approach at LIRF has consisted of two major irrigation events throughout the entire season (May to September): First irrigation during Mid-July (before vegetation rapid growth) and second irrigation water application during the canopy maturity stage when vegetation reaches maximum values of LAI and canopy height (Mid-August).

Table 3.1: Cumulative soil wetting events (irrigation and rainfall) at LIRF Fields from 2017, 2020, 2021, and 2022.

Irrigation Scheduling	Growing Season	Research Field	Irrigation Events	Cumulative Gross Irrigation (mm)	Cumulative Rainfall (mm)
Fully Irrigated	2017	E	2	118	90
	2020	W	5	472	36
	2021	E	4	330	98
	2022	W	7	509	79
Deficit Irrigated	2017	W	8	368	90
	2020	E	3	309	36
	2021	W	2	176	98
	2022	E	6	336	79

The LIRF fields have different soil texture properties (Figure 3.10). Field 1 has a larger, lighter (sandy) area than Field 2, with sandy loam as the predominant soil texture. Field 2 has a thin layer

comprised of a sandy loam envelope at a shallow root zone soil depth (< 20 cm) that becomes loamy sand to clay loam at the remaining soil depths (for more details, see Costa-Filho et al., 2020). The maize plant density was 9 plants/m^2 (86,487 plants/ha) for all years of data collection. In 2020, seed planting and maize emergence happened on 5/6/2020 and 5/18/2020, respectively. Maize planting and emergence occurred on 5/13/2021 and 5/25/2021 during the 2021 season, respectively. The maize fields did not lack nutrients (e.g., macro-nutrients Nitrogen, Phosphorus, and Potassium) in all years of data collection.

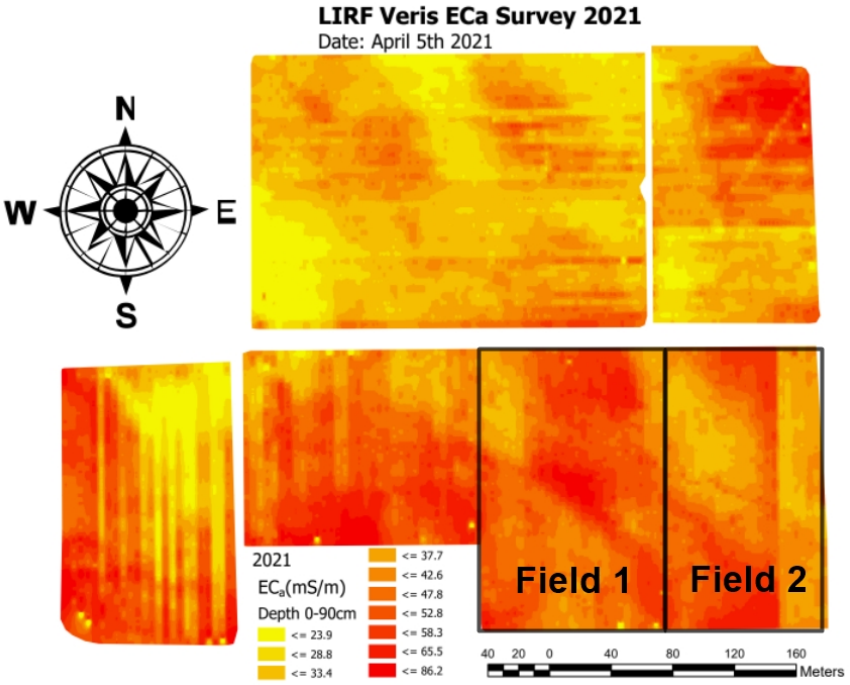

Figure 3.10: Soil apparent electrical conductivity (ECa, mS/m) map during the LIRF pre-season in April 2021. Spatial ECa data were measured using a Veris soil scanning sensor (Veris Technologies, Salina, KS). ECa is associated with the soil's capacity to conduct electricity. Figure credits to Kevin Yemoto.

The experiment design at LIRF in 2017 and 2022 was quite similar to the 2020 and 2021 seasons (Figure 3.11). Nonetheless, each maize field had two ancillary measurement stations. An EC system provided measured ETa data in 2017 from July to August. Furthermore, each field had its weather tower with hygrometer instruments to measure air temperature (T_a) and relative humidity

(RH) at five heights AGS. These weather towers provided data to determine surface heat fluxes (e.g., H and LE fluxes) and daily maize ETa through the BR method. Soil water content sensors (Decagon Devices Inc., Pullman, WA) provided measured ETa through the SWB approach at locations F1, F2, D1, and D2 (Figure 3.11).

The maize variety was Dekalb 51–20 (Bayer Crop Science, Leverkusen, Germany) in 2017 at LIRF. The plant density was 87,500 plants/ha. Tillage was accomplished by strip-tilling before planting, which occurred on the day of the year (DOY) 152 in 2017. Nitrogen fertilizer was applied as urea ammonium nitrate (UAN) at a 32 $\%$ concentration rate. In 2017, nitrogen was applied on DOY 186 and 213 at a rate of 39 and 76 kilograms per hectare, respectively. Irrigation scheduling followed the paper FAO-56 standard approach method (Allen et al. 1998), based on crop coefficient and reference alfalfa evapotranspiration calculated as indicated by ASCE-EWRI (2005).

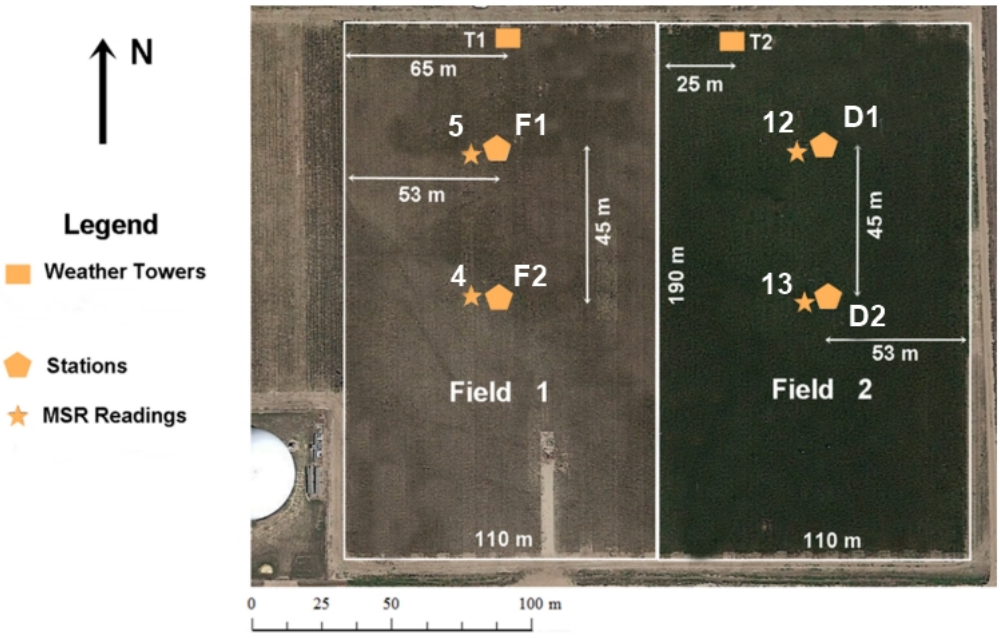

Figure 3.11: The 2017 LIRF experiment.

An agricultural weather station from Colorado Agricultural Meteorological Network (COAGMET) provided micrometeorological data to determine daily ET_o and ET_r, an essential component of each ETa model in this study (e.g., RBCC, OSEB, and TSEB). At LIRF, the COAGMET weather station (Greeley 04 or GLY04) is located within the research farm, 125 m Northwest of the lateral edge that separates Fields W and E. The GLY04 station (Figure 3.12) is a pristine 12-cm clipped tall fescue (cool-season) grass with the same micrometeorological instrumentation installed at the maize fields. Nonetheless, the GLY04 weather data have been measured at heights above the ground surface (AGS) to conform to the standardized guidelines to calculate ET_o and ET_r (ASCE-EWRI, 2005). Air temperature and relative humidity sensors (Vaisala, Vantaa, Finland) are 1.5 m AGS. Wind speed (RM Young Company, Traverse City, MI, USA) and solar radiation (LI-COR, Lincoln, NE, USA) instruments are 2 m AGS. The GLY04 data are provided in 5-minute, hourly, and daily time steps. More details about the instrumentation used to collect data at the LIRF site are in Appendix D.

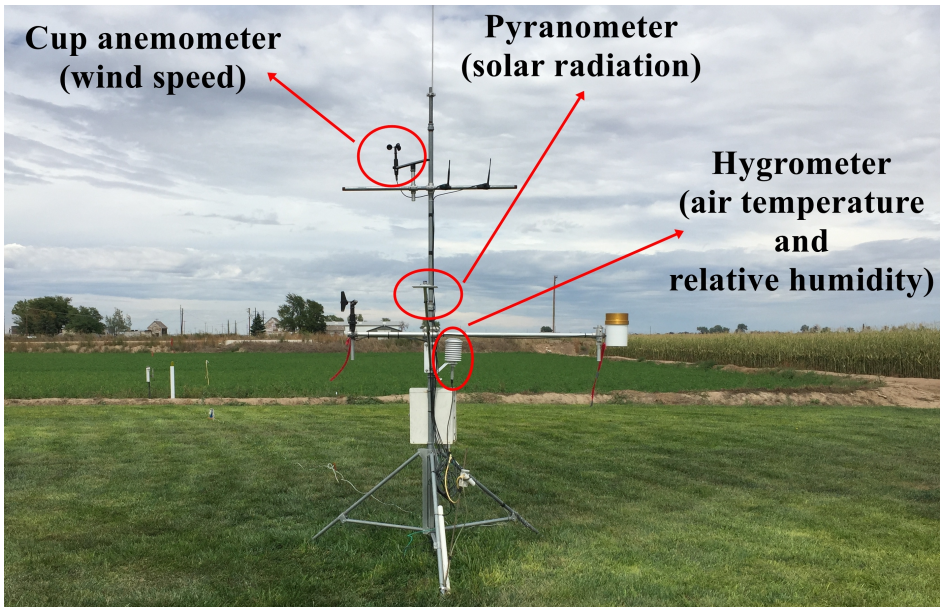

Figure 3.12: The GLY04 COAGMET station at LIRF.

3.6.2 Irrigation Innovation Consortium (IIC)

The IIC site (Figure 3.13) is in Fort Collins, Colorado, USA, at 40.5542^o N latitude, 105.0038^o W longitude, and 1486 m above sea level. The local climate is described as subtropical steppe with cold semi-arid trends (Peel et al., 2007). Data collection happened on two surface-irrigated maize fields (furrow irrigation system) in 2020 and 2021, from July to September. Maize row orientation was East-West with 17 cm row spacing. The fields had a relatively uniform soil texture comprised of sandy loam with volumetric soil water contents at field capacity (θ_{FC}), permanent wilting point (θ_{PWP}), and saturation (θ_{SAT}) were equal to 0.189, 0.069, and 0.410 m^3/m^3, respectively. Aluminum 4 cm-diameter siphon tubes provided water to the field furrows. The water-stressed maize field had 50% fewer irrigation events than the non-water-stressed field throughout the farming seasons.

The irrigation waterfront moved from East (central canal) to West on the fully irrigated field (Fig. 3.13). The irrigation front moved from Northwest to Southeast at the deficit irrigated field. The irrigation events were set to happen within 2 to 3 days after water acquisition from the Sand Dike Lateral Company (Fort Collins, CO, USA). The irrigation event duration varied from 6 to 12 hours. Both fields did not have nutrient deficiency (e.g., Nitrogen, Phosphorus, and Potassium) during the two-year data collection period. The weather conditions at the IIC during the data collection campaigns in 2020 and 2021 were nearly the same in terms of mean T_a and RH. In 2020, from July to September, the total amount of rainfall was 42% less than in 2021.

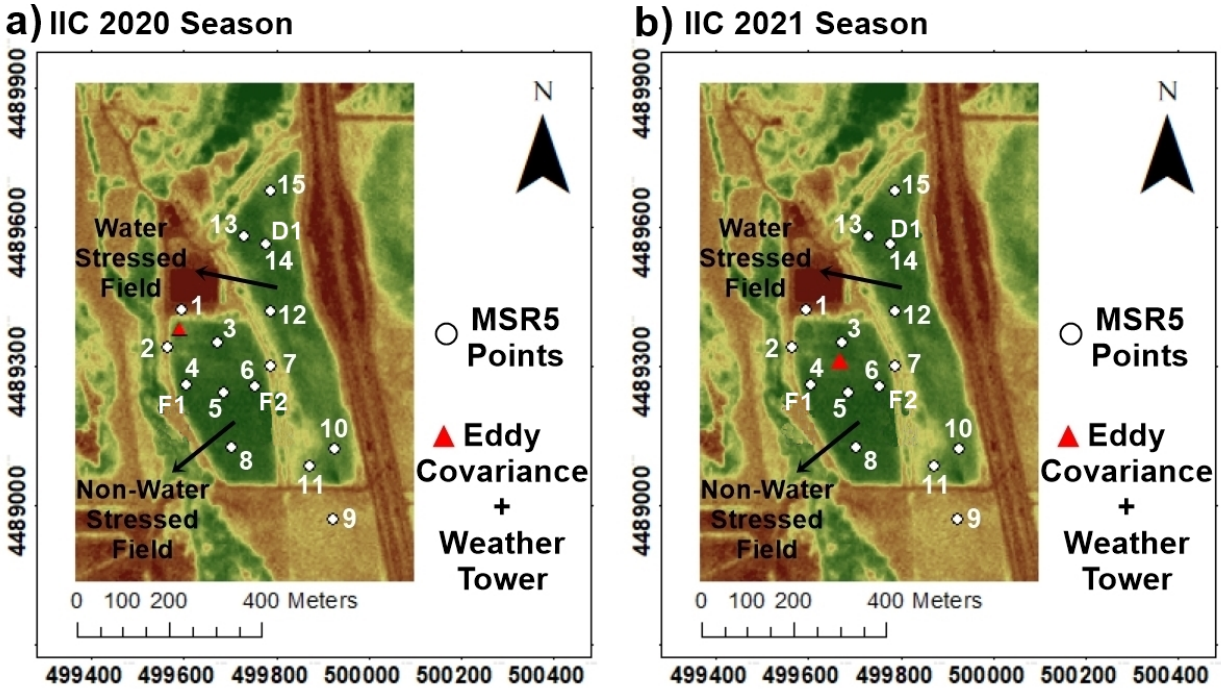

Figure 3.13: The IIC facility in Fort Collins, CO. Locations 1 to 15 are sampling points for ground-based surface reflectance and nadir-looking T_s data using an MSR handheld radiometer. At points 4, 6, and 14, ancillary data were measured. Soil water content sensors were buried at locations F1, F2, and D1 to provide measured ETa through the SWB approach. A weather tower with an EC energy balance system was installed at the non-water stress field. Fig. 8a and 8b show the measurements' locations for the 2020 and 2021 seasons, respectively.

Figure 3.14: An irrigation event at the IIC non-water stressed field in 2021. The waterfront moved from East to West. Photo provided by Ansley Brown.

The ClimaVUE50 weather station (Campbell Scientific Inc., Logan, Utah, USA) was installed over a grass surface (location 9 in Fig. 3.13) that was partly irrigated at the South side of the IIC in 2020 and 2021 (Figure 3.15). To avoid violating the assumptions of the ET_o and ET_r calculation (ASCE-EWRI, 2005), the nearest COAGMET weather station with pristine 12-cm clipped fescue grass was selected (GLY04, the COAGMET station within the LIRF research site in Greeley, CO). There are COAGMET weather stations in Fort Collins (e.g., FCL01, FTC01, FTC02, FTC03, FTC04). Nonetheless, they are not operated on a pristine grass surface of recommended field size and sitting conditions. Hence, the GLY04 station was chosen to provide data to determine hourly and daily ET_o and ET_r for the IIC research site because it has pristine grass and is located under similar climate conditions as in Fort Collins.

Figure 3.15: The ClimaVUE50 IIC weather station in a non-pristine grass. Photo provided by Ansley Brown.

The choice of maize varieties differed between 2020 and 2021. In 2020, G02K39-3120 (Golden Harvest, Minnetonka, Minnesota, USA) was planted on May 13 at an approximate rate of 8 seeds

per m^2. For the year 2021, the NK0243-3120 and NK0314-5122 varieties (Syngenta AG, Basel, Switzerland) were planted in both fields, as indicated in Figure 3.17. The seeding date for 2021 was May 13, and the planting rate was 8 seeds per m^2. All maize varieties used in this study were selected for their drought-tolerance capabilities.

The irrigation scheduling was determined based on the FAO-56 methodology (Allen et al., 1998) and implemented in the Water Irrigation Scheduler for Efficient (WISE) Application (Andales et al., 2014). The WISE application uses a water balance approach to determining irrigation amounts and timing based on a dual crop coefficient approach for ETa estimation from tabularized crop coefficient (Kc) values, a water stress coefficient (Ks), and daily alfalfa reference ET. In Appendix D, there are more details about the instrumentation used to collect data at the IIC site. A summary of the data related to soil wetting events, encompassing both irrigation and rainfall events, for the years 2020 and 2021, is given in Table 3.2.

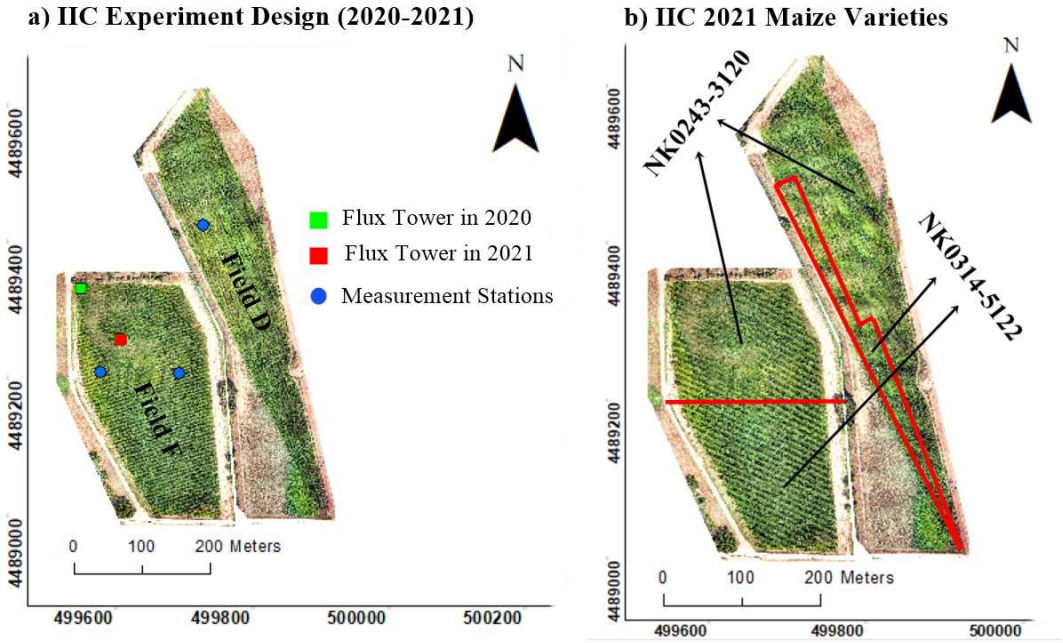

Figure 3.16: RGB (Red-Green-Blue) map of the IIC research fields (Figure 5.10a) and the maize varieties planted in 2021 (Figure 5.10b). The study maize fields were Fields F and D. Areas in green are vegetation surfaces.

Table 3.2: Cumulative soil wetting events (irrigation and rainfall) at IIC Fields in 2021 and 2022.

Growing Season	Research Field	Irrigation Events	Cumulative Gross Irrigation (mm)	Cumulative Rainfall (mm)
2020	F	7	1,620	34
	D	5	870	34
2021	F	8	1,081	104
	D	4	1,064	104

3.6.3 Arkansas Valley Research Center (AVRC)

The AVRC site, administered by the Agricultural Experiment Station at Colorado State University (AES-CSU), is in Rocky Ford, CO, USA, at 38.03847^o N latitude, 103.69329^o W longitude, and 1273 m above sea level. The local climate is described as subtropical steppe with cold semi-arid trends (Peel et al., 2007). Two precision monolith-weighing lysimeters provided data from May to September 2020 and 2021 (Figure 3.17). The small lysimeter (SL), with 1.50 m x 1.50 m x 2.4 m dimensions, had grass in both years of data collection and was located in a triangular-shaped field (34,000 m^2). In 2020 and 2021, the large lysimeter (LL), with 3 m x 3 m x 2.4 m dimensions, had maize and pinto beans, respectively. The LL was within the boundaries of a rectangular-shaped field (50,098 m^2). The SL and LL have the same uniform soil texture (silty clay loam) with θ_{FC}, θ_{PWP}, and θ_{SAT} equal to 0.314, 0.176, and 0.430 m^3/m^3, respectively (USDA-NRCS, 2009).

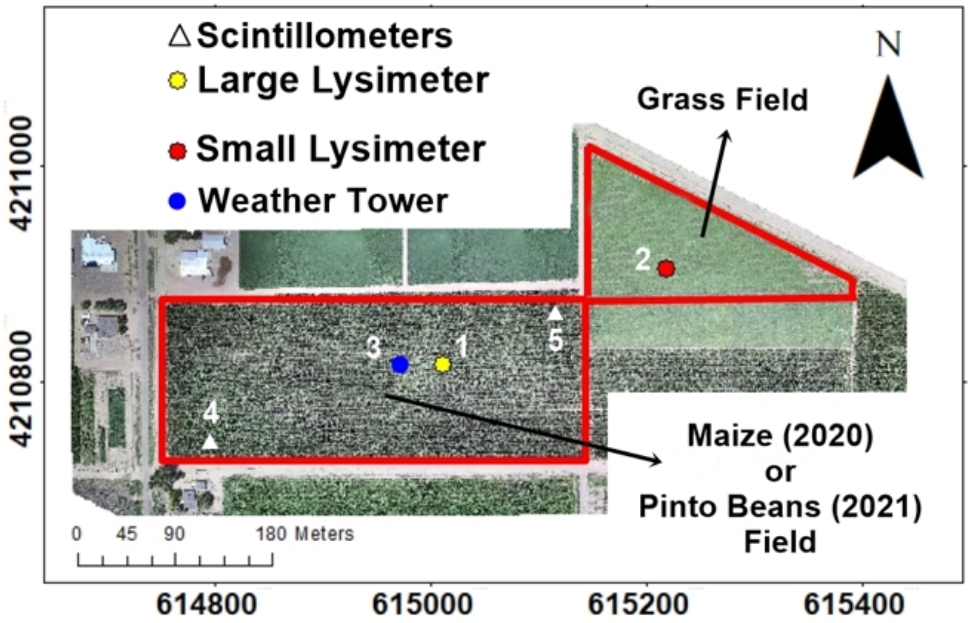

Figure 3.17: The AVRC facility in Rocky Ford, CO. Locations 1 and 2 are sampling points for ground-based surface reflectance and nadir radiometric temperature using a handheld radiometer and the spatial points where ancillary data were measured. Only in 2021, location 3 had a weather tower that provided T_a and RH data at two heights above ground to calculate BR ETa.

Both lysimeters at the AVRC (Figure 3.18) operate using an automated scale-load cell that records temporal changes in mass within the lysimeter's physical boundaries in millivolts (mV) with a sensitivity of 0.02%. The calibration coefficient to convert the change in mass volume to water depth is 76 mm/mV (e.g., 1 mV change detected by the lysimeter scale-load cell represents 76 mm of water depth). Excess water from irrigation or rainfall events percolates the soil through the lysimeter scale area. The excess water is drained out of the system to ensure that previous wetting events do not compromise ETa measurements using soil water mass balance. The local AVRC weather station provided hourly micrometeorological data to calculate ET_{ref}. The weather station is located in a pristine alfalfa field (100 m x 150 m) within the AVRC research site, 180 m Northwest and 330 m East of the LL and SL fields, respectively.

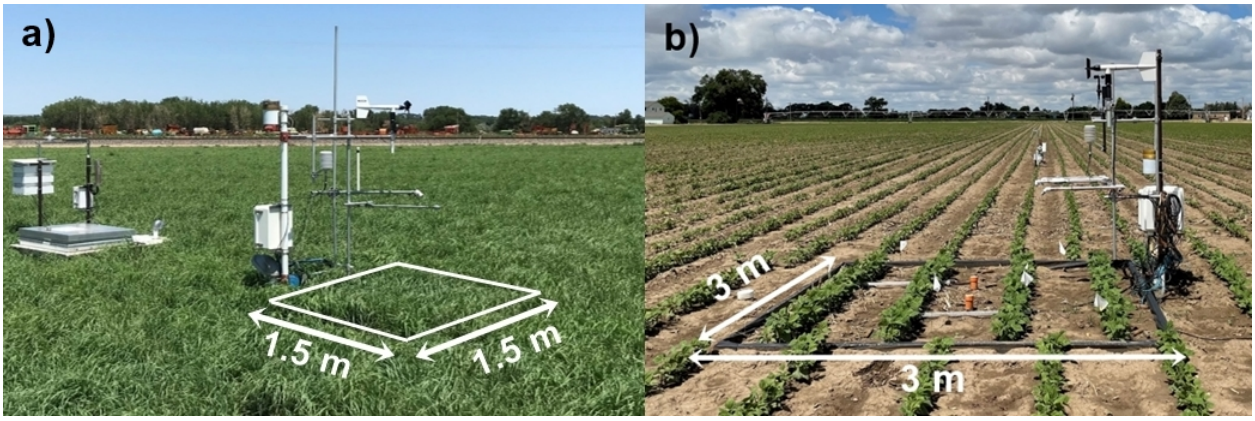

Figure 3.18: Figure 3.18a shows the SL located at the grass field. Figure 3.18b shows the LL when pinto beans were the crop type in 2021. In 2020, the crop type at the large lysimeter was maize. Figure 3.18 is not scaled and was provided by Lane Simmons.

For both years of data collection at the AVRC site, the irrigation system was sprinkler (linear move) and furrow irrigation for the LL and SL fields, respectively. The sprinkler nozzles were 2.3 m above ground level and 1.5 m apart. In 2020, the LL maize field had seeds planted and plant emergence on 4/29/2020 and 5/6/2020, respectively. The maize plant density was approximately 8 plants/m^2 (75,684 plants/ha). Maize harvest occurred on 10/19/2020. No lack of nutrients or water stress conditions was observed in 2020 at both the LL and SL fields. Information about the sensors used for data collection at the AVRC research site is found in Appendix D.

3.7 Methods for Measuring Crop Evapotranspiration

3.7.1 Eddy Covariance Energy Balance System

This research project has installed EC SEB systems at the LIRF and IIC sites. At LIRF, a LI-7500DS open-path gas analyzer (LI-COR Biosciences, Lincoln, Nebraska, USA) and a Windmaster 3D sonic anemometer (Gill Instruments, Lymington, United Kingdom) alongside secondary equipment were installed in between the two maize fields (Fig. 3.19a). The data was sampled at 10 Hz (e.g., ten measurements per second), averaged, and recorded at half-hour intervals. At the

IIC site, an LI-7500A open-path gas analyzer (LI-COR Biosciences, Lincoln, Nebraska, USA) and a CSAT 3D sonic anemometer (Campbell Scientific, Logan, Utah, USA) and respective auxiliary instrumentation were installed at the non-water stressed field in 2020 and 2021 (as indicated on Figure 3.19b). The data were sampled at 10 Hz, averaged, and recorded at 15-min time intervals. Table 3.3 presents the high-frequency data correction approaches for the LIRF and IIC EC systems.

At LIRF in 2017, the same EC system installed at the IIC provided H in the fully irrigated treatment plot only (Field E) from July to September (Figure 3.20). Lag time issues caused by dataloggers were corrected by estimating each averaging interval through a cross-correlation analysis between the scalar of interest and the vertical wind component. Then, the correlations between the two signals lagged by different delays are compared. The time lag produces the highest correlation. The corrected sensible heat flux (H_c) was based on H measurements from the sonic anemometer-based air temperature (H_s) and the corrected LE (LE_c). Values of measured H were recorded as 15-minute averaged data obtained from 20 Hz high-frequency measurements. The EC system at LIRF in 2017 was installed on the North side of Field E, 3.5 m above ground surface at an azimuth angle of 135^o.

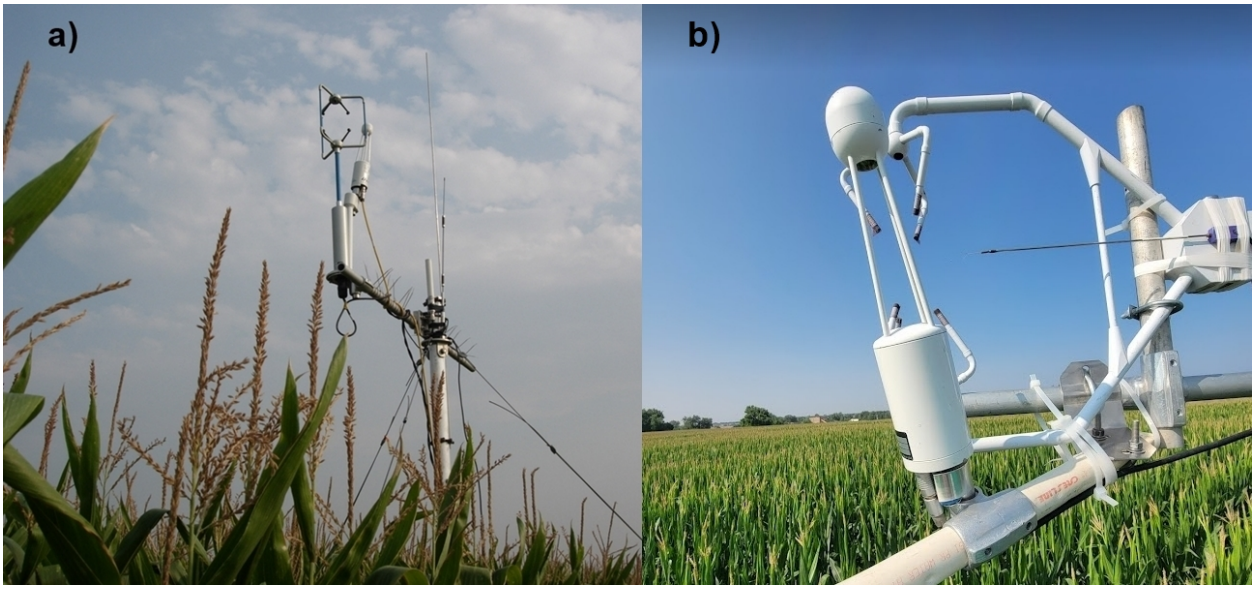

Figure 3.19: EC systems installed at LIRF (Figure 3.19a) and IIC (Figure 3.19b) sites in 2020 and 2021. The instruments have been 3.5 m AGS at both sites. Jon Altenhofen provided Figure 3.19a.

Figure 3.20: The EC system at LIRF in 2017 (Field E) with aerodynamic profile sensors (e.g., cup anemometers and hygrometers).

Table 3.3: Summary of the correction methods applied to the EC data at LIRF and IIC.

Correction Method	References	Research Site
Wind coordinate or tilt correction	Tanner and Thurtell (1969); Kaimal and Finnigan (1994)	LIRF and IIC
Air density fluctuation - The Webb-Pearman-Leuning (WPL) correction	Webb et al. (1980)	LIRF and IIC
Humidity correction of sonic temperature	Schotanus et al. (1983); van Dijk et al. (2004)	LIRF and IIC
Statistical analysis for data screening	Vickers and Mahrt (1997)	LIRF
The angle of attack correction for wind 3D components	Nakai and Shimoyama (2012)	LIRF

The EC system provides unbalanced turbulent fluxes regarding SEB closure (Foken et al., 2006). That is due to the EC system not capturing all range of turbulent scales in the field, asymmetric turbulent transport of heat and water vapor causing reduced measured H and LE, and continuous larger air vortex (or eddies) circulations not being captured by one EC station alone (Liu et al., 2011; Yanzhao and Xin, 2018; Liu et al., 2021). The flux data from EC systems have the SEB closure ratio $(H + LE)/(R_n - G)$ ranging from 70% to 90% in the literature (Goulden et al., 1997; Wilson et al., 2002; Meyers and Hollinger, 2004; Oncley et al., 2007; Liu et al., 2011). Hence, the H and LE data are underestimated depending on surface roughness and micrometeorological conditions during the crop growing season (Mauder et al., 2007; Foken, 2008; Burba, 2013; Liu et al., 2021; Peltola et al., 2021). Figure 3.21 indicates the SEB flux closure issue at the IIC and LIRF during the data collection campaigns around solar noon time (11 am to 1 pm). Thus, to improve the representativeness of H, LE, and ETa measurements from the EC system, the residual-LE closure approach was chosen in this study to ensure the closure of the surface heat fluxes. Twine et al. (2000) indicate that the residual-LE method calculates LE as the difference among measured

R_n, G, and H (from the EC system). Twine et al. (2000) indicate that most of the unresolved EC system closure issues are due to LE rather than H.

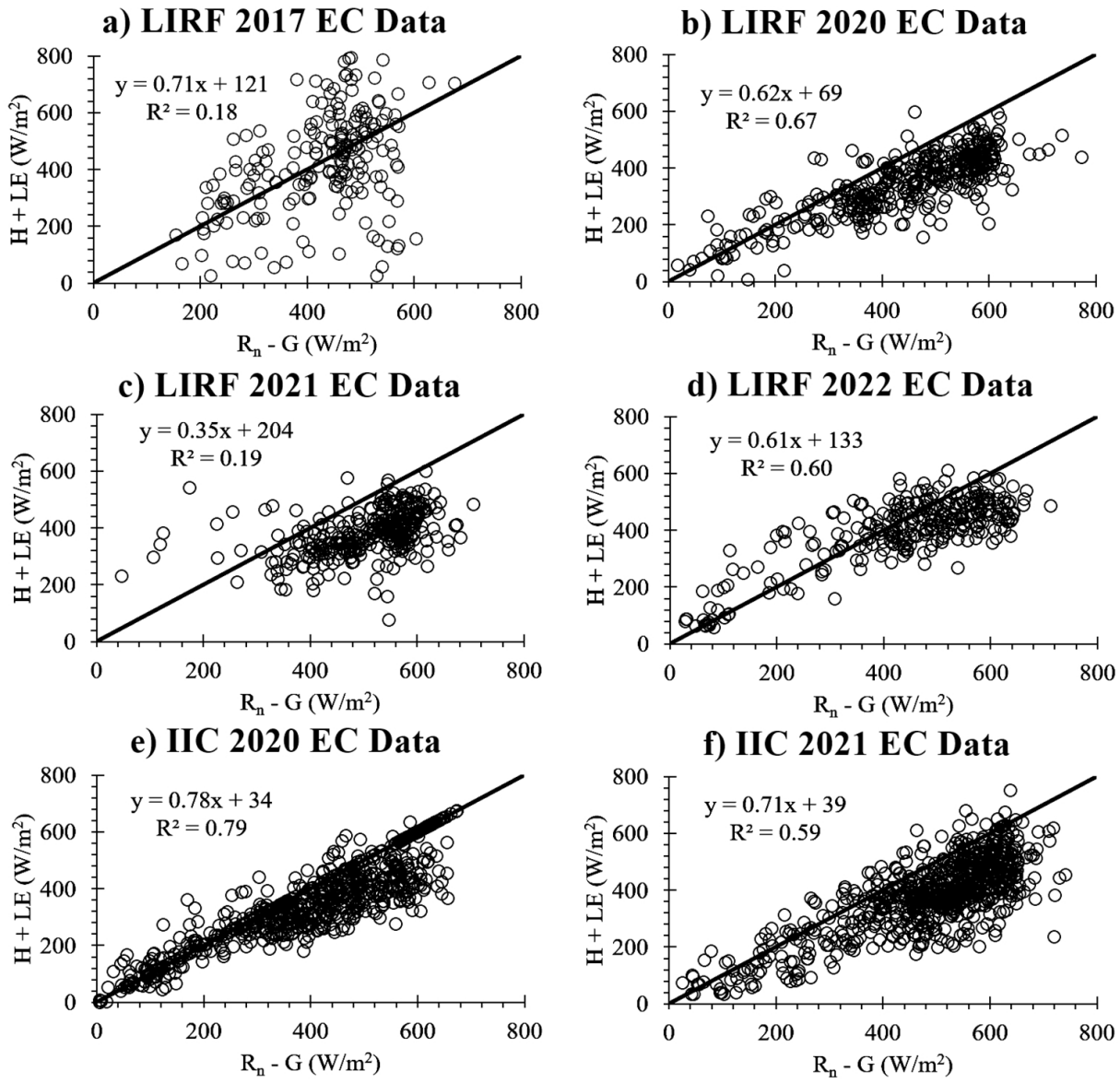

Figure 3.21: The EC closure analysis for LIRF and IIC considering H and LE data measured around solar noon (11 am to 1 pm Mountain Standard Time). The black line represents the 1:1 line.

In this study, A two-dimensional (2D) EC heat flux (source) footprint analysis was performed to filter the EC-derived heat flux data to consider only flux source areas contributing to H and LE fluxes coming strictly from the maize fields at both LIRF and IIC sites. The 2D analytical EC foot-

print model developed by Kljun et al. (2015) was used to identify the upwind source area of H and LE fluxes at all sites. The Kljun et al. (2015) model can integrate georeferenced data to generate footprint maps of a given AOI. More details about the footprint approach are found in Kljun et al. (2004) and Kljun et al. (2015). The 2D footprint model is an analytical flux-source approach that provides 2D footprint extents based on turbulence characteristics of the airflow and surfaces such as Monin-Obukhov stability length (L_{MO}), friction velocity (u*), the standard deviation of lateral velocity (σ_v), the height above ground of wind speed measurement (Z_u), roughness length for momentum transfer (Z_{om}), and the atmospheric boundary layer height (H_L).

Thus, to compare the predictions of ETa at each station of measurement with the hourly and daily EC ETa data, it was assumed that the fixed measurement instrumentation stations that were within the 2D EC footprint were representative of observed ETa data from the EC system during the RS sensor overpass date and time. At the IIC site, the EC flux tower was located at the North-west corner of the field in 2020. Since the West and East measurement stations were further from the footprint area for H and LE fluxes, the data from the West station was assumed to represent a maize ETa comparison between the EC data and remote sensing of ETa predictions since it was the closest station to the flux tower. Figures 3.22 and 3.23 show the 2D EC footprints that served as a reference to filter the EC data at the LIRF and IIC sites, respectively.

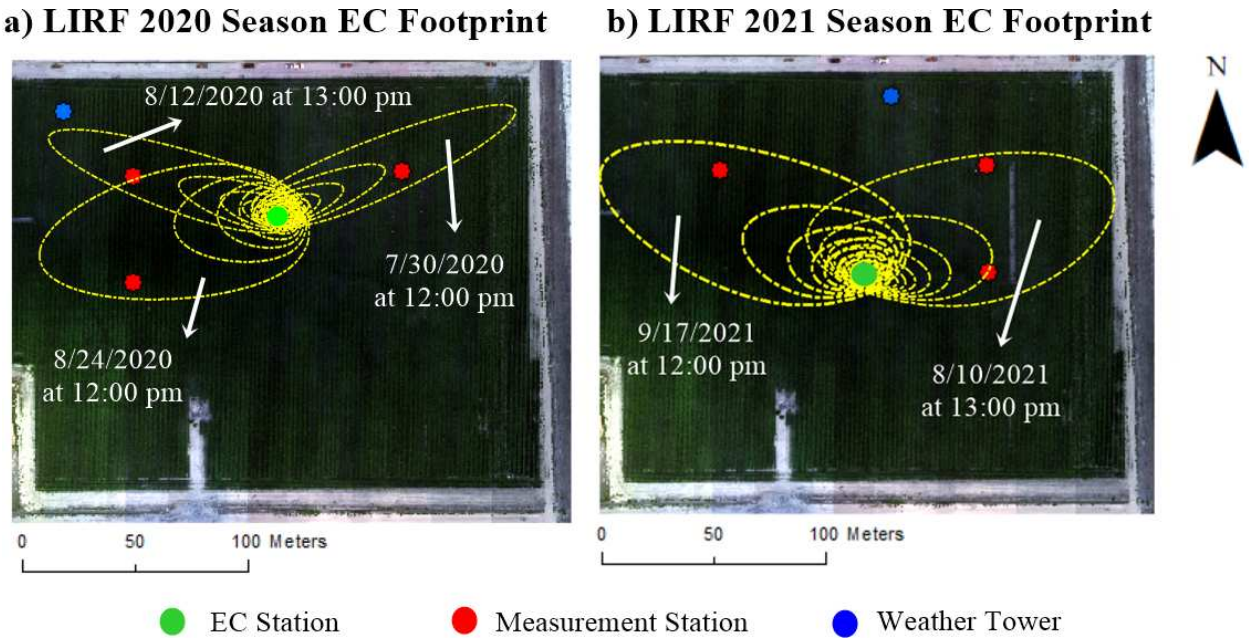

Figure 3.22: 2D EC footprint (yellow areas) at LIRF maize fields in 2020 (Figure 3.22a) and 2021 (Figure 3.22b).

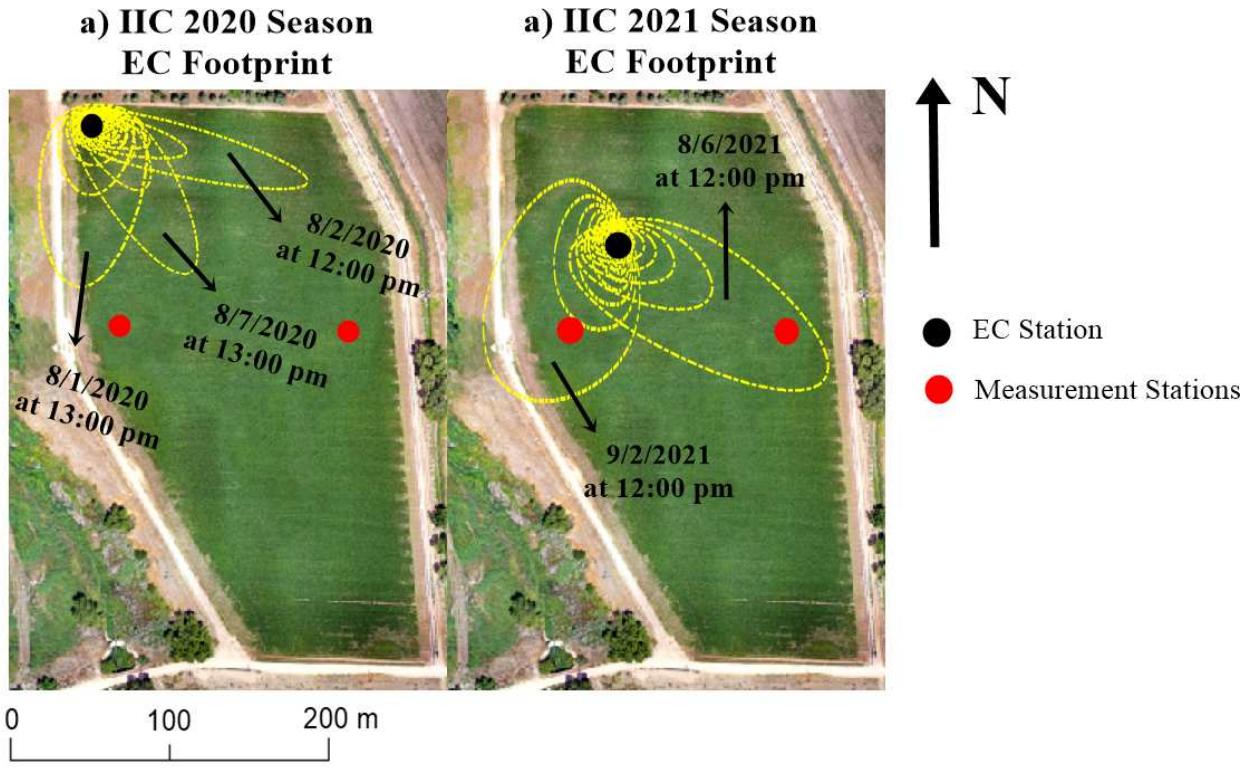

Figure 3.23: 2D EC footprint (yellow areas) at the IIC maize field F in 2020 (Figure 3.23a) and 2021 (Figure 3.23b).

Since the Remote Sensing of ETa models in this study provided hourly (OSEB and TSEBs) and daily ETa estimates (RBCC) for crop water management purposes, LE data from the EC SEB systems were converted to evaporated water depth for hourly and daily timesteps at all sites using Eqs. 3.97 and 3.98, respectively:

$$ET_h^{[EC]} = \frac{LE}{\lambda_w} \tag{3.97}$$

$$ET_d^{[EC]} \cong \left[\frac{c \cdot 86,400}{\rho_w \cdot \lambda_w}\right]\left[\frac{LE^{[EC]}}{(R_n - G)_{inst}}\right](R_n - G)_{daily} \tag{3.98}$$

where $ET_d^{[EC]}$ is the daily ETa from the EC system (mm/d); ρ_w is the density of liquid water (kg/m^3); $ET_h^{[EC]}$ is the instantaneous ETa from the EC system (mm/h); λ_w is the latent heat of vaporization (J/kg); $LE^{[EC]}$ is the latent heat flux at around solar noon time (W/m^2); $(R_n - G)_{inst}$ and $(R_n - G)_{daily}$ are the instantaneous (around solar noon) and daily-averaged available energy, respectively. The parameter c is a unit conversion factor (1000 mm/m). The λ_w is calculated as described in Henderson-Sellers (1984).

3.7.2 Bowen Ratio Turbulent Heat Fluxes

The Bowen ratio method (BR) gives indirect measurements of H and LE by determining the ratio between these two heat fluxes (Perez et al., 1999; Comunian et al., 2018; Buttar et al., 2018). Eq. 3.99 outlines the fundamental approach of the BR method (Bowen, 1926):

$$\beta_o = \frac{H}{LE} \tag{3.99}$$

where β_o is the Bowen ratio (dimensionless).

According to Perez et al. (1999), accurately determining H and LE depends on obtaining accurate values for β_o since it helps minimize the spread of bias that occurs when errors from

measurements of R_n and G are considered. Bowen (1926) suggested that β_o could be estimated by approximating the ratio using the gradients of heat and vapor. This approximation is valid under the assumption that the diffusivity of heat and vapor transfer have the same magnitude. Eq. 3.100 presents the algebraic representation of this assumption:

$$\beta_o \cong \frac{Cp_a \cdot K_h \cdot \Delta T}{\lambda_w \cdot K_v \cdot \Delta e} = \left(\frac{Cp_a}{\lambda_W}\right) \cdot \left(\frac{\Delta T}{\Delta e}\right) \tag{3.100}$$

where Cp_a is the specific heat of the air (J/Kg/K); K_h and K_v are, respectively, the diffusivity coefficients for heat and vapor transfer (m^2/s); λ is the latent heat of vaporization of water (J/Kg/K); ΔT and Δe are, respectively, the temperature (°C) and actual vapor pressure (kPa) difference at two different heights.

According to ASCE-EWRI (2005), the ratio $\frac{Cp_a}{\lambda}$ is commonly represented as the psychometric constant (γ). It is determined based on the local atmospheric pressure, as outlined in Eq. 3.101:

$$\gamma = \frac{Cp_a}{\lambda} = 0.000665 \cdot P_a \tag{3.101}$$

where P_a is the local atmospheric pressure (kPa). γ has units of kPa/C. P_a might be calculated as indicated by ASCE-EWRI (2005) as a function of local ground elevation (Eq. 3.126):

$$P_a = 101.3 \cdot \left(\frac{293 - 0.0065 \cdot Z_g}{293}\right)^{5.256} \tag{3.102}$$

where Z_g is the local ground elevation (m).

The calculation of actual vapor pressure from each height of micrometeorological measurement was done as indicated by Eq. 3.127 below:

$$e_a = RH \cdot e_s \tag{3.103}$$

where e_a is the actual vapor pressure (kPa); RH is the relative humidity (dimensionless); e_s refers to the saturation vapor pressure (kPa). The e_s term was calculated using the approach developed by Buck (1981) and indicated by Eq. 3.104:

$$e_s = 0.61121 \cdot exp\left(\frac{17.502 \cdot T_a}{T_a + 240.97}\right) \tag{3.104}$$

where T_a is given in °C.

At LIRF and the IIC, the change in air temperature and actual vapor pressure were obtained from measurements of T_a and relative humidity at two different heights. For the year 2017, the LIRF heights selected were 2.7 m and 3.7 m AGS. For the year 2018, the LIRF heights that provided data for the BR fluxes calculations were located at 2.6 m and 3.2 m above ground surface for field W and at 2.6 m and 4.2 m for field E, respectively. Those data were obtained from the aerodynamic flux towers located at the north side of both fields W and E in both years. In 2020 and 2021 at LIRF and IIC, as well as LIRF 2022 years, the measurement heights of micrometeorological data for the BR method were 3.5 m and 4.5 m AGS. Indirect H and LE measurement values from the BR approach were determined as indicated by Eqs. 3.105 and 3.106 :

$$H_{BR} = \left(\frac{\beta_o}{1 + \beta_o}\right) \cdot (R_n - G) \tag{3.105}$$

$$LE_{BR} = \left(\frac{1}{1 + \beta_o}\right) \cdot (R_n - G) \tag{3.106}$$

where R_n and G are given in W/m^2.

A quality control analysis of BR flux data was performed to ensure that the derived indirect measurements of H and LE fluxes were valid for LIRF and IIC sites. The BR flux data quality control was implemented to avoid counter gradient effects in the H_{BR} data when the T_a gradient above the canopy and the H_{BR} flux have different signs (Perez et al., 1999). The H_{BR} and LE_{BR}

data were not included in the calculation when $\Delta e_a + \gamma \Delta T_a < 0$ when $(R_n - G) \geq 0$ (Ohmura, 1982). The 1D footprint extent of BR fluxes is calculated based on the method described in Brutsaert (1982) and Payero et al. (2003), which accounts for the geometric boundaries of the fields and surface roughness parameters. The H_{BR} and LE_{BR} fluxes have been measured at all three sites. Since the BR fluxes need to be filtered for wind direction to ensure the data are representative of the AOI, hourly and daily BR maize ETa were to be defined in the same as the EC hourly and daily maize ETa calculations. The standard BR station of measurement layout is indicated by Figure 3.24.

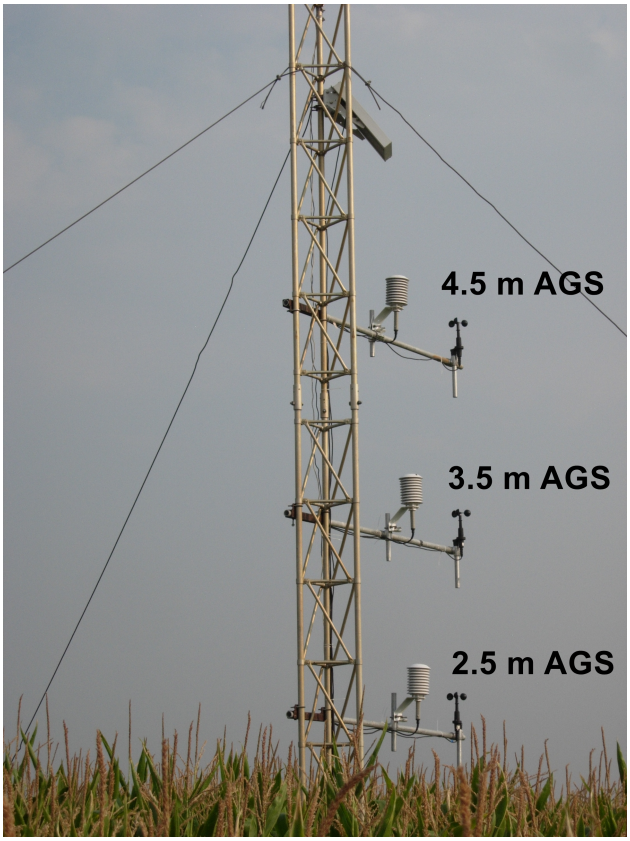

Figure 3.24: The micrometeorological tower at LIRF, with hygrometers measuring T_a and RH for the BR fluxes calculation at 3.5 and 4.5 m AGS in 2020 to 2022. The weather tower at the IIC site had the same sensors at the same heights AGS. Photo provided by Jon Altenhofen.

3.7.3 Soil Water Balance Approach

Volumetric soil water content (VWC) data have been collected at all sites to determine observed daily ETa through the SWB approach (Allen et al., 1998). Observed ETa from VWC data was considered for the periods when neither irrigation nor precipitation events were recharging the soil profile (Allen et al., 1998). Hence, Eq. 1.1 is simplified as follows (Eqs. 3.107 and 3.108):

$$ET_i^{[SWB]} = \sum_{j=1}^{n} (SWD_{i+1,j} - SWD_{i,j}) \tag{3.107}$$

$$SWD_{i,j} = \begin{cases} 0, & \theta_{FC_j} \leq \theta_{VWC} \\ (\theta_{FC_j} - \theta_{VWC_{i,j}}) \cdot R_j, & \text{otherwise} \end{cases} \tag{3.108}$$

where $ET_i^{[SWB]}$ is the daily observed ETa from the SWB approach (mm/d); $SWD_{i+1,j}$ is the soil water deficit at the j^{th} soil layer and next i^{th} day (mm); $SWD_{i,j}$ is the soil water deficit the j^{th} soil layer and current i^{th} day (mm); R_j is the j^{th} soil layer thickness (mm); θ_{FC_j} is the VWC at field capacity (m^3/m^3); $VWC_{i,j}$ is the VWC measured data at the i^{th} current day and j^{th} soil layer. In Eqs. 3.107 and 3.108, the root zone is divided into layers assumed to represent the VWC measurements (Figure 3.25).

At LIRF, VWC measurements occurred at each measurement station at 4, 20, 50, 80, and 110 cm depths within the soil-root zone profile (Figure 3.25). The VWC data from 5TE sensors at 4 cm depth were cross-calibrated at each sampling location using a mini-trace time-domain reflectometer (TDR) data. The VWC data for other depths were adjusted based on neutron probe (NP), which was WC data taken biweekly. The respective depths of TDR and NP readings were 15, 30, 60, 90, and 120 cm. A linear calibration approach per sampling location was considered to adjust the quality of the 5TE VWC data. The resulting linear calibration equations were given as follows (Eq. 3.109):

$$VWC_i = a_1 \cdot VWC_{5TE} + a_2 \tag{3.109}$$

where VWC_{5TE} represents the volumetric water content from 5TE sensor (m^3/m^3), VWC_i refers to the volumetric water content from TDR or NP (m^3/m^3), and a_1 and a_2 are the empirical fitted coefficients for the linear calibration model.

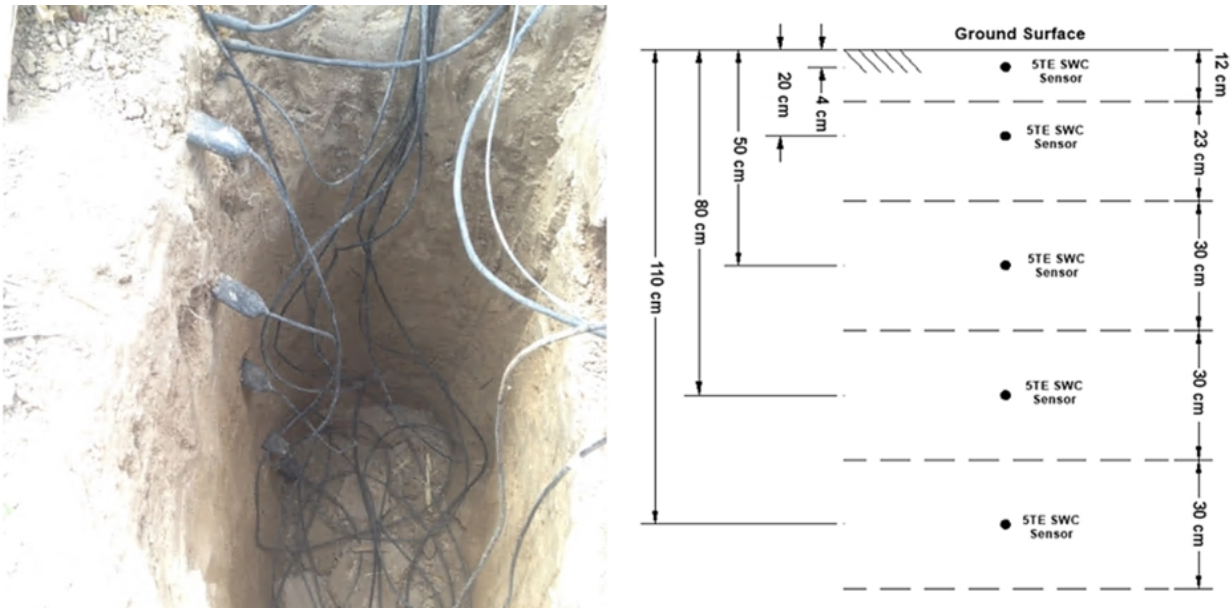

Figure 3.25: A schematic drawing of the SWB approach for the LIRF site. Each black dot represents a VWC sensor buried at a given depth. The local arrangements of the instrumentation define the respective soil layer associated with each sensor. At the IIC, there were only three VWC sensors installed at 15 cm, 50 cm, and 100 cm.

Soil temperature affects the quality of VWC data from sensors such as the 5TE Decagon, CS655, and CS650 types (Chávez and Evett, 2012; Walthert and Schleppi, 2018). Thus, the measured SWB ETa was obtained from Eqs. 3.107 and 3.108 were calculated using data collected at 1 am to minimize the conditions in which soil temperature impacts SWC data. Furthermore, the VWC data at each measurement depth have been adjusted based on neutron probe (NP) VWC readings (LIRF and AVRC sites) or VWC from soil gravimetric samples (IIC site), which have happened on a weekly to biweekly basis during the multi-year data collection campaign.

3.8 Surface Heat Fluxes Measurement

3.8.1 Net Radiation Flux

At LIRF and IIC, three net radiometers, placed at a height of 3.3 m AGS, measured R_n. At the IIC site, a two-way NR-Lite and two four-way CNR1 net radiometers (Kipp and Zonen, Delft, The Netherlands) measured R_n. At the LIRF site, all three net radiometers were a two-way NR-Lite in 2020 and 2021. The CNR1 radiometer was installed on Field F (West station). NR-Lite radiometers measure net short-wave and long-wave radiation within a spectral range from 0.2 to 100 μm, temperature dependency of 0.12 $\%/^oC$, and a directional error of less than 30 W/m^2 at least 1000 W/m^2. The CNR1 radiometer provides data regarding all four terms of the net radiation budget, and it has a measurement uncertainty that is within 10 to 35 $\mu V/W/m^2$ and a directional error of 25 W/m^2 at 1,000 W/m^2.

At LIRF in 2017 and 2018, two-way NR-Lite and four-way CNR1 net radiometers (Kipp and Zonen, Delft, The Netherlands) measured R_n (Figure 3.26. The CNR1 unit was installed at the F2 station in 2018, and the D2 unit will be used for the remaining years of observation. The NR-Lite sensors measured the net short-wave and long-wave radiation with a spectral range from 0.2 to 100 μm, temperature dependency of 0.12 $\%/^oC$, and a directional error of less than 30 W/m^2 at 1000 W/m^2 or higher order of magnitude. For both fields, R_n measurements were recorded every minute and averaged every 15 minutes using Campbell Scientific dataloggers (e.g., CR1000, CR3000).

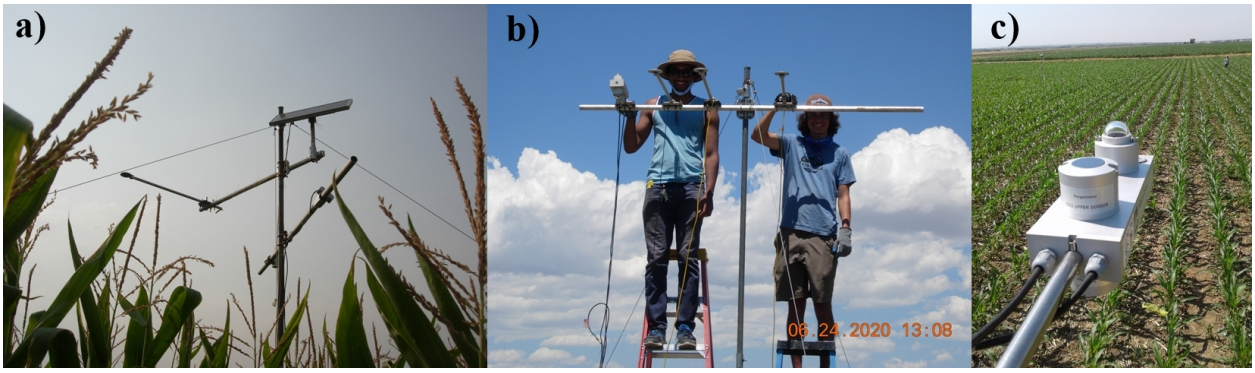

Figure 3.26: The 2-way and 4-way net radiometers installed at LIRF and IIC during the data collection years.

3.8.2 Surface Soil Heat Flux

The Soil Heat Flux Plate method (SHFP) was applied to determine measured G at the ground surface level. This indirect measurement technique involved installing small sensor plates with known heat conductivity to measure heat transfer at a fixed and shallow depth within the root zone, considering the heat storage capacity of the soil layer between the sensor plate and the ground surface (see Figure 3.27). Two identical plates were buried per station per field each year, one immediately below the maize row and another in the inter-row. Similar to measured R_n data collection, recordings of measured G at the plate depths were stored every minute and averaged over a period of 15 minutes in Campbell Scientific dataloggers (e.g., CR1000, CR3000). The HFT3-L sensors (Figure 3.28 have a thermal conductivity of 1.22 $W/m/K$, 3.91 mm, and 38.2 mm thickness and diameter, respectively, and a reading uncertainty of 5$\%$.

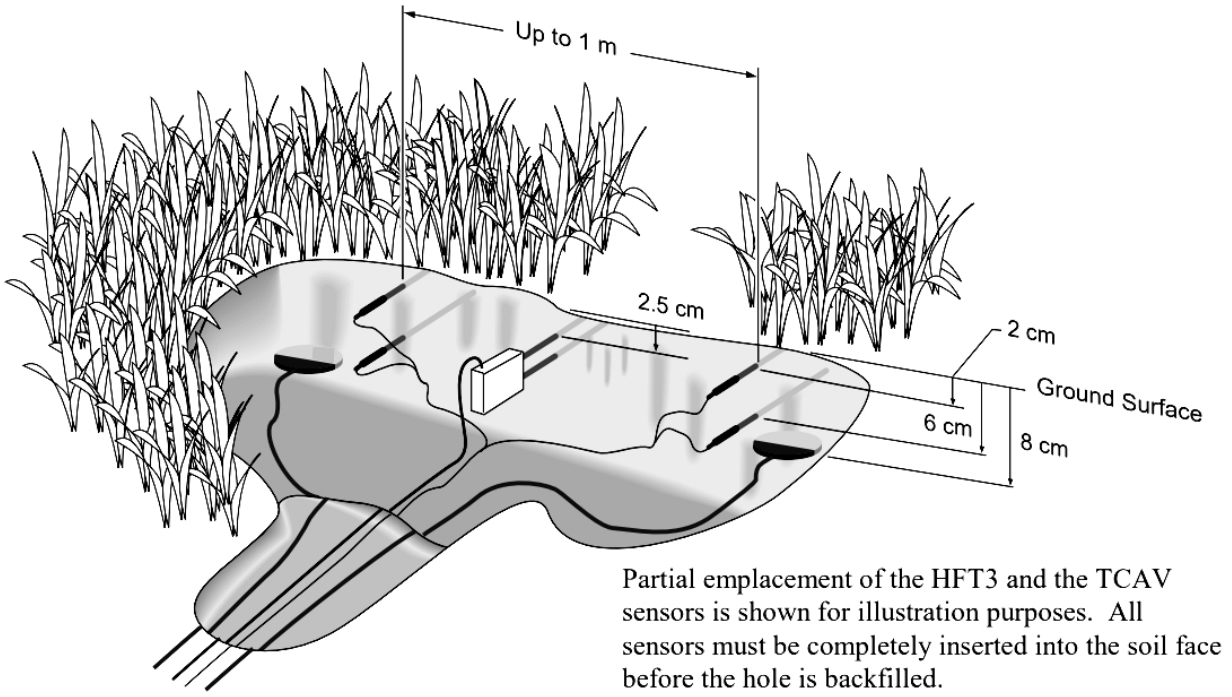

Figure 3.27: Schematic of the soil heat flux sensors installation (Figure from Campbell Scientific).

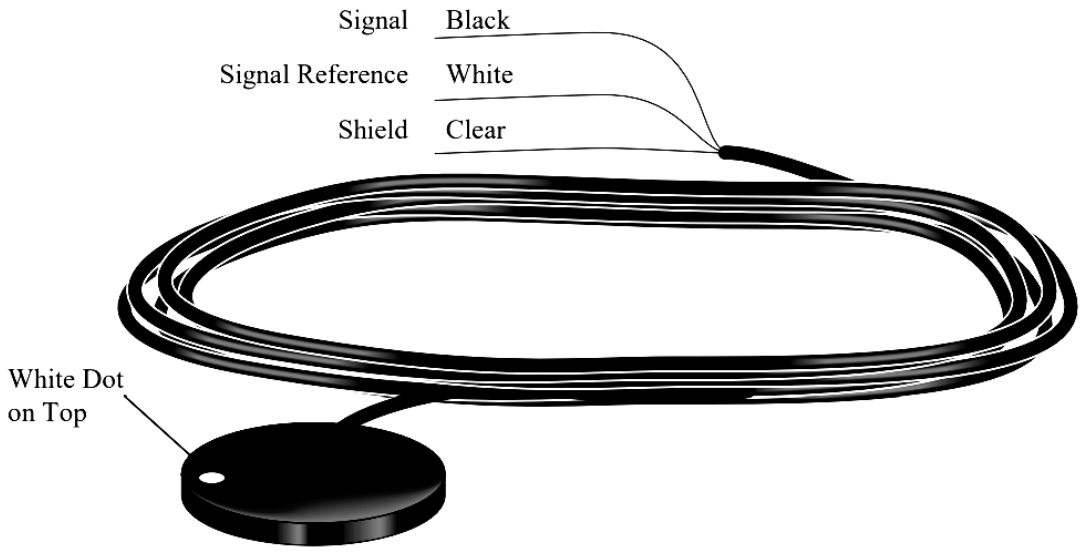

Figure 3.28: Soil heat flux plate installed on the fields on both underneath corn row and on the inter-row (Figure from Campbell Scientific).

The measured G at the ground surface level was calculated following the approach reported by Ochsner et al. (2006) and indicated by Eq. 3.110:

$$G = G_p + S \tag{3.110}$$

where G_p is the soil heat flux measured by the plate (W/m^2) and S is the storage heat term of the soil layer immediately above the plate and below ground surface (W/m^2).

Soil heat storage is determined by the gradient of soil temperature within the profile, the heat capacity of the soil, and the thickness of the layer, as indicated by Eq. 3.111

$$S = \frac{\Delta T_s \cdot C_s \cdot d_z}{t} \tag{3.111}$$

where ΔT_s is the shallow soil layer temperature difference above the plate's location (K); C_s is the heat capacity of moist soil (J/Kg/K); d_z is the depth where the soil heat flux plates were buried (m), and t is the time interval between the readings of soil temperature (s).

The heat capacity of moist soils is affected by soil bulk density, heat capacity of soil minerals, volumetric soil water content, and water heat capacity. The soil heat flux plates were buried at a depth of 8 cm below the ground surface, and soil temperature was measured at 2 cm and 6 cm below the ground surface (BGS). Soil water content readings on the 8 cm soil layer were done using a capacitance-based soil water content sensor at a depth of 4 cm. One 5TE (Decagon Devices Inc., Pullman, Washington, USA) soil water content sensor and two T107 (Campbell Scientific Inc., Logan, Utah, USA) temperature probes were installed above each soil heat flux plate per sampling station at LIRF and IIC sites. The soil heat storage between the buried plates and the ground surface level is calculated as indicated by Eq. 3.112 below:

$$C_s = \rho_b \cdot (C_d + \theta_v \cdot \rho_w \cdot C_w) \tag{3.112}$$

where ρ_b is the soil bulk density (Kg/m^3); C_d is the heat capacity of soil minerals and it is often taken as 840 J/Kg/K (Hanks and Ashcroft, 1980); θ_v is the volumetric soil water content (m^3/m^3), and C_w is the water heat capacity (J/Kg/K).

3.9 Micrometeorological Data

The HMP45C sensor (Figure 3.29) has a 1000-ohm platinum resistance thermometer to measure T_a with 0.2 to 0.3 ^oC accuracy at a temperature range of 20 to 40 ^oC (Figure 3.30). A HUMICAP H-chip provides relative humidity data with an uncertainty of approximately $\pm$ 2% for RH values from 0 to 90% and $\pm$ 3% for RH measured values greater than 90%. The HUMICAP H-chip has a temperature dependence of RH measurement of $\pm$ 0.05% RH/^oC. The HMP45C sensor consumes less than 4 mA current at 12 V and needs only 0.15 s for the sensor to warm up (settling time). The probe length is 25 cm, with an equivalent diameter of 3 cm.

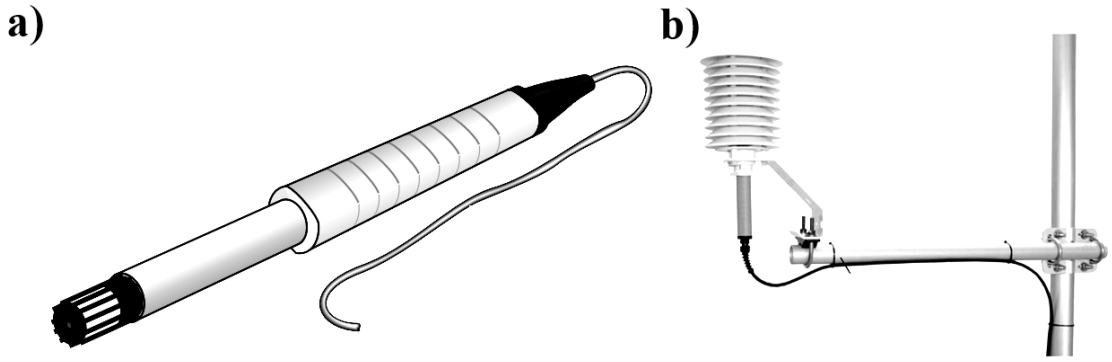

Figure 3.29: The HMP45C probe (Figure 3.29a) and installation guide (Figure 3.29b) setup (Campbell Scientific, 2004).

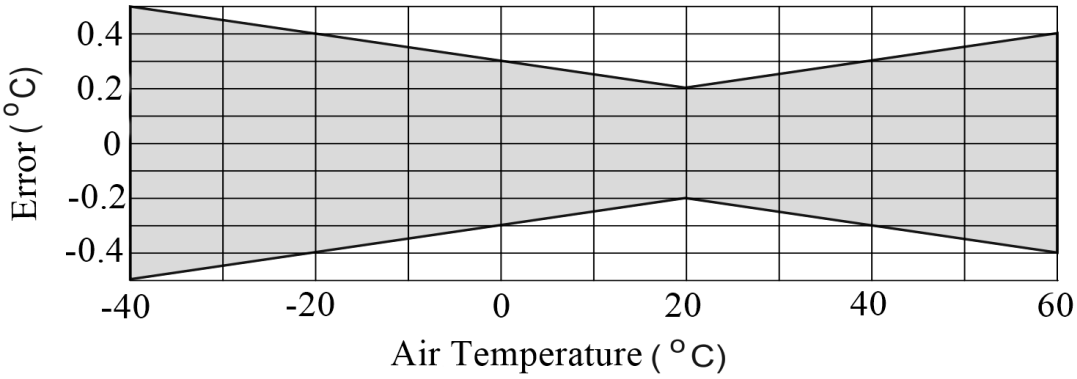

Figure 3.30: Uncertainty associated with the HMP45C sensor regarding measured T_a (Campbell Scientific, 2004).

The 0301-L cup anemometer (Figure 3.32 measures mean horizontal wind speed. The wind speed is measured with a rotating three-cup anemometer. The rotation of the cups creates a sine wave volta g frequency proportional to wind speed. The cup anemometer range of measurements varies from 0 to 50 m/s. Each rotating cup has a 0.40 cm diameter cup. The accuracy associated with the measurements of wind speed is $\pm$ 0.50 m/s. All micrometeorological data were recorded every minute and averaged over 15 minutes, being stored in CR3000 Campbell Scientific dataloggers.

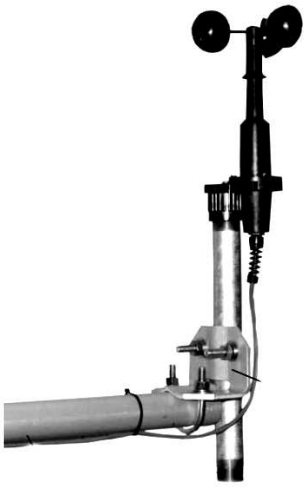

Figure 3.31: The R.M. Young wind cup anemometer sensor (Campbell Scientific, 2004).

3.10 Measurements of Canopy Architecture

3.10.1 Fractional Vegetation Cover

Indirect measurements of f_c happened at LIRF and IIC to assess the vegetation conditions and to evaluate the errors associated with predicting f_c. An LI-190R and LI-191R line quantum sensor (LI-COR Biosciences, Lincoln, Nebraska, USA) connected to a CR3000 datalogger (Campbell Scientific Inc., Logan, UT, USA) measured the above and within canopy photosynthetically active radiation (PAR), respectively. The instruments were placed in the frequently irrigated field at LIRF and IIC. The PAR data were recorded at 1 minute and averaged over 15 minutes. The LI-190R sensor was mounted on a 4-m tall vertical post at 3.5 m AGS.

The LI-190R and LI-191R line quantum sensor outputs are a current (μA) signal that is directly proportional to PAR (400 to 700 nm wavelength) due to a calibration multiplier used to convert the current signal into PAR units ($\mu mol/s/m^2$). The LI-190R consists of a flat sensor surface that is sensitive to incoming light and is placed above the canopy to measure light radiation before being intercepted by the plants. The LI-191R provides PAR measurements at the ground surface, indicating the amount of light radiation that reaches the ground after canopy PAR absorption. Indirect measurements of f_c are obtained through Eq. 3.113 as follows:

$$f_c^{[M]} = 1 - \frac{PAR_{\text{down}}}{PAR_{\text{up}}} \tag{3.113}$$

where PAR_{down} means the PAR radiation measured at the ground surface level from the LI-191R line quantum sensor ($\mu mol/s/m^2$), and PAR_{up} means the PAR radiation measured above the canopy ($\mu mol/s/m^2$). The superscript "[M]" alludes to the measured f_c label.

3.10.2 Leaf Area Index and Canopy Height

LAI measurements were done weekly using the LAI-2200C Plant Canopy Analyzer (LI-COR Biosciences, Lincoln, Nebraska, USA), a modern and non-destructive instrument designed for point-based measurements of canopy foliage architecture. The LAI measurements were obtained at each LIRF and IIC maize field sampling location. The LAI-2200C analyzer utilized a unique combination of upward and downward sensors, with passive and optical parts and five concentric detectors measuring diffuse light transmittance above and within the canopy at five different zenith angles. Maize h_c data were obtained through a commercial measuring tape at the LAI sampling locations on a weekly to biweekly basis at LIRF and IIC sites. The h_c measurements were considered from the ground surface to the upper leaves.

A cubic convolution gap-filling approach provided temporal interpolated LAI and h_c data for the days without measurements, similar to the interpolation methods implemented by Vorobiova and Chernov (2017). The interpolation method for measured LAI was explicitly applied to each data collection time series per measurement station within the frequently irrigated fields at LIRF and IIC. Temporal extrapolation of vegetation indices assumes that for irrigated fields with no lack of nutrients, water availability, and pristine vegetation, the changes in canopy leaves arrangement are minimal within shorter periods under similar environmental conditions (e.g., cloudless skies, air temperature, wind speed, etc.).

3.11 Remote Sensing sensors

3.11.1 Spaceborne Systems

This study selected three satellite sensors to provide spatial data to evaluate ETa mapping products and develop the multi-scale SR data adjustment algorithm: Landsat-8, Sentinel-2, and Planet CubeSat. Landsat-8 is a spaceborne remote sensing sensor managed by the United States Ge-

ological Service (USGS) and the National Space Agency (NASA). A Landsat-8 satellite has an Operational Land Imager (OLI) and a Thermal Infrared Sensor (TIRS) that take images of the earth's landscape at a 30-m and 100-m spatial resolution every sixteen days, respectively. The OLI sensor provides short-wave multispectral data, and the TIRS camera measures LWIR thermal radiation images. If the AOI resides between the overlap region of two Landsat-8 path/row scenes (185 km x 180 km, each), the revisiting time becomes eight days (almost weekly).

The LIRF and IIC sites are located within the overlap region of 33/32 and 34/32 (path/row) Landsat-8 scenes, so the temporal resolution is weekly. The AVRC site is located in the 32/34 scene, which gives images of the SL and LL fields every sixteen days. A cubic convolution resampling approach downscales the TIRS image to the OLI imagery spatial resolution (Roy et al., 2014). Landsat-8 has a sun-synchronous orbit around Earth at 705 km altitude and with Equator time around 11:30 pm local time. The original radiometric resolution Landsat-8 imagery is 12 bits, converted to 16 bits after USGS/NASA post-processed data.

The radiometric resolution of a remote sensing image indicates the capacity to record a wide range of brightness levels. The metadata imagery file provides linear calibration coefficients to convert a digital number (DN) to surface reflectance and nadir-looking surface temperature (Landsat-8 Level-2 imagery). The Level-2 images undergo rigorous calibration procedures and do not require further post-processing after the final surface reflectance and temperature images are appropriately converted from the original DN values (Roy et al., 2014). More details about atmospheric corrections applied to Landsat-8 imagery are found in Vermote et al. (2016) and Vermote et al. (2018). Table 3.4 presents the spectral characteristics of the Landsat-8 bands that have been considered in the research.

Table 3.4: List of Landsat-8 multispectral and thermal bands used in this project.

Bands	Description	Central Wavelength (nm)	Bandwidth (nm)	Spatial Resolution (m)
Landsat-8 Band 2	Blue	480	60	30
Landsat-8 Band 3	Green	560	60	30
Landsat-8 Band 4	Red	655	30	30
Landsat-8 Band 5	NIR	870	30	30
Landsat-8 Band 10	LWIR Thermal	1090	60	100 (resampled to 30)

Sentinel-2 satellites are maintained and operated by the European Space Agency (ESA), an intergovernmental entity of twenty-two European countries. The Copernicus Programme is responsible for managing the Sentinel satellite missions. Details about the satellite design, operation, and components can be found in Drusch et al. (2012) and Spoto et al. (2012). There are two Sentinel-2 satellites (S2A and S2B) that each provide multispectral image scenes (290 km x 290 km, each) of the earth every ten days for one satellite device around the Equator, five days when the two satellites are combined, and two to three days revisiting time for landscape areas located at mid-latitudes.

The S2A and S2B satellites have a sun-synchronous orbit at an average altitude of 786 km and an Equator time around noon local time. Thermal images are not provided by Sentinel-2 satellites. The spatial resolution of Sentinel-2 images depends on the type of multispectral bands and varies from 10 m to 60 m. Only Sentinel-2 bands 2, 3, 4, and 8 (10 m pixel size) have been considered in the project since they are provided at their original spatial resolution. In contrast, the other images at 20 m and 60 m do not have BLUE, GREEN, and RED surface reflectance bands (Table 3.5).

Table 3.5: List of Sentinel-2 multispectral bands and their spatial resolution.

Bands	Description	Central Wavelength (nm)	Bandwidth (nm)	Spatial Resolution (m)
Sentinel-2 Band 2	Blue	492	66	10
Sentinel-2 Band 3	Green	560	36	
Sentinel-2 Band 4	Red	665	31	
Sentinel-2 Band 8	NIR	833	106	
Sentinel-2 Band 5	Red-Edge	704	15	20
Sentinel-2 Band 6	Red-Edge	740	15	
Sentinel-2 Band 7	Red-Edge	782	20	
Sentinel-2 Band 8A	Narrow NIR	865	21	
Sentinel-2 Band 11	SWIR*	1614	91	
Sentinel-2 Band 12	SWIR*	2202	175	
Sentinel-2 Band 1	Coastal Blue	443	21	60
Sentinel-2 Band 9	Water Vapor	945	20	
Sentinel-2 Band 10	Cirrus	1374	31	

* SWIR stands for short-wave infrared.

The original radiometric resolution of Sentinel-2 images is 12 bits. However, when ESA post-processes images, they are converted to 16 bits. The current radiometric accuracy of Sentinel-2 imagery is less than 5%, and it is comparable to Landsat-8 (Phiri et al., 2020). The Sentinel-2 Level-2 images are calibrated and pre-processed to provide surface reflectance through a calibration factor of 10,000. That is, dividing the DN values of each band by 10,000 generates surface reflectance images already corrected for atmospheric effects between the land surface and the spaceborne sensor. The atmospheric corrections involve using a radiative transfer algorithm developed by the ESA (Sen2Cor). More details about the use of Sen2Cor to atmospherically correct S2A and S2B satellite images are found in Main-Knorn et al. (2017) and Wei et al. (2018).

Sentinel-2 does not provide thermal imagery. Thus, ground-based and stationary IRT data were used with Sentinel-2 multispectral data to run the SEB ETa algorithms on a point-based data source. More details about IRT surface temperature data processing are shown in Appendix E. Re-

cent studies have indicated that the quality of the Sentinel-2 multispectral data resembles and, in some cases, outperforms Landsat-8 images in the visible and invisible light spectrum (Sekertekin et al., 2017; Chakar et al., 2020; Ghayour et al., 2021). Details about the corrections of stationary IRT data are in Appendix D.

Planet CubeSat is a low-cost and commercial constellation of satellites operated and maintained by Planet Labs (Planet Labs, Inc., San Francisco, CA, USA). More than 130 CubeSats units survey Earth's landscape (24 km x 16 km scene) on high temporal (daily) and spatial (3 m) spatial resolutions, providing multispectral imagery in the visible and NIR wavelengths of the light spectrum (Planet Team, 2017). The radiometric resolution of Planet CubeSat is 12-bit when the image is acquired and converted to 16-bit after post-processing steps before imagery is made available. Planet CubeSat satellites are smaller and lighter than Landsat-8 and Sentinel-2 (0.10 m x 0.10 m x 0.30 m; 4 kg weight). The satellites have a sun-synchronous orbit, with an altitude range from 450 km to 580 km and an Equator crossing time from 9:30 to 11:30 am local time (Planet Team, 2017). The CubeSat sensor only provides multispectral images (Table 3.6).

Table 3.6: List of Planet CubeSat multispectral bands used in this project.

Bands	Description	Central Wavelength (nm)	Bandwidth (nm)	Spatial Resolution (m)
CubeSat Band 1	Blue	491	60	3
CubeSat Band 2	Green	566	90	3
CubeSat Band 3	Red	666	80	3
CubeSat Band 4	NIR	867	80	3

The current Planet Satellite sensors provide no thermal images. Thus, ground-based and stationary IRT data were used with Planet CubeSat multispectral data to run the SEB ETa algorithms. The Planet CubeSat surface reflectance images are calibrated and pre-processed with a calibration factor of 10,000. The accuracy of radiometric calibration of at-sensor reflectance is within 5%.

Prior atmospheric corrections account for the gases and aerosol concentration and their changes with an altitude between the landscape and the at-sensor camera in space. MODIS water vapor, ozone, and aerosol quality control products serve as complementary data to improve the calibration of Planet CubeSat imagery using the 6SV2.1 radiative transfer model (Planet Team, 2017).

However, the atmospheric corrections are still a work in progress since the approach by Planet Labs does not include stray light, haze, and thin cirrus clouds effects; it assumes Earth's landscape to behave as a Lambertian surface (homogeneous light scattering in all directions) and that all scenes to be at sea level (Planet Team, 2017). During imagery post-processing, geometric corrections are done using sensor telemetry, ground control points (GCP), and fine digital elevation models (DEM). Planet Team (2017) released a harmonized version of Planet imagery (including CubeSat data) that adjusts the quality of the multispectral data to Sentinel-2 standards. More information about the imagery harmonization processes is found in Csillik et al. (2019) and Kington et al. (2019). The CubeSat harmonized images were considered the primary data in this study.

Only clear-sky images at LIRF, IIC, and AVRC sites were used for all three spaceborne remote sensing sensors for the multi-year datasets. That is to avoid clouds affecting the research fields' surface reflectance and temperature values. Regarding the Landsat-8 sensor, the ETa evaluation included the original Landsat-8 sensor (OLIS SR and TIRS T_s imagery data) and the combination of OLIS SR and ground-based IRT data. Both the TIRS and ground-based T_s measured data were considered for the Landsat-8 spaceborne sensor since Planet CubeSat and Sentinel-2 relied on point-based IRT data to be able to apply the SEB ETa algorithms (OSEB and TSEB). The TIRS T_s data were also included to evaluate Landsat-8 with the complete dataset available to the public since TIRS is the primary source of T_s data for the Landsat-8 sensor.

The reason that supports Landsat-8 as one of the remote sensing sensors in this study is that it is a well-known remote sensing sensor that has been relevant to ETa applications at the farm and

regional scales since its launch on 2/11/2013 (Tang et al., 2013; Senay et al., 2016; Madugundu et al., 2017; Wang et al., 2021; Hassan et al., 2022). Since the launch of S2A (6/23/2015) and S2B satellites (3/7/2017), Sentinel-2 imagery data have become a reliable open-access remote sensing sensor for research and application towards sustainable agricultural water management and ETa modeling at the farm and regional landscape scales (Immitzer et al., 2016; Rozenstein et al., 2018; Segarra et al., 2020; Jiang et al., 2020). Planet CubeSat imagery products have shown vast capabilities to improve agricultural water management due to their high temporal and spatial resolution. When it comes to precision agriculture, several studies have evaluated the benefits and limitations of using low-cost CubeSat data to support daily decision-making processes at the farm scale (Houborg and McCabe, 2016; McCabe et al., 2017; Cai et al., 2019; Breunig et al., 2020; Kimm et al., 2020; Aragon et al., 2021). Spaceborne imagery pre-processing has been done using ArcGIS 10.8 (ESRI, Redlands, CA). Table 3.7 summarizes the characteristics of each spaceborne sensor in this study.

Table 3.7: Summary information about this study's spaceborne remote sensing sensors.

Satellite Characteristics	Landsat-8	Sentinel-2	Planet CubeSat
Sun-Synchronous Orbit	Yes	Yes	Yes
Satellite Altitude (km)	705	786	450 to 580
Equator Time (Local Time)	11:30 am	12:00 pm	9:30 to 11:30 am
Scene Size (km x km)	185 x 180	290 x 290	24 x 16
Temporal Resolution (days)	8 to 16	5 to 10	Daily
Multispectral Pixel Size (m)	30	10	3
Thermal Pixel Size (m)	100 (Resampled to 30)	N/A*	N/A*
Radiometric Resolution (bits)	16	16	16
Imagery Coordinate System	WGS84 UTM	WGS84 UTM	WGS84 UTM

* N/A stands for not applicable.

3.11.2 Proximal System

Proximal surface reflectance and nadir-looking T_s data have been measured with a portable Cropscan multispectral (MSR) radiometer (CropScan Inc., Rochester, MN) at all research sites during the years of data collection. An MSR radiometer is a lightweight handheld device that includes a quasi-cubic radiometer (8 x 8 x 10 cm) and an attached IRT (Exergen Corporation, Watertown, MA) that is mounted on a telescopic pole to allow readings at the nadir-looking position above the canopy (Figure 3.32).

The MSR radiometer has a field of view (FOV) of 28º, and it has taken readings at 2.2 m AGS, which has provided a ground sampling area equivalent to a 1-m diameter circle (2V:1H aspect ratio). The Exergen IRT has a 3V:1H ratio that has given a spatial footprint of 1-m diameter. An MSR is a passive sensor that relies on natural incoming light from the sun and emulates Landsat-5 spectral bands in the visible and invisible light spectrum. The MSR radiometer is named after the maximum number of SR bands supported in the multispectral detector.

In this study, MSR (five bands) units were deployed at the LIRF and IIC sites, while an MSR16 (sixteen bands, but only eight channels were used in this has been used at the AVRC during the years of data collection. Multispectral data from the MSR have been sampled two times at the row and inter-row (total of four readings) and averaged at each point-based location at all three sites. This research project used MSR radiometers as part of the remote sensing sensor portfolio since they have been relevant to providing data to improve crop management approaches at the farm scale (Bronson et al., 2003; Elwadie et al., 2005; Jongschaap, 2006; Costa-Filho et al., 2020; Costa-Filho et al., 2021). Table 3.8 provides a summary of the data collected using the proximal radiometers.

Figure 3.32: A MSR survey at LIRF weather station (GLY04) grass area in 2020. Photo provided by José Chávez.

Table 3.8: Summary of the multispectral and thermal data from the MSR radiometers.

Instrument Characteristics	MSR	MSR16
Blue Band Central Wavelength (nm)	485	510
Blue Band Bandwidth (nm)	70	70
Green Band Central Wavelength (nm)	560	560
Green Band Bandwidth (nm)	80	80
Red Band Central Wavelength (nm)	660	660
Red Band Bandwidth (nm)	60	60
NIR Band Central Wavelength (nm)	830	810
NIR Band Bandwidth (nm)	140	140
Multispectral Spatial Scale (m)	1	1
Thermal Spatial Scale (m)	0.80	0.80
Temporal Data Acquisition	Weekly to Biweekly	Biweekly

3.11.3 Airborne System

When it comes to new technology applied toward precision agriculture, several studies have been evaluating the use of Unmanned Aerial Systems (UAS), particularly drones (henceforth, UAS), to provide very fine spatial resolution images to help implement, among other applications, variable rate irrigation, ETa mapping, crop phenotyping, and yield monitoring at the farm scale (Ehsani and Maja. 2013; Yang et al., 2017; Sarron et al., 2018; Maes and Steppe, 2019; Shi et al., 2019; Niu et al., 2020; Vandermaesen et al., 2021).

The UAS missions (Figure 3.33) were scheduled at all three research sites during the growing seasons by the USDA-ARS Water Management division and the CSU Drone Center. Both groups provided SR and LWIR images of the AVRC research fields. In 2021, however, only the CSU Drone Center could schedule three missions at the AVRC. Furthermore, the USDA-ARS team has been responsible for UAS images at the LIRF, while the CSU Drone Center has provided imagery at the IIC site.

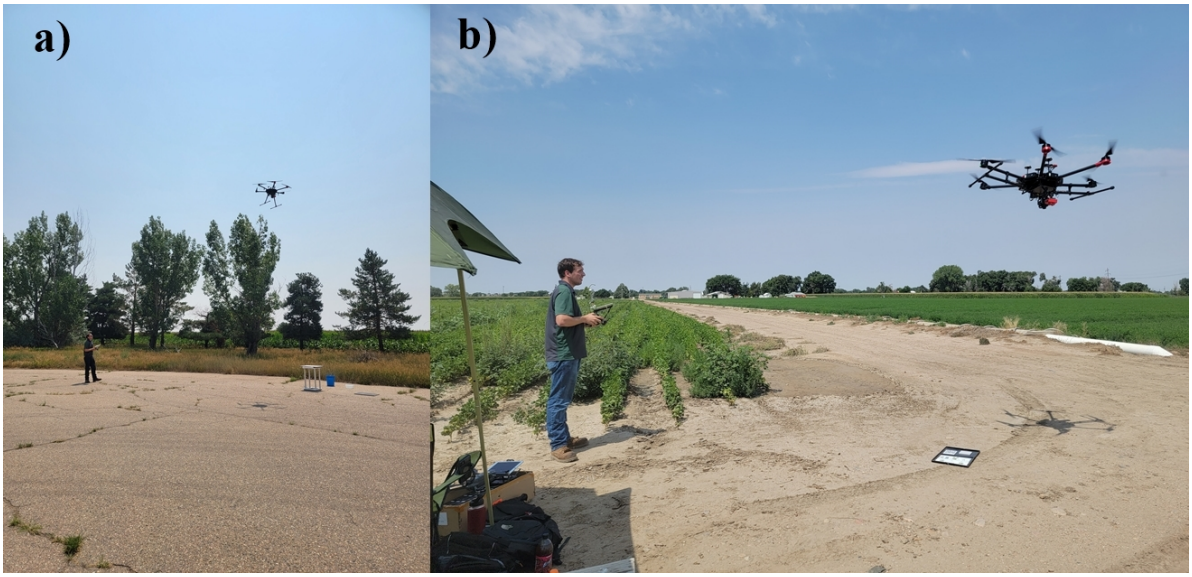

Figure 3.33: The UAS missions in this study. Figure 3.33a and Figure 3.33b are from the IIC and AVRC sites, respectively. Photos provided by Leonardy Tan.

The UAS images were obtained from two cameras attached to a drone unit. A FLIR Duo Pro R (FLIR Systems, Inc., Wilsonville, OR, USA) and a MicaSense RedEdge-MX (MicaSense Inc., Seattle, WA, USA) were used. The thermal detector has LWIR spectral data ranging from 750 to 1350 nm. The MicaSense RedEdge-MX camera took multispectral imagery. The RedEdge-MX detector has a five-band composition in the visible and invisible light spectrum: BLUE (475 nm, 32 nm bandwidth), GREEN (560 nm, 27 nm bandwidth), RED (668 nm, 14 nm bandwidth), Red-Edge (717 nm, 12 nm bandwidth), and NIR (842 nm, 57 nm bandwidth). Table 3.9 summarizes the UAS mission details for the USDA-ARS and CSU Drone Center operations at all three research sites.

Table 3.9: UAS mission summary for the USDA-ARS and CSU Drone Center at all sites.

	USDA-ARS	CSU Drone Center
UAS Model Type	DJI S900	DJI M600
Flight Altitude (m)	120	100
UAS Speed (m/s)	5	5
Temporal Resolution at LIRF and IIC	Weekly	Weekly
Temporal Resolution at AVRC	Biweekly or Monthly	Biweekly or Monthly
Multispectral Image Pixel Size (m)	0.03	0.08
Thermal Image Pixel Size (m)	0.10	0.15
Multispectral Radiometric Resolution (bits)	32	32
Thermal Radiometric Resolution (bits)	16	16
Overlap/Sidelap Percentage ($\%$)	88/70	80/70
Calibrated Reflectance Panel (Micasense)	Yes	Yes
Orthorectified Image Coordinate System	WGS84 UTM	WGS84 UTM
Number of Flights Surveying the Fields	Two	One
Post-processing Imagery Software	Agisoft Metashape	Pix4D v4.5.6
Total Number of Missions at IIC (2020 and 2021)	N/A	14
Total Number of Missions at LIRF (2017 to 2021)	29	N/A
Total Number of Missions at AVRC (2020 and 2021)	2	5

The thermal images provided by the CSU Drone Center have issues regarding the FLIR DuoR camera settings. In the literature, the technical term is sensor calibration drift (Nugent et al., 2013; Kelly et al., 2019; Aragon et al., 2020; Maguire et al., 2021). Aragon et al. (2020) define thermal camera drift as undesired changes in target temperature due to uncompensated focal plane array (FPA) temperature. The thermal camera might not be in thermal equilibrium with the surrounding environment when taking images of a given area, which leads to less LWIR radiation measured by the camera at certain zones in the field since the camera is adjusting its internal calibration to compensate for temperature fluctuations caused by FPA.

Consequently, this thermal calibration issue leads to areas in a thermal image with cooler surface temperatures than the expected values, given the current weather and field conditions when the image was taken (Fig. 3.34). Due to the CSU Drone Center images having large areas of insufficient accurate data (i.e., low accuracy in T_s data), no UAS LWIR data were used at all three research sites. Instead, the UAS surface reflectance data were combined with nadir-looking T_s data from stationary IRT sensors at each research site and served as input data to estimate ETa using the SEB approaches.

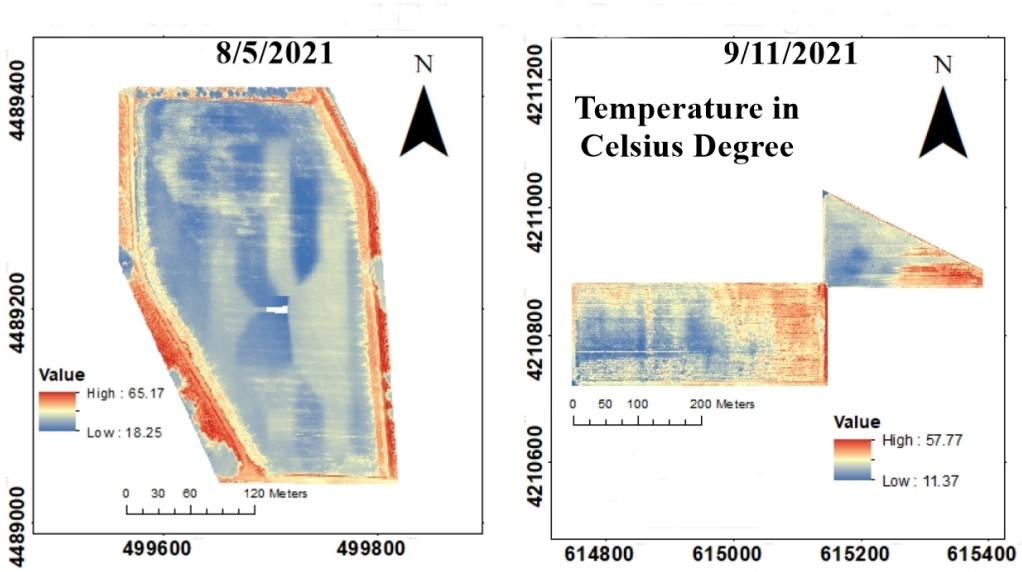

Figure 3.34: The thermal drift issue from the CSU drone center thermal images at IIC and AVRC sites. The blue areas are the cooler zones identified due to uncompensated FPA temperatures during the drone flights.

3.12 Statistical Analysis

3.12.1 Global Sensitivity Analysis Regarding the Novel Pixel Decomposition Approach

The Sobol global sensitivity (SGS) approach (Sobol, 1990; Sobol, 2001) is based on quantifying uncertainty to determine the impact of any given input parameter in a mathematical model over the entire input parameter space. The SGS technique uses variance-based metrics to assess the contribution of individual parameters to the total variance of the model prediction output. By decomposing the total variance of the model output into components attributed to particular parameters and their combinations, the Sobol indices offer a quantitative measure of global sensitivity for a given model. These Sobol indices provide insights into which parameters are more relevant to affect model prediction variability. Furthermore, the SGS approach is advantageous for high-dimensional models (multiple parameters). The SGS approach calculates the Sobol sensitivity indices using an Analysis of Variance (ANOVA) decomposition, as indicated by Eqs. 3.114 and 3.115 below:

$$D_{i_1 \ldots i_s} = \int_0^1 f^2_{i_1 \ldots i_s} dx_{i_1} \ldots dx_{i_s} \tag{3.114}$$

$$D = \int_0^1 f^2(x)dx - f_o^2 = \sum_{S=1}^{n} \sum_{i_1 < \ldots < i_S} D_{i_1 \ldots i_s} \tag{3.115}$$

where $f(x)$ is an integrable function of a given model parametrization, with $f(x) \in R$ and $x \in R^n$; x_{i_1} to x_{i_s} are the predictors of the function $f(x)$; $D_{i_1 \ldots i_s}$ is the variance associated to a given model parameter; D is the total variance observed; f_o is a generic initial value of function $f(x)$.

The Sobol global sensitivity index is calculated as the ratio between the variances, as indicated by Eq. 3.116:

$$S_{i_1 \ldots i_s} = \frac{D_{i_1 \ldots i_s}}{D} = \frac{\int_0^1 f^2_{i_1 \ldots i_s} dx_{i_1} \ldots dx_{i_s}}{\sum_{S=1}^{n} \sum_{i_1 < \ldots < i_S} D_{i_1 \ldots i_s}} \tag{3.116}$$

where $S_{i_1 \ldots i_s}$ means the Sobol global sensitivity index for each parameter of a given mathematical model.

The Global Sensitivity Analysis Toolbox (GSAT) for MATLAB developed by Cannavó (2012) was used to calculate the Sobol global sensitivity indices for the spatial k_p novel model (Eq. 3.30), the NDVI$_{soil}$ and NDVI$_c$ novel approaches (Eqs. 3.27 and 3.28, respectively), and the novel pixel decomposition algorithm (Eqs. 3.6 and 3.13). The parameters with higher Sobol global sensitivity indices are the ones that have more influence on model variability and accuracy (Cannavó, 2012). For more details on how to access the GSAT for MATLAB package and intrinsic information about the SGS approach, refer to Cannavó (2012).

3.12.2 Statistical Analysis of the Thermal Data

Since there were three different sources of thermal data in this study (MSR T_s, SI-111 T_s, and TIRS from Landsat-8), to identify any pertinent differences among thermal data from the remote sensing sensors, a non-parametric statistical test for differences in population means was used. The non-parametric Kruskal-Wallis (KW) test for differences in population means (Kruskal and Wallis, 1952) was used to identify overall differences among multispectral data from the different remote sensing sensors. The test statistic is calculated as indicated by Eq. 3.117 (Kruskal and Wallis, 1952):

$$TS = \frac{12}{N_T \cdot (N_T + 1)} \cdot \sum \left[\frac{T_i^2}{N_i} - 3(N_T + 1) \right] \tag{3.117}$$

where TS denotes the test statistic (dimensionless); Ni is the number of observations in each sample size for variable "i"; NT is the total sample size that is the sum of all observations across variables;

Ti is the sum of the ranks for the data from a given sample size for variable "i" after combining the datasets.

The null and alternative hypotheses (i.e., H_o and H_A) for the KW test in this study are the following, respectively:

a) H_o: The mean value of each remote sensing sensor thermal data is the same.

b) H_A: At least one thermal data population mean is different from all the remaining sensors.

The KW non-parametric test is an alternative to an Analysis of Variance (ANOVA) test for the case that one or more ANOVA assumptions are violated (Ott and Longnecker, 2015). In this study, the null hypothesis assumed that the mean value of each thermal data source is the same. On the other hand, the alternative hypothesis assumed that at least one nadir-looking T_s sensor data is statistically different than all the remaining sensors.

To further investigate the statistical differences across the three T_s sensors, a multiple pairwise comparison among the three thermal data sources was used. The post-hoc test developed by Dunn (1964) was the one used in this study since it is the most common non-parametric pairwise comparison method (Pohlert, 2014; Dinno, 2015). All statistical analyses were done assuming a level of confidence equal to 0.05. The p-values were corrected for multiple pairwise comparisons using the approach developed by Sidák (1967). If the comparison with p-values were less than 0.025, then the H_o hypothesis was rejected (Dunn, 1964). The stats package in RStudio (R Core Team, 2020) was used to run the pairwise comparison analysis for the thermal data.

3.12.3 Measured Evapotranspiration Error Assessment

Before evaluating the ETa estimation across different models and remote sensing sensors, the first step is to define the best ground-truthing method for determining ETa among the EC system,

SWB, and BR approaches at LIRF and IIC sites regarding the evaluation of the optimal multispectral sensors for estimating maize ETa for a given ETa algorithm. Every ETa measurement approach in this study is biased due to inherited assumptions, different measuring footprints, and systematic errors. Selecting the most accurate ETa measurement technique is critical to ensure the RBCC, OSEB, TSEBpar, and TSEBser predictions are fairly assessed using quasi-unbiased measured ETa data.

This study chose an extended triple collocation method (TCe) to evaluate the best measurement technique for ETa at LIRF and IIC 2020 and 2021 datasets. The TCe method proposed by McColl et al. (2014) is an improved version of the original triple collocation (TC) approach from Stoffelen (1998) that includes the calculation of the correlation coefficient alongside the calculated variance between each of the measured data and the unknown true value of a given variable. A TC and TCe analysis assumes that errors in each independently measured data set are uncorrelated with each other. Even though all three ETa measurement approaches (EC, SWB, and BR methods) are not collocated (at the same location) at the IIC and LIRF sites in 2020 and 2021, the analysis considered the BR and EC footprint that coincides with the locations of the point-based SWB ETa measurements to obtain representative values of all three measured ETa data for this TCe analysis.

The TCe approach determines the unknown error of a given measured data regarding the expected actual value (also unknown) through a set of linear functions. The TC approach has been used in the field of hydrology and remote sensing to evaluate the errors from environmental variables such as rainfall (Roebeling et al., 2012; Massari et al., 2017; Tanin et al., 2021), LAI (Fang et al., 2012; Jiang et al., 2017), ETa (Khan et al., 2018; Kibria et al., 2021), and soil VWC (Scipal et al. 2010; Gruber et al., 2016; Xu et al., 2021). In an ETa analysis, the standard deviation and correlation coefficients for each measured data technique are calculated using Eq. 3.118 to 3.120, as follows (McColl et al., 2014):

$$\sigma_\epsilon = \begin{bmatrix} \sqrt{Q_{11} - \dfrac{Q_{12} \cdot Q_{13}}{Q_{23}}} \\ \sqrt{Q_{22} - \dfrac{Q_{12} \cdot Q_{23}}{Q_{13}}} \\ \sqrt{Q_{33} - \dfrac{Q_{13} \cdot Q_{23}}{Q_{12}}} \end{bmatrix} \tag{3.118}$$

$$Q_{ij} = Cov(X_i, X_j) = \begin{cases} \mu_i \cdot \mu_j, & i \neq j \\ \mu_i^2 + \sigma_{\epsilon i}^2, & \text{otherwise} \end{cases} \tag{3.119}$$

$$\mu_i = \beta_i \cdot \sigma_t \tag{3.120}$$

where σ_ϵ is the standard deviation of the error between a given measured data and its actual unknown value; Q_{ij} is the covariance between two different measurement systems; μ is defined as the product between the slope (β) of the linear model between the measured and actual value and the variance of the actual variable value (σ_t).

The correlation coefficient introduced by McColl et al. (2014) is calculated using Eq. 3.121:

$$R_{t,X} = \pm \begin{bmatrix} \sqrt{\dfrac{Q_{12} \cdot Q_{13}}{Q_{11} \cdot Q_{23}}} \\ sign(Q_{13} \cdot Q_{23}) \sqrt{\dfrac{Q_{12} \cdot Q_{23}}{Q_{22} \cdot Q_{13}}} \\ sign(Q_{12} \cdot Q_{23}) \sqrt{\dfrac{Q_{13} \cdot Q_{23}}{Q_{33} \cdot Q_{12}}} \end{bmatrix} \tag{3.121}$$

where $R_{t,X}$ is the correlation coefficient between the true value and measured data of a given variable. The TCe coefficient of determination is given as $R_{t,X}^2$. More information about the TCe

method is found in McColl et al. (2014).

3.12.4 Statistical Error Metrics

The following statistical measures were considered to compare the performance of the different ETa models across the spaceborne and airborne remote sensing sensors: mean bias error (MBE), root mean square error (RMSE), normalized MBE (NMBE), normalized RMSE (NRMSE), and the coefficient of determination (R^2). Eqs. 3.122 to 3.125 indicate MBE, NMBE, RMSE, and NRMSE, respectively:

$$MBE = \frac{1}{n}\sum_{i=1}^{n}(E_i - O_i) \tag{3.122}$$

$$NMBE = \left(\frac{MBE}{\bar{O}}\right) \cdot 100\% \tag{3.123}$$

$$RMSE = \sqrt{\frac{1}{n}\sum_{i=1}^{n}(E_i - O_i)^2} \tag{3.124}$$

$$\text{NRMSE} = \left(\frac{RMSE}{\bar{O}}\right) \cdot 100\% \tag{3.125}$$

where, $\bar{O}$ is the mean of the observed data; E_i and O_i are the estimated and observed data values, respectively. NMBE and NRMSE are given in percent, while MBE and RMSE (Eqs. 3.122 and 3.124, respectively) have the same units of the primary variable. Based on Jamieson et al. (1991) guidelines, the performance of the ETa models has been classified into one of the following categories: excellent (NRMSE $\leq 10\%$), good (10% < NRMSE $\leq 20\%$), fair (20% < NRMSE $\leq 30\%$), and poor (NRMSE > 30%).

The R^2 term is given by Eq. 3.126 as follows (as in Ott and Longnecker, 2015):

$$R^2 = \frac{\left[\sum_{i=1}^{n}(E_i - \bar{E})(O_i - \bar{O})\right]^2}{\sum_{i=1}^{n}(E_i - \bar{E})^2 \sum_{i=1}^{n}(O_i - \bar{O})^2} \tag{3.126}$$

The MBE and RMSE are error metrics associated with the residuals between estimated (or predicted) and measured (or observed) data. MBE provides information about the model's trend to overestimate or underestimate its output on an average basis. The RMSE is an indicator of accuracy when modeling approaches are used for prediction efforts. The NRMSE is the relative error compared to the mean measured data and compares performance across different models of the same response variable. The R^2, in the context of model performance, is a statistical measure that indicates the capacity of model output to explain the variability in the measured data of the same variable. All these statistical error metrics in the literature have been used to characterize the performance of crop coefficients, SEB, and ETa models (e.g., Kamble et al., 2013; Bhavsar and Patel, 2016; Wagle et al., 2017; Zhang et al., 2019; Costa-Filho et al., 2020; Costa-Filho et al., 2021).

3.12.5 Data Outliers' Filtering

Outliers have been excluded from the analysis based on the Median Absolute Deviation Approach ($MADA$). The $MADA$ method for filtering extreme values in a dataset uses the median instead of the mean as a central tendency measure. The median allows for flagging points that are not in conformity with the trends in the sampled data (Leys et al., 2013). The $MADA$ index is defined by Eq. 3.127 when a Gaussian distribution assumption is considered for the data without the influence of extreme values (Rousseeuw and Croux, 1993; Huber, 2004):

$$MADA = 1.4826 \cdot Median\left[|x_i - Median(x)|\right] \tag{3.127}$$

where x_i is the value at a given timestep, $Median(x)$ is the median of the entire sample size. In this study, the criteria for filtering the data for potential outliers was the recommendation by Leys et al. (2013). The median $\pm$ 2.5 times the $MADA$ index serves as the range of values expected in a given sampled dataset. $MADA$ was chosen as the outlier filtering method because it has been extensively used in ETa studies and does not require tabulated values for further refinement (Bisquert et al., 2016; Miller and Miller, 2018; Guillevic et al., 2019; Li et al., 2019; Helbig et al., 2020).

3.12.6 Machine-Learning Regression Model Selection

The k-fold cross-validation is a resource-intensive technique used to validate a machine-learning model (Figure 3.35), which allows the use of the entire training dataset for validating the model without the need for a distinct and independent dataset for validation (Fushiki, 2011; Jiang and Wang, 2017). This cross-validation method involves the random division of the learning dataset into a given number of sections (folds). The stratification of the training dataset is based on the outcome variable of interest. It is a way to secure a uniform distribution of outcomes across each of the selected data subsets. Within this process, one fold is set aside to be used as an independent validation dataset. In contrast, the remaining folds are combined to form the first iteration training dataset for the model-building process. The complete k-fold cross-validation procedure iterates k times, each time with a unique fold being reserved for testing in each iteration (Rodriguez-Fernandez et al., 2009; Pohjankukka et al., 2017; Jung, 2018).

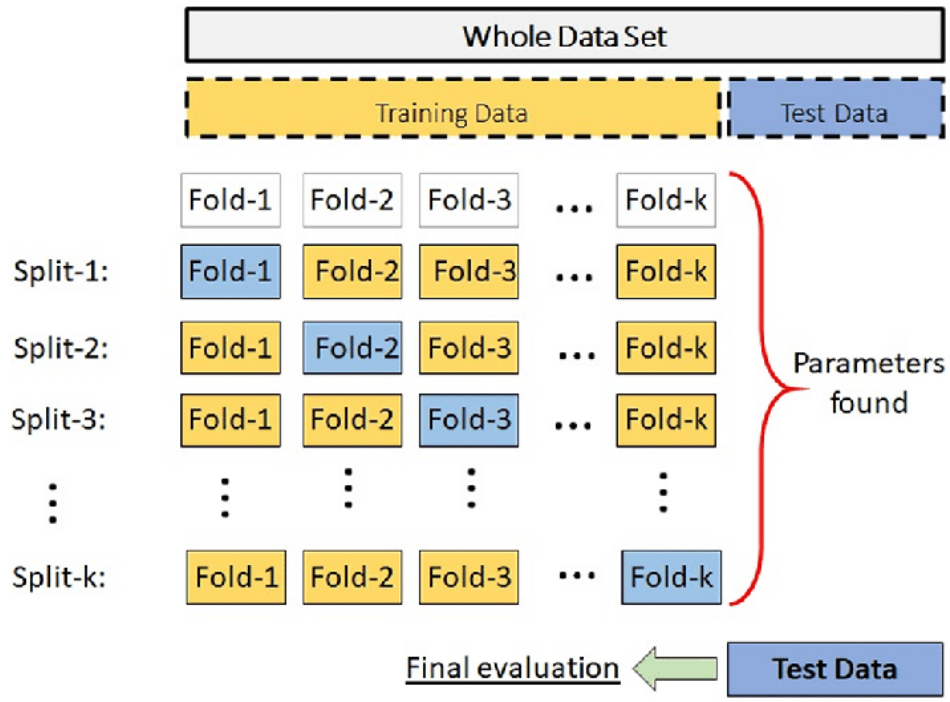

Figure 3.35: The k-fold cross-validation approach for machine-learning model accuracy assessment (Sevinç, 2022).

Consequently, k unique models are created, and each learned model is subjected to evaluation against the respective independent fold that serves as an independent dataset subgroup. The average performance across the k fold evaluation steps is assumed to represent the performance of the original model, constructed using the entire training dataset for future prediction. In this study, the number of folds was ten since most applications rely on ten data subsets for making predictions (Anguita et al., 2012; Wong and Yeh, 2019; Nti et al., 2021). In this study, the model error metrics from the k-fold cross-validation were the RMSE and R^2.

Chapter 4

Results and Discussion

4.1 Measured Crop Evapotranspiration Error Assessment

The measured maize ETa error analysis results indicated that measured ETa data from the EC SEB system was the best measuring technique compared to the BR and SWB approaches (Fig. 4.1). The EC system has had the highest $R^2_{t,X}$ and lowest σ_ϵ compared to the remaining two measurement ETa techniques. The $R^2_{t,X}$ values for LIRF and IIC from the EC ETa data were 0.98 and 1, respectively, with standard deviation values less than 0.10 mm/d, which indicates that the data from the EC is the closest to the true value of ETa. At LIRF, the BR and SWB methods have had a moderate $R^2_{t,X}$ value ($< 60\%$), with larger standard deviation values compared to the EC ETa measured data.

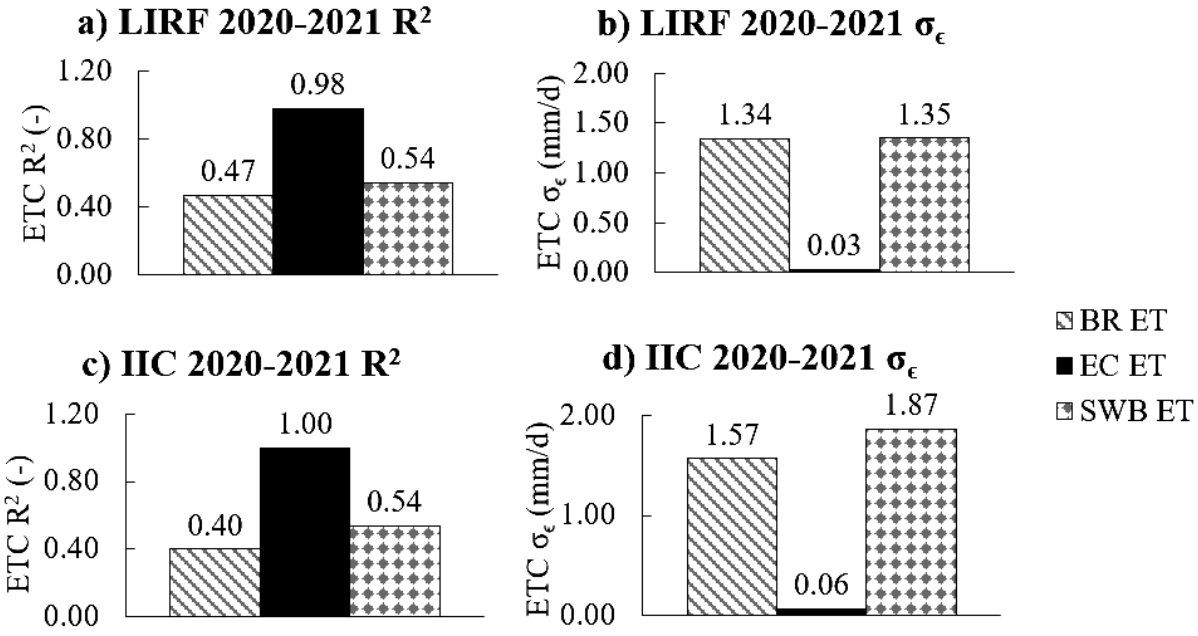

Figure 4.1: A TCe analysis comparing BR, EC, and SWB measurements of daily maize ETa at LIRF and IIC sites in 2020-2021.

When measuring ETa using the SWB approach and soil water content sensors, substantial spatial and vertical variations in soil bulk density and water retention properties may lead to bias in the measured soil water content data. Spatial variations in irrigation or precipitation moving through the soil root zone can lead to differential wetting patterns of the unsaturated soil zone. The necessity for sensor calibration based on soil type, density, and depth further contributes to the intricacies of environmental data acquisition (Allen et al., 2011; Ghiberto et al., 2011; Gurski et al., 2016).

Regarding the indirect BR method of measuring ETa, the assumption regarding uniformity in both horizontal and vertical heat and water vapor sources is not often valid in agricultural fields. Furthermore, since BR H and LE fluxes are representative of a given upwind footprint area, the accuracy of BR ETa data depends on having cropland fields with moderately to extensively sized areas (Allen et al., 2011).

4.2 Statistical Analysis of the Multispectral Data from Remote Sensing Sensors

4.2.1 Statistical Comparison Among Vegetation Indices Data Sources

The KW analysis of the NDVI, OSAVI, and SAVI calculated from RED and NIR surface reflectance indicates significant differences among at least two or more remote sensing sensors. The respective p-values from the KW test for the NDVI, OSAVI, and SAVI were all less than 0.025. More specifically, when interpreting Dunn's pairwise comparison test, results indicate no statistical significance in differences among the multispectral VIs from spaceborne sensors (e.g., Landsat-8 at 30 m, Sentinel-2 at 10 m, and Planet CubeSat at 3 m). However, when comparing the spaceborne

sensors with both the MSR at 1 m (proximal) and airborne at 0.03 m (UAS) counterparts, Dunn's test indicates that VIs were statistically different (Tables 4.1 to 4.3).

Table 4.1: Summary of Dunn's test results to analyze the NDVI spectral index from all remote sensing sensors in this study. The '*' symbol indicates the statistically different pairwise comparisons.

RS Sensors	Landsat-8 (30 m)	MSR ($1m$)	Planet (3 m)	Sentinel-2 (10 m)	Variable
MSR ($1m$)	-5.890	-	-	-	Test-Statistic
	$\ll$ 0.025*	-	-	-	p-value
Planet (3 m)	-1.015	7.258	-	-	Test-Statistic
	0.815	$\ll$ 0.025*	-	-	p-value
Sentinel-2 (10 m)	-0.448	7.322	0.828	-	Test-Statistic
	0.981	$\ll$ 0.025*	0.898	-	p-value
UAS (0.03 m)	-4.435	0.437	-4.606	-4.880	Test-Statistic
	$\ll$ 0.025*	0.982	$\ll$ 0.025*	$\ll$ 0.025*	p-value

Table 4.2: Summary of Dunn's test results to analyze the OSAVI spectral index from all remote sensing sensors in this study.

RS Sensors	Landsat-8 (30 m)	MSR ($1m$)	Planet (3 m)	Sentinel-2 (10 m)	Variable
MSR ($1m$)	-5.181	-	-	-	Test-Statistic
	$\ll$ 0.025*	-	-	-	p-value
Planet (3 m)	-1.292	5.874	-	-	Test-Statistic
	0.644	$\ll$ 0.025*	-	-	p-value
Sentinel-2 (10 m)	-0.558	6.234	1.075	-	Test-Statistic
	0.967	$\ll$ 0.025*	0.782	-	p-value
UAS (0.03 m)	-4.375	-0.145	-4.282	-4.708	Test-Statistic
	$\ll$ 0.025*	0.997	$\ll$ 0.025*	$\ll$ 0.025*	p-value

Table 4.3: Summary of Dunn's test results to analyze the SAVI spectral index from all remote sensing sensors in this study.

RS Sensors	Landsat-8 (30 m)	MSR ($1m$)	Planet (3 m)	Sentinel-2 (10 m)	Variable
MSR ($1m$)	-4.550	-	-	-	Test-Statistic
	$\ll$ 0.025*	-	-	-	p-value
Planet (3 m)	-1.411	4.808	-	-	Test-Statistic
	0.562	$\ll$ 0.025*	-	-	p-value
Sentinel-2 (10 m)	-0.612	5.325	1.169	-	Test-Statistic
	0.957	$\ll$ 0.025*	0.725	-	p-value
UAS (0.03 m)	-4.271	-0.606	-4.047	-4.536	Test-Statistic
	$\ll$ 0.025*	0.958	$\ll$ 0.025*	$\ll$ 0.025*	p-value

The fact that spaceborne sensors would have similar spectral indices is supported in the literature. Multispectral data from Landsat-8 and Sentinel-2 are consistent within a $\pm$ 2.5 to 6% difference (Barsi et al., 2018; Pahlevan et al., 2019). Given that Planet CubeSat data in this study were harmonized based on Sentinel-2 bands, the consistency between Landsat-8 and harmonized CubeSat data is justified. Regarding MSR and UAS sensors, the VIs differed statistically from each spaceborne data. Proximal and airborne sensors do not have atmospheric corrections associated with the data processing since their readings and imagery are obtained close to the ground ($< 120\ m$ AGS).

In the case of spaceborne imagery, the main difference between the data from each sensor (e.g., Landsat-8, Sentinel-2, and harmonized Planet CubeSat) is mainly due to spatial scale. When comparing proximal and airborne sensors, the main difference in the data is also associated with the spatial scale since Dunn's test indicated no statistical evidence that NDVI, OSAVI, and SAVI indices were different between MSR and UAS data. When comparing any spaceborne with the airborne or proximal sensor, the data quality differences were the radiometric and spatial resolutions.

4.2.2 Statistical Comparison Among Thermal Data Sources

When comparing the T_s data from Landsat-8 (resampled from 100 m to 30 m), MSR (1 m), and stationary IRT (1 m), the KW test indicated that not all the T_s data from the three measurement sources were statistically the same since the p-value was significantly less than 0.025 (p-value < 2.2 x 10-16). The post-hoc Dunn's test indicated that Landsat-8 TIRS at 30 m resampled differs from the T_s data from the roaming MSR Exergen IRT and SI-111 stationary IRTs (Sentinel-2 and Planet CubeSat ancillary data for running the OSEB algorithm), which is shown on Table 4.4.

Since Landsat-8 TIRS imagery have an original spatial resolution of 100 m, the maize fields at IIC and LIRF are within only one to two pixels. When Landsat-8 TIRS imagery are resampled to 30 m, it uses a passing filter window that incorporates variability in pixels outside the maize fields, which hinders its ability to adequately characterize the thermal conditions of the surface (canopy and soil combined). Since the roaming and stationary IRTs were closer to the ground and had a much smaller footprint, their data were statistically consistent.

Table 4.4: Summary of Dunn's test results to analyze the T_s data from Landsat-8, Exergen MSR, and Apogee SI-111 IRT used in this study. The '*' symbol indicates the statistically different pairwise comparisons.

RS Sensors	SI-111 IRT (1 m)	Landsat-8 TIRS (30 m)	Variable
Landsat-8 TIRS (30 m)	-8.103	-	Test-Statistic
	$\ll$ 0.025*	-	p-value
MSR IRT ($1m$)	2.203	8.280	Test-Statistic
	0.041	$\ll$ 0.025*	p-value

4.3 Remote Sensing Sensors: Evaluation of Vegetation Indices Performance

When evaluating f_c, the Trout and DeJonge (2018) model had better performance using the UAS data since the NRMSE had the lowest value among the remote sensing sensors (Figure 4.2). Although the UAS performed slightly better than the other sensors, it is evident that the NRMSE values from Planet CubeSat and Sentinel-2 were quite like the UAS results for the f_c model. Johnson and Trout (2012) f_c predictions in all remote sensing sensors were overestimated, with the highest overestimation being observed when using the Landsat-8 (30 m) and MSR (1 m) sensors (11%) and the lowest overestimation presented in the UAS (0.03 m) sensor (5%). Since the linear K_{cr} model for Trout and DeJonge (2018), RBCC is a function of f_c, an overestimated f_c value leads to a subsequent overestimation of K_{cr}, due to a linear propagation of error. Also, since the f_c model from Trout and Johnson (2012) is a linear function of NDVI, the overestimation of f_c is due to NDVI values being affected by soil background effects since 90% of the f_c data around solar noon was less than 0.86 for the frequently irrigated fields at both research sites.

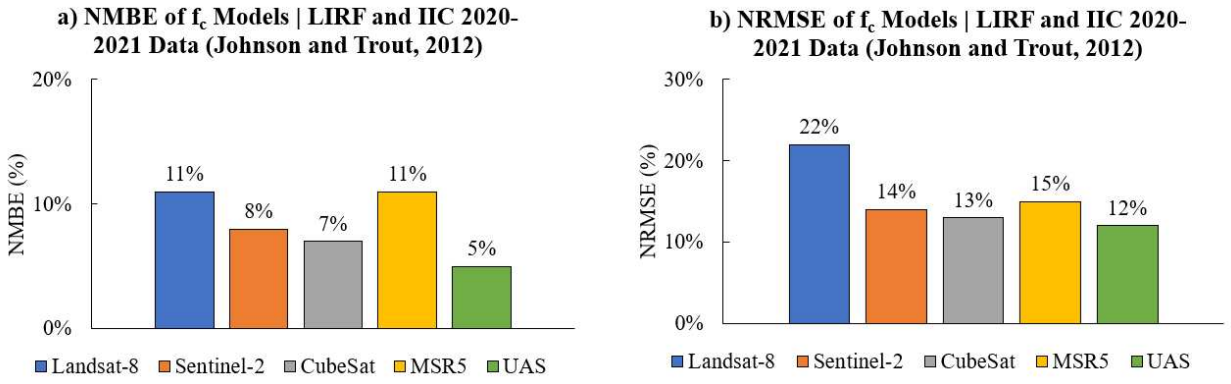

Figure 4.2: Error Analysis regarding the f_c modeling results for LIRF and IIC 2020-2021 data combined.

Regarding LAI estimates, the Chávez et al. (2009) non-linear model performed better when using the MSR (1 m) sensor since the NRMSE was 13%. The sensor/imagery that performed the poorest was Landsat-8 (30 m), with the highest observed NRMSE values among all RS sensors in this study (26%) and the highest underestimation of LAI estimates (-21%). Even though the MSR provided slightly better results than the remaining sensors, it is evident that, besides Landsat-8, the performance of MSR, Planet CubeSat, Sentinel-2, and UAS were considered good since their NRMSE values were within 10% to 20%, with CubeSat (3 m) and UAS (0.03 m) having same NRMSE of 15% (Figure 4.3). There was an underestimation of LAI estimates in all sensors except MSR (1 m). The explained variability in the observed LAI for each RS sensor was affected by the performance of the LAI model at each year of data collection across each research site. For instance, the UAS-based LAI had a low R^2 (0.29) since there was a large underestimation of LAI estimates in 2021 at the IIC site (-12%) and with a higher NRMSE of 20% compared to a 4% overestimation of LAI and NRMSE of 12% at LIRF site in 2020 and 2021 datasets. The R^2 for the LAI analysis of LIRF 2020 and 2021 data was 0.50, almost 60% higher than the R^2 from the IIC in 2021.

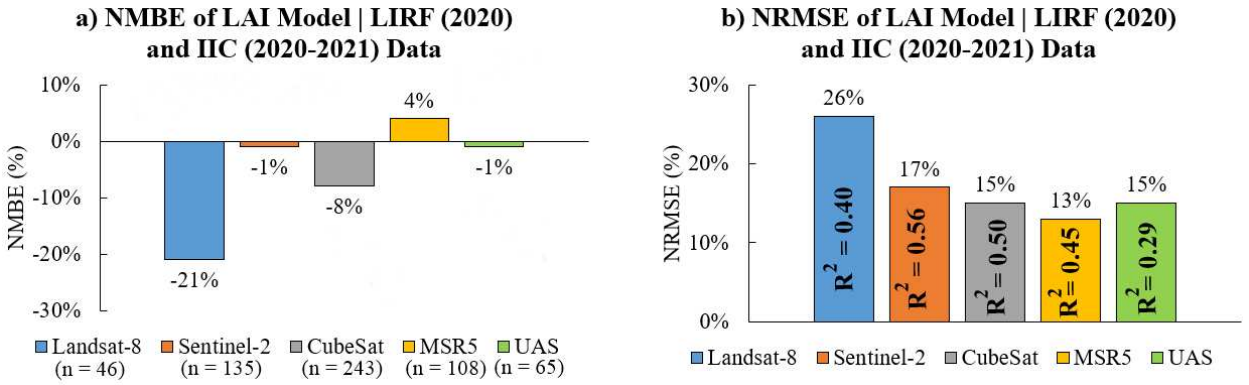

Figure 4.3: Error analysis of estimated LAI across the remote sensing sensors in this study using combined multi-year IIC and LIRF data.

Chávez et al. (2009) calibrated their LAI model considering data from both irrigated maize and sorghum and dryland sorghum, which could justify the underestimation of LAI since the data used by Chávez et al. (2009) for calibrating their LAI model considered dryland conditions, which would have lower LAI values than fully irrigated fields. Thus, the explained variability of observed LAI values in this study was also due to the limitation of the LAI model in addressing the entire range of canopy architecture values during the multi-year dataset in this study. Nonetheless, the errors associated with LAI estimates for the majority of the remote sensing sensors were consistent with a good model performance ($10\% <$ NRMSE $< 20\%$).

Regarding maize h_c estimates, the Anderson et al. (2004) model performed better when using the UAS (0.03 m) sensor since the NRMSE was 17% (Figure 4.4a). The sensor that performed the poorest was Planet CubeSat (3 m), followed by Landsat-8 (30 m), with observed NRMSE values among all RS sensors in this study being 21% and 22%, respectively. Furthermore, the underestimation of maize h_c was evident across all RS sensors. The range of underestimation varied from -14% (UAS) to -19% (Planet CubeSat). The performance of MSR (1 m), UAS (0.03 m), and Sentinel-2 (10 m) was considered good since NRMSE was within 10% to 20% (Figure 4.4b). The apparent underestimation of h_c is related to the calibration coefficients of the model from Anderson et al. (2004). Anderson et al. (2004) developed a model for rainfed maize and soybeans using data collected with a regular aircraft near Ames, Iowa, USA, which has a more humid climate than Colorado, USA. Overall, the explained variability of observed maize h_c was good since all R^2 was greater than 0.70 across all the remote sensing sensors (Figure 4.4b).

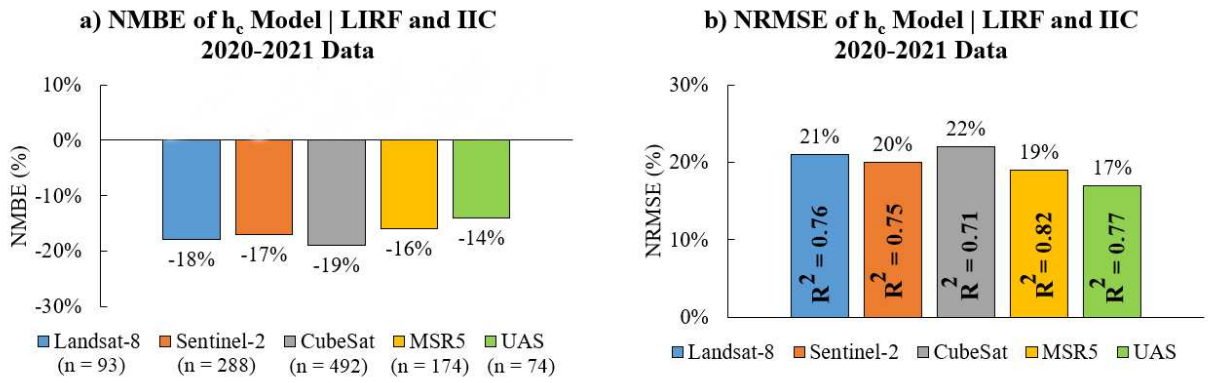

Figure 4.4: Error analysis of estimated h_c across the remote sensing sensors in this study using combined multi-year IIC and LIRF data.

The uncertainty also caused the errors associated with LAI, h_c, and f_c due to calibrated coefficients being representative of maize and other crops that had similar, but not the exact crop water requirements observed during the maize growing seasons at LIRF and IIC in 2020 and 2021. The empirical models for LAI, h_c, and f_c considered maize or analogous crops under particular conditions and irrigation management practices that could have led to systematic errors when applied to the maize varieties used in this study. Different maize crop varieties under different climate conditions have the potential to determine canopy architecture significantly. Thus, differences in maize canopy physiology characteristics can lead to divergent growth patterns and structural development that may not be captured by purely empirical models that were previously published and calibrated under different local conditions.

4.4 Determination of Optimal Remote Sensing Sensors

4.4.1 The Reflectance-based Crop Coefficient Assessment

Sentinel-2 multispectral data provided the best results when estimating daily maize ETa using the Neale et al. (1990) and Trout and DeJonge (2018) RBCC models, while the MSR sensor gave the best results when Bausch (1995) RBCC model was evaluated with LIRF and IIC 2020/2021 data combined (Figure 4.5). The daily maize ETa errors (MBE $\pm$ RMSE) associated with the Sentinel-2 sensor were 0.21 (5%) $\pm$ 0.78 (18%) mm/d and 0.59 (14%) $\pm$ 1.07 (25%) mm/d for the Neale et al. (1990) and Trout and DeJonge (2018) models, respectively.

Overestimation of daily maize ETa ranging from 5% to 24% was observed in the error analysis from all sensors when NDVI and f_c were the predictors of K_{cr} and maize ETa. For the SAVI RBCC model (Bausch, 1995), the predictions of daily maize ETa had a -0.13 (-3%) $\pm$ 0.67 (16%) mm/d error for the proximal MSR sensor. There was an underestimation of maize ETa observed in the Landsat-8 (-3%), Sentinel-2 (-6%), and MSR (-3%) sensors, while overestimation of maize ETa occurred when using Planet CubeSat (8%) and UAS (0.10%) multispectral data.

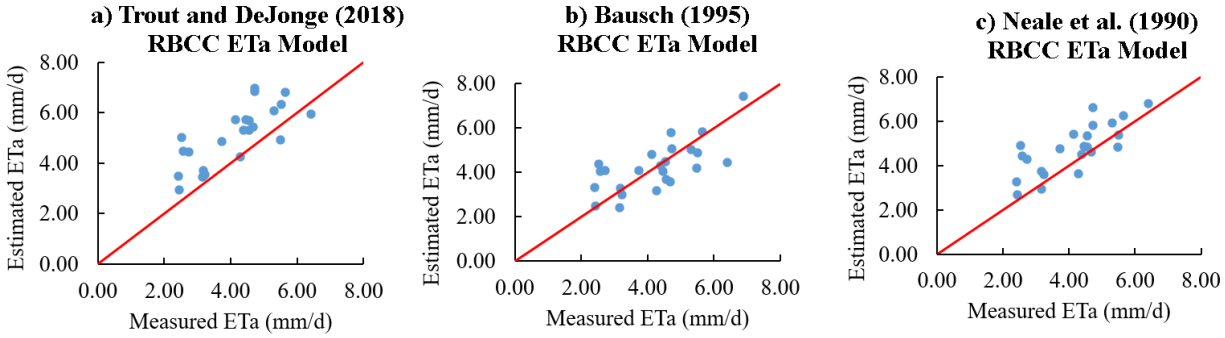

Figure 4.5: The scatter plot of measured EC ETa vs. estimated RBCC daily maize ETa regarding LIRF-IIC data combined (2020 and 2021). The red line is the 1:1 line.

The NDVI sensitivity to soil (and other materials) background reflectance in the RED and NIR bands could be another explanation for why the Neale et al. (1990) RBCC approach also overestimated daily maize ETa values. Bausch (1993), Jones et al. (2015), and Duan et al. (2017) indicated that NDVI data for row crops such as maize and wheat are subject to soil background effects and other ground-based material that mask the signals (sunlight radiation) from plant leaves alone. When SAVI was used in the Bausch (1995) RBCC model, the trend of overestimation did not appear in the data from all sensors, apart from Planet CubeSat (3 m).

Furthermore the accuracy of the RBCC predictions can be significantly influenced by several key factors such as maize variety, calibration of remote sensing data, and empirical model calibration. Different maize varieties exhibit unique growth patterns and canopy structures, which can affect how light is reflected from the leaves and consequently influence the crop coefficients derived from remote sensing data. Regarding the RS data, local atmospheric conditions may differ from when data were collected for RBCC model calibration, which could also indicate a cause of overestimation of RBCC daily maize ETa predictions.

The underestimation of daily maize ETa from Bausch (1995) could be due to the soil background adjustment factor (L) prescription. Most studies that use SAVI assume L to be 0.50 for most environmental and field conditions (e.g., Huete, 1988; Xue and Su, 2017). However, Huete (1988) highlighted that different ranges of LAI might influence the adjustment factor L, even though Qi et al. (1994) indicated that $L = 0.50$ would buffer most of the variations in the canopy signal due to soil and other elements background effects, which seems acceptable in this study given that the underestimation of daily maize ETa from Bausch (1995) RBCC model ranged from -3$\%$ to -6$\%$.

When independently evaluating the LIRF 2020/2021 data, the results were similar to the previous analysis with both fields' data combined (Table 4.5). At the LIRF site, Planet CubeSat and Sentinel-2 had the exact NRMSE (21$\%$) for the Neale et al. (1990) and Trout and DeJonge (2018)

RBCC models. The CubeSat sensor had a slightly better R^2 (0.83) value than the Sentinel-2 sensor ($R^2 = 0.82$). For the Bausch (1995) model, the MSR sensor provided the best data, with an error of 0.15 (4%) $\pm$ 0.53 (14%) mm/d and 84% of explained variability in daily maize ETa observed data from the EC system. Trout and DeJonge (2018) and Neale et al. (1990) RBCC models continued the trend of maize ETa overestimation from the LIRF and IIC data analysis. For the Trout and DeJonge (2018) RBCC model, the overestimation of daily maize ETa ranged from 7% (Landsat-8) to 27% (MSR), while Neale et al. (1990) RBCC predicted ETa overestimation varied from 8% (Planet CubeSat) to 24% (UAS).

When independently evaluating the IIC 2020/2021 data, the results were similar to the previous analysis with both fields' data combined (Table 4.6). At the IIC site, Sentinel-2 was the optimal remote sensing sensor when considering the Neale et al. (1990) and Trout and DeJonge (2018) RBCC models. The error for the Neale et al. (1990) RBCC model was 0.06 (1%) $\pm$ 0.79 (21%) mm/d, while the associated error when predicting daily maize ETa for Trout and DeJonge (2018) RBCC model was 0.61 (13%) $\pm$ 1.20 (25%) mm/d. For the Bausch (1995) model, the MSR proximal sensor provided the best results, with an error of -0.30 (-7%) $\pm$ 0.75 (17%) mm/d and 81% of explained variability in daily maize ETa observed data from the EC system. Similar to the LIRF data analysis, Trout and DeJonge (2018) and Neale et al. (1990) RBCC models continued the trend of maize ETa overestimation from the combined LIRF and IIC data analysis. For the Neale et al. (1990) model, the overestimation of daily maize ETa ranged from 1% (Sentinel-2) to 14% (UAS), while Trout and DeJonge (2018) RBCC predicted ETa overestimation varied from 13% (Sentinel-2) to 30% (MSR).

Table 4.5: Error analysis for the RBCC daily maize ETa estimation for LIRF 2020-2021 data.

RBCC Model	RS Sensor	Spatial Resolution	n	MBE	NMBE	RMSE	NRMSE	R^2
		[m]	[-]	[mm/d]	[-]	[mm/d]	[-]	[-]
Neale et al. (1990)	Landsat-8	30	14	0.29	7%	0.89	23%	0.62
	Sentinel-2	10	34	0.35	9%	0.79	21%	0.82
	Planet	3	60	0.49	13%	0.80	21%	0.83
	MSR	1	17	1.00	27%	1.18	31%	0.77
	UAS	0.03	11	0.70	18%	1.13	29%	0.34
Bausch (1995)	Landsat-8	30	14	-0.17	-4%	0.65	17%	0.70
	Sentinel-2	10	34	-0.11	-3%	0.62	16%	0.83
	Planet	3	60	0.84	22%	1.12	30%	0.77
	MSR	1	17	0.15	4%	0.53	14%	0.84
	UAS	0.03	11	0.09	2%	0.92	24%	0.26
Trout and DeJonge (2018)	Landsat-8	30	14	0.62	16%	1.05	27%	0.63
	Sentinel-2	10	34	0.57	15%	0.93	25%	0.83
	Planet	3	60	0.32	8%	0.80	21%	0.77
	MSR	1	17	0.68	18%	0.90	24%	0.84
	UAS	0.03	11	0.92	24%	1.24	32%	0.41

Table 4.6: Error analysis for the RBCC daily maize ETa estimation for IIC 2020-2021 data.

RBCC Model	RS Sensor	Spatial Resolution	n	MBE	NMBE	RMSE	NRMSE	R^2
		[m]	[-]	[mm/d]	[-]	[mm/d]	[-]	[-]
Neale et al. (1990)	Landsat-8	30	12	0.44	12%	0.89	23%	0.62
	Sentinel-2	10	32	0.06	1%	0.79	21%	0.82
	Planet	3	59	0.31	8%	0.80	21%	0.83
	MSR	1	27	0.49	11%	1.18	31%	0.77
	UAS	0.03	13	0.63	14%	1.13	29%	0.34
Bausch (1995)	Landsat-8	30	12	-0.07	-2%	1.04	29%	0.44
	Sentinel-2	10	32	-0.42	-9%	0.79	17%	0.65
	Planet	3	59	-0.21	-5%	0.73	19%	0.69
	MSR	1	27	-0.30	-7%	0.75	17%	0.81
	UAS	0.03	13	-0.07	-2%	0.92	20%	0.57
Trout and DeJonge (2018)	Landsat-8	30	12	0.57	16%	1.35	37%	0.34
	Sentinel-2	10	32	0.61	13%	1.20	25%	0.54
	Planet	3	59	0.85	22%	1.16	30%	0.62
	MSR	1	27	1.37	30%	1.49	33%	0.83
	UAS	0.03	13	1.09	24%	1.31	29%	0.77

4.4.2 The One-Source Energy Balance Performance Assessment

The results from the OSEB ETa algorithm indicate that the Planet CubeSat (3 m) resulted with the best performance when estimating hourly maize ETa compared to the other RS sensors since its NRMSE had a value of 13%. The overall error in predicting hourly maize ETa using CubeSat (3 m) was -0.02 (-3%) $\pm$ 0.07 (13%) mm/h. Sentinel-2 (10 m) and MSR (1 m) had very similar performance when predicting hourly maize ETa, with associated error equal to -0.03 (-5%) $\pm$ 0.08 (14%) mm/h and 0.01 (1%) $\pm$ 0.09 (15%) mm/h. Concerning model performance evaluation based on NRMSE, all sensors/sensors resulted in overall good predictions ($10\% < \text{NRMSE} \leq 20\%$) of maize ETa, apart from the Landsat-8 (30 m) with TIRS (30 m, resampled). The errors associated

with Landsat-8 (30 m) and TIRS data were -0.05 (-10%) ± 0.17 (31%) mm/h, while a reduction of 55% and 50% in NMBE and NRMSE was observed when the TIRS was replaced by the Apogee SI-111 IRT T_s data, respectively (Figure 4.6).

The Landsat-8 TIRS data did not represent the actual field thermal conditions since the original TIRS pixel size or spatial scale (100 m) represented just a few pixels in the maize research site at LIRF and IIC and may not have incorporated well the crop conditions within the fields (i.e., contaminated pixels). Thus, the Landsat sensor presented unrealistic nadir-looking T_s data for the ETa model for the conditions encountered in this experiment (Figure 4.7). Errors in T_s compromise the prediction accuracy of the H model from the OSEB approach since it relies on using accurate temperature difference "T_o - T_a". Costa-Filho et al. (2021) showed that the multivariate model for maize T_o presented larger uncertainty when T_s data were inaccurate, i.e., not representing well actual surface/field thermal conditions.

The NRMSE when estimating H using Landsat-8 and its TIRS data were greater than 30%. In contrast, the NRMSE values associated with the remaining spaceborne, airborne, and proximal sensors varied from 20% to 30%. The replacement of TIRS data with proximal IRT T_s data to estimate maize ETa using Landsat-8 (30 m), RED, and NIR surface reflectance data provided better results, with error equals to -0.03 (-5%) ± 0.11 (20%) mm/h. Using the stationary IRT data with Landsat-8 (30 m) SR data improved the estimation of H, R_n, and G by 15%, 9%, and 11%, respectively. Sentinel-2 (10 m) and Planet CubeSat (3 m) had similar performances since the CubeSat data were harmonized using Sentinel-2 data. Since the T_s data came from the same source (stationary SI-111 IRT), it was expected that both sensors would have similar errors when predicting hourly maize ETa. Furthermore, the R^2 values for Sentinel-2 and Planet CubeSat were nearly the same (0.84 and 0.83, respectively).

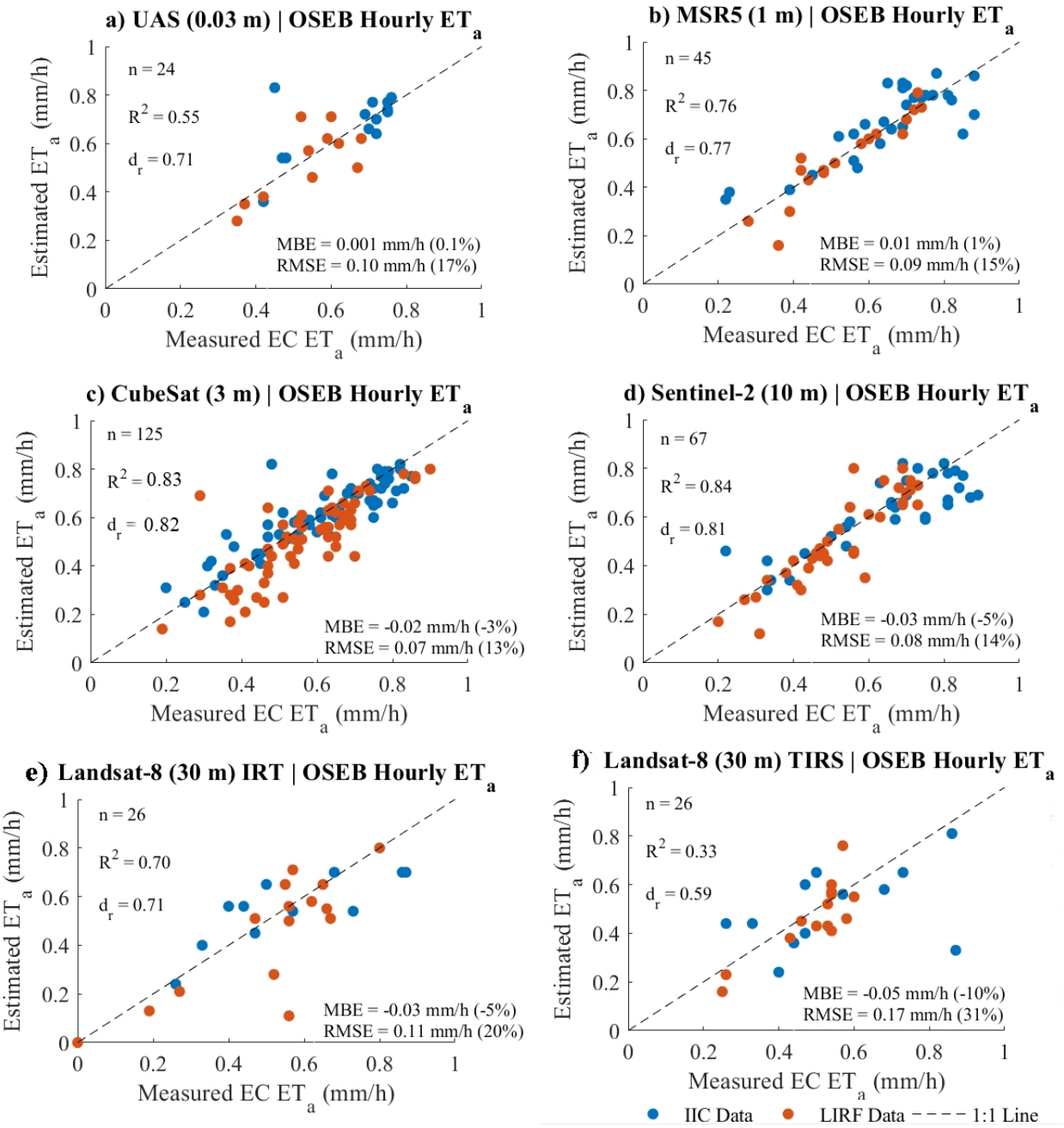

Figure 4.6: Scatter plots (1:1 line) and error analysis results regarding the OSEB maize hourly ETa modeling for the combined LIRF and IIC 2020-2021 data. The sample size (n) of each sensor is indicated in the legend of the figure.

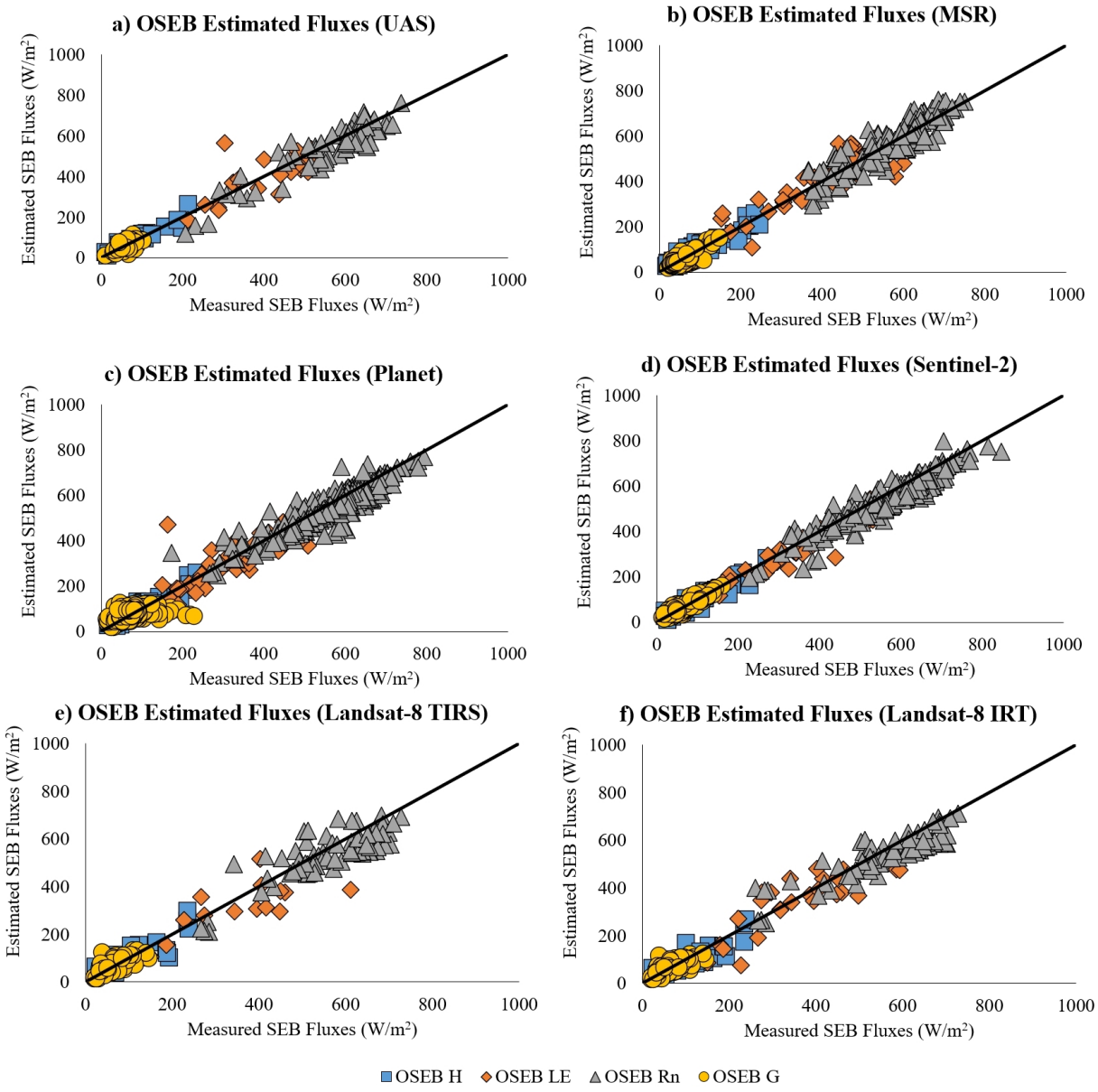

Figure 4.7: Scatter plots (1:1 line) and error analysis results regarding the OSEB SEB flux modeling for the combined LIRF and IIC 2020-2021 data.

When evaluating the LIRF 2020-2021 data, the hourly estimated ETa results were consistent with the previous combined data from LIRF and IIC. The Planet CubeSat (3 m) provided better results than the other spaceborne, airborne, and proximal sensors since it had the smallest NRMSE equal to 12% (Table 4.7). All sensors observed the underestimation of hourly maize ETa

predictions, with NMBE ranging from -4% to -12%. The underestimation of hourly maize ETa predictions across all the remote sensing sensors was due to the underestimation of the majority of canopy architecture variables in the study (LAI and h_c).

All sensors, apart from Landsat-8 with TIRS data, explained at least 70% of the variability in the observed hourly maize ETa data from the EC system. Again, when Landsat-8 TIRS data were replaced by IRT data (point-based), there was an improvement in the prediction of maize ETa, with a 30% reduction in NRMSE. When evaluating the IIC 2020-2021 data, the results were consistent with the previous analysis regarding LIRF and the combined LIRF-IIC data. Again, Planet CubeSat performed better than the others, with an error of 0 (0%) $\pm$ 0.08 (13%) mm/h.

For the IIC dataset, underestimation of hourly maize ETa predictions was observed in Landsat-8 (both with TIRS and IRT data) and Sentinel-2 (10 m). A slight overestimation of ETa was present in the predictions of hourly maize ETa using MSR (1 m) and UAS (0.03 m) data. When Landsat-8 TIRS data were replaced by IRT data (point-based), there was an improvement in the prediction of maize ETa, with a 40% reduction in NRMSE. The accuracy of ETa estimation was within the common values of NRMSE previously published in the literature since our accuracy across all sensors varied from 10% to 25%, which is within the 10% to 40% error observed in other studies using similar OSEB algorithms for crop ETa (Bhattarai et al., 2016; Acharya and Sharma, 2021).

Table 4.7: Error analysis results of the OSEB hourly maize ETa evaluation for LIRF and IIC 2020-2021 data, respectively.

Site	RS Sensor	Spatial Resolution	n	MBE	NMBE	RMSE	NRMSE	R^2
		[m]	[-]	[mm/d]	[-]	[mm/d]	[-]	[-]
LIRF	Landsat-8 IRT	30	14	-0.05	-9%	0.10	19%	0.82
	Sentinel-2	10	35	-0.04	-7%	0.07	13%	0.92
	Planet	3	63	-0.03	-6%	0.06	12%	0.89
	MSR	1	17	-0.02	-4%	0.08	14%	0.82
	UAS	0.03	11	-0.04	-7%	0.09	16%	0.70
IIC	Landsat-8 IRT	30	12	-0.01	-1%	0.12	21%	0.64
	Sentinel-2	10	32	-0.02	-4%	0.10	15%	0.72
	Planet	3	62	0.00	0%	0.08	13%	0.78
	MSR	1	28	0.02	3%	0.10	15%	0.69
	UAS	0.03	13	0.04	5%	0.12	18%	0.37

4.4.3 The Two-Source Energy Balance Performance Assessment

The results from TSEBpar and TSEBser of ETa algorithms indicated that RS data used from the MSR (1 m) sensor resulted in the best performance when estimating hourly maize ETa compared to the use of other RS sensors' data since the smallest NRMSE was 11% and 14%, respectively for both TSEB algorithms used. The overall errors in predicting hourly maize ETa using MSR (1 m) data were -0.02 (-3%) $\pm$ 0.07 (11%) mm/h and -0.02 (-4%) $\pm$ 0.09 (14%) mm/h, for the TSEBpar and TSEBser, respectively. The errors associated with Landsat-8 (30 m) TIRS data used in the RS of ETa estimation were -0.03 (-5%) $\pm$ 0.16 (29%) mm/h and -0.07 (-13%) $\pm$ 0.15 (29%) mm/h. At the same time, a reduction of 31% and 34% in NRMSE was observed when the TIRS was replaced by the ground-based IRT data for the TSEBpar and TSEBser, respectively (Figures 4.8 and 4.9).

The NRMSE errors of estimating H using Landsat-8 multispectral visible and NIR and TIRS data were more significant than 30% for the TSEBpar and TSEBser, while the NRMSE from the remaining spaceborne, airborne, and proximal sensors were within 20% to 30%. Using IRT data to estimate maize ETa with Landsat-8 (30 m) surface reflectance improved the estimation of hourly maize ETa, with reduced performance errors of 0.02 (4%) $\pm$ 0.10 (19%) mm/h and -0.04 (-8%) $\pm$ 0.11 (20%) mm/h for the TSEBpar and TSEBser, respectively. For the TSEBpar, the performance of the R_n model did not significantly change when using TIRS and IRT data since the NRMSE was 13% and 14%, respectively. The TSEB G model NRMSE ranged from 20% to 45% across all the remote sensing sensors in this study, which had a fair to poor performance since NRMSE $>$ 20%. However, since the magnitude of G is much smaller than R_n and H, the error propagation in LE estimates due to G is also smaller than the other two SEB input fluxes. Furthermore, the original TSEB G model assumes that G varies linearly with the R_n flux associated with bare soil. However, Colaizzi et al. (2012) indicated that G and bare soil R_n have a time-phased difference between the two fluxes that requires a specific local calibration using G and bare soil R_n measurements.

The TSEBser hourly maize ETa underestimation range was within -3% (CubeSat) to -13% (Landsat-8 TIRS). When considering the TSEBpar algorithm, there was an underestimation of hourly maize ETa when using UAS (-3%), MSR (-3%), Sentinel-2 (-3%), and Landsat-8 TIRS (-5%). The slight overestimation of hourly maize ETa for CubeSat (3 m) and Landsat-8 IRT (30 m) were 2% and 4%, respectively. Sentinel-2 (10 m) and Planet CubeSat (3 m) had similar performance since the NRMSE for TSEBpar and TSEBser had a 6% difference between the two high-resolution spaceborne sensors.

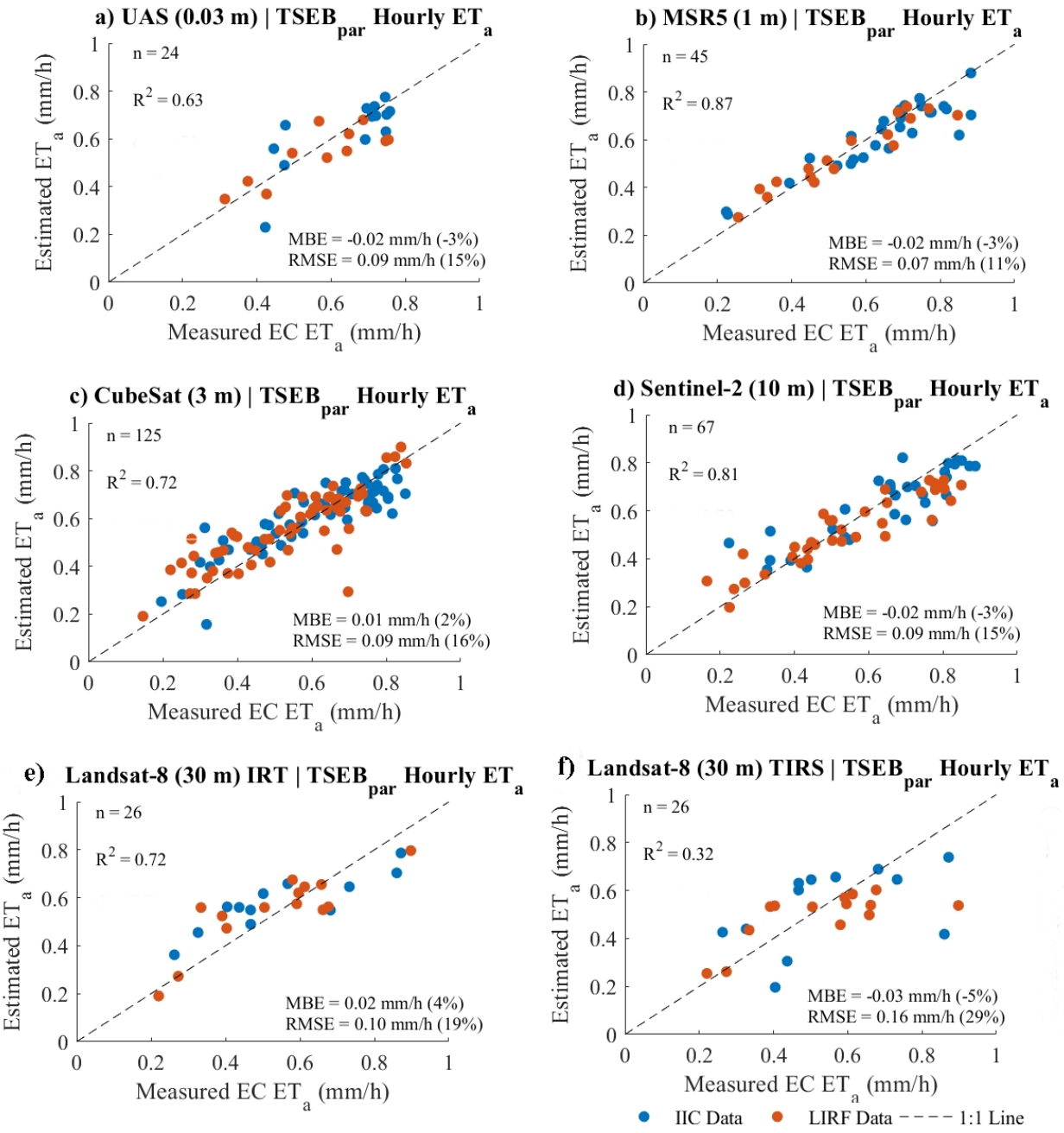

Figure 4.8: Scatter plots (1:1 line) and error analysis results regarding the TSEB parallel (TSEBpar) maize hourly ETa modeling results for the combined LIRF and IIC 2020-2021 data. The sample size (n) of each sensor is indicated in the legend of the figure.

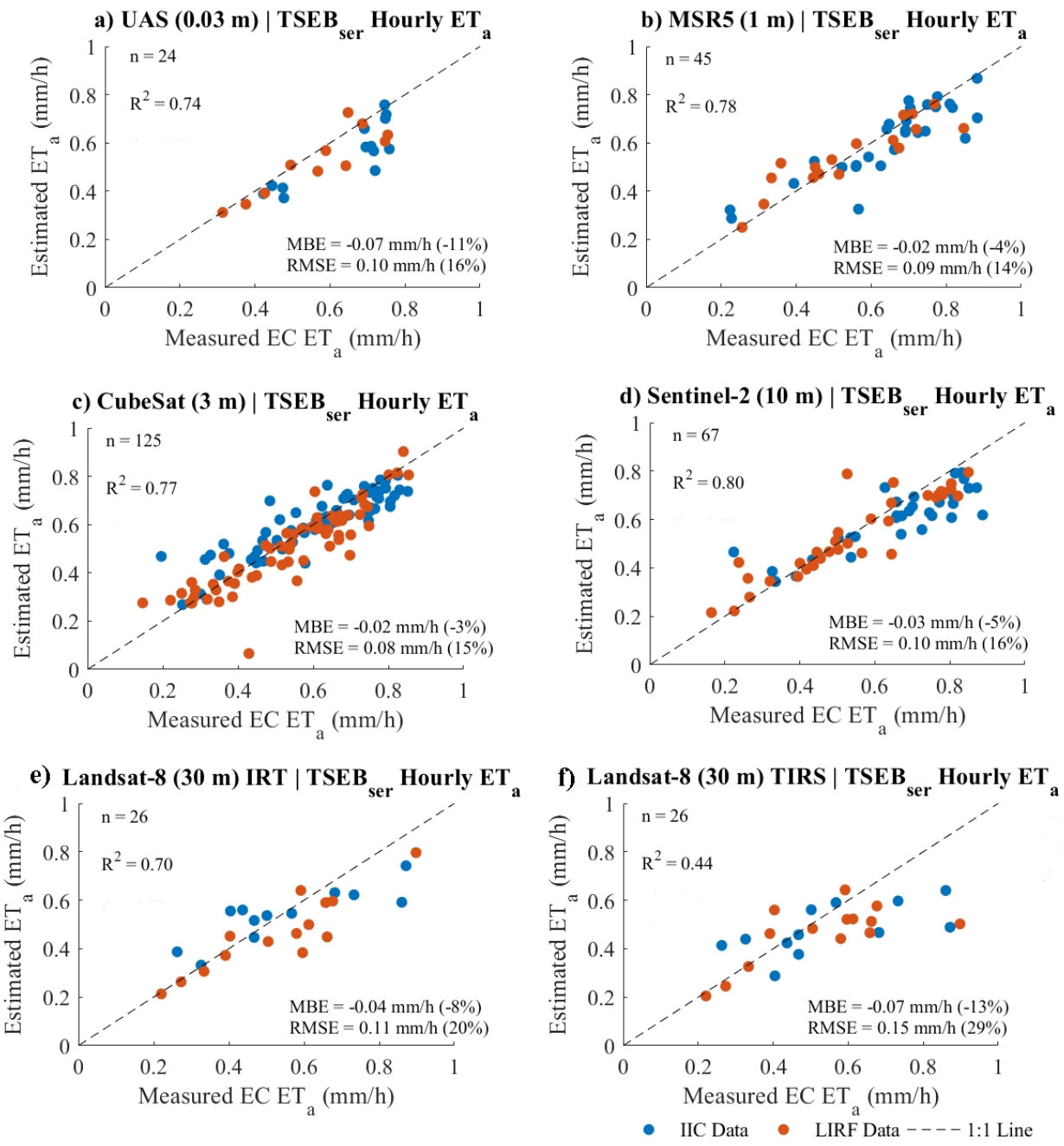

Figure 4.9: Scatter plots (1:1 line) and error analysis results regarding the TSEB series (TSEBser) maize hourly ETa modeling results for the combined LIRF and IIC 2020-2021 data. The sample size (n) of each sensor is indicated in the legend of the figure.

The range of accuracy of both TSEB approaches for maize ETa (10%-30%) was consistent with previously reported values in the currently existing literature for other row crops such as vineyards (Nassar et al., 2021). The similar results obtained between maize ETa observed and estimated

values across from previous studies using different spatial and spectral resolution remote sensing sensors reinforces the reliability of selecting finer remote sensing spatial resolution sensors to use as input for predicting crop ETa from a TSEB RS of ETa algorithm to advance sustainable agricultural water management. Nassar et al. (2021) indicated that the smallest errors observed when predicting LE and crop ETa occurred at spatial resolutions less than 15 m. Figures 4.10 and 4.11 show the scatter plots of the SEB fluxes from TSEBpar and TSEBser, respectively.

The comparative analysis of multiple RS sensors presented a relevant understanding of their data quality as input for predicting maize ETa using the TSEB RS of ETa algorithms evaluated in the study. Despite the overall agreement in ETa accuracy observed in the existing literature, it is important to consider factors such as spectral resolution, revisit frequency, and sensor-specific limitations when deciding which RS sensor is better given the site-specific conditions and irrigation sustainable needs. Since the MSR (proximal RS sensor) has limitations regarding the spatial coverage of large fields in a timely manner, operational costs, and data processing, its use could be hindered throughout different stages of the growing season. Given that the high-spatial-resolution spaceborne sensors (e.g., Sentinel-2 and Planet CubeSat) had similar accuracy performance (NMBE and NRMSE) compared to the MSR, their use could be justified when proximal RS devices are not ideal for collecting data in large agriculture fields with significant areas of canopy heterogeneity that make on-site data acquisition challenging and unrealistic.

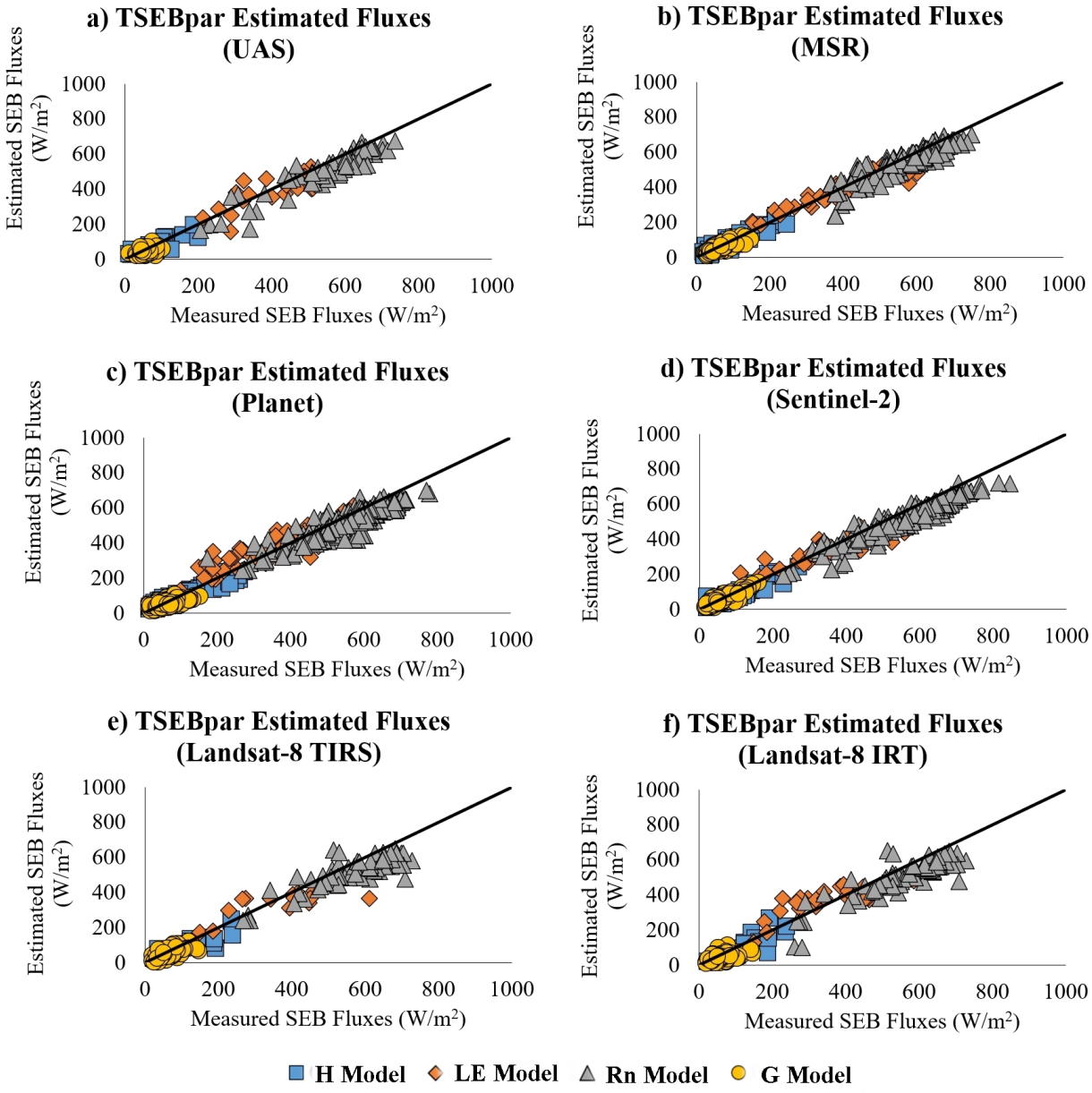

Figure 4.10: Scatter plots (1:1 line) and error analysis results regarding the TSEBpar SEB flux modeling for the combined LIRF and IIC 2020-2021 data.

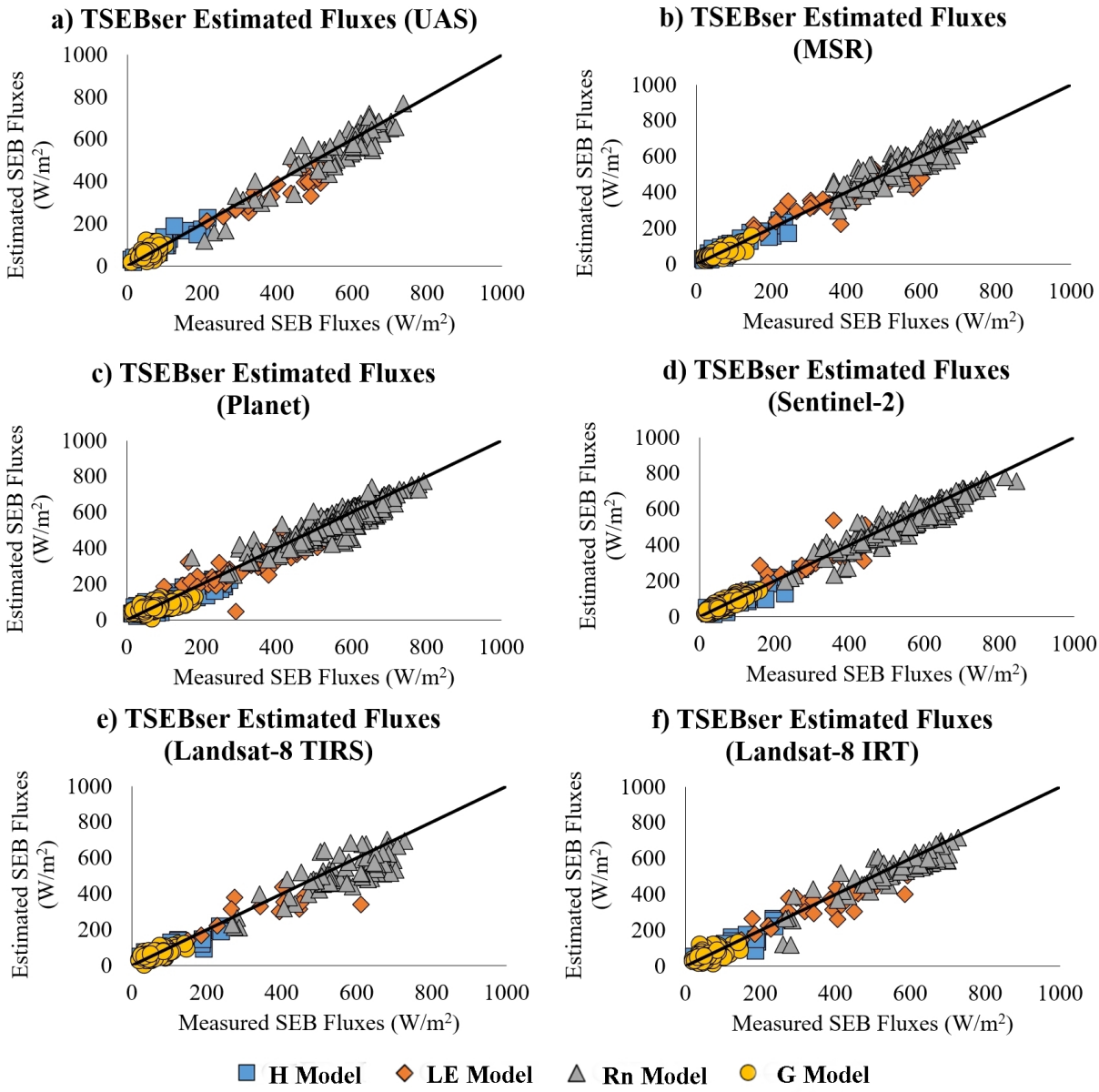

Figure 4.11: Scatter plots (1:1 line) and error analysis results regarding the TSEBser SEB flux modeling for the combined LIRF and IIC 2020-2021 data.

When evaluating the LIRF 2020-2021 data alone, the results were also consistent with the previous combined data from LIRF and IIC regarding both the TSEBser and TSEBpar algorithms. The proximal sensor MSR (1 m) provided better results to estimate hourly maize ETa when compared to all other RS sensors since it had the smallest NRMSE equal to 10% (TSEBpar) and 14% (TSEBser). See Tables 4.8 and 4.9. Underestimation of TSEBpar hourly maize ETa predictions

ranged from -1% to -7% for the Landsat-8 TIRS (30 m), Sentinel-2 (10 m), MSR (1 m), and UAS (0.03 m).

Overestimation of TSEBpar maize ETa was observed in the case of RS data used from Planet CubeSat (3 m) and Landsat-8 IRT sensors, with respective NMBE equal to 4% and 3%. Regarding the TSEBser RS of ETa algorithm, similar trends of underestimation and overestimation of hourly maize ETa were observed compared to the TSEBpar algorithm. There was a 28% and a 26% reduction in NRMSE for the TSEBpar and TSEBser RS of ETa results when Landsat-8 surface reflectance and IRT T_s data were used to estimate hourly maize ETa. When evaluating the IIC 2020-2021 data alone, the results were again consistent with the previous analysis regarding LIRF and the combined LIRF-IIC data. Similarly, the MSR (1 m) provided the best results compared to the spaceborne and airborne sensors, with an overall error equal to -0.03 (-4%) $\pm$ 0.08 (12%) mm/h and -0.04 (-6%) $\pm$ 0.09 (14%) for the TSEBpar and TSEBser, respectively.

Table 4.8: Error analysis from the TSEBpar hourly maize ETa evaluation for LIRF and IIC 2020-2021 data.

Site	RS Sensor	Spatial Resolution	n	MBE	NMBE	RMSE	NRMSE	R^2
		[m]	[-]	[mm/d]	[-]	[mm/d]	[-]	[-]
LIRF	Landsat-8 TIRS	30	14	-0.04	-7%	0.13	25%	0.51
	Landsat-8 IRT	30	14	0.02	3%	0.09	18%	0.73
	Sentinel-2	10	35	-0.02	-4%	0.09	16%	0.85
	Planet	3	63	0.02	4%	0.10	18%	0.69
	MSR	1	17	-0.01	-1%	0.06	10%	0.91
	UAS	0.03	11	-0.03	-5%	0.09	15%	0.67
IIC	Landsat-8 TIRS	30	12	-0.02	-3%	0.18	33%	0.24
	Landsat-8 IRT	30	12	0.03	5%	0.11	21%	0.76
	Sentinel-2	10	32	-0.01	-2%	0.09	15%	0.73
	Planet	3	62	0.00	0%	0.08	14%	0.76
	MSR	1	28	-0.03	-4%	0.08	12%	0.82
	UAS	0.03	13	-0.01	-2%	0.09	14%	0.58

Table 4.9: Error analysis from the TSEBser hourly maize ETa evaluation for LIRF and IIC 2020-2021 data.

Site	RS Sensor	Spatial Resolution	n	MBE	NMBE	RMSE	NRMSE	R^2
		[m]	[-]	[mm/d]	[-]	[mm/d]	[-]	[-]
LIRF	Landsat-8 TIRS	30	14	-0.07	-13%	0.14	27%	0.48
	Landsat-8 IRT	30	14	-0.07	-13%	0.10	20%	0.81
	Sentinel-2	10	35	-0.01	-2%	0.08	15%	0.83
	Planet	3	63	-0.03	-6%	0.09	16%	0.79
	MSR	1	17	0	0%	0.08	14%	0.82
	UAS	0.03	11	-0.04	-8%	0.08	14%	0.78
IIC	Landsat-8 TIRS	30	12	-0.07	-13%	0.16	30%	0.41
	Landsat-8 IRT	30	12	-0.01	-2%	0.12	21%	0.71
	Sentinel-2	10	32	-0.05	-8%	0.11	17%	0.75
	Planet	3	62	0.01	1%	0.08	13%	0.78
	MSR	1	28	-0.04	-6%	0.09	14%	0.75
	UAS	0.03	13	-0.09	-13%	0.11	17%	0.72

4.5 The Remote Sensing Calibration Protocol Results

4.5.1 The Novel Light Extinction Model Results

The calibration of the k_p model using LIRF 2020 and IIC 2020-2021 datasets resulted in the following k_p model with an R^2 of 0.95 (Eq. 4.1):

$$k_p = -0.05 + 0.78 \cdot \left(\frac{1}{LAI}\right) \cdot ln\left(\frac{\text{NDVI} - \text{NDVI}_c}{\text{NDVI}_{soil} - \text{NDVI}_c}\right) \tag{4.1}$$

The calibrated k_p model accounts for 95% of the variability observed in the k_p data, which is a good indication that the developed model has a strong and positive statistical linear relationship between k_p and k_v (Figure 4.12), as observed in the literature (Baret et al., 1995). The intercept

and slope regression coefficients have a 95% confidence interval ranging from -0.06 to -0.03 and 0.76 to 0.81, respectively (Table 4.10). The p-values are statistically significant (< 5%), which indicates that the regressed coefficient estimates are statistically validated for future model predictions.

Table 4.10: Summary statistics* of the k_p regression model using LIRF 2020 and IIC 2020-2021 datasets combining data from all remote sensing sensors in this study.

Parameters	Estimate	95% Confidence Interval	Standard Error	Test-Statistics	p-value
Intercept (β_o)	-0.05	[-0.06, -0.03]	0.01	-5.19	5.23e-07
Slope (β_1)	0.78	[0.76, 0.81]	0.01	62	2.82e-130

*Number of observations: 197; Error degrees of freedom: 195; RMSE: 0.02; F-statistic: 3.84e+03

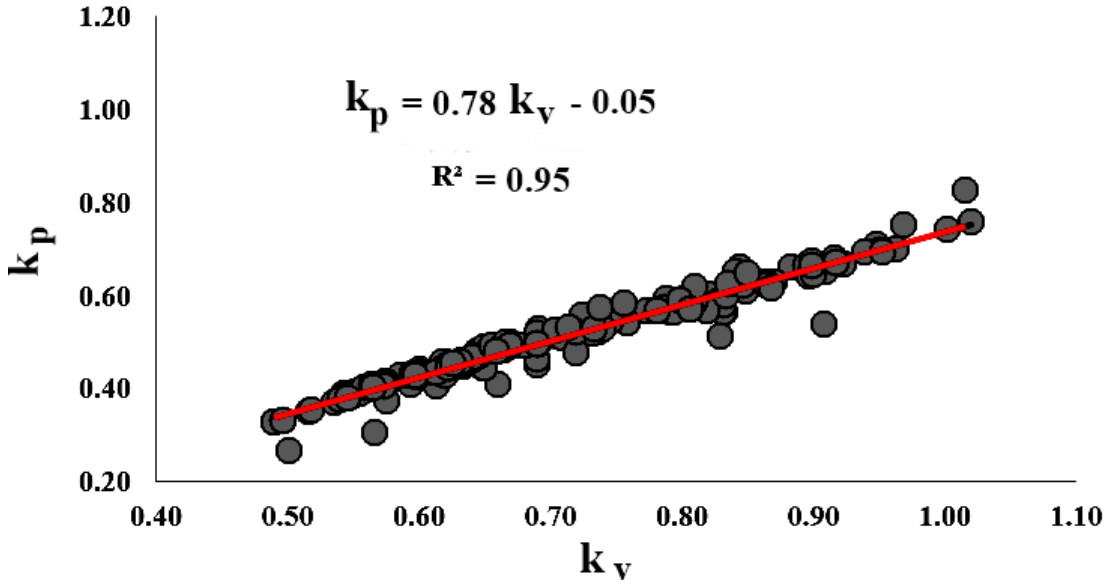

Figure 4.12: The fitted k_p model considering LIRF 2020 and IIC 2020-2021 datasets across all remote sensing sensors in this study.

When resorting the analysis to an individual model regression product per remote sensing sensor (e.g., spaceborne, proximal, airborne), similar results were obtained compared to the full regressed model combining all remote sensing datasets for LIRF and IIC 2020 and 2021 data (Figure 4.13). When comparing the regressed intercept estimation per remote sensing sensor, the values are within the range of -0.03 to -0.08. Planet CubeSat and the MSR had the same intercept value

(-0.03). Similarly, Landsat-8 and UAS had a model intercept of -0.08. Only Sentinel-2 had a different intercept value (-0.05) compared to the remaining remote sensing sensor.

All the regressed intercepts were statistically significant (p-value < 0.05), as indicated in Table 4.11. Regarding the regressed slopes, the estimated values varied from 0.76 to 0.84. Landsat-8 had the same slope as the UAS. The remaining remote sensing sensors had slopes ranging from 0.76 to 0.79. With the exception of Landsat-8, all the regressed slopes were statistically significant. Regarding the fitted R^2, all remote sensing sensors had extreme and positive R^2 values (Table 4.11), with the lowest being Planet CubeSat (R^2 = 0.93) and the highest being the MSR (R^2 = 0.99). Given that the combined calibration of the k_p model using all the remote sensing sensors has a more robust statistical analysis since the sample size is large enough to support the validation of the model ($n = 197$), its regressed coefficients should be used for when predicting k_p.

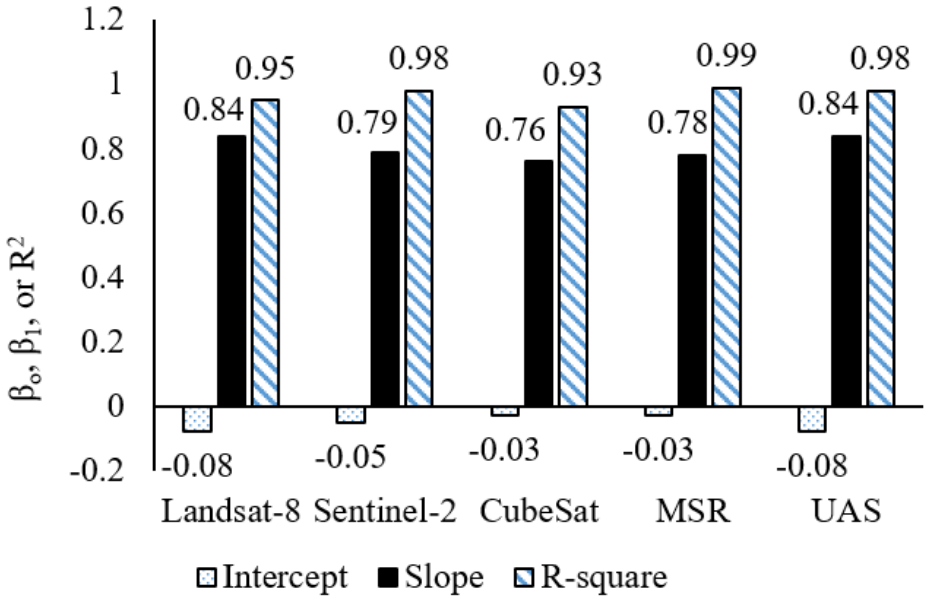

Figure 4.13: The fitted k_p model considering LIRF 2020 and IIC 2020-2021 datasets for each remote sensing sensor in this study.

Table 4.11: The summary statistics of the k_p regression model using LIRF 2020 and IIC 2020-2021 datasets per remote sensing sensors in this study.

RS sensor	n	R^2	Parameters	Estimate	95% Confidence Interval	Standard Error	Test-Statistics	p-value
Landsat-8	16	0.95	Intercept (β_o)	-0.08	[-0.17, 0.01]	0.04	-1.95	8.00e-03
			Slope (β_1)	0.84	[0.71, 0.95]	0.05	15.38	0.95
Sentinel-2	31	0.98	Intercept (β_o)	-0.05	[-0.07, -0.02]	0.01	-3.92	1.45e-03
			Slope (β_1)	0.79	[0.75, 0.83]	0.02	40.89	3.40e-27
Planet	90	0.93	Intercept (β_o)	-0.03	[-0.07, 0.01]	0.02	-2.27	0.03
			Slope (β_1)	0.76	[0.72, 0.81]	0.02	34.63	4.79e-53
MSR	39	0.99	Intercept (β_o)	-0.03	[-0.05, -0.02]	0.01	-3.74	6.16e-04
			Slope (β_1)	0.78	[0.75, 0.81]	0.01	52.66	2.12e-36
UAS	21	0.98	Intercept (β_o)	-0.08	[-0.12, -0.04]	0.02	-3.96	8.32e-04
			Slope (β_1)	0.84	[0.78, 0.90]	0.03	30.83	1.09e-17

When calculating the $d(\text{NDVI})/df_c$ term, the linear regression between the minimum and maximum NDVI and respective measured f_c values (Figure 4.14 and Table 4.12) provided the two distinct values of $d(\text{NDVI}_{min})/df_c$ and $d(\text{NDVI}_{max})/df_c$ for the linear interpolation to determine any $d(\text{NDVI})/df_c$ for any given f_c between 0 and 0.85. The respective calculated values for $d(\text{NDVI}_{min})/df_c$ and $d(\text{NDVI}_{max})/df_c$ were 0.25 ($f_c = 0$) and 0.39 ($f_c = 0.85$). These results are $d(\text{NDVI}_{min})/df_c$ less than $d(\text{NDVI}_{max})/df_c$ since the linear regression slopes for each case scenario (minimum and maximum NDVI groups) are proportional to the magnitude of NDVI values used for the regression approach.

Table 4.12: The data to determine minimum and maximum $d(\text{NDVI})/df_c$ values. Data included all remote sensing sensors in this study from LIRF 2020, IIC 2020, and 2021 datasets.

Measured f_c	f_c Value	Minimum NDVI	f_c Value	Maximum NDVI
$f_c < 0.10$	0	0.106	0.10	0.590
$0.10 < f_c \leq 0.35$	0.14	0.289	0.19	0.788
$0.35 < f_c \leq 0.45$	0.40	0.277	0.44	0.868
$0.45 < f_c \leq 0.55$	0.53	0.253	0.54	0.857
$0.55 < f_c \leq 0.65$	0.61	0.301	0.65	0.907
$0.65 < f_c \leq 0.75$	0.69	0.399	0.70	0.933
$0.75 < f_c \leq 0.85$	0.84	0.358	0.85	0.921

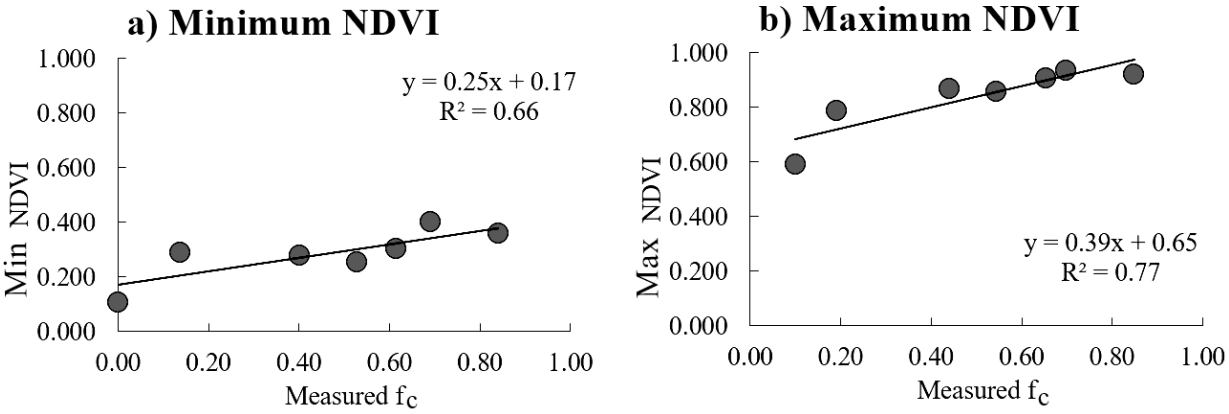

Figure 4.14: Scatter plots of the data used to determine $d(\text{NDVI}_{min})/df_c$ and $d(\text{NDVI}_{max})/df_c$.

When assessing the performance of f_c (Norman et al., 1995; Norman and Kustas, 2000) and LAI (Chávez et al., 2009) models as input for the novel k_p approach, it is evident that both models provided canopy architecture predictions that were in good agreement with observed values of their respective variables (Figure 4.15). For the case of f_c, the error was 0.02 (2%) $\pm$ 0.07 (10%), with the f_c model explaining 53% of the variability observed in the indirect measurements of f_c using the PAR sensors. Similar performance was observed from the LAI model, with an error of 0.08 m^2/m^2 (3%) $\pm$ 0.36 m^2/m^2 (11%). Both f_c and LAI models overestimated their respective

predictions of maize canopy architecture in this study. However, the overestimation was minor in magnitude (2% for f_c and 3% for LAI predictions). Since LAI is an input in the f_c model, it is clear that part of the overestimation in f_c is primarily due to the LAI overestimation.

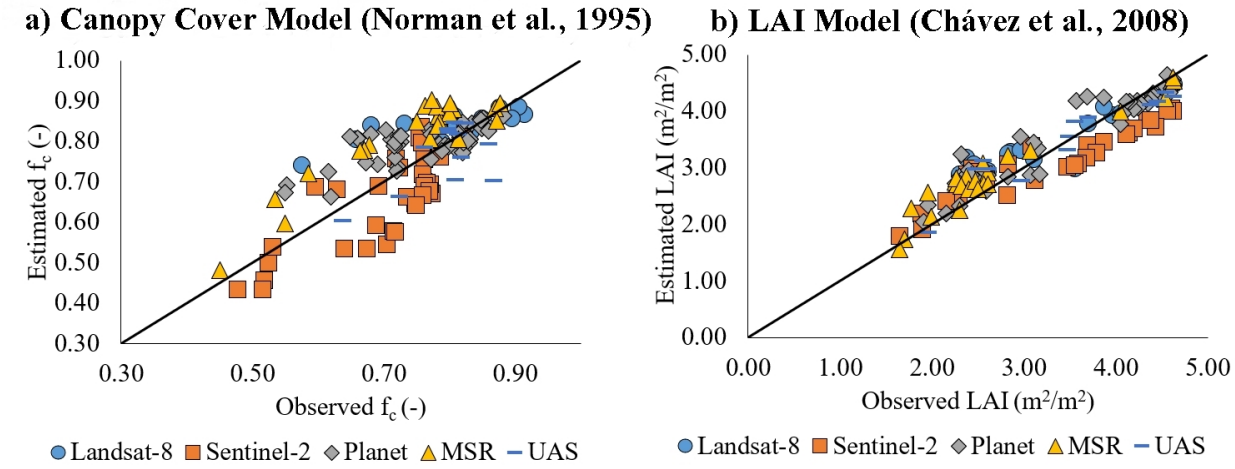

Figure 4.15: Scatter plots of observed f_c vs. estimated f_c (Figure 4.15a) and observed LAI vs. estimated LAI (Figure 4.15b) with the error analysis statistics. LIRF 2018 and 2022 datasets.

When considering the performance of each LAI and f_c (Norman et al., 1995; Norman and Kustas, 2000) model per remote sensing sensor (Tables 4.13 and 4.14), the NRMSE values for LAI prediction ranged from 9% (UAS) to 13% (Sentinel-2). There was only an underestimation of LAI when using the Sentinel-2 multispectral data as input (-4%). Clearly, the underestimation of LAI due to Sentinel-2 was not significant enough to cause an overall underestimation of LAI when combining all the remote sensing sensor data in the analysis. The most considerable overestimation of LAI was obtained from the MSR multispectral sensor (8%), which could be associated with induced systematic errors in the data collection process, given the nature of the measurements being manually done in the field. The lowest overestimation of LAI predictions was observed when the UAS data were used as input (1%). Given the fine spatial scale of the UAS multispectral imagery data ($< 0.10\ m$), the assessment of point-based conditions seemed more adequate compared to larger spatial scale remote sensing sensors in this study. The explained variability in LAI data

ranged from 84% (Landsat-8) to 93% (MSR).

The error analysis of f_c predictions (Norman et al., 1995; Norman and Kustas, 2000) across each remote sensing sensor indicated that the NRMSE ranged from 8% (UAS) to 11% (Sentinel-2), which presented the same remote sensing sensors as the lowest and highest NRMSE compared to the LAI model assessment. Regarding the underestimation or overestimation of f_c, underestimation of f_c was observed when using Sentinel-2 and UAS multispectral data as inputs to predict f_c. The underestimation of f_c from Sentinel-2 data (-6%) can be related to the underestimation of LAI when using the same remote sensing sensor (-4%) since LAI is an input to estimate f_c in this study. However, the same pattern is not observed regarding the UAS multispectral data. For the UAS, there was a slight overestimation of LAI (1%), while f_c predictions were overestimated (-3%). Given the spatial scale nature of UAS imagery ($< 0.10\ m$) and the fact that the f_c model from Norman et al. (1995) and Norman and Kustas (2000) introduce the concept of a vegetation clumping factor, it is expected that the clumping factor calculations may not completely represent the vegetated point-based conditions observed in the UAS data, which could contribute to an overestimation of f_c values.

Table 4.13: The error analysis of LAI across each of the remote sensing sensors in the study. LIRF 2018 and 2022 datasets combined.

Measured f_c	n	MBE (NMBE)	RMSE (NRMSE)	R^2
Landsat-8	16	0.20 (6%)	0.39 (12%)	0.84
Sentinel-2	34	-0.11 (-4%)	0.43 (13%)	0.88
Planet	49	0.13 (4%)	0.33 (10%)	0.91
MSR	24	0.22 (8%)	0.33 (12%)	0.93
UAS	13	0.03 (1%)	0.31 (9%)	0.89

Table 4.14: The error analysis of f_c across each of the remote sensing sensors in the study. LIRF 2018 and 2022 datasets combined.

Measured f_c	n	MBE (NMBE)	RMSE (NRMSE)	R^2
Landsat-8	16	0.04 (5%)	0.08 (10%)	0.40
Sentinel-2	34	-0.04 (-6%)	0.08 (11%)	0.64
Planet	49	0.03 (4%)	0.07 (9%)	0.49
MSR	24	0.07 (10%)	0.08 (11%)	0.84
UAS	13	-0.03 (-3%)	0.07 (8%)	0.38

Regarding the analysis of $NDVI_c$ and $NDVI_{soil}$ predictions using the novel approaches derived in this study, there were smaller errors associated with $NDVI_c$ compared to $NDVI_{soil}$ predictions (Figure 4.16). The $NDVI_c$ estimation had an error of -0.01 (-2%) $\pm$ 0.07 (9%). In comparison, the $NDVI_{soil}$ error was 0.01 (3%) $\pm$ 0.02 (17%). The larger NRMSE associated with $NDVI_{soil}$ could be due to the fact that the $NDVI_{soil}$ model uses NDVI as one input. The NDVI values often change significantly over time since plants' seasonal growth is not a linear process. However, given that the dry soil surface reflectance responses over time do not change significantly, it is evident that the predictions of $NDVI_{soil}$ would differ from the most constant values observed from NDVI of bare soil parts of the maize fields at LIRF in 2018 and 2022. Now, given that $NDVI_c$ theoretically varies more as the plants grow and increase their green foliage through time and space, it was expected that the $NDVI_c$ model would agree more with on-site values of NDVI for plants.

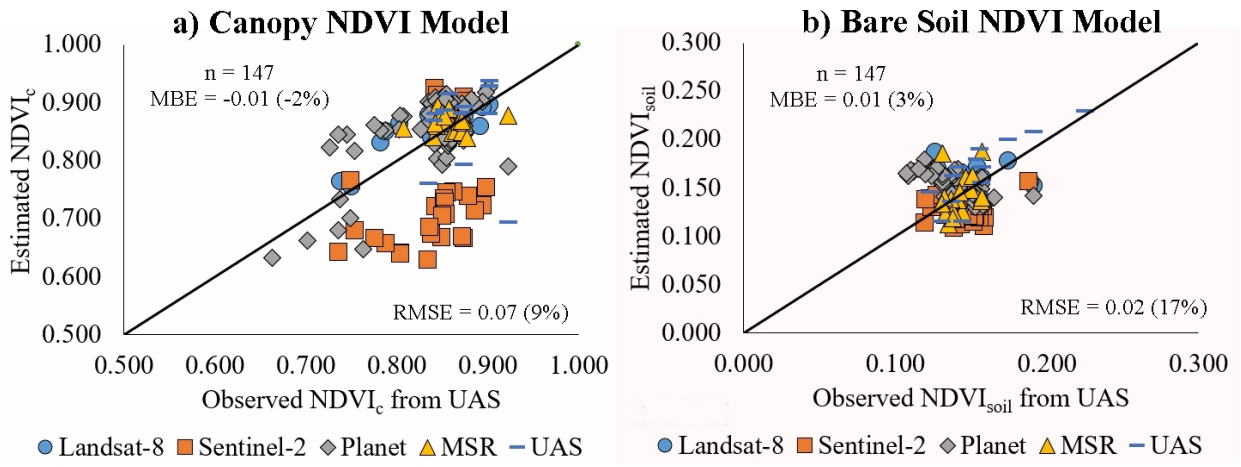

Figure 4.16: Scatter plots of observed NDVI$_c$ vs. estimated NDVI$_c$ (Figure 4.16a) and observed NDVI$_{soil}$ vs. estimated NDVI$_{soil}$ (Figure 4.16b) with the error analysis statistics. LIRF 2018 and 2022 datasets.

The SGS analysis of the k_p model indicated that NDVI is the primary variable that accounts for most of the variability in the predictions of k_p since it had the highest Sobol index compared to the other variables in the model across the remote sensing sensors (Figure 4.17). The Sobol index for NDVI varied from 0.54 (Sentinel-2) to 0.67 (Landsat-8). The other inputs (LAI, NDVI$_c$, and NDVI$_{soil}$) have lower Sobol indices (< 0.30), which indicates that those input variables have less accountability for the accuracy of k_p predictions. When evaluating the NDVI$_c$ and NDVI$_{soil}$ models, the NDVI input variable was also more relevant to explain the variability observed in partitioning NDVI values in canopy and soil composites (Table 4.15). The Sobol index for the NDVI variable ranged from 0.88 to 0.94 regarding the NDVI$_c$ model and from 0.55 to 0.64 regarding the NDVI$_{soil}$ approach.

Regardless of the NDVI composite model for canopy and bare soil, the $d(\text{NDVI})/df_c$ input variable had a negligible contribution to explaining the variance of k_p predictions (Sobol indices near zero). Since the total sum of all the Sobol indices for a given model is equal to one, it is evident that there were differences in how relevant f_c is for either NDVI$_c$ or NDVI$_{soil}$. When looking at the Sobol indices for f_c only, the NDVI$_c$ model had lower Sobol index values for f_c compared to the NDVI$_{soil}$ Sobol index values for the same input (Table 4.15). This is, the f_c input variable is

more important to explain the variability of $NDVI_{soil}$ prediction than to $NDVI_c$.

One reason to justify this research finding is to look at the apparent connection between NDVI and $NDVI_c$. For near fully grown vegetated surfaces, NDVI, and $NDVI_c$ values are alike since there is little bare soil exposure due to leaves covering most of the ground surface. Thus, most of the variability of $NDVI_c$ can be explained by NDVI values under those conditions, which leads to a small contribution to the $NDVI_c$ variance from f_c in the proposed novel $NDVI_c$ model. For the $NDVI_{soil}$ model, the predictions are associated with NDVI values during the same crop growing season, which means that the estimation of $NDVI_{soil}$ is for conditions that are also associated with plants entering the complete canopy growth stages.

In that case, NDVI values are at their maximum while the $NDVI_{soil}$ must remain nearly constant within root zone wetting periods (e.g., irrigation or rainfall events). Thus, the f_c input variable tends to be more important for explaining the variance of $NDVI_{soil}$ estimation than for $NDVI_c$ model predictions. Nonetheless, it is essential to emphasize that $NDVI_{soil}$ and $NDVI_c$ prediction variances are mainly dependent on NDVI, which was the input variable with the highest Sobol index in both NDVI composite models.

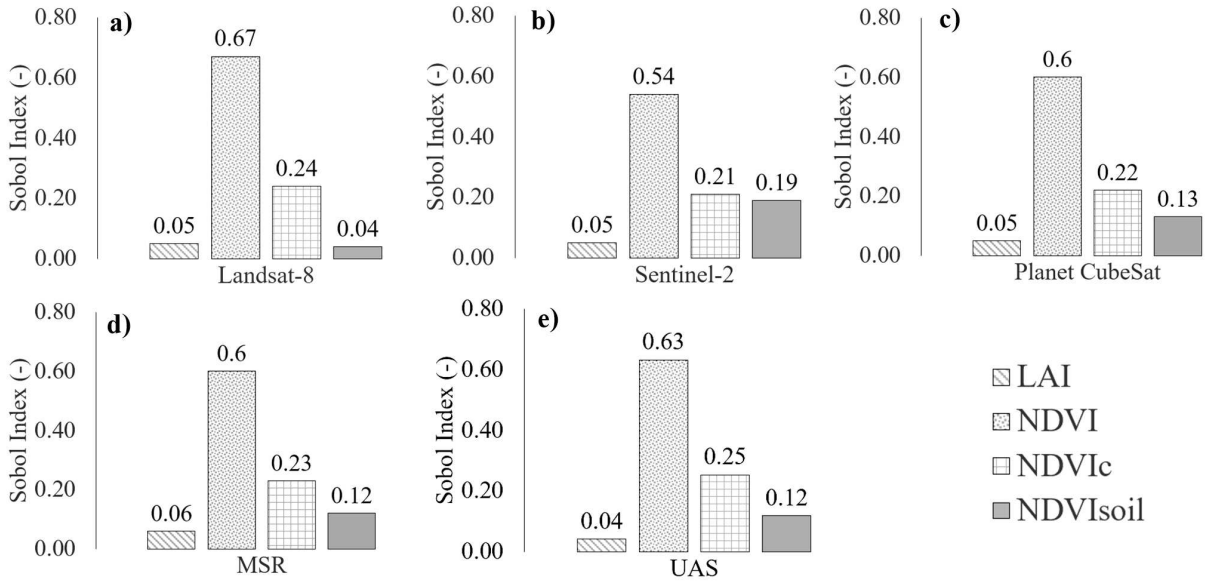

Figure 4.17: Bars plots of observed Sobol global sensitivity indices for the novel k_p model.

Table 4.15: The Sobol global sensitivity indices for the novel NDVI$_c$ and NDVI$_{soil}$ models.

Novel Model	Sensor	NDVI	f_c	$d(\text{NDVI})/df_c$
NDVI$_c$	Landsat-8	0.88	0.12	0
	Sentinel-2	0.93	0.06	0.01
	Planet	0.90	0.09	0.01
	MSR	0.91	0.09	0
	UAS	0.94	0.06	0
NDVI$_{soil}$	Landsat-8	0.55	0.40	0.04
	Sentinel-2	0.64	0.33	0.03
	Planet	0.58	0.38	0.04
	MSR	0.58	0.38	0.04
	UAS	0.60	0.36	0.04

4.5.2 The Machine-Learning Regression Cross-Calibration Results

The best machine-learning regression model for a given composite of surface reflectance (canopy or soil) and for a given remote sensing of the ETa algorithm was not the same. Considering the two TSEB and Bausch (1995) algorithms, the GPR machine-learning model seemed to be the best approach for the visible bands (soil and canopy composites) for both Landsat-8 and Planet CubeSat. For the invisible light spectrum (NIR), the best machine-learning model for adjusting the soil and canopy data was different for Landsat-8 and Planet CubeSat. For Landsat-8, SVM had the best performance in adjusting NIR soil and canopy data, while Regression Tree was the best machine-learning model for adjusting NIR (soil and canopy) for Planet CubeSat.

For the Landsat-8 sensor (Figure 4.18), the GPR model had the lowest RMSE (0.007) for the BLUE canopy surface reflectance and the highest R^2 (0.89) among the five models (Figure 4.18). Similarly, for the soil, GPR also performed the best, with the lowest RMSE (0.006) and the highest R^2 (0.79). For the GREEN spectral reflectance of the canopy, GPR again showed the best performance with the lowest RMSE (0.011) and the highest R^2 (0.83). For the soil composite of the GREEN spectral band, the GPR model had the lowest RMSE (0.009) and the highest R^2 (0.83). The GPR had the lowest RMSE (0.010) and the highest R^2 (0.93) when considering the RED spectral reflectance of the canopy and the lowest RMSE (0.011) and the highest R^2 (0.87) for the RED soil. Within the invisible light spectrum, for the NIR canopy composite, the Regression Tree had the lowest RMSE (0.022) and the highest R^2 (0.73) for the canopy composite. Similarly, for the soil component of NIR, the Regression Tree also performed better with the lowest RMSE (0.017) and the highest R^2 (0.73).

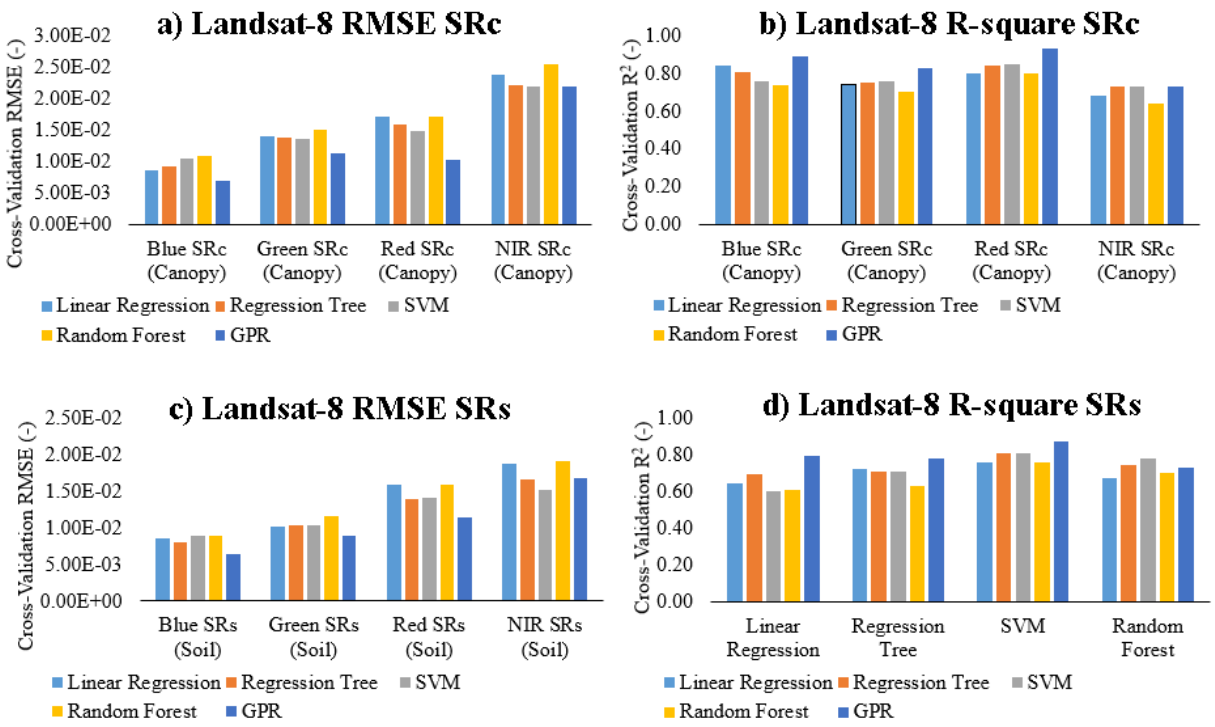

Figure 4.18: Landsat-8 cross-validation RMSE and R^2 for the machine-learning model cross-validation (k-fold method) for the two TSEB (parallel and series) and the RBCC Bausch (1995) algorithms.

Considering the Planet CubeSat sensor (Figure 4.19), the GPR model had the lowest RMSE (0.006) for the BLUE canopy surface reflectance and the highest R^2 (0.78) among the five models (Figure 4.19). Similarly, for the soil, GPR also performed the best, with the lowest RMSE (0.005) and the highest R^2 (0.76). The GREEN spectral reflectance of the canopy, GPR, again showed the best performance with the lowest RMSE (0.006) and the highest R^2 (0.82). For the soil composite of the GREEN spectral band, the GPR model had the lowest RMSE (0.006) and the highest R^2 (0.79). The GPR had the lowest RMSE (0.007) and the highest R^2 (0.92) when considering the RED spectral reflectance of the canopy and the lowest RMSE (0.006) and the highest R^2 (0.87) for the RED soil. Within the invisible light spectrum, for the NIR canopy composite, the Regression Tree had the lowest RMSE (0.021) and the highest R^2 (0.83) for the canopy composite. Similarly, for the soil component of NIR, the Regression Tree also performed better with the lowest RMSE (0.016) and the highest R^2 (0.82).

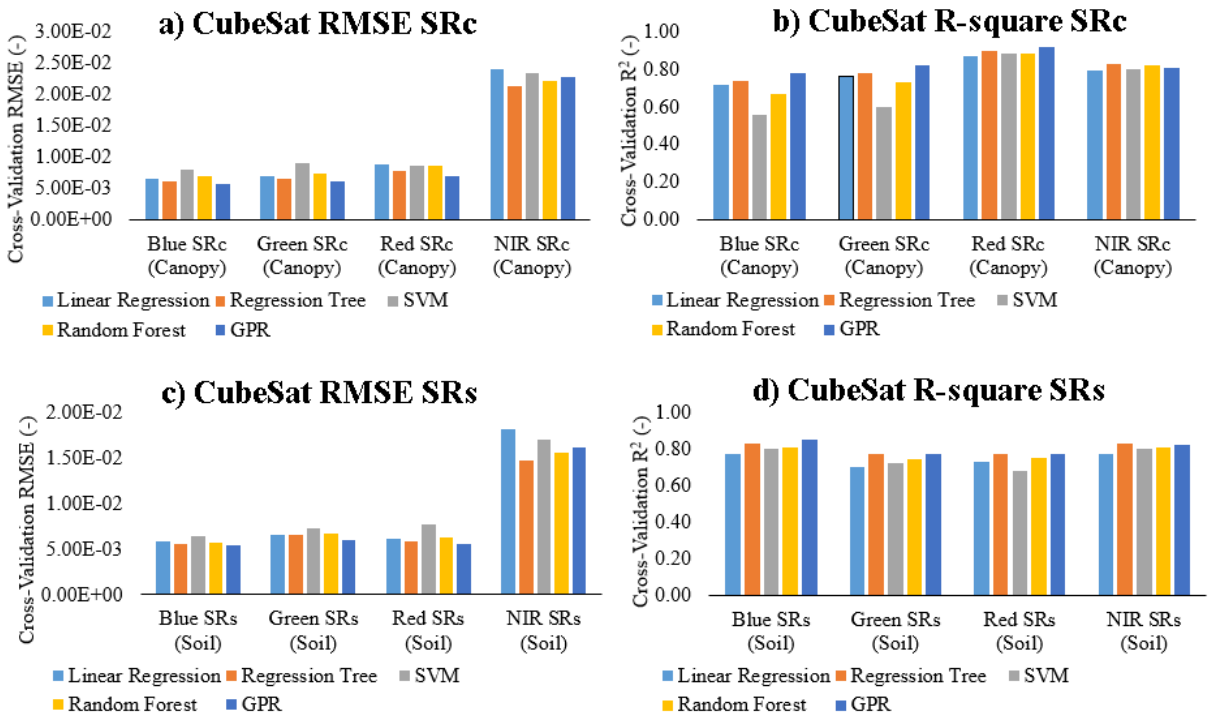

Figure 4.19: Planet CubeSat cross-validation RMSE and R^2 for the machine-learning model cross-validation (k-fold method) for the two TSEB (parallel and series) and the RBCC Bausch (1995) algorithms.

For the Sentinel-2 (Figure 4.20), For the BLUE spectral reflectance of the canopy, the Regression Tree achieved the lowest RMSE (0.004) and the highest R^2 (0.69) among the five models, indicating a better fit (Figure 4.20). For the soil, GPR performed the best, with the lowest RMSE (0.004) and the highest R^2 (0.83). For the GREEN spectral reflectance of the canopy, the Regression Tree again showed the best performance with the lowest RMSE (0.006) and the highest R^2 (0.65). Similarly, for the soil composite, the Regression Tree had the lowest RMSE (0.006) and the highest R^2 (0.77). For the RED spectral reflectance of the canopy, GPR had the lowest RMSE (0.006) and the highest R^2 (0.91), indicating the best-fitted model. For the soil, the Regression Tree performed the best with the lowest RMSE (0.006) and the highest R^2 (0.77). For the NIR spectral reflectance of the canopy and soil, the Regression Tree had the lowest RMSE (0.018) and the highest R^2 (0.89) for the canopy and the lowest RMSE (0.016) and the highest R^2 (0.83) for the soil terms.

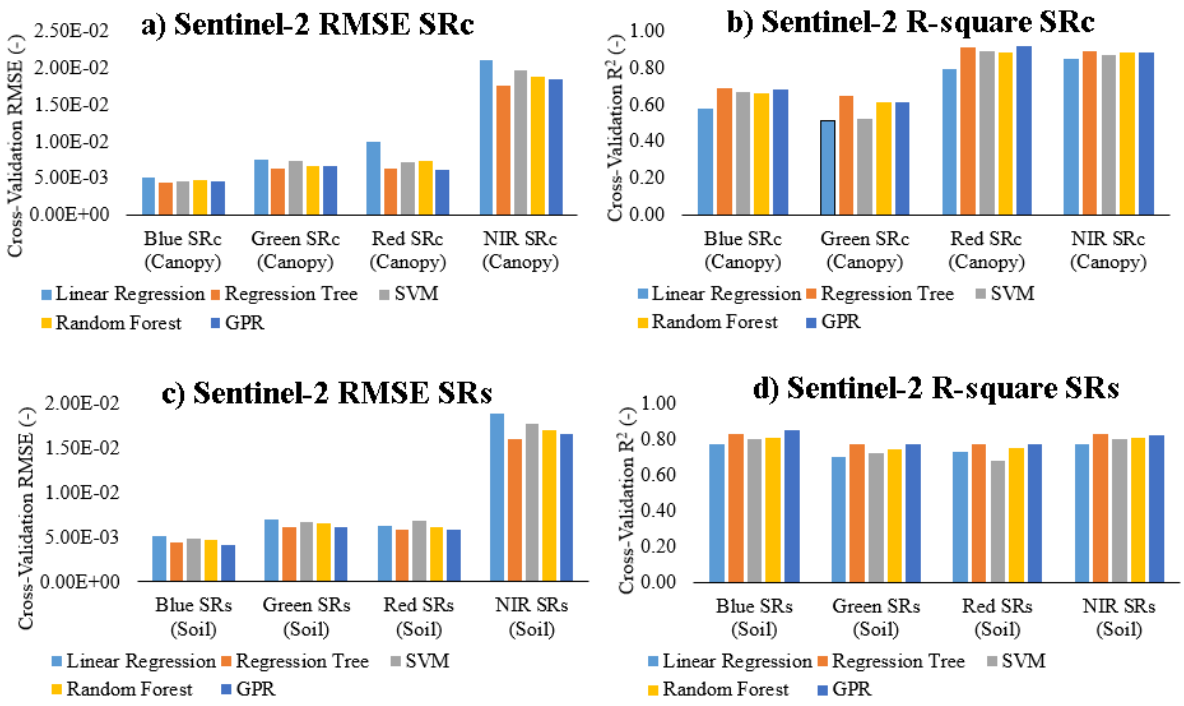

Figure 4.20: Sentinel-2 cross-validation RMSE and R^2 for the machine-learning model cross-validation (k-fold method) for the two TSEB (parallel and series) and the RBCC Bausch (1995) algorithms.

For the UAS sensor (Figure 4.21), the Linear Regression model consistently demonstrated weak performance across all spectral bands and surfaces. The best machine-learning models varied for each surface reflectance band and composite type (soil and canopy), with GPR and Regression Tree being the most common best models for that airborne sensor. For the BLUE spectral reflectance of the canopy, the GPR had the lowest RMSE (0.004) and the highest R^2 (0.75). This result was different for the respective soil composite, in which the Regression Tree outperformed the other models by having the lowest RMSE (0.006) and the highest R^2 (0.62).

For the GREEN spectral reflectance of the canopy and soil, the Regression Tree showed the best performance with the lowest RMSE (0.006) and the highest R^2 (0.67) for the canopy and RMSE (0.008) and R^2 (0.57) for the soil composite. For the RED spectral reflectance of the canopy, the GPR had the lowest RMSE (0.007) and the highest R^2 (0.84). Similarly, for the soil, the GPR also performed the best, with the lowest RMSE (0.005) and the highest R^2 (0.78). For

the NIR spectral reflectance of the canopy, the Regression Tree had the lowest RMSE (0.024) and the highest R^2 (0.78) compared to the remaining machine-learning model evaluated. Similarly, the GPR model outperformed the other machine-learning models for the soil composite by having the lowest RMSE (0.016) and the highest R^2 (0.76).

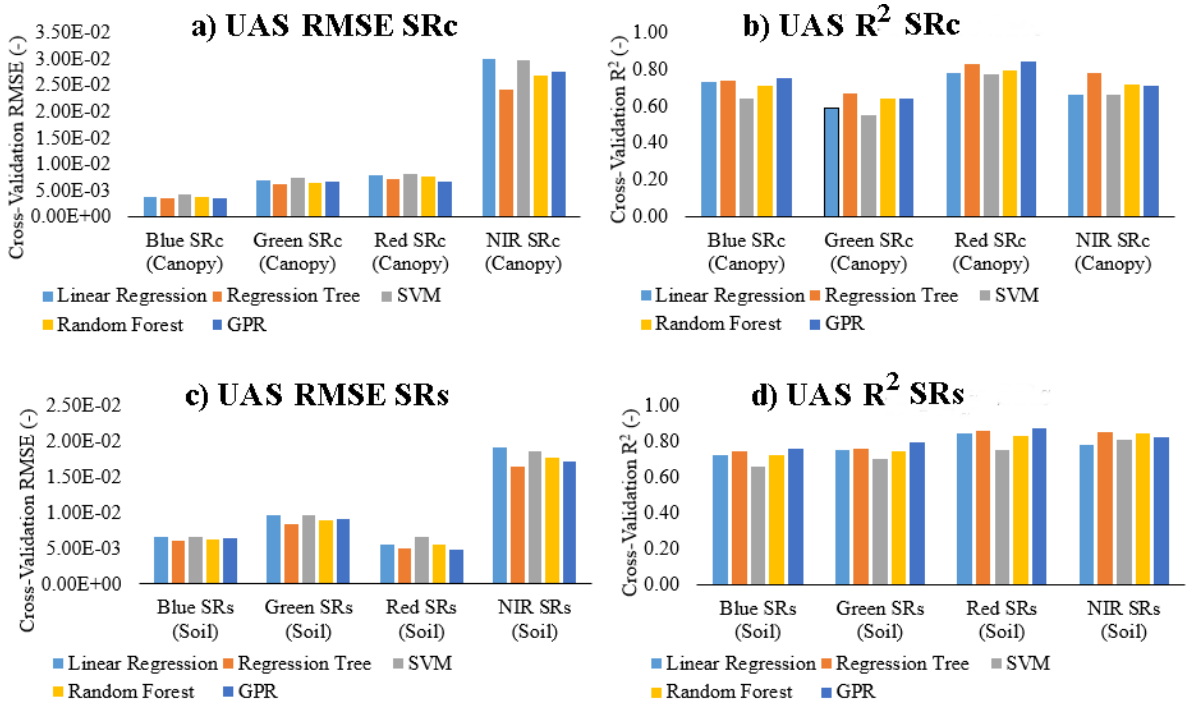

Figure 4.21: The UAS cross-validation RMSE and R^2 for the machine-learning model cross-validation (k-fold method) for the two TSEB (parallel and series) and the RBCC Bausch (1995) algorithms.

For the RBCC models from Trout and DeJonge (2018) and Neale et al. (1990), considering the Sentinel-2 surface reflectance data as the optimal input for those two algorithms, the best machine-learning models also varied depending on the surface reflectance band and respective composite (soil and canopy). For the Landsat-8 (Figure 4.22) and the BLUE SRc, Linear Regression showed the lowest RMSE (0.004) and highest R^2 (0.66), indicating a better fit compared to other models evaluated. Similar results were obtained for BLUE SRs since the Linear Regression model also displayed the lowest RMSE (0.010) but with a lower R^2 (0.47). However, despite differences in R^2 values, the RMSE values for both canopy and soil reflectance are within relatively close range

across models.

Similar trends were observed regarding the GREEN soil and canopy model calibration. For GREEN SRc, all tested ML models showed equivalent goodness-of-fit, with R^2 values ranging from 0.61 to 0.63. However, GREEN SRs showed more variability in goodness-of-fit among models, with the SVM model having the highest R^2 (0.73) and lowest RMSE (0.010). Considering the Red surface reflectance band, The Linear Regression model provided a better fit for both canopy and soil reflectance, with lower RMSE and higher R^2 compared to other models. For RED SRs, all models exhibit relatively high R^2 values, indicating strong goodness-of-fit. In the NIR spectral range, Linear Regression consistently showed the best fit across both canopy and soil reflectance data. Overall, the Linear Regression model outperformed other ML models across different spectral bands and reflectance types.

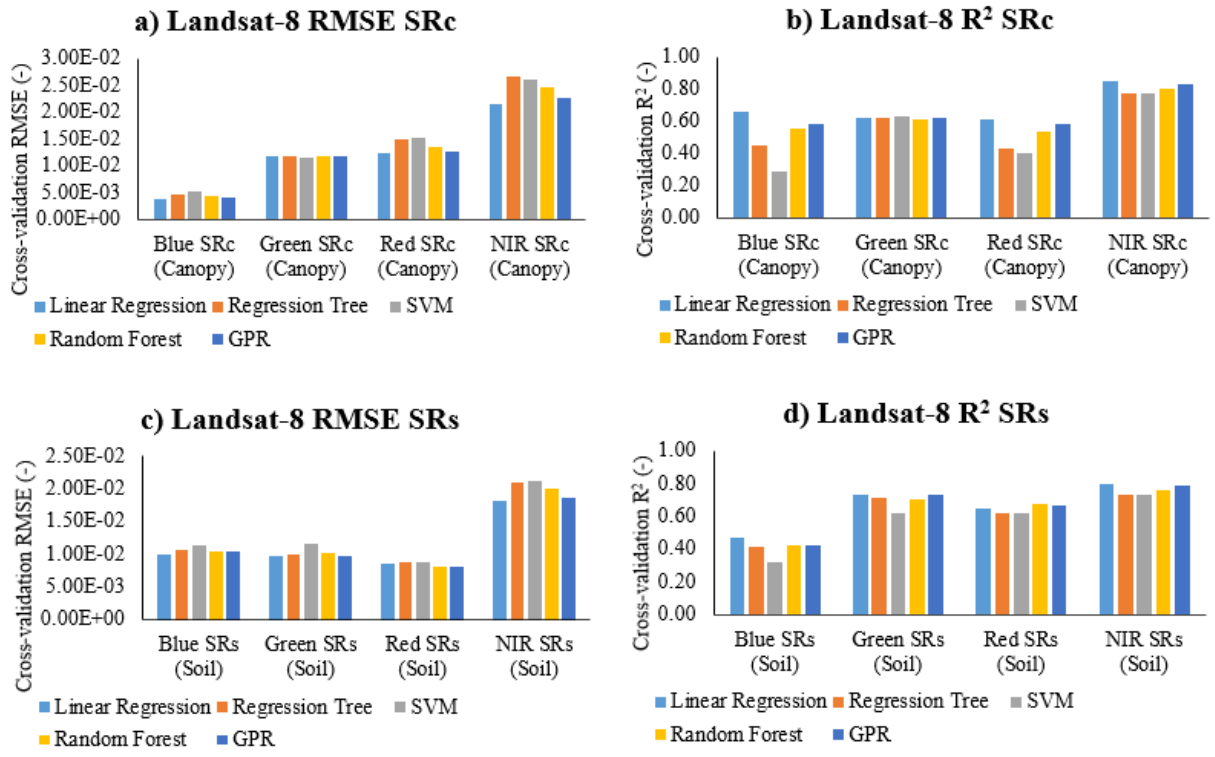

Figure 4.22: The Landsat-8 cross-validation RMSE and R^2 for the machine-learning model cross-validation (k-fold method) for the RBCC algorithms from Neale et al. (1990) and Trout and DeJonge (2018).

For the Planet CubeSat (Figure 4.23) and the BLUE SRc, the GPR model showed the lowest RMSE (0.009) and highest R^2 (0.69). However, for the BLUE SRs, the Linear Regression model displayed the lowest RMSE (0.010) but with a similar R^2 (0.70) compared to the other ML models. Similar trends were observed regarding the GREEN soil and canopy model calibration. For GREEN SRc, all tested ML models showed a varying range of goodness-of-fit results, with R^2 values ranging from 0.63 to 0.75.

However, GREEN SRs showed more variability in goodness-of-fit among models, with the Linear Regression model having the highest R^2 across the ML models evaluated ($R^2 = 0.75$). Considering the RED surface reflectance band, The Linear Regression model provided a better fit for the canopy, and the GPR model was the best fit for the RED SRs. In the NIR spectral range, the GPR consistently showed the best fit across both canopy and soil reflectance data, with RMSE for canopy and soil equal to 0.022 and 0.018, respectively. Overall, the Linear Regression and GPR models outperformed other ML models across different spectral bands and reflectance types.

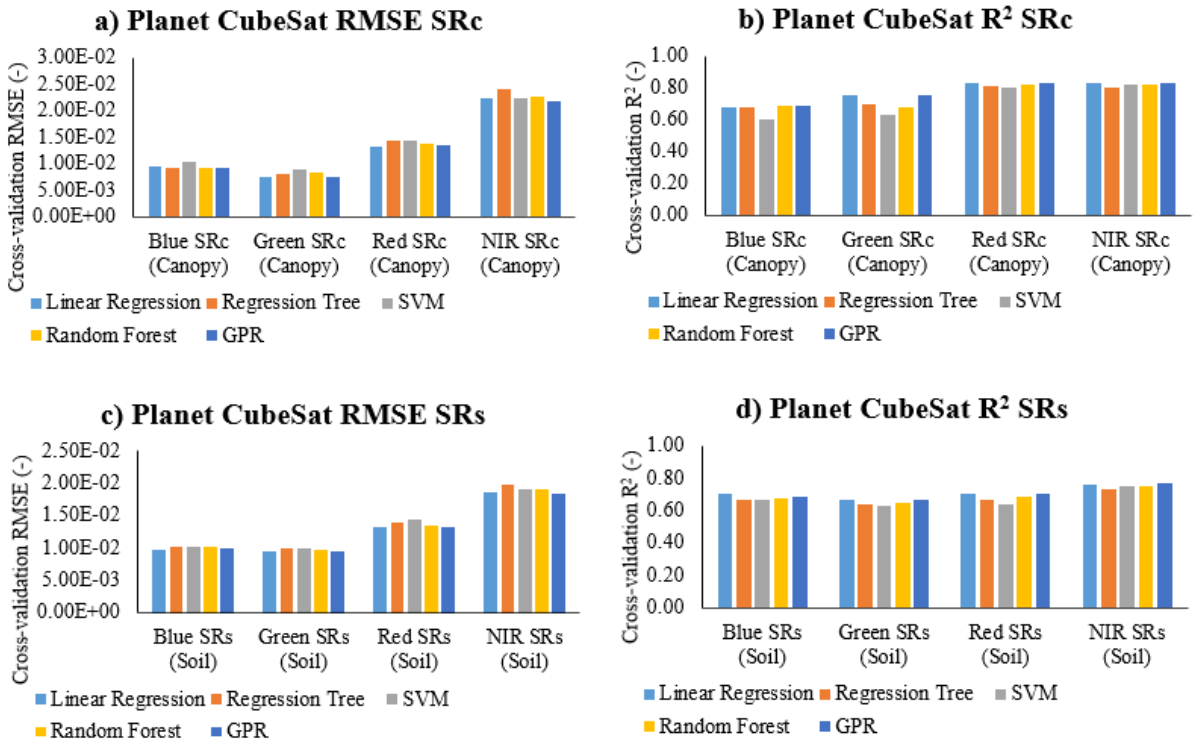

Figure 4.23: The Planet CubeSat cross-validation RMSE and R^2 for the machine-learning model cross-validation (k-fold method) for the RBCC algorithms from Neale et al. (1990) and Trout and DeJonge (2018).

For the MSR (Figure 4.24) and the BLUE SRc, the Linear Regression model showed the lowest RMSE (0.009) and highest R^2 (0.59) among the models evaluated. However, all ML models had low R^2, which varied from 0.46 to 0.58. For the BLUE SRs, similarly to BLUE SRc, the Linear Regression model displayed the lowest RMSE (0.010) but with a higher R^2 (0.76) compared to the other ML models. Despite the SVM model ($R^2 = 0.58$), all the other ML-calibrated models had R^2 results with similar values (0.70 to 0.76). For the GREEN soil and canopy model calibration, the GPR model was the best-calibrated fit since it had RMSE 0.007 and 0.009, respectively.

Considering the RED surface reflectance band, the Linear Regression model provided a better fit for the canopy and soil reflectance. The respective RMSE were 0.012 and 0.007. In the NIR spectral range, the GPR showed the best fit across for the NIR SRc, and the Linear Regression

was the best ML model for the NIR SRs, with RMSE equal to 0.019 and 0.016, respectively. The R^2 values for all the ML models evaluated regarding the NIR SRc ranged from 0.80 to 0.85. The Linear Regression and GPR models had the same R^2 (0.85) but slightly different RMSE (0.019 compared to 0.019, respectively). Overall, the Linear Regression and GPR models outperformed other ML models across different spectral bands and reflectance types.

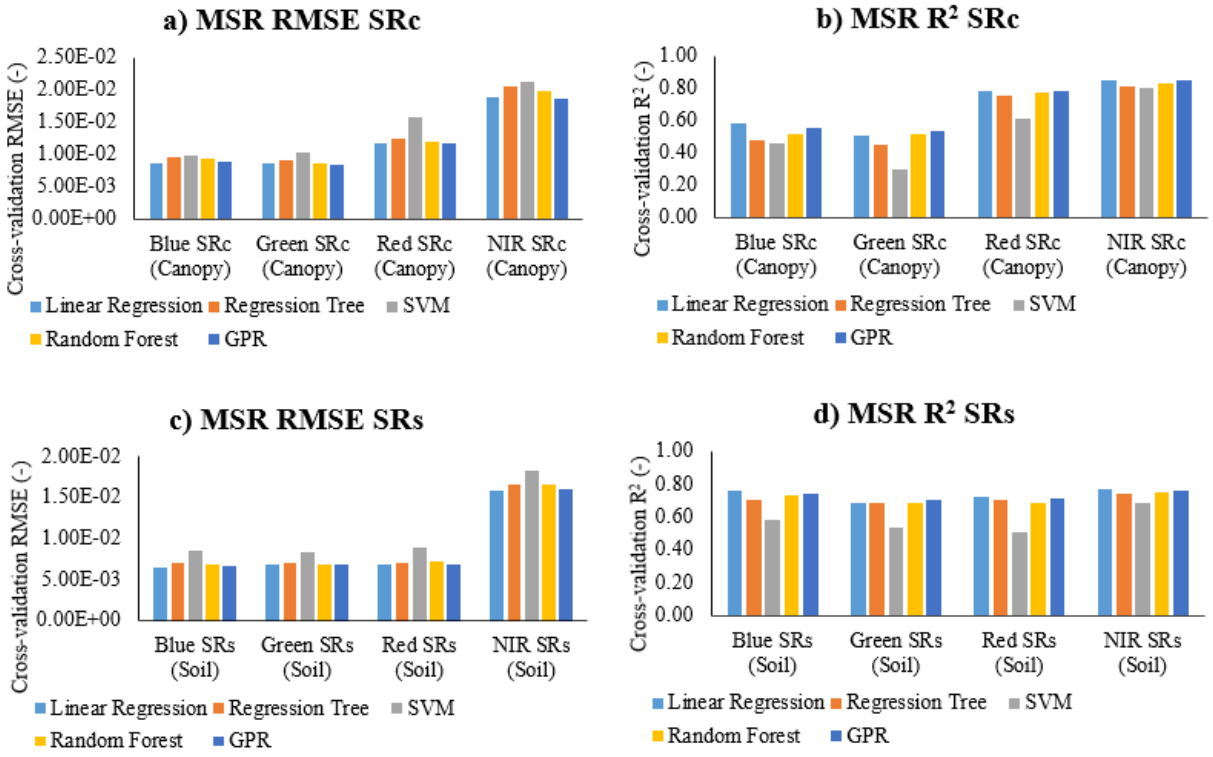

Figure 4.24: The MSR cross-validation RMSE and R^2 for the machine-learning model cross-validation (k-fold method) for the RBCC algorithms from Neale et al. (1990) and Trout and DeJonge (2018).

For the UAS (Figure 4.25) and the BLUE surface reflectance band, the GPR model showed the lowest RMSE and highest R^2 among the models evaluated for both the soil and canopy composites. The RMSE values for BLUE SRc and BLUE SRs were 0.017 and 0.012, respectively. There was large variability in R^2 values for both soil and canopy composites of the BLUE spectral range. Considering BLUE SRc, the R^2 ranged from 0.23 (Regression Tree) to 0.74 (GPR). For the BLUE SRs, the R^2 values were from 0.07 (SVM) to 0.78 (GPR). Despite the SVM model ($R^2 = 0.58$), all

the other ML-calibrated models had R^2 results with similar values (0.70 to 0.76). For the GREEN soil and canopy model calibration, the SVM model was the best-calibrated fit since it had RMSE 0.009 for both variables.

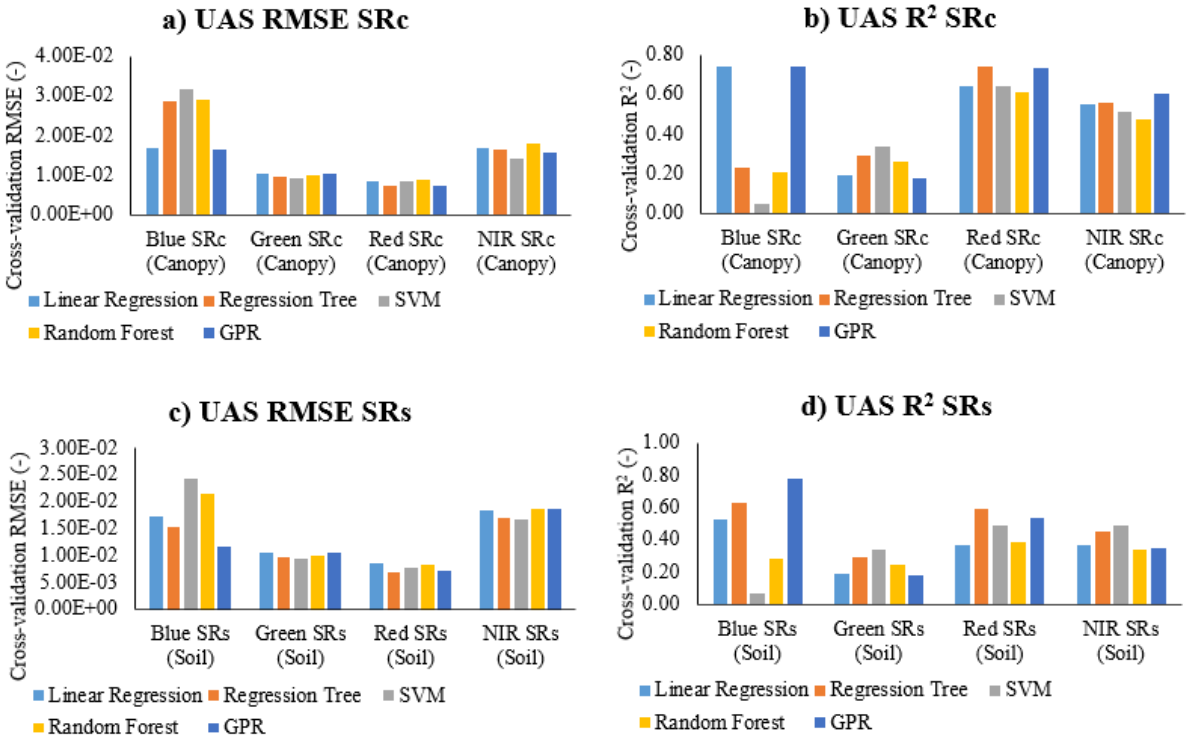

Figure 4.25: The UAS cross-validation RMSE and R^2 for the machine-learning model cross-validation (k-fold method) for the RBCC algorithms from Neale et al. (1990) and Trout and DeJonge (2018).

Considering the RED surface reflectance band, the Regression Tree model provided a better fit for the canopy and soil reflectance. The respective RMSE were 0.007 and 0.007. In the NIR spectral range, the GPR showed the best fit across for the NIR SRc, and the SVM was the best ML model for the NIR SRs, with RMSE equal to 0.016 and 0.017, respectively. The R^2 values for all the ML models evaluated regarding the NIR SRc ranged from 0.47 to 0.60.

For the OSEB algorithm from Costa-Filho et al. (2021), considering the Planet CubeSat surface reflectance data as the optimal input for predicting maize hourly ETa, the best machine-learning models also varied depending on the surface reflectance band and respective composite (soil and

canopy). Regarding the Landsat-8 data (Figure 4.26), for the BLUE surface reflectance band, the GPR model showed the lowest RMSE and highest R^2 among the models evaluated for BLUE SRc and the Regression Tree was the best fit for the BLUE SRs. The RMSE values for BLUE SRc and BLUE SRs were 0.005 and 0.006, respectively.

There was considerable variability in R^2 values for the canopy composite compared to the BLUE soil variable. Considering BLUE SRc, the R^2 ranged from 0.62 (SVM) to 0.83 (GPR). For the BLUE SRs, the R^2 values were from 0.74 (SVM) to 0.78 (Regression Tree). Despite the SVM model ($R^2 = 0.62$), all the other ML-calibrated models had R^2 results with similar values (0.70 to 0.76) for the BLUE SRc variable. For the GREEN soil and canopy model calibration, the GPR model was the best-calibrated fit since it had RMSE equal to 0.005 and 0.005 for the GREEN SRc and GREEN SRs variables, respectively. The R^2 values for both soil and canopy composites of the GREEN surface reflectance band were greater than 0.70, which is an overall indicator that the ML models evaluated had a satisfactory calibration.

Considering the RED surface reflectance band, the Regression Tree model provided a better fit for the RED soil reflectance, and the GPR model was the best option for adjusting the Landsat-8 data. The respective RMSE values were 0.006 and 0.006. In the NIR spectral range, the Regression Tree was the best ML model for the NIR SRs and NIR SRc, with RMSE equal to 0.011 and 0.015, respectively. The R^2 values for all the ML models evaluated were greater than 0.85, which indicated a strong fit across the ML-assessed models.

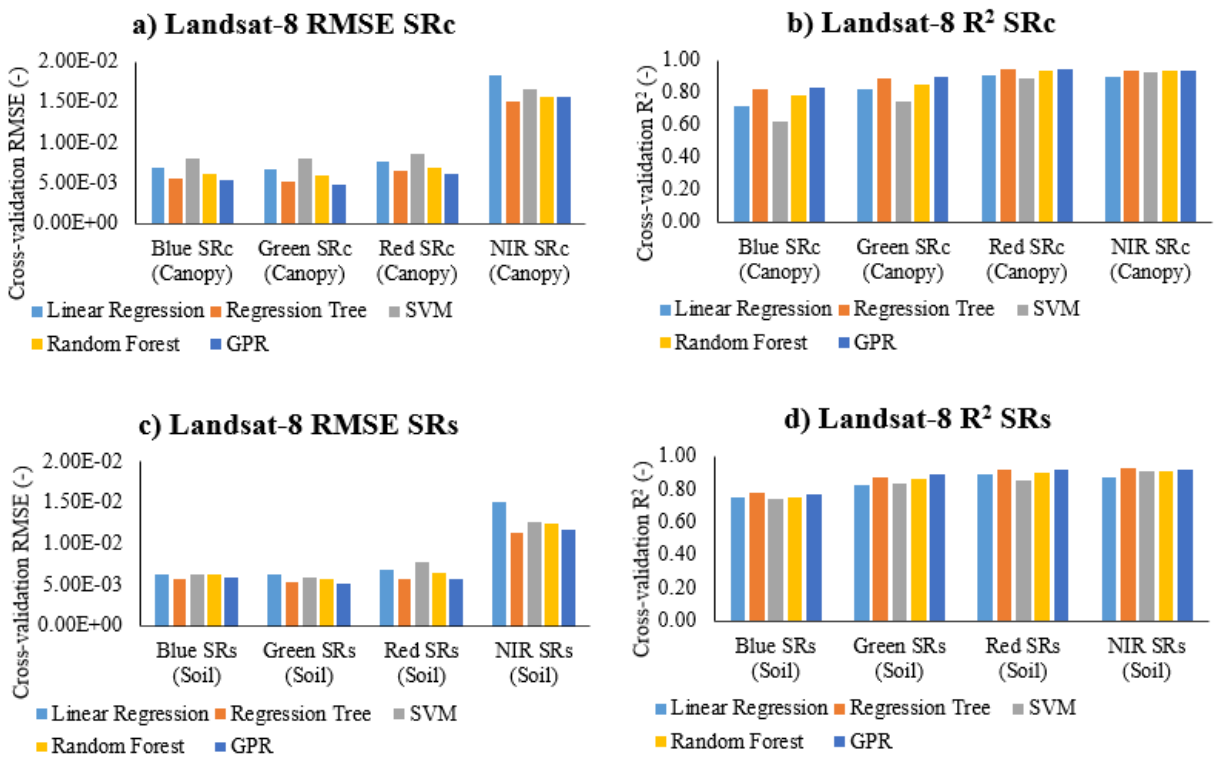

Figure 4.26: The Landsat-8 cross-validation RMSE and R^2 for the machine-learning model cross-validation (k-fold method) for the OSEB algorithm from Costa-Filho et al. (2021).

Regarding the Sentinel-2 data (Figure 4.27), for the BLUE surface reflectance band, the Regression model showed the lowest RMSE and highest R^2 among the models evaluated for BLUE SRc and BLUE SRs data. The RMSE values for BLUE SRc and BLUE SRs were 0.005 and 0.006, respectively. For the GREEN soil and canopy model calibration, the GPR and Regression Tree model was the best-calibrated fit since they had RMSE equal to 0.005 and 0.007 for the GREEN SRc and GREEN SRs variables, respectively. The R^2 values for both soil and canopy composites of the GREEN surface reflectance band were greater than 0.70, which is an overall indicator that the ML models evaluated had a satisfactory calibration.

Considering the RED surface reflectance band, the Regression Tree model provided a better fit for the RED soil and canopy reflectance data. The respective RMSE values were 0.007 and 0.008, with R^2 value for the RED SRc greater than RED SRs (0.87 > 0.79). In the NIR spectral

range, similarly to the RED surface reflectance data, the Regression Tree was the best ML model for the NIR SRs and NIR SRc, with RMSE equal to 0.018 and 0.022, respectively. The R^2 values for all the ML models evaluated were greater than 0.75, which indicated a strong fit across the ML-assessed models.

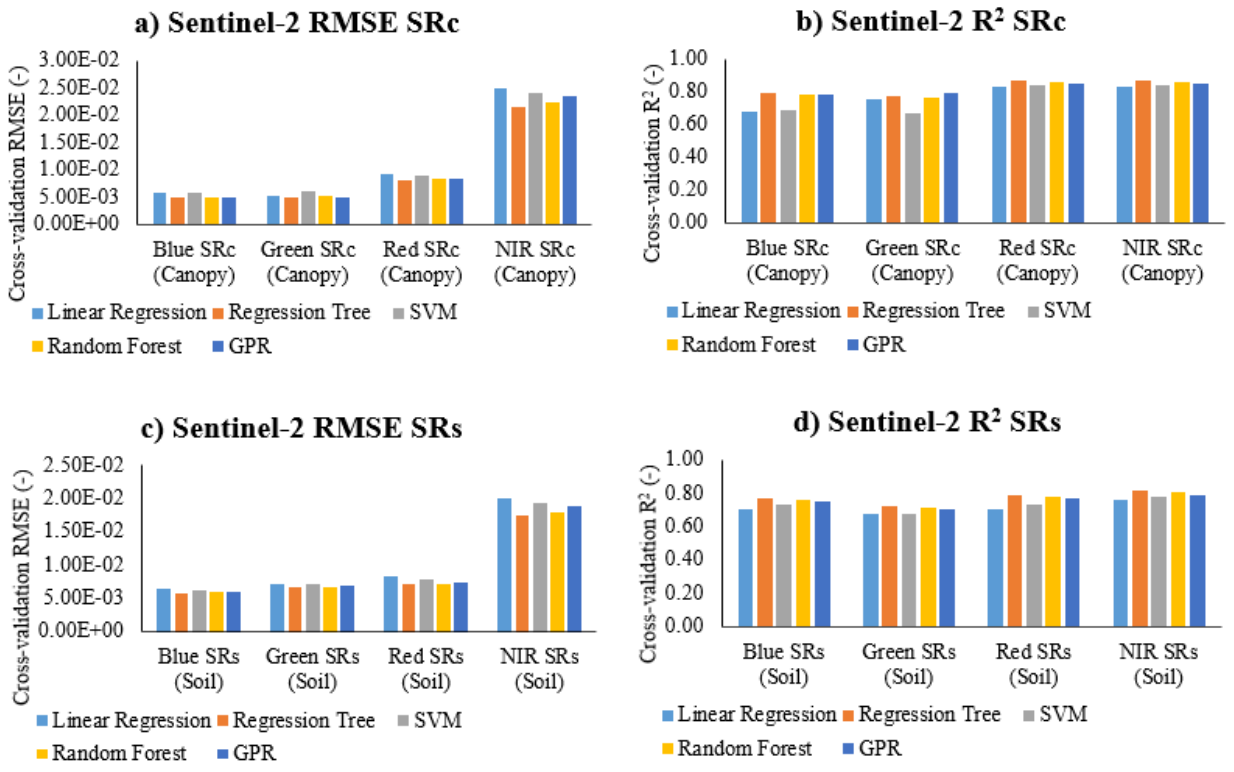

Figure 4.27: The Sentinel-2 cross-validation RMSE and R^2 for the machine-learning model cross-validation (k-fold method) for the OSEB algorithm from Costa-Filho et al. (2021).

The GPR and Regression Tree ML models were the best-performing models, particularly for visible spectral bands, where GPR consistently showed lower RMSE and higher R^2 throughout the data analysis. However, for NIR reflectance, the best model varied depending on the sensor and the specific reflectance data (soil or canopy), with Regression Tree often outperforming others. The variations in ML model performance could be related to differences in RS sensor characteristics, spectral data type, and local field conditions when the data from each RS sensor were collected. Models generally failed to maintain high accuracy across all local environmental conditions due

to these variations, which created an added challenge for having a single ML model as the best choice across the different RS sensors and ETa algorithms evaluated. Thus, the best ML regression models depended on the specific characteristics of the dataset and the RS sensor used.

4.6 Adjusted Surface Reflectance Data: Crop ETa Prediction Assessment

Results indicated that the adjusted RS data improved the accuracy of both hourly and daily maize ETa values. At the LIRF site (2017 and 2022 datasets combined), regarding the remote sensing crop coefficient models for daily maize ETa, the Trout and DeJonge (2018) model had better-improved performance when adjusted data from Planet CubeSat were used. The errors in daily maize ETa from the original and adjusted Planet CubeSat data went from 0.59 (13%) $\pm$ 0.97 (21%) mm/d to 0.36 (8%) $\pm$ 0.75 (16%) m/d.

For the Bausch (1995) remote sensing crop coefficient model for daily maize ETa, the remote sensing sensor that had better performance after the use of the remote sensing calibration functions was the UAS since the errors were reduced from -0.42 (-11%) $\pm$ 0.76 (20%) mm/d to -0.21 (-5%) $\pm$ 0.41 (11%) mm/d. For the Neale et al. (1990) model for daily maize ETa, the UAS was the remote sensing sensor that showed more improvements in predicting daily maize ETa after implementing the calibration protocol. The improved accuracy of Neale et al. (1990) daily ETa estimation using UAS data was 0.32 (8%) $\pm$ 0.40 (10%) mm/d.

Regarding the OSEB, TSEBpar, and TSEBser algorithm predictions of hourly ETa using LIRF data, the remote sensing products that had more improvements when serving as input data to predict maize ETa varied among the three surface energy balance algorithms. For OSEB, the UAS remote sensing sensor improved best when comparing hourly ETa predictions before and after

surface reflectance data adjustments. The normalized RMSE went from 0.11 (19%) mm/h (with original UAS remote sensing data) to 0.07 (13%) mm/h (after the novel calibration protocol adjusted the UAS remote sensing original data).

For the UAS, there was a decrease in overestimation of hourly maize ETa after the use of the calibration protocol since the normalized MBE decreased from 0.03 (6%) mm/h overestimation to a -0.01 (-1%) mm/h slight underestimation of hourly maize ETa. For the TSEBpar, the Landsat-8/9 remote sensing sensor with its original surface temperature imagery had the best improvements when the calibration protocol for remote sensing data was used. The normalized RMSE went from 0.19 (34%) mm/h to 0.11 (20%) mm/h. A slight decrease in underestimation was observed since the normalized MBE went from -0.04 (-7%) mm/h to -0.03 (-6%) mm/h. Regarding the TSEBser, the adjusted UAS remote sensing sensor data provided the greatest improvements in hourly maize ETa estimation since the normalized RMSE went from 0.10 (18%) mm/h to 0.05 (9%) mm/h. Underestimation of hourly maize ETa prediction was not observed when the adjusted UAS remote sensing data was used with the TSEBser since the normalized MBE changed from -0.04 (-8%) mm/h to -0.0001 (-0.03%) mm/h.

At the AVRC site for the maize field data in 2020, regarding the remote sensing crop coefficient models for daily maize ETa, the Trout and DeJonge (2018) algorithm performed better when adjusted data from MSR were used. The errors in daily maize ETa from the original and adjusted MSR data went from -1.45 (-16%) $\pm$ 1.58 (17%) mm/d to -1.25 (-14%) $\pm$ 1.36 (15%) mm/d. For the Bausch (1995) remote sensing crop coefficient model for daily maize ETa, the remote sensing sensor that had better performance after the use of the remote sensing calibration functions was the Landsat-8 since the errors were reduced from -1.84 (-28%) $\pm$ 2.61 (39%) mm/d to -1.14 (-17%) $\pm$ 1.79 (27%) mm/d. For the Neale et al. (1990) model for daily maize ETa, similar to Trout and DeJonge (2018) model performance, the MSR was the remote sensing sensor that showed more improvements in predicting daily maize ETa after implementing the calibration protocol. The im-

proved accuracy of Neale et al. (1990) daily ETa estimation using ground-based MSR data was -0.11 (-1%) $\pm$ 0.47 (5%) mm/d.

For OSEB, regarding the maize field at the AVRC, the Sentinel-2 remote sensing sensor had the best improvements when comparing daily maize ETa predictions before and after surface reflectance data adjustments. The normalized RMSE went from 1.66 (24%) mm/d (with original Sentinel-2 data) to 1.19 (17%) mm/d (after the novel calibration protocol adjusted Sentinel-2 original data). There was a decrease in underestimation of daily maize ETa after using the calibration protocol since the normalized MBE decreased from -1.37 (-20%) mm/d to -0.93 (-13%) mm/d of maize ETa.

For the TSEBpar, the Planet CubeSat remote sensing sensor had the best improvements when the calibration protocol for remote sensing data was used. The normalized RMSE went from 1.45 (23%) mm/d to 0.77 (13%) mm/d, a 47% improvement in predicted daily maize ETa accuracy. A slight decrease in underestimation was observed since the normalized MBE went from -0.23 (-4%) mm/d to -0.17 (-3%) mm/d. Regarding the TSEBser, the adjusted Landsat-8 remote sensing sensor data, with local surface temperature data from infrared thermometry, provided the greatest improvements in hourly maize ETa estimation since the normalized RMSE went from 1.68 (32%) mm/d to 1.30 (25%) mm/d, almost a 23% error reduction. However, there was a slight increase in underestimation of daily maize ETa prediction since the normalized MBE changed from -0.66 (-13%) mm/d to -0.88 (-17%) mm/d.

4.7 Discussion of the Study's Main Findings

4.7.1 Potential Field Heterogeneity Conditions

The developed calibration protocol for improving the quality of RS data considered maize fields under surface homogeneous conditions for most of the data collection years across the research sites investigated. Thus, when field heterogeneity is significant, such as variations in irrigation efficiency, soil texture, and vegetation types (e.g., maize fields with cover crops, different crop types at the edges of cropland fields, etc.), the calibration protocol application must be used with caution. That is because on-site field variability can significantly influence the effectiveness of RS techniques for estimating crop ETa.

Surface heterogeneity adds more uncertainty to the calibration of surface reflectance data to improve image quality and subsequent data analysis. For instance, varied vegetation densities due to a mixture of row and cover crops within a given RS pixel image may result in variable surface albedo, plant moisture content, and surface heat exchange patterns with the surrounding atmosphere, which can affect the spectral signatures captured by RS sensors. If the goal is to predict row crop ETa, the mixed pixel spectral response (e.g., soil, row crop, cover crop) may introduce extra uncertainty in vegetation indices (e.g., NDVI, SAVI, f_c, LAI).

The prospective use of ML algorithms such as Regression Tree and GPR to adjust RS data shows potential in managing field heterogeneity since these ML models can learn complex patterns from the data associated with field heterogeneous conditions, which could potentially overcome the limitations of the current study if new training data could be incorporated more frequently throughout a given crop growing season.

4.7.2 Transferability of k_p Spatial Model

The range of LAI for maize in this study was from 1.5 to 3.5 m^2/m^2 across all research sites investigated from 2017 to 2022. Thus, since the novel spatial k_p model was calibrated with local maize data in Colorado, with LAI values within the range provided, the transferability of the k_p approach to other crops or structural conditions would depend significantly on how the differences in canopy structure, leaf geometry, and surface reflectance properties are similar to the data used for calibrating the proposed k_p model.

Crops with denser or more clumped leaves at maximum canopy growth (e.g., wheat, rice, soybeans) can exhibit different light interaction dynamics compared to maize since the light interception by the canopy is a direct function of, among many parameters, the shape of the vegetation architecture. Thus, using the proposed k_p model for crops that have different leaf structures would require some parameterization adjustments to ensure the incorporation of crop-specific calibration data. Nonetheless, since the study considered maize crop types that were from different varieties, the k_p model could be used for maize in regions where the local climate is similar to semi-arid, such as Colorado, USA.

Moreover, the accuracy and applicability of the k_p model to different crops would also depend on the availability and quality of RS data across different spectral bands, as the sensitivity to variations in LAI predictions from different models might differ depending on RS sensor characteristics and the spectral reflectance properties of different crops' leaves and canopies. The study used the f_c model from Norman et al. (1995) and the LAI non-linear model from Chávez et al. (2008) to characterize the maize canopy architecture. The use of f_c and LAI, which are different from the ones used in this study, may also contribute to either improving or worsening the accuracy of k_p predictions when considering the proposed spatial novel approach.

Regarding the evaluation of NDVI products related to the novel k_p model, denser and healthier vegetation have high NDVI values, which might correspond to higher ETa rates due to increased transpiration when there are no water stress conditions. The variability in NDVI readings across different RS sensors could be associated with differences in sensor surface reflectance data calibration, spatial resolution, spectral data quality, and the timing of data acquisition, which directly influences the reflection of light radiation from the surface due to the position of the sun when the imagery is acquired. Such inconsistencies in RS data types might justify the different performance of maize ETa estimation when using the evaluated RS sensors since any vegetation index may not accurately reflect the true vegetation state when the RS data from the same surface, but with sensors providing measurements of surface reflectance with different post-processing standards.

4.7.3 The RS Optimal Data, Crop ETa Algorithms, ML Algorithms Recommendations, and Limitations

Overall, the use of RS data from fine-resolution sensors (e.g., MSR, Planet, and Sentinel-2) provided the necessary spatial and spectral resolutions to support accurate predictions of maize ETa (hourly and daily timesteps). Since most RS of ETa algorithms evaluated in this study were not calibrated using UAS multispectral data at very fine spatial resolutions, the use of UAS RS data for predicting maize ETa was not considered an optimal RS sensor. However, when the adjustment of the UAS data using the proposed calibration protocol provided the means to support the use of UAS to better estimate maize ETa.

Regarding the RS of crop ETa models evaluated, the TSEB algorithms were promising approaches to estimating maize ETa when compared to the OSEB and the three RBCC models. The TSEB algorithms incorporate more input parameters that allow for a better field assessment of soil water evaporation and plant transpiration rates. However, the OSEB model was also a promising

approach for estimating maize ETa, with errors similar to those of the TSEB algorithms when canopy conditions reach maximum growth stages. The main assumption of the OSEB approach for ETa modeling is that soil and vegetation could be considered as one unique surface, which is often the case when soil background exposure is minimized when most of the ground surface is covered by vegetation.

Furthermore, ML models such as GPR and Regression Trees have shown considerable promise in validating the calibration of remote sensing data used for ETa estimations. These two ML regression models have advantages over the other ML approaches evaluated since they can account for more complexities inherent in agricultural datasets and enhance the predictive accuracy of ETa calculations. The Regression Tree partitioning of the RS data into smaller clusters allows for a more localized prediction of groups of RS data with similar patterns. The GPR provides an added advantage by determining uncertainty estimates in its predictions based on probability theory, which allows the model to adjust the predictions to represent the training datasets better.

Variability in field sizes, crop types, and farming practices can add more complexity that was not initially identified in the controlled environments where the data for developing the calibration protocol for RS surface reflectance were obtained. Regarding the RS data, differences in temporal resolution can limit the frequency of data acquisition for refinement of the RS calibration protocol in different geographical areas, which might not aid the need for optimal agricultural decision-making on a daily to weekly basis. Furthermore, RS data uncertainty in sensor calibration across different types of data (e.g., proximal, airborne, spaceborne) can lead to inconsistencies in the final imagery products, affecting the reliability of the developed calibration protocol and the accuracy of crop ETa calculations. Regular calibration against ground truth data is essential. Still, it can be resource-intensive, which might have long-term implications on the reliability of crop ETa and "improved" RS surface reflectance data within the context of climate change.

Chapter 5

Conclusions

This study assessed the impact of different remote sensing data on the estimation of crop ETa modeling, focusing on both hourly and daily time steps to develop a comprehensive calibration protocol to enhance the quality of the data of non-optimal remote sensing data to predict crop ETa accurately. Furthermore, this study evaluated the accuracy of ETa rates derived from calibrated and standardized imagery obtained through selected RS-based ETa algorithms using just surface reflectance data and a combination of surface reflectance and point-based thermal data. The study hypothesized that the ability to characterize crop ETa from different remote sensing of ETa algorithms depended on the spatial and spectral resolution of the multispectral input data.

The multispectral surface reflectance values from the different sensors, for the most part, are statistically different, and different remote sensing of ETa models perform better with RED and NIR surface reflectance data for specific remote sensing sensors. For the RBCC models from Neale et al. (1990) and Trout and DeJonge (2018), the best remote sensing sensor (optimal spatial and spectral resolutions) was that from the Sentinel-2 (10 m) sensor, while the RBCC from Bausch (1995) had the proximal sensor MSR (1 m) as the optimal remote sensing data.

For the OSEB algorithm from Costa-Filho et al. (2021), the best RS input data were from Planet CubeSat (3 m) and in-situ IRT data. Even though estimating crop ETa can be achieved using any RS sensor, considering the use of optical remote sensing input data (multispectral images from a given sensor) for a given RS ETa algorithm has the potential to yield more accurate ETa estimates and thus optimize irrigation water management.

For the TSEB approaches evaluated, TSEBpar and TSEBser, the best remote sensing-based data for predicting maize ETa was that from the proximal or ground-based MSR instrument. The second-best RS data were multispectral reflectance images from the UAS, Planet, and Sentinel-2 remote sensing sensors (plus surface temperature from stationary IRT sensors). Using RS data from Landsat-8 resulted in larger ETa estimation errors.

A novel spatial k_p coefficient model, combined with machine learning regression, provided alternative ways to validate an approach for pixel decomposition of surface reflectance into soil and vegetation composites, which contributed to enhancing the quality of surface reflectance imagery data for crop ETa prediction. The novel k_p model provided a spatial approach to refine calculations of how much light is absorbed or reflected by vegetation and soil on a spatial basis. The spatial prediction of k_p contributed to adjusting the accuracy of reflectance data.

Furthermore, the novel spatial k_p model, determined with a regression coefficient of determination R^2 value of 0.95, demonstrated a strong statistical linear relationship between k_p and k_v. The regression coefficients, including the intercept and slope, exhibited 95$\%$ confidence intervals and p-values that validated the k_p model's reliability for future predictions. The k_p model performance analysis considered maize surface multispectral data from several remote sensing sensors, revealing similar statistical results across the various sensors investigated. Although slight variations existed in intercept and slope values, for the k_p model, among the remote sensing sensors, all sensors exhibit strong R^2 values, which emphasizes the novel k_p model's consistent performance.

The results of the study demonstrated some improvements in the accuracy of maize crop ETa estimation at both daily and hourly time steps, with the utilization of adjusted surface reflectance data across various spatial resolutions and sensors. At the LIRF site, the Trout and DeJonge (2018) model for daily maize ETa had improved performance when adjusted data from the Planet CubeSat (spaceborne) sensor was used. Additionally, the Bausch (1995) and Neale et al. (1990) models

showed improved accuracy with the utilization of remote sensing calibration functions, particularly with UAS data (airborne). The results of this study regarding crop ETa model performance for maize fields in semi-arid climates similar to Colorado (USA) highlight the importance of remote sensing data calibration for agricultural water applications regarding irrigation scheduling.

Furthermore, regarding the AVRC site, daily maize ETa estimations were also improved with the application of remote sensing calibration functions. Accuracy improvements in ETa model performance occurred across different remote sensing sensors, including MSR (proximal) and Landsat-8, highlighting the versatility of the calibration protocol across varied remote sensing sensors. Additionally, Sentinel-2 and Planet CubeSat RS sensors exhibited improvements in daily maize ETa predictions with the implementation of the calibration protocol.

Even though estimating crop ETa can be achieved using multispectral data from different remote sensing sensors, considering the use of optimal sensors/data for a given remote sensing ETa algorithm has the potential to improve crop ETa and, therefore, optimize irrigation water. It is essential to mention that, depending on the location of cropland fields and farming management practices, the suggested optimal remote sensing sensors in this study might not be practical.

For instance, larger fields might offer challenges to use handheld (proximal) devices to measure surface reflectance and temperature; spaceborne sensors might not offer high-quality data due to sensor issues (missing or uncorrected pixel data), cloudiness conditions, and other environmental factors. Thus, this study recognizes the need for further investigation to improve the data quality of sub-optimal remote sensing sensors to enable the use of a desirable remote sensing sensor with the best data accuracy possible for irrigation water management purposes.

Regarding the factors that may compromise the quality of remote sensing data for crop ETa modeling, atmospheric conditions such as subtle cloud cover and aerosols could significantly af-

fect the accuracy of the data by scattering and absorbing light before it reaches the spaceborne sensors (camera). Other issues, such as imagery calibration assumptions being violated by local field conditions, sensor noise (data uncertainty), and spatio-temporal resolution limitations, also contribute to data quality degradation throughout the crop growing seasons.

With respect to the use of machine learning regression for a remote sensing calibration approach, the overall best machine learning regression model for remote sensing applications will depend on the surface reflectance data characteristics. However, the GPR and Regression Tree were the algorithms that performed better during the cross-validation assessment due to their flexibility and effectiveness in handling complex nonlinear patterns in data. The GPR has particular advantages when used for remote sensing data adjustment since it can learn from the training data and make iterative adjustments for modeling data without a predetermined function or transforming the original data into different variables.

Furthermore, a thorough investigation needs to be done to evaluate the performance of different remote sensing of ETa algorithms that are used in large-scale modeling of ETa. When moving from a farm to a large-scale area (e.g., irrigation districts, watersheds), the spatial scale of a given remote sensing imagery may contain more than just vegetation and include other surface elements (mixed pixel scenario).

In that case, more research needs to be done to accommodate modeling strategies that are able to extract the vegetation features in a given pixel and provide reliable data for modeling ETa without having contaminated pixels hindering prediction accuracy. Nonetheless, our research findings support the idea that, when estimating daily maize ETa, it is essential to focus on using the best multispectral data from a variety of remote sensing sensors to ensure more accurate predictions of ETa that can serve as input for irrigation water management decision-making processes.

While the study provided insights into model performance, future research directions should focus on addressing observed underestimations and variations in specific sensors due to their spectral and spatial differences. Since the importance of sensor-specific characteristics is critical to addressing the quality of data inputs for modeling environmental variables, the use and application of the calibrated and novel k_p model must be interpreted with care, given the nature of the calibration process and data collection used in this research.

For a more robust validation, more research must be performed regarding other valuable row crops under different climate zones to evaluate any potential differences in the calibration coefficients. Also, incorporating more RS sensors at a much larger spatial scale might provide the conditions to use the novel k_p model for large-scale modeling (e.g., watershed). Therefore, the continuous refinement and validation of the k_p model using diverse datasets and additional sensors will further enhance its applicability to different local field conditions and provide the means to expand the use of this novel k_p model for a wide range of environmental applications.

For practical applications regarding the use of the RS calibration protocol in irrigation scheduling, the following strategies could be implemented to ensure the appropriate use of the proposed RS imagery data quality enhancement: Integrating the proposed calibration protocol with geospatial software (e.g., ArcGIS, QGIS, Google Earth Engine) that integrates RS data acquisition, preprocessing, calibration, and analysis, users should be able to optimize time and handle a large amount of RS imagery data. The use of the adjusted calibrated RS data crop ETa products in decision-making tools for irrigation scheduling that apply the SWB could be the next step towards the practical use of the calibration RS imagery products. Irrigation schedule tools often provide real-time irrigation advice to water stakeholders in cropland settings and could use adjusted RS data to support precision irrigation.

References

Abdi, H., & Williams, L. J. (2010). Principal component analysis. *Wiley interdisciplinary reviews: computational statistics*, *2*(4), 433–459.

Agam, N., Kustas, W. P., Anderson, M. C., Li, F., & Neale, C. M. (2007). A vegetation index based technique for spatial sharpening of thermal imagery. *Remote Sensing of Environment*, *107*(4), 545–558.

Ahmad, S., Kalra, A., & Stephen, H. (2010). Estimating soil moisture using remote sensing data: A machine learning approach. *Advances in water resources*, *33*(1), 69–80.

Alexandratos, N., & Bruinsma, J. (2012). World agriculture towards 2030/2050: the 2012 revision.

Alexandratos, N., Bruinsma, J., Boedeker, G., Schmidhuber, J., Broca, S., Shetty, P., & Ottaviani, M. (2006). World agriculture: Towards 2030/2050. interim report. prospects for food, nutrition, agriculture and major commodity groups.

Alface, A. B., Pereira, S. B., Filgueiras, R., & Cunha, F. F. (2019). Sugarcane spatial-temporal monitoring and crop coefficient estimation through ndvi. *Revista Brasileira de Engenharia Agrícola e Ambiental*, *23*, 330–335.

Allam, M., Bakr, N., & Elbably, W. (2019). Multi-temporal assessment of land use/land cover change in arid region based on landsat satellite imagery: Case study in fayoum region, egypt. *Remote Sensing Applications: Society and Environment*, *14*, 8–19.

Allen, R. G. (2000). Using the fao-56 dual crop coefficient method over an irrigated region as part of an evapotranspiration intercomparison study. *Journal of hydrology*, *229*(1-2), 27–41.

Allen, R. G., Pereira, L. S., Howell, T. A., & Jensen, M. E. (2011). Evapotranspiration information reporting: I. factors governing measurement accuracy. *Agricultural Water Management*, *98*(6), 899–920.

Allen, R. G., Pereira, L. S., Raes, D., Smith, M., et al. (1998). Crop evapotranspiration-guidelines for computing crop water requirements-fao irrigation and drainage paper 56. *Fao, Rome*, *300*(9), D05109.

Allen, R. G., Pereira, L. S., Smith, M., Raes, D., & Wright, J. L. (2005). Fao-56 dual crop coefficient method for estimating evaporation from soil and application extensions. *Journal of irrigation and drainage engineering*, *131*(1), 2–13.

Allen, R. G., Tasumi, M., & Trezza, R. (2007). Satellite-based energy balance for mapping evapotranspiration with internalized calibration (metric)—model. *Journal of irrigation and drainage engineering*, *133*(4), 380–394.

Alves, I., & Pereira, L. S. (2000). Modelling surface resistance from climatic variables? *Agricultural Water Management*, *42*(3), 371–385.

Amatya, D. M., Irmak, S., Gowda, P., Sun, G., Nettles, J. E., & Douglas-Mankin, K. R. (2016). Ecosystem evapotranspiration: challenges in measurements, estimates, and modeling. *Transactions of the ASABE*, *59*(2), 555–560.

Anapalli, S. S., Fisher, D. K., Pinnamaneni, S. R., & Reddy, K. N. (2020). Quantifying evapotranspiration and crop coefficients for cotton (gossypium hirsutum l.) using an eddy covariance approach. *Agricultural Water Management*, *233*, 106091.

Anapalli, S. S., Fisher, D. K., Reddy, K. N., Wagle, P., Gowda, P. H., & Sui, R. (2018). Quantifying soybean evapotranspiration using an eddy covariance approach. *Agricultural Water Management*, *209*, 228–239.

Anderson, M., Neale, C., Li, F., Norman, J., Kustas, W., Jayanthi, H., & Chavez, J. (2004). Upscaling ground observations of vegetation water content, canopy height, and leaf area index during smex02 using aircraft and landsat imagery. *Remote sensing of environment*, *92*(4), 447–464.

Anderson, M., Norman, J., Diak, G., Kustas, W., & Mecikalski, J. (1997). A two-source time-integrated model for estimating surface fluxes using thermal infrared remote sensing. *Remote sensing of environment*, *60*(2), 195–216.

Anderson, M. C. (1966). Stand structure and light penetration. ii. a theoretical analysis. *Journal of applied ecology*, 41–54.

Anderson, M. C., Norman, J. M., Kustas, W. P., Li, F., Prueger, J. H., & Mecikalski, J. R. (2005).

Effects of vegetation clumping on two–source model estimates of surface energy fluxes from an agricultural landscape during smacex. *Journal of Hydrometeorology*, *6*(6), 892–909.

Anderson, R. G., & French, A. N. (2019). *Crop evapotranspiration* (Vol. 9) (No. 10). MDPI.

Anguita, D., Ghelardoni, L., Ghio, A., Oneto, L., Ridella, S., et al. (2012). The'k'in k-fold cross validation. In *Esann* (pp. 441–446).

Aragon, B., Johansen, K., Parkes, S., Malbeteau, Y., Al-Mashharawi, S., Al-Amoudi, T., ... McCabe, M. F. (2020). A calibration procedure for field and uav-based uncooled thermal infrared instruments. *Sensors*, *20*(11), 3316.

Aragon, B., Ziliani, M. G., Houborg, R., Franz, T. E., & McCabe, M. F. (2021). Cubesats deliver new insights into agricultural water use at daily and 3 m resolutions. *Scientific reports*, *11*(1), 1–12.

Aragon, B., Ziliani, M. G., & McCabe, M. F. (2021). Revisiting the spatial scale effects on remotely sensed evaporation. In *2021 ieee international geoscience and remote sensing symposium igarss* (pp. 6579–6582).

Arya, P. S. (2001). *Introduction to micrometeorology*. Elsevier.

ASCE-EWRI. (2005). The asce standardized reference evapotranspiration equation. *Technical Committee Rep. to the Environmental and Water Resources Institute of ASCE from the Task Committee on Standardization of Reference Evapotranspiration*, 173.

Aschonitis, V., Touloumidis, D., ten Veldhuis, M.-C., & Coenders-Gerrits, M. (2021). Correcting thornthwaite potential evapotranspiration using a global grid of local coefficients to support temperature-based estimations of reference evapotranspiration and aridity indices. *Earth System Science Data*, *14*(1), 163–177.

Atzberger, C. (2013). Advances in remote sensing of agriculture: Context description, existing operational monitoring systems and major information needs. *Remote sensing*, *5*(2), 949–981.

Awad, M. M. (2019). Toward precision in crop yield estimation using remote sensing and optimization techniques. *Agriculture*, *9*(3), 54.

Baboo, S. S., & Devi, M. R. (2010). An analysis of different resampling methods in coimbatore, district. *Global Journal of Computer Science and Technology*.

Baret, F., Clevers, J., & Steven, M. (1995). The robustness of canopy gap fraction estimates from red and near-infrared reflectances: A comparison of approaches. *Remote Sensing of Environment*, *54*(2), 141–151.

Baret, F., & Guyot, G. (1991). Potentials and limits of vegetation indices for lai and apar assessment. *Remote sensing of environment*, *35*(2-3), 161–173.

Barsi, J. A., Alhammoud, B., Czapla-Myers, J., Gascon, F., Haque, M. O., Kaewmanee, M., ... Markham, B. L. (2018). Sentinel-2a msi and landsat-8 oli radiometric cross comparison over desert sites. *European Journal of Remote Sensing*, *51*(1), 822–837.

Bastiaanssen, W. G., Menenti, M., Feddes, R., & Holtslag, A. (1998). A remote sensing surface energy balance algorithm for land (sebal). 1. formulation. *Journal of hydrology*, *212*, 198–212.

Batchelor, G. (1949). Diffusion in a field of homogeneous turbulence. i. eulerian analysis. *Australian Journal of Chemistry*, *2*(4), 437–450.

Bausch, W. C. (1995). Remote sensing of crop coefficients for improving the irrigation scheduling of corn. *Agricultural Water Management*, *27*(1), 55–68.

Bausch, W. C., & Neale, C. M. (1987). Crop coefficients derived from reflected canopy radiation: a concept. *Transactions of the ASAE*, *30*(3), 703–0709.

Belgiu, M., & Stein, A. (2019). Spatiotemporal image fusion in remote sensing. *Remote sensing*, *11*(7), 818.

Belitz, K., & Stackelberg, P. (2021). Evaluation of six methods for correcting bias in estimates from ensemble tree machine learning regression models. *Environmental Modelling & Software*, *139*, 105006.

Ben-Hur, A., Ong, C. S., Sonnenburg, S., Schölkopf, B., & Rätsch, G. (2008). Support vector machines and kernels for computational biology. *PLoS computational biology*, *4*(10), e1000173.

Bhakta, I., Phadikar, S., & Majumder, K. (2019). State-of-the-art technologies in precision agriculture: a systematic review. *Journal of the Science of Food and Agriculture*, *99*(11), 4878–4888.

Bhavsar, H., & Panchal, M. H. (2012). A review on support vector machine for data classification. *International Journal of Advanced Research in Computer Engineering & Technology (IJARCET)*, *1*(10), 185–189.

Bhavsar, P. N., & Patel, J. N. (2016). Development of relationship between crop coefficient and ndvi using geospatial technology. *Journal of Agrometeorology*, *18*(2), 261–264.

Bian, L., & Butler, R. (1999). Comparing effects of aggregation methods on statistical and spatial properties of simulated spatial data. *Photogrammetric engineering and remote sensing*, *65*, 73–84.

Bisquert, M., Sánchez, J., López-Urrea, R., & Caselles, V. (2016). Estimating high resolution evapotranspiration from disaggregated thermal images. *Remote sensing of environment*, *187*, 423–433.

Bizzell, R., & Prior, H. (1985). Thematic mapper data quality and performance assessment in renewable resources/agriculture/remote sensing. *NASA. Goddard Space Flight Center LANDSAT-4 Sci. Characterization Early Results, Vol. 4*.

Blaney, H. F., & Criddle, W. D. (1962). *Determining consumptive use and irrigation water requirements* (No. 1275). US Department of Agriculture.

Bossie, M., Tilahun, K., & Hordofa, T. (2009). Crop coefficient and evaptranspiration of onion at awash melkassa, central rift valley of ethiopia. *Irrigation and drainage systems*, *23*(1), 1–10.

Boucher, A. (2009). Sub-pixel mapping of coarse satellite remote sensing images with stochastic simulations from training images. *Mathematical geosciences*, *41*(3), 265–290.

Boulet, G., Olioso, A., Ceschia, E., Marloie, O., Coudert, B., Rivalland, V., ... Chehbouni, G. (2012). An empirical expression to relate aerodynamic and surface temperatures for use within single-source energy balance models. *Agricultural and Forest Meteorology*, *161*,

148–155.

Bowen, I. S. (1926). The ratio of heat losses by conduction and by evaporation from any water surface. *Physical review*, *27*(6), 779.

Brauman, K. A., Siebert, S., & Foley, J. A. (2013). Improvements in crop water productivity increase water sustainability and food security—a global analysis. *Environmental Research Letters*, *8*(2), 024030.

Breiman, L. (2001). Random forests. *Machine learning*, *45*, 5–32.

Breunig, F. M., Galvão, L. S., Dalagnol, R., Dauve, C. E., Parraga, A., Santi, A. L., ... Chen, S. (2020). Delineation of management zones in agricultural fields using cover–crop biomass estimates from planetscope data. *International Journal of Applied Earth Observation and Geoinformation*, *85*, 102004.

Bro, R., & Smilde, A. K. (2014). Principal component analysis. *Analytical methods*, *6*(9), 2812–2831.

Brocca, L., Morbidelli, R., Melone, F., & Moramarco, T. (2007). Soil moisture spatial variability in experimental areas of central italy. *Journal of Hydrology*, *333*(2-4), 356–373.

Bronson, K. F., Chua, T. T., Booker, J., Keeling, J. W., & Lascano, R. J. (2003). In-season nitrogen status sensing in irrigated cotton: Ii. leaf nitrogen and biomass. *Soil Science Society of America Journal*, *67*(5), 1439–1448.

Bruinsma, J., et al. (2009). The resource outlook to 2050: by how much do land, water and crop yields need to increase by 2050? In *How to feed the world in 2050. proceedings of a technical meeting of experts, rome, italy, 24-26 june 2009* (pp. 1–33).

Brunsell, N. A., & Gillies, R. R. (2002). Incorporating surface emissivity into a thermal atmospheric correction. *Photogrammetric engineering and remote sensing*, *68*(12), 1263–1270.

Brutsaert, W. (1982). Evaporation into the atmosphere: Theory. *History, and Applications*, *1*.

Brutsaert, W., & Sugita, M. (1992). Application of self-preservation in the diurnal evolution of the surface energy budget to determine daily evaporation. *Journal of Geophysical Research: Atmospheres*, *97*(D17), 18377–18382.

Burns, T. J., Rogers, S. K., Ruck, D. W., & Oxley, M. E. (1994). Discrete, spatiotemporal, wavelet multiresolution analysis method for computing optical flow. *Optical Engineering*, *33*(7), 2236–2247.

Businger, J. A., Wyngaard, J. C., Izumi, Y., & Bradley, E. F. (1971). Flux-profile relationships in the atmospheric surface layer. *Journal of Atmospheric Sciences*, *28*(2), 181–189.

Buttar, N. A., Yongguang, H., Shabbir, A., Lakhiar, I. A., Ullah, I., Ali, A., ... Yasin, M. A. (2018). Estimation of evapotranspiration using bowen ratio method. *IFAC-PapersOnLine*, *51*(17), 807–810.

Byonocore, M. H., Brody, W. R., & Macovski, A. (1981). A natural pixel decomposition for two-dimensional image reconstruction. *IEEE Transactions on Biomedical Engineering*(2), 69–78.

Cai, X., & Rosegrant, M. (1999). Irrigated and rainfed crop area and yield. *International Food Policy Research Institute, Washington, DC*.

Cai, Y., Guan, K., Nafziger, E., Chowdhary, G., Peng, B., Jin, Z., ... Wang, S. (2019). Detecting in-season crop nitrogen stress of corn for field trials using uav-and cubesat-based multispectral sensing. *IEEE Journal of Selected Topics in Applied Earth Observations and Remote Sensing*, *12*(12), 5153–5166.

Cammalleri, C., Anderson, M., Gao, F., Hain, C., & Kustas, W. (2014). Mapping daily evapotranspiration at field scales over rainfed and irrigated agricultural areas using remote sensing data fusion. *Agricultural and forest meteorology*, *186*, 1–11.

Campbell, G. (1990). Derivation of an angle density function for canopies with ellipsoidal leaf angle distributions. *Agricultural and forest meteorology*, *49*(3), 173–176.

Campbell, G. S. (1986). Extinction coefficients for radiation in plant canopies calculated using an ellipsoidal inclination angle distribution. *Agricultural and forest meteorology*, *36*(4), 317–321.

Campbell, G. S., & Norman, J. M. (2012). *An introduction to environmental biophysics*. Springer Science & Business Media.

Campbell, J. B., & Wynne, R. (2011). Introduction to remote sensing guilford press. *New York*.

Cannavó, F. (2012). Sensitivity analysis for volcanic source modeling quality assessment and model selection. *Computers & geosciences*, *44*, 52–59.

Carlson, T. N., & Ripley, D. A. (1997). On the relation between ndvi, fractional vegetation cover, and leaf area index. *Remote sensing of Environment*, *62*(3), 241–252.

Carpintero, E., Mateos, L., Andreu, A., & González-Dugo, M. P. (2020). Effect of the differences in spectral response of mediterranean tree canopies on the estimation of evapotranspiration using vegetation index-based crop coefficients. *Agricultural Water Management*, *238*, 106201.

Carrasco, L., O'Neil, A. W., Morton, R. D., & Rowland, C. S. (2019). Evaluating combinations of temporally aggregated sentinel-1, sentinel-2 and landsat 8 for land cover mapping with google earth engine. *Remote Sensing*, *11*(3), 288.

Carrasco-Benavides, M., Ortega-Farias, S., Morales-Salinas, L., Poblete-Echeverría, C., & Chávez, J. L. (2017). Calibration and validation of an aerodynamic method to estimate the spatial variability of sensible and latent heat fluxes over a drip-irrigated merlot vineyard. *International Journal of Remote Sensing*, *38*(24), 7473–7496.

Carter, C., & Liang, S. (2019). Evaluation of ten machine learning methods for estimating terrestrial evapotranspiration from remote sensing. *International Journal of Applied Earth Observation and Geoinformation*, *78*, 86–92.

Caselles, E., Abad, F. J., Valor, E., & Caselles, V. (2011). Automatic generation of land surface emissivity maps. *Climate Change-Research and Technology for Adaptation and Mitigation*, *15*.

Cava, D., Katul, G., Scrimieri, A., Poggi, D., Cescatti, A., & Giostra, U. (2006). Buoyancy and the sensible heat flux budget within dense canopies. *Boundary-layer meteorology*, *118*(1), 217–240.

Chakhar, A., Ortega-Terol, D., Hernández-López, D., Ballesteros, R., Ortega, J. F., & Moreno, M. A. (2020). Assessing the accuracy of multiple classification algorithms for crop classifi-

cation using landsat-8 and sentinel-2 data. *Remote sensing*, *12*(11), 1735.

Chapelle, O., Sindhwani, V., & Keerthi, S. S. (2008). Optimization techniques for semi-supervised support vector machines. *Journal of Machine Learning Research*, *9*(2).

Chávez, J., Gowda, P., Howell, T., Garcia, L., Copeland, K., & Neale, C. (2012). Et mapping with high-resolution airborne remote sensing data in an advective semiarid environment. *Journal of irrigation and drainage engineering*, *138*(5), 416–423.

Chávez, J., Howell, T., Gowda, P., Copeland, K., & Prueger, J. (2010a). Surface aerodynamic temperature modeling over rainfed cotton. *Transactions of the ASABE*, *53*(3), 759–767.

Chávez, J., & López-Urrea, R. (2019). One-step approach for estimating maize actual water use: Part i. modeling a variable surface resistance. *Irrigation Science*, *37*(2), 123–137.

Chávez, J., Neale, C. M., Hipps, L. E., Prueger, J. H., & Kustas, W. P. (2005). Comparing aircraft-based remotely sensed energy balance fluxes with eddy covariance tower data using heat flux source area functions. *Journal of Hydrometeorology*, *6*(6), 923–940.

Chávez, J. L. (2015). Using canopy temperature as an indicator of plant stress. In *Proceedings of the 27th annual central plains irrigation conference (cpic), colby, ks* (pp. 17–18).

Chávez, J. L., & Evett, S. R. (2012). Using soil water sensors to improve irrigation management. In *Proceedings of the 2012 central plains irrigation conference, colby, kansas, february 21-22*.

Chávez, J. L., Gowda, P., Howell, T., Neale, C., & Copeland, K. (2009b). Estimating hourly crop et using a two-source energy balance model and multispectral airborne imagery. *Irrigation Science*, *28*(1), 79–91.

Chávez, J. L., Howell, T. A., & Copeland, K. S. (2009a). Evaluating eddy covariance cotton et measurements in an advective environment with large weighing lysimeters. *Irrigation Science*, *28*(1), 35–50.

Chávez, J. L., Neale, C. M., Prueger, J. H., & Kustas, W. P. (2008). Daily evapotranspiration estimates from extrapolating instantaneous airborne remote sensing et values. *Irrigation Science*, *27*(1), 67–81.

Chávez, J. L., Straw, D., Garcia, L. A., Ley, T. W., Andales, A. A., Simmons, L. H., & Bartolo,

M. E. (2010b). Mapping et in southeastern colorado using a surface aerodynamic temperature model. In *Meeting irrigation demands in a water-challenged environment* (p. 297).

Chávez, J. L., Zhang, H., Brown, A. J., Andales, A., Costa-Filho, E., et al. (2024). Maize evapotranspiration estimates using planet dove mini-satellites and field-level infrared thermometers.

Chehbouni, A., Seen, D. L., Njoku, E., & Monteny, B. (1996). Examination of the difference between radiative and aerodynamic surface temperatures over sparsely vegetated surfaces. *Remote Sensing of Environment*, *58*(2), 177–186.

Chen, P.-H., Fan, R.-E., & Lin, C.-J. (2006). A study on smo-type decomposition methods for support vector machines. *IEEE transactions on neural networks*, *17*(4), 893–908.

Chen, Y., Xia, J., Liang, S., Feng, J., Fisher, J. B., Li, X., ... others (2014). Comparison of satellite-based evapotranspiration models over terrestrial ecosystems in china. *Remote Sensing of Environment*, *140*, 279–293.

Cheng, J., Liu, H., Liu, T., Wang, F., & Li, H. (2015). Remote sensing image fusion via wavelet transform and sparse representation. *ISPRS journal of photogrammetry and remote sensing*, *104*, 158–173.

Chia, M. Y., Huang, Y. F., & Koo, C. H. (2020). Support vector machine enhanced empirical reference evapotranspiration estimation with limited meteorological parameters. *Computers and Electronics in Agriculture*, *175*, 105577.

Choi, M. (2006). A new intensity-hue-saturation fusion approach to image fusion with a tradeoff parameter. *IEEE Transactions on Geoscience and Remote sensing*, *44*(6), 1672–1682.

Choudhury, B., Idso, S., & Reginato, R. (1987). Analysis of an empirical model for soil heat flux under a growing wheat crop for estimating evaporation by an infrared-temperature based energy balance equation. *Agricultural and Forest Meteorology*, *39*(4), 283–297.

Choudhury, B. J., Ahmed, N. U., Idso, S. B., Reginato, R. J., & Daughtry, C. S. (1994). Relations between evaporation coefficients and vegetation indices studied by model simulations. *Remote sensing of environment*, *50*(1), 1–17.

Choudhury, B. J., & Monteith, J. (1988). A four-layer model for the heat budget of homogeneous land surfaces. *Quarterly Journal of the Royal Meteorological Society*, *114*(480), 373–398.

Christiansen, J. E. (1968). Pan evaporation and evapotranspiration from climatic data. *Journal of the Irrigation and Drainage Division*, *94*(2), 243–266.

Chung, U., Gbegbelegbe, S., Shiferaw, B., Robertson, R., Yun, J. I., Tesfaye, K., ... Sonder, K. (2014). Modeling the effect of a heat wave on maize production in the usa and its implications on food security in the developing world. *Weather and Climate Extremes*, *5*, 67–77.

Claverie, M., Ju, J., Masek, J. G., Dungan, J. L., Vermote, E. F., Roger, J.-C., ... Justice, C. (2018). The harmonized landsat and sentinel-2 surface reflectance data set. *Remote sensing of environment*, *219*, 145–161.

Claverie, M., Masek, J. G., Ju, J., & Dungan, J. L. (2017). Harmonized landsat-8 sentinel-2 (hls) product user's guide. *National Aeronautics and Space Administration (NASA): Washington, DC, USA*.

Clevers, J. (1989). Application of a weighted infrared-red vegetation index for estimating leaf area index by correcting for soil moisture. *Remote Sensing of Environment*, *29*(1), 25–37.

Colaizzi, P. D., Agam, N., Tolk, J. A., Evett, S. R., Howell, T. A., Gowda, P. H., ... Anderson, M. C. (2014). Two-source energy balance model to calculate e, t, and et: Comparison of priestley-taylor and penman-monteith formulations and two time scaling methods. *Transactions of the ASABE*, *57*(2), 479–498.

Colaizzi, P. D., Kustas, W. P., Anderson, M. C., Agam, N., Tolk, J. A., Evett, S. R., ... O'Shaughnessy, S. A. (2012). Two-source energy balance model estimates of evapotranspiration using component and composite surface temperatures. *Advances in water resources*, *50*, 134–151.

Comunian, A., Giudici, M., Landoni, L., & Pugnaghi, S. (2018). Improving bowen-ratio estimates of evaporation using a rejection criterion and multiple-point statistics. *Journal of hydrology*, *563*, 43–50.

Condon, L. E., & Maxwell, R. M. (2019). Simulating the sensitivity of evapotranspiration and streamflow to large-scale groundwater depletion. *Science Advances*, *5*(6), eaav4574.

Consoli, S., & Vanella, D. (2014). Comparisons of satellite-based models for estimating evapotranspiration fluxes. *Journal of hydrology*, *513*, 475–489.

Cortes, C., & Vapnik, V. (1995). Support vector machine. *Machine learning*, *20*(3), 273–297.

Costa, L., Nunes, L., & Ampatzidis, Y. (2020). A new visible band index (vndvi) for estimating ndvi values on rgb images utilizing genetic algorithms. *Computers and Electronics in Agriculture*, *172*, 105334.

Costache, R., Arabameri, A., Blaschke, T., Pham, Q. B., Pham, B. T., Pandey, M., ... Costache, I. (2021). Flash-flood potential mapping using deep learning, alternating decision trees and data provided by remote sensing sensors. *Sensors*, *21*(1), 280.

Costa-Filho, E., Chávez, J. L., Andales, A. A., & Brown, A. J. (2022). Updating corn crop coefficients with remote sensing-based actual evapotranspiration algorithms. In *World environmental and water resources congress 2022* (pp. 618–633).

Costa-Filho, E., Chávez, J. L., & Comas, L. (2020). Determining maize water stress through a remote sensing-based surface energy balance approach. *Irrigation Science*, *38*(5), 501–518.

Costa-Filho, E., Chávez, J. L., Zhang, H., & Andales, A. A. (2021). An optimized surface aerodynamic temperature approach to estimate maize sensible heat flux and evapotranspiration. *Agricultural and Forest Meteorology*, *311*, 108683.

Cotterman, K. A., Kendall, A. D., Basso, B., & Hyndman, D. W. (2018). Groundwater depletion and climate change: future prospects of crop production in the central high plains aquifer. *Climatic change*, *146*(1), 187–200.

Coulston, J. W., Blinn, C. E., Thomas, V. A., & Wynne, R. H. (2016). Approximating prediction uncertainty for random forest regression models. *Photogrammetric Engineering & Remote Sensing*, *82*(3), 189–197.

Crago, R., & Brutsaert, W. (1996). Daytime evaporation and the self-preservation of the evaporative fraction and the bowen ratio. *Journal of Hydrology*, *178*(1-4), 241–255.

Crago, R. D. (1996). Conservation and variability of the evaporative fraction during the daytime. *Journal of Hydrology*, *180*(1-4), 173–194.

Csillik, O., Kumar, P., Mascaro, J., O'Shea, T., & Asner, G. P. (2019). Monitoring tropical forest carbon stocks and emissions using planet satellite data. *Scientific reports*, *9*(1), 1–12.

Daly, B. J., & Harlow, F. H. (1970). Transport equations in turbulence. *The physics of fluids*, *13*(11), 2634–2649.

De Bruin, H. (1983). A model for the priestley-taylor parameter α. *Journal of Applied Meteorology and Climatology*, *22*(4), 572–578.

De Costa, W., & Dennett, M. (1992). Is canopy light extinction coefficient a species-specific constant? *Tropical Agricultural Research*, *4*, 123–137.

Deka, P. C., et al. (2014). Support vector machine applications in the field of hydrology: a review. *Applied soft computing*, *19*, 372–386.

Deng, L., Mao, Z., Li, X., Hu, Z., Duan, F., & Yan, Y. (2018). Uav-based multispectral remote sensing for precision agriculture: A comparison between different cameras. *ISPRS journal of photogrammetry and remote sensing*, *146*, 124–136.

Denich, C., & Bradford, A. (2010). Estimation of evapotranspiration from bioretention areas using weighing lysimeters. *Journal of Hydrologic Engineering*, *15*(6), 522–530.

Devulapalli, S., & Krishnan, R. (2019). Synthesized pansharpening using curvelet transform and adaptive neuro-fuzzy inference system. *Journal of Applied Remote Sensing*, *13*(3), 034519.

Ding, R., Kang, S., Li, F., Zhang, Y., Tong, L., & Sun, Q. (2010). Evaluating eddy covariance method by large-scale weighing lysimeter in a maize field of northwest china. *Agricultural Water Management*, *98*(1), 87–95.

Dingman, S. L. (2015). *Physical hydrology*. Waveland press.

Dingre, S., Gorantiwar, S., & Kadam, S. (2021). Correlating the field water balance derived crop coefficient (kc) and canopy reflectance-based ndvi for irrigated sugarcane. *Precision Agriculture*, *22*(4), 1134–1153.

Dinno, A. (2015). Nonparametric pairwise multiple comparisons in independent groups using

dunn's test. *The Stata Journal*, *15*(1), 292–300.

Do, M. N., & Vetterli, M. (2005). The contourlet transform: an efficient directional multiresolution image representation. *IEEE Transactions on image processing*, *14*(12), 2091–2106.

Doorenbos, J., & Pruitt, W. (1977). Crop water requirements. fao irrigation and drainage paper 24. *Land and Water Development Division, FAO, Rome*, *144*(1).

Drouet, J.-L., Moulia, B., & Bonhomme, R. (1999). Do changes in the azimuthal distribution of maize leaves over time affect canopy light absorption? *Agronomie*, *19*(3-4), 281–294.

Drusch, M., Del Bello, U., Carlier, S., Colin, O., Fernandez, V., Gascon, F., ... others (2012). Sentinel-2: Esa's optical high-resolution mission for gmes operational services. *Remote sensing of Environment*, *120*, 25–36.

Du, Y., Zhang, Y., Ling, F., Wang, Q., Li, W., & Li, X. (2016). Water bodies' mapping from sentinel-2 imagery with modified normalized difference water index at 10-m spatial resolution produced by sharpening the swir band. *Remote Sensing*, *8*(4), 354.

Dube, T., & Mutanga, O. (2015). Evaluating the utility of the medium-spatial resolution landsat 8 multispectral sensor in quantifying aboveground biomass in umgeni catchment, south africa. *ISPRS Journal of Photogrammetry and Remote Sensing*, *101*, 36–46.

Dubois, O., et al. (2011). *The state of the world's land and water resources for food and agriculture: managing systems at risk.* Earthscan.

Dunn, O. J. (1964). Multiple comparisons using rank sums. *Technometrics*, *6*(3), 241–252.

Dyer, A. (1974). A review of flux-profile relationships. *Boundary-Layer Meteorology*, *7*, 363–372.

Dyer, A., & Hicks, B. (1970). Flux-gradient relationships in the constant flux layer. *Quarterly Journal of the Royal Meteorological Society*, *96*(410), 715–721.

Ehsani, R., & Maja, J. M. (2013). The rise of small uavs in precision agriculture. *Resource Magazine*, *20*(4), 18–19.

Elachi, C. (1988). Spaceborne radar remote sensing: applications and techniques. *New York*.

Elhaddad, A., & Garcia, L. A. (2011). Reset-raster: Surface energy balance model for calculating evapotranspiration using a raster approach. *Journal of Irrigation and Drainage Engineering*,

137(4), 203–210.

Elmahdy, S., Ali, T., & Mohamed, M. (2021). Regional mapping of groundwater potential in ar rub al khali, arabian peninsula using the classification and regression trees model. *Remote Sensing*, *13*(12), 2300.

El Naqa, I., & Murphy, M. J. (2015). What is machine learning? In *machine learning in radiation oncology* (pp. 3–11). Springer.

El-Shirbeny, M. A., Ali, A., Badr, M. A., & Bauomy, E. M. (2014). Assessment of wheat crop coefficient using remote sensing techniques. *World Research Journal of Agricultural Sciences*, *1*(2), 12–17.

Elwadie, M. E., Pierce, F. J., & Qi, J. (2005). Remote sensing of canopy dynamics and biophysical variables estimation of corn in michigan. *Agronomy Journal*, *97*(1), 99–105.

Engle, J. L., & Weinstein, O. (1983). The thematic mapper—an overview. *IEEE transactions on geoscience and remote sensing*(3), 258–265.

Evangelisti, L., Guattari, C., & Asdrubali, F. (2019). On the sky temperature models and their influence on buildings energy performance: A critical review. *Energy and Buildings*, *183*, 607–625.

Ezzahar, J., Chehbouni, A., Er-Raki, S., & Hanich, L. (2009). Combining a large aperture scintillometer and estimates of available energy to derive evapotranspiration over several agricultural fields in a semi-arid region. *Plant Biosystems*, *143*(1), 209–221.

Famiglietti, J. S., Rudnicki, J. W., & Rodell, M. (1998). Variability in surface moisture content along a hillslope transect: Rattlesnake hill, texas. *Journal of hydrology*, *210*(1-4), 259–281.

Fang, H., Wei, S., Jiang, C., & Scipal, K. (2012). Theoretical uncertainty analysis of global modis, cyclopes, and globcarbon lai products using a triple collocation method. *Remote Sensing of Environment*, *124*, 610–621.

Faostat, F. (2019). *Food and agriculture organization of the united nations-statistic division https://www. fao. org/faost at/en/# data.* QC.

Faraji, Z., Kaviani, A., & Danesh Kar Arasteh, P. (2021). Evaluation of distrad and tsharp down-

scaling methods to increase the spatial resolution of modis thermal images. *Journal of Water and Soil Resources Conservation*, *11*(2), 133–147.

Farrell, M. D., & Mersereau, R. M. (2005). On the impact of pca dimension reduction for hyperspectral detection of difficult targets. *IEEE Geoscience and Remote Sensing Letters*, *2*(2), 192–195.

Federer, C. (1975). Evapotranspiration. *Reviews of Geophysics*, *13*(3), 442–445.

Fereres, E., & Connor, D. (2004). Sustainable water management in agriculture. In *Challenges of the new water policies for the xxi century: Proceedings of the seminar on challenges of the new water policies for the 21st century, valencia, 29-31 october 2002* (Vol. 164).

Fernando, H. J. (2012). Handbook of environmental fluid dynamics, volume one: overview and fundamentals.

Figuerola, P. I., & Berliner, P. R. (2005). Evapotranspiration under advective conditions. *International journal of biometeorology*, *49*(6), 403–416.

Finnigan, J. (1985). Turbulent transport in flexible plant canopies. In *The forest-atmosphere interaction* (pp. 443–480). Springer.

Finnigan, J. (2010). Waving plants and turbulent eddies. *Journal of Fluid Mechanics*, *652*, 1–4.

Fisher, J. B., Tu, K. P., & Baldocchi, D. D. (2008). Global estimates of the land–atmosphere water flux based on monthly avhrr and islscp-ii data, validated at 16 fluxnet sites. *Remote Sensing of Environment*, *112*(3), 901–919.

Foken, T. (2008). The energy balance closure problem: an overview. *Ecological Applications*, *18*(6), 1351–1367.

Foken, T., & Napo, C. J. (2008). *Micrometeorology* (Vol. 308). Springer.

Foley, J. A., Ramankutty, N., Brauman, K. A., Cassidy, E. S., Gerber, J. S., Johnston, M., ... others (2011). Solutions for a cultivated planet. *Nature*, *478*(7369), 337–342.

French, A. N., Hunsaker, D. J., Sanchez, C. A., Saber, M., Gonzalez, J. R., & Anderson, R. (2020). Satellite-based ndvi crop coefficients and evapotranspiration with eddy covariance validation for multiple durum wheat fields in the us southwest. *Agricultural Water Management*, *239*,

106266.

French, A. N., Hunsaker, D. J., & Thorp, K. R. (2015). Remote sensing of evapotranspiration over cotton using the tseb and metric energy balance models. *Remote Sensing of Environment*, *158*, 281–294.

Fushiki, T. (2011). Estimation of prediction error by using k-fold cross-validation. *Statistics and Computing*, *21*, 137–146.

Gao, F., Masek, J., Schwaller, M., & Hall, F. (2006). On the blending of the landsat and modis surface reflectance: Predicting daily landsat surface reflectance. *IEEE Transactions on Geoscience and Remote sensing*, *44*(8), 2207–2218.

Garrigues, S., Shabanov, N., Swanson, K., Morisette, J., Baret, F., & Myneni, R. (2008). Intercomparison and sensitivity analysis of leaf area index retrievals from lai-2000, accupar, and digital hemispherical photography over croplands. *agricultural and forest meteorology*, *148*(8-9), 1193–1209.

Gates, D. M. (2012). *Biophysical ecology*. Springer Science & Business Media.

Gautam, R. S., Singh, D., & Mittal, A. (2007). Application of principal component analysis and information fusion technique to detect hotspots in noaa/avhrr images of jharia coalfield, india. *Journal of Applied Remote Sensing*, *1*(1), 013523.

Gavilan, P., Berengena, J., & Allen, R. G. (2007). Measuring versus estimating net radiation and soil heat flux: Impact on penman–monteith reference et estimates in semiarid regions. *Agricultural water management*, *89*(3), 275–286.

Gebler, S., Hendricks Franssen, H.-J., Pütz, T., Post, H., Schmidt, M., & Vereecken, H. (2015). Actual evapotranspiration and precipitation measured by lysimeters: a comparison with eddy covariance and tipping bucket. *Hydrology and earth system sciences*, *19*(5), 2145–2161.

Gemitzi, A., Dalampakis, P., & Falalakis, G. (2021). Detecting geothermal anomalies using landsat 8 thermal infrared remotely sensed data. *International Journal of Applied Earth Observation and Geoinformation*, *96*, 102283.

Gergel, D. R., Nijssen, B., Abatzoglou, J. T., Lettenmaier, D. P., & Stumbaugh, M. R. (2017). Ef-

fects of climate change on snowpack and fire potential in the western usa. *Climatic Change*, *141*(2), 287–299.

Ghayour, L., Neshat, A., Paryani, S., Shahabi, H., Shirzadi, A., Chen, W., ... others (2021). Performance evaluation of sentinel-2 and landsat 8 oli data for land cover/use classification using a comparison between machine learning algorithms. *Remote Sensing*, *13*(7), 1349.

Ghiberto, P. J., Libardi, P. L., Brito, A. d. S., & Trivelin, P. C. O. (2011). Components of the water balance in soil with sugarcane crops. *Agricultural Water Management*, *102*(1), 1–7.

Gianquinto, G., Orsini, F., Fecondini, M., Mezzetti, M., Sambo, P., & Bona, S. (2011). A methodological approach for defining spectral indices for assessing tomato nitrogen status and yield. *European Journal of Agronomy*, *35*(3), 135–143.

Gilabert, M., Garcıa-Haro, F., & Melia, J. (2000). A mixture modeling approach to estimate vegetation parameters for heterogeneous canopies in remote sensing. *Remote Sensing of Environment*, *72*(3), 328–345.

Gilabert, M., González-Piqueras, J., Garcıa-Haro, F., & Meliá, J. (2002). A generalized soil-adjusted vegetation index. *Remote Sensing of environment*, *82*(2-3), 303–310.

Gillies, R., Kustas, W., & Humes, K. (1997). A verification of the'triangle'method for obtaining surface soil water content and energy fluxes from remote measurements of the normalized difference vegetation index (ndvi) and surface e. *International journal of remote sensing*, *18*(15), 3145–3166.

Gillies, R. R., & Carlson, T. N. (1995). Thermal remote sensing of surface soil water content with partial vegetation cover for incorporation into climate models. *Journal of Applied Meteorology and Climatology*, *34*(4), 745–756.

Glenn, E. P., Nagler, P. L., & Huete, A. R. (2010). Vegetation index methods for estimating evapotranspiration by remote sensing. *Surveys in Geophysics*, *31*(6), 531–555.

Godfray, H., Pretty, J., Thomas, S., Warham, E., & Beddington, J. (2011). Linking policy on climate and food. *Science*, *331*(6020), 1013–1014.

Gong, D., Kang, S., Yao, L., & Zhang, L. (2007). Estimation of evapotranspiration and its compo-

nents from an apple orchard in northwest china using sap flow and water balance methods. *Hydrological Processes: An International Journal*, *21*(7), 931–938.

Gong, P., Miller, J. R., & Spanner, M. (1994). Forest canopy closure from classification and spectral unmixing of scene components-multisensor evaluation of an open canopy. *IEEE Transactions on Geoscience and Remote Sensing*, *32*(5), 1067–1080.

González-Audícana, M., Saleta, J. L., Catalán, R. G., & García, R. (2004). Fusion of multispectral and panchromatic images using improved ihs and pca mergers based on wavelet decomposition. *IEEE Transactions on Geoscience and Remote sensing*, *42*(6), 1291–1299.

Gonzalez-Dugo, M., Neale, C., Mateos, L., Kustas, W., Prueger, J., Anderson, M., & Li, F. (2009). A comparison of operational remote sensing-based models for estimating crop evapotranspiration. *Agricultural and Forest Meteorology*, *149*(11), 1843–1853.

Goodman, J. A., & Ustin, S. L. (2007). Classification of benthic composition in a coral reef environment using spectral unmixing. *Journal of Applied Remote Sensing*, *1*(1), 011501.

Goudriaan, J. (1977). *Crop micrometeorology: a simulation study*. Wageningen University and Research.

Goudriaan, J., & Van Laar, H. (1994). Modelling potential crop growth processes. current issues in production ecology. *Kluwer Academic Publishers. doi*, *10*, 978–94.

Goulden, M. L., Daube, B. C., Fan, S.-M., Sutton, D. J., Bazzaz, A., Munger, J. W., & Wofsy, S. C. (1997). Physiological responses of a black spruce forest to weather. *Journal of Geophysical Research: Atmospheres*, *102*(D24), 28987–28996.

Gowda, P., Chavez, J., Colaizzi, P., Evett, S., Howell, T., & Tolk, J. (2007). Remote sensing based energy balance algorithms for mapping et: Current status and future challenges. *Transactions of the ASABE*, *50*(5), 1639–1644.

Graetz, R., & Gentle, M. (1982). The relationships between reflectance in the landsat wavebands and the composition of an australian semi-arid shrub rangeland. *Photogrammetric Engineering and Remote Sensing*, *48*(11), 1721–1730.

Granata, F. (2019). Evapotranspiration evaluation models based on machine learning algo-

rithms—a comparative study. *Agricultural Water Management*, *217*, 303–315.

Grassini, P., Yang, H., Irmak, S., Thorburn, J., Burr, C., & Cassman, K. G. (2011). High-yield irrigated maize in the western us corn belt: Ii. irrigation management and crop water productivity. *Field crops research*, *120*(1), 133–141.

Grömping, U. (2009). Variable importance assessment in regression: linear regression versus random forest. *The American Statistician*, *63*(4), 308–319.

Grossmann, A., Kronland-Martinet, R., & Morlet, J. (1990). Reading and understanding continuous wavelet transforms. In *Wavelets* (pp. 2–20). Springer.

Grossmann, A., & Morlet, J. (1984). Decomposition of hardy functions into square integrable wavelets of constant shape. *SIAM journal on mathematical analysis*, *15*(4), 723–736.

Gruber, A., Su, C.-H., Zwieback, S., Crow, W., Dorigo, W., & Wagner, W. (2016). Recent advances in (soil moisture) triple collocation analysis. *International Journal of Applied Earth Observation and Geoinformation*, *45*, 200–211.

Guillevic, P. C., Olioso, A., Hook, S. J., Fisher, J. B., Lagouarde, J.-P., & Vermote, E. F. (2019). Impact of the revisit of thermal infrared remote sensing observations on evapotranspiration uncertainty—a sensitivity study using ameriflux data. *Remote Sensing*, *11*(5), 573.

Guitjens, J. C. (1982). Models of alfalfa yield and evapotranspiration. *Journal of the irrigation and drainage division*, *108*(3), 212–222.

Guo, J., Mei, X., Lu, Z., & Zhao, Q.-s. (2004). Field evapotranspiration measurement based on eddy covariance technology. *Scientia Agricultura Sinica*, *37*(8), 1172–1176.

Gurjar, S., & Padmanabhan, N. (2005). Study of various resampling techniques for high-resolution remote sensing imagery. *Journal of the Indian Society of Remote Sensing*, *33*(1), 113–120.

Gurski, B. C., de Souza, J. L. M., Jerszurki, D., Armindo, R. A., & Evangelista, A. W. P. (2016). Periodicity of crop coefficient and soil water depletion fraction in a climatological water balance. *African Journal of Agricultural Research*, *11*(45), 4619–4626.

Gutman, G., & Ignatov, A. (1998). The derivation of the green vegetation fraction from noaa/avhrr data for use in numerical weather prediction models. *International Journal of remote sens-*

ing, *19*(8), 1533–1543.

Ha, W., Gowda, P. H., & Howell, T. A. (2013a). A review of downscaling methods for remote sensing-based irrigation management: Part i. *Irrigation Science*, *31*(4), 831–850.

Ha, W., Gowda, P. H., & Howell, T. A. (2013b). A review of potential image fusion methods for remote sensing-based irrigation management: Part ii. *Irrigation Science*, *31*(4), 851–869.

Ha, W., Gowda, P. H., Howell, T. A., Paul, G., Hernandez, J. E., & Basu, S. (2010). Downscaling surface temperature image with tsharp. In *5th national decennial irrigation conference proceedings, 5-8 december 2010, phoenix convention center, phoenix, arizona usa* (p. 1).

Hafeez, M., Chatha, Z. A., Khan, A. A., Bakhsh, A., Basit, A., & Tahira, F. (2020b). Estimating reference evapotranspiration by hargreaves and blaney-criddle methods in humid subtropical conditions. *Current Research in Agricultural Sciences*, *7*(1), 15–22.

Hafeez, M., Chatha, Z. A., Khan, A. A., Gulshan, A. B., Basit, A., & Tahira, F. (2020a). Comparative analysis of reference evapotranspiration by hargreaves and blaney-criddle equations in semi-arid climatic conditions. *Current Research in Agricultural Sciences*, *7*(2), 52–57.

Hall, F. G., Huemmrich, K. F., Goetz, S. J., Sellers, P. J., & Nickeson, J. E. (1992). Satellite remote sensing of surface energy balance: Success, failures, and unresolved issues in fife. *Journal of Geophysical Research: Atmospheres*, *97*(D17), 19061–19089.

Halliwell, D. H., & Rouse, W. R. (1989). A comparison of sensible and latent heat flux calculations using the bowen ratio and aerodynamic methods. *Journal of Atmospheric and Oceanic Technology*, *6*(4), 563–574.

Ham, J. M. (2005). Useful equations and tables in micrometeorology. *Micrometeorology in agricultural systems*, *47*, 533–560.

Han, L., Yang, G., Dai, H., Xu, B., Yang, H., Feng, H., … Yang, X. (2019). Modeling maize above-ground biomass based on machine learning approaches using uav remote-sensing data. *Plant methods*, *15*(1), 1–19.

Han, M., Zhang, H., Chávez, J. L., Ma, L., Trout, T. J., & DeJonge, K. C. (2018). Improved soil water deficit estimation through the integration of canopy temperature measurements into a

soil water balance model. *Irrigation Science*, *36*(3), 187–201.

Hansen, M., DeFries, R., Townshend, J., Carroll, M., Dimiceli, C., & Sohlberg, R. (2003). Global percent tree cover at a spatial resolution of 500 meters: First results of the modis vegetation continuous fields algorithm. *Earth Interactions*, *7*(10), 1–15.

Hargreaves, G. H. (1975). Moisture availability and crop production. *Transactions of the ASAE*, *18*(5), 980–0984.

Hasegawa, K., Matsuyama, H., Tsuzuki, H., & Sweda, T. (2006). The effect of bi-directional reflectance distribution function on the estimation of vegetation indices and leaf area index (lai) a case study of the vegetation in succession stages after forest fire in northwestern canada. *Journal of the Remote Sensing Society of Japan*, *26*(3), 186–201.

Hasegawa, K., Matsuyama, H., Tsuzuki, H., & Sweda, T. (2010). Improving the estimation of leaf area index by using remotely sensed ndvi with brdf signatures. *Remote Sensing of Environment*, *114*(3), 514–519.

Hassan, D. F., Abdalkadhum, A. J., Mohammed, R. J., & Shaban, A. (2022). Integration remote sensing and meteorological data to monitoring plant phenology and estimation crop coefficient and evapotranspiration. *Journal of Ecological Engineering*, *23*(4), 325–335.

Hatfield, J., Kanemasu, E., Asrar, G., Jackson, R., Pinter Jr, P., Reginato, R., & Idso, S. (1985). Leaf-area estimates from spectral measurements over various planting dates of wheat. *International Journal of Remote Sensing*, *6*(1), 167–175.

He, H. S., Ventura, S. J., & Mladenoff, D. J. (2002). Effects of spatial aggregation approaches on classified satellite imagery. *International Journal of Geographical Information Science*, *16*(1), 93–109.

Heilman, J., Heilman, W., & Moore, D. G. (1982). Evaluating the crop coefficient using spectral reflectance. *Agronomy Journal*, *74*(6), 967–971.

Helbig, M., Waddington, J. M., Alekseychik, P., Amiro, B. D., Aurela, M., Barr, A. G., ... others (2020). Increasing contribution of peatlands to boreal evapotranspiration in a warming climate. *Nature Climate Change*, *10*(6), 555–560.

Helsel, D. R., & Hirsch, R. M. (1992). *Statistical methods in water resources* (Vol. 49). Elsevier.

Hemakumara, H., Chandrapala, L., & Moene, A. F. (2003). Evapotranspiration fluxes over mixed vegetation areas measured from large aperture scintillometer. *Agricultural water management*, *58*(2), 109–122.

Henderson-Sellers, B. (1984). A new formula for latent heat of vaporization of water as a function of temperature. *Quarterly Journal of the Royal Meteorological Society*, *110*(466), 1186–1190.

Heusinkveld, B. G., Jacobs, A., Holtslag, A., & Berkowicz, S. (2004). Surface energy balance closure in an arid region: role of soil heat flux. *Agricultural and Forest Meteorology*, *122*(1-2), 21–37.

Hilker, T., Wulder, M. A., Coops, N. C., Seitz, N., White, J. C., Gao, F., ... Stenhouse, G. (2009). Generation of dense time series synthetic landsat data through data blending with modis using a spatial and temporal adaptive reflectance fusion model. *Remote Sensing of Environment*, *113*(9), 1988–1999.

Hinojosa, L., Kumar, N., Gill, K. S., & Murphy, K. M. (2019). Spectral reflectance indices and physiological parameters in quinoa under contrasting irrigation regimes. *Crop Science*, *59*(5), 1927–1944.

Hinton, J. (1996). Gis and remote sensing integration for environmental applications. *International Journal of Geographical Information Systems*, *10*(7), 877–890.

Hoffman, G. J., Evans, R. G., Jensen, M. E., Martin, D. L., & Elliott, R. L. (2007). *Design and operation of farm irrigation systems*. American Society of Agricultural and Biological Engineers St. Joseph, MI.

Hollander, M., Wolfe, D. A., & Chicken, E. (2013). *Nonparametric statistical methods* (Vol. 751). John Wiley & Sons.

Hollinger, D., & Richardson, A. (2005). Uncertainty in eddy covariance measurements and its application to physiological models. *Tree physiology*, *25*(7), 873–885.

Homer, C. G., Aldridge, C. L., Meyer, D. K., & Schell, S. J. (2012). Multi-scale remote sensing

sagebrush characterization with regression trees over wyoming, usa: laying a foundation for monitoring. *International Journal of Applied Earth Observation and Geoinformation*, *14*(1), 233–244.

Hong, G., Zhang, Y., & Mercer, B. (2009). A wavelet and ihs integration method to fuse high resolution sar with moderate resolution multispectral images. *Photogrammetric Engineering & Remote Sensing*, *75*(10), 1213–1223.

Hope, T. M. (2020). Linear regression. In *Machine learning* (pp. 67–81). Elsevier.

Hopkins, W. G., et al. (2009). *Introduction to plant physiology*. John Wiley & Sons.

Houborg, R., & McCabe, M. F. (2016). High-resolution ndvi from planet's constellation of earth observing nano-satellites: A new data source for precision agriculture. *Remote Sensing*, *8*(9), 768.

Houborg, R., & McCabe, M. F. (2018a). A cubesat enabled spatio-temporal enhancement method (cestem) utilizing planet, landsat and modis data. *Remote Sensing of Environment*, *209*, 211–226.

Houborg, R., & McCabe, M. F. (2018b). Daily retrieval of ndvi and lai at 3 m resolution via the fusion of cubesat, landsat, and modis data. *Remote Sensing*, *10*(6), 890.

Howell, T., Schneider, A., Dusek, D., Marek, T., & Steiner, J. (1995). Calibration and scale performance of bushland weighing lysimeters. *Transactions of the ASAE*, *38*(4), 1019–1024.

Howell, T. A., Schneider, A. D., & Jensen, M. E. (1991). History of lysimeter design and use for evapotranspiration measurements. In *Grouting in geotechnical engineering* (pp. 1–9).

Hu, Y. H., Lee, H., & Scarpace, F. (1999). Optimal linear spectral unmixing. *IEEE Transactions on Geoscience and Remote Sensing*, *37*(1), 639–644.

Huang, D., Wang, J., & Khayatnezhad, M. (2021). Estimation of actual evapotranspiration using soil moisture balance and remote sensing. *Iranian Journal of Science and Technology, Transactions of Civil Engineering*, *45*(4), 2779–2786.

Huber, P. J. (2004). *Robust statistics* (Vol. 523). John Wiley & Sons.

Huete, A. R. (1988). A soil-adjusted vegetation index (savi). *Remote sensing of environment*,

25(3), 295–309.

Hultquist, C., Chen, G., & Zhao, K. (2014). A comparison of gaussian process regression, random forests and support vector regression for burn severity assessment in diseased forests. *Remote sensing letters*, *5*(8), 723–732.

Hupet, F., & Vanclooster, M. (2002). Intraseasonal dynamics of soil moisture variability within a small agricultural maize cropped field. *Journal of Hydrology*, *261*(1-4), 86–101.

Immitzer, M., Vuolo, F., & Atzberger, C. (2016). First experience with sentinel-2 data for crop and tree species classifications in central europe. *Remote sensing*, *8*(3), 166.

Irmak, A., & Irmak, S. (2008). Reference and crop evapotranspiration in south central nebraska. ii: Measurement and estimation of actual evapotranspiration for corn. *Journal of Irrigation and Drainage Engineering*, *134*(6), 700–715.

Jackson, R. D., Moran, M. S., Gay, L. W., & Raymond, L. H. (1987). Evaluating evaporation from field crops using airborne radiometry and ground-based meteorological data. *Irrigation Science*, *8*(2), 81–90.

Jacob, F., Olioso, A., Gu, X. F., Su, Z., & Seguin, B. (2002). Mapping surface fluxes using airborne visible, near infrared, thermal infrared remote sensing data and a spatialized surface energy balance model. *Agronomie*, *22*(6), 669–680.

Jain, S., Sachdeva, M., Dubey, P., & Vijan, A. (2019). Multi-sensor image fusion using intensity hue saturation technique. In *International conference on advanced informatics for computing research* (pp. 147–157).

Jamieson, P., Porter, J., & Wilson, D. (1991). A test of the computer simulation model arcwheat1 on wheat crops grown in new zealand. *Field crops research*, *27*(4), 337–350.

Jarvis, P. (1976). The interpretation of the variations in leaf water potential and stomatal conductance found in canopies in the field. *Philosophical Transactions of the Royal Society of London. B, Biological Sciences*, *273*(927), 593–610.

Jayanthi, H., Neale, C. M., & Wright, J. L. (2007). Development and validation of canopy reflectance-based crop coefficient for potato. *Agricultural water management*, *88*(1-3), 235–

246.

Jensen, M. (1968). *Water consumption by agricultural plants. chap. 1 in water deficits and plant growth. vol. ii, tt kozlowski, ed.* Academic Press, New York.

Jensen, M., Burman, R., & Allen, R. (1990). Evapotranspiration and irrigation water requirements. asce manuals and reports on engineering practice no. 70. am. soc. civil eng., new york. *Evapotranspiration and irrigation water requirements. ASCE Manuals and Reports on Engineering Practice No. 70. Am. Soc. of Civil Engineers, New York.*.

Jeong, S., Ko, J., Choi, J., Xue, W., & Yeom, J.-m. (2018). Application of an unmanned aerial system for monitoring paddy productivity using the grami-rice model. *International Journal of Remote Sensing*, *39*(8), 2441–2462.

Ji, L., Zhang, L., Wylie, B. K., & Rover, J. (2011). On the terminology of the spectral vegetation index (nir- swir)/(nir+ swir). *International journal of remote sensing*, *32*(21), 6901–6909.

Jia, X., Dukes, M. D., Jacobs, J. M., & Irmak, S. (2006). Weighing lysimeters for evapotranspiration research in a humid environment. *Transactions of the ASABE*, *49*(2), 401–412.

Jiang, C., Ryu, Y., Fang, H., Myneni, R., Claverie, M., & Zhu, Z. (2017). Inconsistencies of interannual variability and trends in long-term satellite leaf area index products. *Global Change Biology*, *23*(10), 4133–4146.

Jiang, G., & Wang, W. (2017). Error estimation based on variance analysis of k-fold cross-validation. *Pattern Recognition*, *69*, 94–106.

Jiang, Y., Lu, Z., Li, S., Lei, Y., Chu, Q., Yin, X., & Chen, F. (2020). Large-scale and high-resolution crop mapping in china using sentinel-2 satellite imagery. *Agriculture*, *10*(10), 433.

Jiang, Z., Huete, A. R., Chen, J., Chen, Y., Li, J., Yan, G., & Zhang, X. (2006). Analysis of ndvi and scaled difference vegetation index retrievals of vegetation fraction. *Remote sensing of environment*, *101*(3), 366–378.

Jing-xua, Y., Hua, S., & Yun-peng, W. (2010). Distrad model for thermal sub-pixel mapping in high vegetation area. *Remote Sensing Technology and Application*, *25*(3), 346–352.

Johansen, K., Coops, N. C., Gergel, S. E., & Stange, Y. (2007). Application of high spatial resolution satellite imagery for riparian and forest ecosystem classification. *Remote sensing of Environment*, *110*(1), 29–44.

Johnson, L., Herwitz, S., Dunagan, S., Lobitz, B., Sullivan, D., & Slye, R. (2003). Collection of ultra high spatial and spectral resolution image data over california vineyards with a small uav. In *Proceedings of the 30th international symposium on remote sensing of environment* (Vol. 20).

Johnson, L. F., & Trout, T. J. (2012). Satellite ndvi assisted monitoring of vegetable crop evapotranspiration in california's san joaquin valley. *Remote Sensing*, *4*(2), 439–455.

Jolliffe, I. T. (1982). A note on the use of principal components in regression. *Journal of the Royal Statistical Society: Series C (Applied Statistics)*, *31*(3), 300–303.

Jones, H. G. (2004). Irrigation scheduling: advantages and pitfalls of plant-based methods. *Journal of experimental botany*, *55*(407), 2427–2436.

Jongschaap, R. E. (2006). Run-time calibration of simulation models by integrating remote sensing estimates of leaf area index and canopy nitrogen. *European Journal of Agronomy*, *24*(4), 316–324.

Jordan, M. I., & Mitchell, T. M. (2015). Machine learning: Trends, perspectives, and prospects. *Science*, *349*(6245), 255–260.

Jung, Y. (2018). Multiple predicting k-fold cross-validation for model selection. *Journal of Nonparametric Statistics*, *30*(1), 197–215.

Jury, W., & Tanner, C. (1975). Advection modification of the priestley and taylor evapotranspiration formula 1. *Agronomy Journal*, *67*(6), 840–842.

Kaimal, J. C., & Finnigan, J. J. (1994). *Atmospheric boundary layer flows: their structure and measurement*. Oxford university press.

Kamble, B., Kilic, A., & Hubbard, K. (2013). Estimating crop coefficients using remote sensing-based vegetation index. *Remote sensing*, *5*(4), 1588–1602.

Kandasamy, S., Baret, F., Verger, A., Neveux, P., & Weiss, M. (2013). A comparison of methods for

smoothing and gap filling time series of remote sensing observations–application to modis lai products. *Biogeosciences*, *10*(6), 4055–4071.

Kasampalis, D. A., Alexandridis, T. K., Deva, C., Challinor, A., Moshou, D., & Zalidis, G. (2018). Contribution of remote sensing on crop models: a review. *Journal of Imaging*, *4*(4), 52.

Katerji, N., & Perrier, A. (1983). Modelisation de l'evapotranspiration reelle etr d'une parcelle de luzerne. role d'un coefficient cultural. *Agronomie*, *3*(6), 513–521.

Katul, G. G., Mahrt, L., Poggi, D., & Sanz, C. (2004). One-and two-equation models for canopy turbulence. *Boundary-layer meteorology*, *113*(1), 81–109.

Kaur, S., Bansal, R., Mittal, M., Goyal, L. M., Kaur, I., Verma, A., & Son, L. H. (2019). Mixed pixel decomposition based on extended fuzzy clustering for single spectral value remote sensing images. *Journal of the Indian Society of Remote Sensing*, *47*(3), 427–437.

Kausar, N., Belhaouari Samir, B., Abdullah, A., Ahmad, I., & Hussain, M. (2011). A review of classification approaches using support vector machine in intrusion detection. In *Informatics engineering and information science: International conference, icieis 2011, kuala lumpur, malaysia, november 14-16, 2011, proceedings, part iii* (pp. 24–34).

Kavitha, S., Varuna, S., & Ramya, R. (2016). A comparative analysis on linear regression and support vector regression. In *2016 online international conference on green engineering and technologies (ic-get)* (pp. 1–5).

Kelly, J., Kljun, N., Olsson, P.-O., Mihai, L., Liljeblad, B., Weslien, P., ... Eklundh, L. (2019). Challenges and best practices for deriving temperature data from an uncalibrated uav thermal infrared camera. *Remote Sensing*, *11*(5), 567.

Keshava, N., & Mustard, J. F. (2002). Spectral unmixing. *IEEE signal processing magazine*, *19*(1), 44–57.

Khan, M. S., Liaqat, U. W., Baik, J., & Choi, M. (2018). Stand-alone uncertainty characterization of gleam, gldas and mod16 evapotranspiration products using an extended triple collocation approach. *Agricultural and Forest Meteorology*, *252*, 256–268.

Khanal, S., Fulton, J., & Shearer, S. (2017). An overview of current and potential applications of

thermal remote sensing in precision agriculture. *Computers and Electronics in Agriculture*, *139*, 22–32.

Kibria, S., Masia, S., Sušnik, J., & Hessels, T. M. (2021). Critical comparison of actual evapotranspiration estimates using ground based, remotely sensed, and simulated data in the usa. *Agricultural Water Management*, *248*, 106753.

Kilic, A., Allen, R., Trezza, R., Ratcliffe, I., Kamble, B., Robison, C., & Ozturk, D. (2016). Sensitivity of evapotranspiration retrievals from the metric processing algorithm to improved radiometric resolution of landsat 8 thermal data and to calibration bias in landsat 7 and 8 surface temperature. *Remote Sensing of Environment*, *185*, 198–209.

Kimm, H., Guan, K., Jiang, C., Peng, B., Gentry, L. F., Wilkin, S. C., ... others (2020). Deriving high-spatiotemporal-resolution leaf area index for agroecosystems in the us corn belt using planet labs cubesat and stair fusion data. *Remote Sensing of Environment*, *239*, 111615.

Kington IV, J., Jordahl, K. A., Kanwar, A. N., Kapadia, A., Schönert, M., & Wurster, K. (2019). Spatially and temporally consistent smallsat-derived basemaps for analytic applications. In *Agu fall meeting abstracts* (Vol. 2019, pp. IN13B–0716).

Kleissl, J., Gomez, J., Hong, S.-H., Hendrickx, J., Rahn, T., & Defoor, W. (2008). Large aperture scintillometer intercomparison study. *Boundary-Layer Meteorology*, *128*(1), 133–150.

Kljun, N., Calanca, P., Rotach, M., & Schmid, H. P. (2015). A simple two-dimensional parameterisation for flux footprint prediction (ffp). *Geoscientific Model Development*, *8*(11), 3695–3713.

Kruskal, W. H., & Wallis, W. A. (1952). Use of ranks in one-criterion variance analysis. *Journal of the American statistical Association*, *47*(260), 583–621.

Kullberg, E. G., DeJonge, K. C., & Chávez, J. L. (2017). Evaluation of thermal remote sensing indices to estimate crop evapotranspiration coefficients. *Agricultural Water Management*, *179*, 64–73.

Kustas, W., Alfieri, J., Nieto, H., Wilson, T., Gao, F., & Anderson, M. (2019). Utility of the two-source energy balance (tseb) model in vine and interrow flux partitioning over the growing

season. *Irrigation Science*, *37*(3), 375–388.

Kustas, W. P., Choudhury, B. J., Moran, M. S., Reginato, R. J., Jackson, R. D., Gay, L. W., & Weaver, H. L. (1989). Determination of sensible heat flux over sparse canopy using thermal infrared data. *Agricultural and forest meteorology*, *44*(3-4), 197–216.

Kustas, W. P., & Daughtry, C. S. (1990). Estimation of the soil heat flux/net radiation ratio from spectral data. *Agricultural and Forest Meteorology*, *49*(3), 205–223.

Kustas, W. P., & Norman, J. M. (2000). A two-source energy balance approach using directional radiometric temperature observations for sparse canopy covered surfaces. *Agronomy Journal*, *92*(5), 847–854.

Kustas, W. P., Norman, J. M., Anderson, M. C., & French, A. N. (2003). Estimating subpixel surface temperatures and energy fluxes from the vegetation index–radiometric temperature relationship. *Remote sensing of environment*, *85*(4), 429–440.

Kustu, M. D., Fan, Y., & Robock, A. (2010). Large-scale water cycle perturbation due to irrigation pumping in the us high plains: A synthesis of observed streamflow changes. *Journal of Hydrology*, *390*(3-4), 222–244.

Kutikoff, S., Lin, X., Evett, S., Gowda, P., Moorhead, J., Marek, G., ... Brauer, D. (2019). Heat storage and its effect on the surface energy balance closure under advective conditions. *Agricultural and Forest Meteorology*, *265*, 56–69.

Lafleur, P. M. (1992). Energy balance and evapotranspiration from a subarctic forest. *Agricultural and Forest Meteorology*, *58*(3-4), 163–175.

Larcher, W. (1983). *Physiological plant ecology, corrected printing of the second printing.* Springer-Verlag, New York.

Latif, S. D. (2021). Developing a boosted decision tree regression prediction model as a sustainable tool for compressive strength of environmentally friendly concrete. *Environmental Science and Pollution Research*, *28*(46), 65935–65944.

Lechner, A. M., Foody, G. M., & Boyd, D. S. (2020). Applications in remote sensing to forest ecology and management. *One Earth*, *2*(5), 405–412.

Leys, C., Ley, C., Klein, O., Bernard, P., & Licata, L. (2013). Detecting outliers: Do not use standard deviation around the mean, use absolute deviation around the median. *Journal of experimental social psychology*, *49*(4), 764–766.

Li, F., Kustas, W. P., Prueger, J. H., Neale, C. M., & Jackson, T. J. (2005). Utility of remote sensing–based two-source energy balance model under low-and high-vegetation cover conditions. *Journal of Hydrometeorology*, *6*(6), 878–891.

Li, J., Pei, Y., Zhao, S., Xiao, R., Sang, X., & Zhang, C. (2020). A review of remote sensing for environmental monitoring in china. *Remote Sensing*, *12*(7), 1130.

Li, L., Yu, Q., Su, Z., & Van Der Tol, C. (2009). A simple method using climatic variables to estimate canopy temperature, sensible and latent heat fluxes in a winter wheat field on the north china plain. *Hydrological Processes: An International Journal*, *23*(5), 665–674.

Li, M., Zhou, Y., Wang, Y., Singh, V. P., Li, Z., & Li, Y. (2020). An ecological footprint approach for cropland use sustainability based on multi-objective optimization modelling. *Journal of Environmental Management*, *273*, 111147.

Li, X., Gentine, P., Lin, C., Zhou, S., Sun, Z., Zheng, Y., ... Zheng, C. (2019). A simple and objective method to partition evapotranspiration into transpiration and evaporation at eddy-covariance sites. *Agricultural and Forest Meteorology*, *265*, 171–182.

Li, Z., Zhang, H. K., Roy, D. P., Yan, L., Huang, H., & Li, J. (2017). Landsat 15-m panchromatic-assisted downscaling (lpad) of the 30-m reflective wavelength bands to sentinel-2 20-m resolution. *Remote Sensing*, *9*(7), 755.

Liaghat, S., Balasundram, S. K., et al. (2010). A review: The role of remote sensing in precision agriculture. *American journal of agricultural and biological sciences*, *5*(1), 50–55.

Lillesand, T. M., Kiefer, R. W., & Chipman, J. (2015). Remote sensing and image interpretation. john willey & sons. *Inc, United States of America*.

Liou, Y.-A., & Kar, S. K. (2014). Evapotranspiration estimation with remote sensing and various surface energy balance algorithms—a review. *Energies*, *7*(5), 2821–2849.

Liu, H., Gao, Z., & Katul, G. G. (2021). Non-closure of surface energy balance linked to asym-

metric turbulent transport of scalars by large eddies. *Journal of Geophysical Research: Atmospheres*, *126*(7), e2020JD034474.

Liu, J. (2000). Smoothing filter-based intensity modulation: A spectral preserve image fusion technique for improving spatial details. *International Journal of Remote Sensing*, *21*(18), 3461–3472.

Liu, S. M., Xu, Z. W., Wang, W., Jia, Z., Zhu, M., Bai, J., & Wang, J. (2011). A comparison of eddy-covariance and large aperture scintillometer measurements with respect to the energy balance closure problem. *Hydrology and Earth System Sciences*, *15*(4), 1291–1306.

Lobell, D. B., Ortiz-Monasterio, J. I., Asner, G. P., Naylor, R. L., & Falcon, W. P. (2005). Combining field surveys, remote sensing, and regression trees to understand yield variations in an irrigated wheat landscape. *Agronomy Journal*, *97*(1), 241–249.

Locascio, S. J. (2005). Management of irrigation for vegetables: Past, present, and future. *HortTechnology*, *15*(3), 482–485.

Loh, W.-Y. (2011). Classification and regression trees. *Wiley interdisciplinary reviews: data mining and knowledge discovery*, *1*(1), 14–23.

Long, D., & Singh, V. P. (2012). A two-source trapezoid model for evapotranspiration (ttme) from satellite imagery. *Remote Sensing of Environment*, *121*, 370–388.

López-Urrea, R., Montoro, A., Mañas, F., López-Fuster, P., & Fereres, E. (2012). Evapotranspiration and crop coefficients from lysimeter measurements of mature 'tempranillo'wine grapes. *Agricultural water management*, *112*, 13–20.

Lumley, J. L. (1979). Computational modeling of turbulent flows. *Advances in applied mechanics*, *18*, 123–176.

Lute, A., Abatzoglou, J., & Hegewisch, K. (2015). Projected changes in snowfall extremes and interannual variability of snowfall in the western u nited s tates. *Water Resources Research*, *51*(2), 960–972.

Lyons, M. B., Keith, D. A., Phinn, S. R., Mason, T. J., & Elith, J. (2018). A comparison of resampling methods for remote sensing classification and accuracy assessment. *Remote*

Sensing of Environment, *208*, 145–153.

Ma, W., Pan, Z., Guo, J., & Lei, B. (2019). Achieving super-resolution remote sensing images via the wavelet transform combined with the recursive res-net. *IEEE Transactions on Geoscience and Remote Sensing*, *57*(6), 3512–3527.

Ma, Y., Liu, S., Song, L., Xu, Z., Liu, Y., Xu, T., & Zhu, Z. (2018). Estimation of daily evapotranspiration and irrigation water efficiency at a landsat-like scale for an arid irrigation area using multi-source remote sensing data. *Remote Sensing of Environment*, *216*, 715–734.

MacDonald, G. M. (2007). Severe and sustained drought in southern california and the west: Present conditions and insights from the past on causes and impacts. *Quaternary International*, *173*, 87–100.

Maček, U., Bezak, N., & Šraj, M. (2018). Reference evapotranspiration changes in slovenia, europe. *Agricultural and forest meteorology*, *260*, 183–192.

Madugundu, R., Al-Gaadi, K. A., Tola, E., Hassaballa, A. A., & Patil, V. C. (2017). Performance of the metric model in estimating evapotranspiration fluxes over an irrigated field in saudi arabia using landsat-8 images. *Hydrology and Earth System Sciences*, *21*(12), 6135–6151.

Maes, W. H., & Steppe, K. (2019). Perspectives for remote sensing with unmanned aerial vehicles in precision agriculture. *Trends in plant science*, *24*(2), 152–164.

Maguire, M. S., Neale, C. M., & Woldt, W. E. (2021). Improving accuracy of unmanned aerial system thermal infrared remote sensing for use in energy balance models in agriculture applications. *Remote Sensing*, *13*(9), 1635.

Mahrt, L., & Vickers, D. (2004). Bulk formulation of the surface heat flux. *Boundary-Layer Meteorology*, *110*(3), 357–379.

Main-Knorn, M., Pflug, B., Louis, J., Debaecker, V., Müller-Wilm, U., & Gascon, F. (2017). Sen2cor for sentinel-2. In *Image and signal processing for remote sensing xxiii* (Vol. 10427, p. 1042704).

Mair, C., Kadoda, G., Lefley, M., Phalp, K., Schofield, C., Shepperd, M., & Webster, S. (2000). An investigation of machine learning based prediction systems. *Journal of systems and software*,

53(1), 23–29.

Malek, E., & Bingham, G. E. (1993). Comparison of the bowen ratio-energy balance and the water balance methods for the measurement of evapotranspiration. *Journal of Hydrology*, *146*, 209–220.

Mammone, A., Turchi, M., & Cristianini, N. (2009). Support vector machines. *Wiley Interdisciplinary Reviews: Computational Statistics*, *1*(3), 283–289.

Marceau, D. J., & Hay, G. J. (1999). Remote sensing contributions to the scale issue. *Canadian journal of remote sensing*, *25*(4), 357–366.

Margonis, A., Papaioannou, G., Kerkides, P., Kitsara, G., & Bourazanis, G. (2018). Canopy resistance and actual evapotranspiration over an olive orchard. *Water Resources Management*, *32*(15), 5007–5026.

Marshall, A. M., Abatzoglou, J. T., Link, T. E., & Tennant, C. J. (2019). Projected changes in interannual variability of peak snowpack amount and timing in the western united states. *Geophysical Research Letters*, *46*(15), 8882–8892.

Marshall, J., & Waring, R. (1986). Comparison of methods of estimating leaf-area index in old-growth douglas-fir. *Ecology*, *67*(4), 975–979.

Marta, S. (2018). Planet imagery product specifications. *Planet Labs: San Francisco, CA, USA*, 91.

Martin, G., & Plaza, A. (2011). Region-based spatial preprocessing for endmember extraction and spectral unmixing. *IEEE Geoscience and Remote Sensing Letters*, *8*(4), 745–749.

Martin, M., & Berdahl, P. (1984). Characteristics of infrared sky radiation in the united states. *Solar energy*, *33*(3-4), 321–336.

Martínez, B., & Gilabert, M. A. (2009). Vegetation dynamics from ndvi time series analysis using the wavelet transform. *Remote sensing of environment*, *113*(9), 1823–1842.

Massari, C., Crow, W., & Brocca, L. (2017). An assessment of the performance of global rainfall estimates without ground-based observations. *Hydrology and earth system sciences*, *21*(9), 4347–4361.

Massman, W. (1992). A surface energy balance method for partitioning evapotranspiration data into plant and soil components for a surface with partial canopy cover. *Water Resources Research*, *28*(6), 1723–1732.

Matese, A., Toscano, P., Di Gennaro, S. F., Genesio, L., Vaccari, F. P., Primicerio, J., ... Gioli, B. (2015). Intercomparison of uav, aircraft and satellite remote sensing platforms for precision viticulture. *Remote Sensing*, *7*(3), 2971–2990.

Matsushima, D. (2005). Relations between aerodynamic parameters of heat transfer and thermal-infrared thermometry in the bulk surface formulation. *Journal of the Meteorological Society of Japan. Ser. II*, *83*(3), 373–389.

Mauder, M., Cuntz, M., Drüe, C., Graf, A., Rebmann, C., Schmid, H. P., ... Steinbrecher, R. (2013). A strategy for quality and uncertainty assessment of long-term eddy-covariance measurements. *Agricultural and Forest Meteorology*, *169*, 122–135.

Mauder, M., Desjardins, R. L., & MacPherson, I. (2007). Scale analysis of airborne flux measurements over heterogeneous terrain in a boreal ecosystem. *Journal of Geophysical Research: Atmospheres*, *112*(D13).

Maulud, D., & Abdulazeez, A. M. (2020). A review on linear regression comprehensive in machine learning. *Journal of Applied Science and Technology Trends*, *1*(2), 140–147.

Maxwell, A. E., Warner, T. A., & Fang, F. (2018). Implementation of machine-learning classification in remote sensing: An applied review. *International Journal of Remote Sensing*, *39*(9), 2784–2817.

McCabe, M. F., Aragon, B., Houborg, R., & Mascaro, J. (2017). Cubesats in hydrology: Ultrahigh-resolution insights into vegetation dynamics and terrestrial evaporation. *Water Resources Research*, *53*(12), 10017–10024.

McCabe, M. F., & Wood, E. F. (2006). Scale influences on the remote estimation of evapotranspiration using multiple satellite sensors. *Remote Sensing of Environment*, *105*(4), 271–285.

McColl, K. A., Vogelzang, J., Konings, A. G., Entekhabi, D., Piles, M., & Stoffelen, A. (2014). Extended triple collocation: Estimating errors and correlation coefficients with respect to an

unknown target. *Geophysical research letters*, *41*(17), 6229–6236.

McDonald, R. I., & Girvetz, E. H. (2013). Two challenges for us irrigation due to climate change: increasing irrigated area in wet states and increasing irrigation rates in dry states. *PloS one*, *8*(6), e65589.

McShane, R. R., Driscoll, K. P., & Sando, R. (2017). A review of surface energy balance models for estimating actual evapotranspiration with remote sensing at high spatiotemporal resolution over large extents. *Scientific Investigations Report 2017–5087. Reston, VA: US Geological Survey. 19 p.*.

Meijninger, W., & De Bruin, H. (2000). The sensible heat fluxes over irrigated areas in western turkey determined with a large aperture scintillometer. *Journal of Hydrology*, *229*(1-2), 42–49.

Meyers, T. P., & Hollinger, S. E. (2004). An assessment of storage terms in the surface energy balance of maize and soybean. *Agricultural and Forest Meteorology*, *125*(1-2), 105–115.

Miller, J., & Miller, J. C. (2018). *Statistics and chemometrics for analytical chemistry*. Pearson education.

Mkhwanazi, M., Chávez, J. L., & Rambikur, E. H. (2012). Comparison of large aperture scintillometer and satellite-based energy balance models in sensible heat flux and crop evapotranspiration determination. *International Journal of Remote Sensing Applications*, *2*(1), 24–30.

Mohajane, M., Costache, R., Karimi, F., Pham, Q. B., Essahlaoui, A., Nguyen, H., … Oudija, F. (2021). Application of remote sensing and machine learning algorithms for forest fire mapping in a mediterranean area. *Ecological Indicators*, *129*, 107869.

Mohammadi, B., & Mehdizadeh, S. (2020). Modeling daily reference evapotranspiration via a novel approach based on support vector regression coupled with whale optimization algorithm. *Agricultural Water Management*, *237*, 106145.

Momeni, M., Zakeri, Z., Esfandiari, M., Behzadian, K., Zahedi, S., & Razavi, V. (2019). Comparative analysis of agricultural water pricing between azarbaijan provinces in iran and the

state of california in the us: A hydro-economic approach. *Agricultural Water Management*, *223*, 105724.

Monin, A., & Obukhov, A. (1954). Basic laws of turbulent mixing in the surface layer of the atmosphere. *Contrib. Geophys. Inst. Acad. Sci. USSR*, *151*(163), e187.

Montandon, L., & Small, E. (2008). The impact of soil reflectance on the quantification of the green vegetation fraction from ndvi. *Remote Sensing of Environment*, *112*(4), 1835–1845.

Monteith, J. (1973). Principles of environmental physics edward arnold. *London, 214p*.

Monteith, J., & Szeicz, G. (1961). The radiation balance of bare soil and vegetation. *Quarterly Journal of the Royal Meteorological Society*, *87*(372), 159–170.

Monteith, J. L. (1965). Evaporation and environment. In *Symposia of the society for experimental biology* (Vol. 19, pp. 205–234).

Moore, I. D., Norton, T. W., & Williams, J. E. (1993). Modelling environmental heterogeneity in forested landscapes. *Journal of Hydrology*, *150*(2-4), 717–747.

Moorhead, J. E., Marek, G. W., Gowda, P. H., Lin, X., Colaizzi, P. D., Evett, S. R., & Kutikoff, S. (2019). Evaluation of evapotranspiration from eddy covariance using large weighing lysimeters. *Agronomy*, *9*(2), 99.

Moran, M. S., Jackson, R. D., Raymond, L. H., Gay, L. W., & Slater, P. N. (1989). Mapping surface energy balance components by combining landsat thematic mapper and ground-based meteorological data. *Remote Sensing of Environment*, *30*(1), 77–87.

Mote, P. W., Hamlet, A. F., Clark, M. P., & Lettenmaier, D. P. (2005). Declining mountain snowpack in western north america. *Bulletin of the American meteorological Society*, *86*(1), 39–50.

Mulla, D. J. (2013). Twenty five years of remote sensing in precision agriculture: Key advances and remaining knowledge gaps. *Biosystems engineering*, *114*(4), 358–371.

Myint, S. W. (2010). Multi-resolution decomposition in relation to characteristic scales and local window sizes using an operational wavelet algorithm. *International Journal of Remote Sensing*, *31*(10), 2551–2572.

Naghibi, S. A., Pourghasemi, H. R., & Dixon, B. (2016). Gis-based groundwater potential mapping using boosted regression tree, classification and regression tree, and random forest machine learning models in iran. *Environmental monitoring and assessment*, *188*, 1–27.

Nakai, T., & Shimoyama, K. (2012). Ultrasonic anemometer angle of attack errors under turbulent conditions. *Agricultural and forest meteorology*, *162*, 14–26.

Nassar, A., Torres-Rua, A., Kustas, W., Alfieri, J., Hipps, L., Prueger, J., ... others (2021). Assessing daily evapotranspiration methodologies from one-time-of-day suas and ec information in the grapex project. *Remote sensing*, *13*(15), 2887.

Navalgund, R. R., Jayaraman, V., & Roy, P. (2007). Remote sensing applications: an overview. *current science*, 1747–1766.

Neale, C. M., Bausch, W. C., & Heermann, D. F. (1990). Development of reflectance-based crop coefficients for corn. *Transactions of the ASAE*, *32*(6), 1891–1900.

Ng, S. (2017). Principal component analysis to reduce dimension on digital image. *Procedia computer science*, *111*, 113–119.

Nikolov, N. T., & Zeller, K. F. (1992). A solar radiation algorithm for ecosystem dynamic models. *Ecological Modelling*, *61*(3-4), 149–168.

Niu, H., Hollenbeck, D., Zhao, T., Wang, D., & Chen, Y. (2020). Evapotranspiration estimation with small uavs in precision agriculture. *Sensors*, *20*(22), 6427.

Noble, W. S. (2006). What is a support vector machine? *Nature biotechnology*, *24*(12), 1565–1567.

Norman, J., Anderson, M., Kustas, W., French, A., Mecikalski, J., Torn, R., ... Tanner, B. (2003). Remote sensing of surface energy fluxes at 101-m pixel resolutions. *Water Resources Research*, *39*(8).

Norman, J., & Jarvis, P. (1975). Photosynthesis in sitka spruce (picea sitchensis (bong.) carr.): V. radiation penetration theory and a test case. *Journal of Applied Ecology*, 839–878.

Norman, J., et al. (1989). Synthesis of canopy processes. *Plant canopies: their growth, form and function*(31), 161.

Norman, J. M., Kustas, W. P., & Humes, K. S. (1995). Source approach for estimating soil and vegetation energy fluxes in observations of directional radiometric surface temperature. *Agricultural and Forest Meteorology*, *77*(3-4), 263–293.

Nti, I. K., Nyarko-Boateng, O., & Aning, J. (2021). Performance of machine learning algorithms with different k values in k-fold cross-validation. *J. Inf. Technol. Comput. Sci*, *6*, 61–71.

Nugent, P. W., Shaw, J. A., & Pust, N. J. (2013). Correcting for focal-plane-array temperature dependence in microbolometer infrared cameras lacking thermal stabilization. *Optical Engineering*, *52*(6), 061304.

Nunez, J., Otazu, X., Fors, O., Prades, A., Pala, V., & Arbiol, R. (1999). Multiresolution-based image fusion with additive wavelet decomposition. *IEEE Transactions on Geoscience and Remote sensing*, *37*(3), 1204–1211.

Ohmura, A. (1982). Objective criteria for rejecting data for bowen ratio flux calculations. *Journal of Applied Meteorology (1962-1982)*, 595–598.

Oncley, S. P., Foken, T., Vogt, R., Kohsiek, W., DeBruin, H. A., Bernhofer, C., ... others (2007). The energy balance experiment ebex-2000. part i: overview and energy balance. *Boundary-Layer Meteorology*, *123*(1), 1–28.

Ott, R. L., & Longnecker, M. T. (2015). *An introduction to statistical methods and data analysis*. Cengage Learning.

Pahlevan, N., Chittimalli, S. K., Balasubramanian, S. V., & Vellucci, V. (2019). Sentinel-2/landsat-8 product consistency and implications for monitoring aquatic systems. *Remote sensing of Environment*, *220*, 19–29.

Pajares, G. (2015). Overview and current status of remote sensing applications based on unmanned aerial vehicles (uavs). *Photogrammetric Engineering & Remote Sensing*, *81*(4), 281–330.

Pal, M. (2005). Random forest classifier for remote sensing classification. *International journal of remote sensing*, *26*(1), 217–222.

Pandya, M., Singh, R., Chaudhari, K., Murali, K., Kirankumar, A., Dadhwal, V., & Parihar, J. (2007). Spectral characteristics of sensors onboard irs-1d and p6 satellites: Estimation and

their influence on surface reflectance and ndvi. *Journal of the Indian Society of Remote Sensing*, *35*(4), 333–350.

Park, J., Baik, J., & Choi, M. (2017). Satellite-based crop coefficient and evapotranspiration using surface soil moisture and vegetation indices in northeast asia. *Catena*, *156*, 305–314.

Park, J., & Kang, M. (2004). Spatially adaptive multi-resolution multispectral image fusion. *International Journal of Remote Sensing*, *25*(23), 5491–5508.

Pasolli, L., Melgani, F., & Blanzieri, E. (2010). Gaussian process regression for estimating chlorophyll concentration in subsurface waters from remote sensing data. *IEEE Geoscience and Remote Sensing Letters*, *7*(3), 464–468.

Patton, E., & Finnigan, J. (2012). Canopy turbulence. *Handbook of environmental fluid dynamics*, *1*, 311–327.

Paulson, C. A. (1970). The mathematical representation of wind speed and temperature profiles in the unstable atmospheric surface layer. *Journal of Applied Meteorology and Climatology*, *9*(6), 857–861.

Payero, J., Neale, C., Wright, J., & Allen, R. (2003). Guidelines for validating bowen ratio data. *Transactions of the ASAE*, *46*(4), 1051.

Peel, M. C., Finlayson, B. L., & McMahon, T. A. (2007). Updated world map of the köppen-geiger climate classification. *Hydrology and earth system sciences*, *11*(5), 1633–1644.

Peltola, O., Aslan, T., Ibrom, A., Nemitz, E., Rannik, Ü., & Mammarella, I. (2021). The high frequency response correction of eddy covariance fluxes. part 2: the empirical approach and its interdependence with the time-lag estimation. *Atmospheric Measurement Techniques Discussions*, *2021*, 1–27.

Penman, H. L. (1948). Natural evaporation from open water, bare soil and grass. *Proceedings of the Royal Society of London. Series A. Mathematical and Physical Sciences*, *193*(1032), 120–145.

Pereira, L., Paredes, P., Melton, F., Johnson, L., Wang, T., López-Urrea, R., ... Allen, R. (2020). Prediction of crop coefficients from fraction of ground cover and height. background and

validation using ground and remote sensing data. *Agricultural Water Management*, *241*, 106197.

Pereira, L., Perrier, R., & Richard, G. (n.d.). Allen and i. alves 1996."evapotranspiration: Review of concepts and future trends.". In *Evapotranspiration and irrigation scheduling (proc. of the international conference november 1996), asae* (pp. 109–115).

Perez, P., Castellvi, F., Ibanez, M., & Rosell, J. (1999). Assessment of reliability of bowen ratio method for partitioning fluxes. *Agricultural and Forest Meteorology*, *97*(3), 141–150.

Perry, C., Steduto, P., Allen, R. G., & Burt, C. M. (2009). Increasing productivity in irrigated agriculture: Agronomic constraints and hydrological realities. *Agricultural water management*, *96*(11), 1517–1524.

Peterson, D. F., & Keller, A. A. (1990). Effects of climate change on us irrigation. *Journal of irrigation and Drainage Engineering*, *116*(2), 194–210.

Petrovic, V., & Cootes, T. (2007). Objectively adaptive image fusion. *Information fusion*, *8*(2), 168–176.

Phiri, D., Simwanda, M., Salekin, S., Nyirenda, V. R., Murayama, Y., & Ranagalage, M. (2020). Sentinel-2 data for land cover/use mapping: A review. *Remote Sensing*, *12*(14), 2291.

Pierce, F. J., & Nowak, P. (1999). Aspects of precision agriculture. *Advances in agronomy*, *67*, 1–85.

Pieri, P., & Fuchs, M. (1990). Comparison of bowen ratio and aerodynamic estimates of evapotranspiration. *Agricultural and Forest Meteorology*, *49*(3), 243–256.

Pinter Jr, P. J., Hatfield, J. L., Schepers, J. S., Barnes, E. M., Moran, M. S., Daughtry, C. S., & Upchurch, D. R. (2003). Remote sensing for crop management. *Photogrammetric Engineering & Remote Sensing*, *69*(6), 647–664.

Pipia, L., Amin, E., Belda, S., Salinero-Delgado, M., & Verrelst, J. (2021). Green lai mapping and cloud gap-filling using gaussian process regression in google earth engine. *Remote Sensing*, *13*(3), 403.

Poblete-Echeverría, C., & Ortega-Farias, S. (2012). Calibration and validation of a remote sensing

algorithm to estimate energy balance components and daily actual evapotranspiration over a drip-irrigated merlot vineyard. *Irrigation Science*, *30*(6), 537–553.

Pohjankukka, J., Pahikkala, T., Nevalainen, P., & Heikkonen, J. (2017). Estimating the prediction performance of spatial models via spatial k-fold cross validation. *International Journal of Geographical Information Science*, *31*(10), 2001–2019.

Pohl, C., & Van Genderen, J. L. (1998). Review article multisensor image fusion in remote sensing: concepts, methods and applications. *International journal of remote sensing*, *19*(5), 823–854.

Pohlert, T. (2014). The pairwise multiple comparison of mean ranks package (pmcmr). *R package*, *27*(2019), 9.

Pope, S. B. (2001). Turbulent flows. *Measurement Science and Technology*, *12*(11), 2020–2021.

Porwal, S., & Katiyar, S. K. (2014). Performance evaluation of various resampling techniques on irs imagery. In *2014 seventh international conference on contemporary computing (ic3)* (pp. 489–494).

Post, D., Fimbres, A., Matthias, A., Sano, E., Accioly, L., Batchily, A., & Ferreira, L. (2000). Predicting soil albedo from soil color and spectral reflectance data. *Soil Science Society of America Journal*, *64*(3), 1027–1034.

Postel, S. L. (2003). Securing water for people, crops, and ecosystems: new mindset and new priorities. In *Natural resources forum* (Vol. 27, pp. 89–98).

Prandtl, L. (1925). 7. bericht über untersuchungen zur ausgebildeten turbulenz. *ZAMM-Journal of Applied Mathematics and Mechanics/Zeitschrift für Angewandte Mathematik und Mechanik*, *5*(2), 136–139.

Price, J. C. (1992). Estimating vegetation amount from visible and near infrared reflectances. *Remote Sensing of Environment*, *41*(1), 29–34.

Price, J. C., & Bausch, W. C. (1995). Leaf area index estimation from visible and near-infrared reflectance data. *Remote Sensing of Environment*, *52*(1), 55–65.

Priestley, C. H. B., & Taylor, R. J. (1972). On the assessment of surface heat flux and evaporation

using large-scale parameters. *Monthly weather review*, *100*(2), 81–92.

Prueger, J. H., Hatfield, J. L., Aase, J. K., & Pikul, J. L. (1997). Bowen-ratio comparisons with lysimeter evapotranspiration. *Agronomy Journal*, *89*, 730–736.

Qi, J., Chehbouni, A., Huete, A. R., Kerr, Y. H., & Sorooshian, S. (1994). A modified soil adjusted vegetation index. *Remote sensing of environment*, *48*(2), 119–126.

Qi, J., Marsett, R., Moran, M., Goodrich, D., Heilman, P., Kerr, Y., ... Zhang, X. (2000). Spatial and temporal dynamics of vegetation in the san pedro river basin area. *Agricultural and forest meteorology*, *105*(1-3), 55–68.

Qiang, X., Cai, H., & Wang, J. (2009). Comparative study of crop evapotranspiration measured by bowen ratio and lysimeter. *Transactions of the Chinese Society of Agricultural Engineering*, *25*(2), 12–17.

Qu, X., Yan, J., Xie, G., Zhu, Z., & Chen, B. (2007). A novel image fusion algorithm based on bandelet transform. *Chinese optics letters*, *5*(10), 569–572.

Quintano, C., Fernández-Manso, A., Shimabukuro, Y. E., & Pereira, G. (2012). Spectral unmixing. *International Journal of Remote Sensing*, *33*(17), 5307–5340.

Quiring, S. M., & Papakryiakou, T. N. (2003). An evaluation of agricultural drought indices for the canadian prairies. *Agricultural and forest meteorology*, *118*(1-2), 49–62.

Raffy, M. (1992). Change of scale in models of remote sensing: A general method for spatialization of models. *Remote Sensing of Environment*, *40*(2), 101–112.

Raj, R., Hamm, N. A., & Kant, Y. (2013). Analysing the effect of different aggregation approaches on remotely sensed data. *International journal of remote sensing*, *34*(14), 4900–4916.

Raj, R., Walker, J. P., Pingale, R., Nandan, R., Naik, B., & Jagarlapudi, A. (2021). Leaf area index estimation using top-of-canopy airborne rgb images. *International Journal of Applied Earth Observation and Geoinformation*, *96*, 102282.

Rao, C. R. (1964). The use and interpretation of principal component analysis in applied research. *Sankhyā: The Indian Journal of Statistics, Series A*, 329–358.

Rasmussen, C. E., & Nickisch, H. (2010). Gaussian processes for machine learning (gpml) tool-

box. *The Journal of Machine Learning Research*, *11*, 3011–3015.

Rawat, K. S., Singh, S. K., Bala, A., & Szabó, S. (2019). Estimation of crop evapotranspiration through spatial distributed crop coefficient in a semi-arid environment. *Agricultural Water Management*, *213*, 922–933.

Ren, H., Zhou, G., & Zhang, F. (2018). Using negative soil adjustment factor in soil-adjusted vegetation index (savi) for aboveground living biomass estimation in arid grasslands. *Remote Sensing of Environment*, *209*, 439–445.

Reyniers, M., Walvoort, D. J., & De Baardemaaker, J. (2006). A linear model to predict with a multi-spectral radiometer the amount of nitrogen in winter wheat. *International Journal of Remote Sensing*, *27*(19), 4159–4179.

Richardson, A., Wiegand, C., Wanjura, D., Dusek, D., & Steiner, J. (1992). Multisite analyses of spectral-biophysical data for sorghum. *Remote Sensing of Environment*, *41*(1), 71–82.

Rim, C.-S. (2000). A comparison of approaches for evapotranspiration estimation. *KSCE Journal of Civil Engineering*, *4*(1), 47–52.

Rocchini, D. (2007). Effects of spatial and spectral resolution in estimating ecosystem α-diversity by satellite imagery. *Remote sensing of Environment*, *111*(4), 423–434.

Rockström, J., Falkenmark, M., Lannerstad, M., & Karlberg, L. (2012). The planetary water drama: Dual task of feeding humanity and curbing climate change. *Geophysical Research Letters*, *39*(15).

Rodarmel, C., & Shan, J. (2002). Principal component analysis for hyperspectral image classification. *Surveying and Land Information Science*, *62*(2), 115–122.

Rodríguez Fernández, J. D., Pérez Martínez, A., & Lozano Alonso, J. A. (2009). A sensitivity study of bias and variance of k-fold cross-validation in prediction error estimation.

Roebeling, R., Wolters, E., Meirink, J., & Leijnse, H. (2012). Triple collocation of summer precipitation retrievals from seviri over europe with gridded rain gauge and weather radar data. *Journal of hydrometeorology*, *13*(5), 1552–1566.

Roerink, G., Su, Z., & Menenti, M. (2000). S-sebi: A simple remote sensing algorithm to estimate

the surface energy balance. *Physics and Chemistry of the Earth, Part B: Hydrology, Oceans and Atmosphere*, *25*(2), 147–157.

Rondeaux, G., Steven, M., & Baret, F. (1996). Optimization of soil-adjusted vegetation indices. *Remote sensing of environment*, *55*(2), 95–107.

Rott, H. (2000). Physical principles and technical aspects of remote sensing. In *Remote sensing in hydrology and water management* (pp. 15–39). Springer.

Rousseeuw, P. J., & Croux, C. (1993). Alternatives to the median absolute deviation. *Journal of the American Statistical association*, *88*(424), 1273–1283.

Roy, D. P., Li, J., Zhang, H. K., & Yan, L. (2016). Best practices for the reprojection and resampling of sentinel-2 multi spectral instrument level 1c data. *Remote Sensing Letters*, *7*(11), 1023–1032.

Roy, D. P., Wulder, M. A., Loveland, T. R., Woodcock, C. E., Allen, R. G., Anderson, M. C., ... others (2014). Landsat-8: Science and product vision for terrestrial global change research. *Remote sensing of Environment*, *145*, 154–172.

Rozenstein, O., Haymann, N., Kaplan, G., & Tanny, J. (2018). Estimating cotton water consumption using a time series of sentinel-2 imagery. *Agricultural Water Management*, *207*, 44–52.

Saitta, D., Vanella, D., Ramírez-Cuesta, J. M., Longo-Minnolo, G., Ferlito, F., & Consoli, S. (2020). Comparison of orange orchard evapotranspiration by eddy covariance, sap flow, and fao-56 methods under different irrigation strategies. *Journal of Irrigation and Drainage Engineering*, *146*(7), 05020002.

Salcedo-Sanz, S., Rojo-Álvarez, J. L., Martínez-Ramón, M., & Camps-Valls, G. (2014). Support vector machines in engineering: an overview. *Wiley Interdisciplinary Reviews: Data Mining and Knowledge Discovery*, *4*(3), 234–267.

Sanchez, J. M., López-Urrea, R., Valentín, F., Caselles, V., & Galve, J. M. (2019). Lysimeter assessment of the simplified two-source energy balance model and eddy covariance system to estimate vineyard evapotranspiration. *Agricultural and Forest Meteorology*, *274*, 172–

183.

Sarron, J., Malézieux, É., Sané, C. A. B., & Faye, É. (2018). Mango yield mapping at the orchard scale based on tree structure and land cover assessed by uav. *Remote Sensing*, *10*(12), 1900.

Sass, J. F., & Horgan, B. P. (2006). Irrigation scheduling on sand-based creeping bentgrass: Evaluating evapotranspiration estimation, capacitance sensors, and deficit irrigation in the upper midwest. *Applied Turfgrass Science*, *3*(1), 1–14.

Sattari, M. T., Apaydin, H., Band, S. S., Mosavi, A., & Prasad, R. (2021). Comparative analysis of kernel-based versus ann and deep learning methods in monthly reference evapotranspiration estimation. *Hydrology and Earth System Sciences*, *25*(2), 603–618.

Scanlon, B. R., Faunt, C. C., Longuevergne, L., Reedy, R. C., Alley, W. M., McGuire, V. L., & McMahon, P. B. (2012). Groundwater depletion and sustainability of irrigation in the us high plains and central valley. *Proceedings of the national academy of sciences*, *109*(24), 9320–9325.

Schläpfer, D., Schaepman, M., & Strobl, P. (2001). Impact of spatial resampling methods on the radiometric accuracy of airborne imaging spectrometer data. In *Fifth international airborne remote sensing conference and exhibition* (p. 8).

Schmugge, T. J., Kustas, W. P., Ritchie, J. C., Jackson, T. J., & Rango, A. (2002). Remote sensing in hydrology. *Advances in water resources*, *25*(8-12), 1367–1385.

Scholkopf, B., Sung, K.-K., Burges, C. J., Girosi, F., Niyogi, P., Poggio, T., & Vapnik, V. (1997). Comparing support vector machines with gaussian kernels to radial basis function classifiers. *IEEE transactions on Signal Processing*, *45*(11), 2758–2765.

Schotanus, P., Nieuwstadt, F., & De Bruin, H. (1983). Temperature measurement with a sonic anemometer and its application to heat and moisture fluxes. *Boundary-Layer Meteorology*, *26*(1), 81–93.

Scientific, C. (2001). Nr-lite net radiometer: Instruction manual. *Campbell Scientific Inc., Logan, Utah*.

Scipal, K., Dorigo, W., & deJeu, R. (2010). Triple collocation—a new tool to determine the error

structure of global soil moisture products. In *2010 ieee international geoscience and remote sensing symposium* (pp. 4426–4429).

Seeger, M. (2004). Gaussian processes for machine learning. *International journal of neural systems*, *14*(02), 69–106.

Seelan, S. K., Laguette, S., Casady, G. M., & Seielstad, G. A. (2003). Remote sensing applications for precision agriculture: A learning community approach. *Remote sensing of environment*, *88*(1-2), 157–169.

Segarra, J., Buchaillot, M. L., Araus, J. L., & Kefauver, S. C. (2020). Remote sensing for precision agriculture: Sentinel-2 improved features and applications. *Agronomy*, *10*(5), 641.

Segura, D., Khatib, E. J., & Barco, R. (2022). Dynamic packet duplication for industrial urllc. *Sensors*, *22*(2), 587.

Sekertekin, A., Marangoz, A., & Akcin, H. (2017). Pixel-based classification analysis of land use land cover using sentinel-2 and landsat-8 data. *Int. Arch. Photogramm. Remote Sens. Spat. Inf. Sci*, *42*, 91–93.

Senay, G. B. (2018). Satellite psychrometric formulation of the operational simplified surface energy balance (ssebop) model for quantifying and mapping evapotranspiration. *Applied Engineering in Agriculture*, *34*(3), 555–566.

Senay, G. B., Bohms, S., Singh, R. K., Gowda, P. H., Velpuri, N. M., Alemu, H., & Verdin, J. P. (2013). Operational evapotranspiration mapping using remote sensing and weather datasets: A new parameterization for the sseb approach. *JAWRA Journal of the American Water Resources Association*, *49*(3), 577–591.

Senay, G. B., Friedrichs, M., Singh, R. K., & Velpuri, N. M. (2016). Evaluating landsat 8 evapotranspiration for water use mapping in the colorado river basin. *Remote Sensing of Environment*, *185*, 171–185.

Sevinç, E. (2022). An empowered adaboost algorithm implementation: A covid-19 dataset study. *Computers & Industrial Engineering*, *165*, 107912.

Shanmugapriya, P., Rathika, S., Ramesh, T., & Janaki, P. (2019). Applications of remote sensing in

agriculture-a review. *International Journal of Current Microbiology and Applied Sciences*, *8*(01), 2270–2283.

Sharma, H., Shukla, M. K., Bosland, P. W., & Steiner, R. (2017). Soil moisture sensor calibration, actual evapotranspiration, and crop coefficients for drip irrigated greenhouse chile peppers. *Agricultural water management*, *179*, 81–91.

Sharma, V., Kilic, A., & Irmak, S. (2016). Impact of scale/resolution on evapotranspiration from landsat and modis images. *Water Resources Research*, *52*(3), 1800–1819.

Sheng, Y., Roberge, D., & Szu, H. H. (1992). Optical wavelet transform. *Optical Engineering*, *31*(9), 1840–1845.

Shi, X., Han, W., Zhao, T., & Tang, J. (2019). Decision support system for variable rate irrigation based on uav multispectral remote sensing. *Sensors*, *19*(13), 2880.

Shrestha, N., & Shukla, S. (2015). Support vector machine based modeling of evapotranspiration using hydro-climatic variables in a sub-tropical environment. *Agricultural and Forest Meteorology*, *200*, 172–184.

Shuttleworth, W., Gurney, R., Hsu, A., & Ormsby, J. (1989). Fife: The variation in energy partition at surface flux sites. *IAHS Publ*, *186*(6), 523–534.

Shuttleworth, W. J. (2008). Evapotranspiration measurement methods. *Southwest Hydrology*, *7*(1), 22–23.

Šidák, Z. (1967). Rectangular confidence regions for the means of multivariate normal distributions. *Journal of the American Statistical Association*, *62*(318), 626–633.

Siebert, S., & Döll, P. (2010). Quantifying blue and green virtual water contents in global crop production as well as potential production losses without irrigation. *Journal of Hydrology*, *384*(3-4), 198–217.

Sinclair, T., Allen, L., & Lemon, E. (1975). An analysis of errors in the calculation of energy flux densities above vegetation by a bowen-ratio profile method. *Boundary-Layer Meteorology*, *8*(2), 129–139.

Siqueira, M., & Katul, G. (2002). Estimating heat sources and fluxes in thermally stratified canopy

flows using higher-order closure models. *Boundary-Layer Meteorology*, *103*(1), 125–142.

Skakun, S., Kalecinski, N. I., Brown, M. G., Johnson, D. M., Vermote, E. F., Roger, J.-C., & Franch, B. (2021). Assessing within-field corn and soybean yield variability from worldview-3, planet, sentinel-2, and landsat 8 satellite imagery. *Remote Sensing*, *13*(5), 872.

Snyder, R., Paw U, K., Duce, P., Spano, D., Ferreira, M., do Paco, T., & Connell, J. (1999). Measuring tree and vine et with eddy covariance. In *Acta horticulturae* (p. 53-60).

Sobol', I. M. (1990). On sensitivity estimation for nonlinear mathematical models. *Matematicheskoe modelirovanie*, *2*(1), 112–118.

Sobol, I. M. (2001). Global sensitivity indices for nonlinear mathematical models and their monte carlo estimates. *Mathematics and computers in simulation*, *55*(1-3), 271–280.

Soegaard, H., & Boegh, E. (1995). Estimation of evapotranspiration from a millet crop in the sahel combining sap flow, leaf area index and eddy correlation technique. *Journal of Hydrology*, *166*(3-4), 265–282.

Solignac, P. A., Brut, A., Selves, J.-L., Béteille, J.-P., Gastellu-Etchegorry, J.-P., Keravec, P., ... Ceschia, E. (2009). Uncertainty analysis of computational methods for deriving sensible heat flux values from scintillometer measurements. *Atmospheric Measurement Techniques*, *2*(2), 741–753.

Song, L., Liu, S., Kustas, W. P., Zhou, J., Xu, Z., Xia, T., & Li, M. (2016). Application of remote sensing-based two-source energy balance model for mapping field surface fluxes with composite and component surface temperatures. *Agricultural and forest meteorology*, *230*, 8–19.

Song, W., Mu, X., Ruan, G., Gao, Z., Li, L., & Yan, G. (2017). Estimating fractional vegetation cover and the vegetation index of bare soil and highly dense vegetation with a physically based method. *International journal of applied earth observation and geoinformation*, *58*, 168–176.

Sousa, D. d. P., Fernandes, T. F. S., Tavares, L. B., Farias, V. D. d. S., de Lima, M. J. A., Nunes,

H. G. G. C., ... Souza, P. J. d. O. P. (2021). Estimation of evapotranspiration and single and dual crop coefficients of acai palm in the eastern amazon (brazil) using the bowen ratio system. *Irrigation Science*, *39*(1), 5–22.

Spittlehouse, D., & Black, T. (1980). Evaluation of the bowen ratio/energy balance method for determining forest evapotranspiration. *Atmosphere-Ocean*, *18*(2), 98–116.

Spokas, K., & Forcella, F. (2006). Estimating hourly incoming solar radiation from limited meteorological data. *Weed science*, *54*(1), 182–189.

Spoto, F., Sy, O., Laberinti, P., Martimort, P., Fernandez, V., Colin, O., ... Meygret, A. (2012). Overview of sentinel-2. In *2012 ieee international geoscience and remote sensing symposium* (pp. 1707–1710).

Sprintsin, M., Karnieli, A., Berliner, P., Rotenberg, E., Yakir, D., & Cohen, S. (2007). The effect of spatial resolution on the accuracy of leaf area index estimation for a forest planted in the desert transition zone. *Remote Sensing of Environment*, *109*(4), 416–428.

Steddom, K., Bredehoeft, M., Khan, M., & Rush, C. (2005). Comparison of visual and multispectral radiometric disease evaluations of cercospora leaf spot of sugar beet. *Plant Disease*, *89*(2), 153–158.

Steinberg, D., & Colla, P. (2009). Cart: classification and regression trees. *The top ten algorithms in data mining*, *9*, 179.

Stewart, J. B., Kustas, W. P., Humes, K. S., Nichols, W. D., Moran, M. S., & de Bruin, H. A. (1994). Sensible heat flux-radiometric surface temperature relationship for eight semiarid areas. *Journal of Applied Meteorology and Climatology*, *33*(9), 1110–1117.

Stoffelen, A. (1998). Toward the true near-surface wind speed: Error modeling and calibration using triple collocation. *Journal of geophysical research: oceans*, *103*(C4), 7755–7766.

Strang, G. (1989). Wavelets and dilation equations: A brief introduction. *SIAM review*, *31*(4), 614–627.

Su, Z. (2002). The surface energy balance system (sebs) for estimation of turbulent heat fluxes. *Hydrology and earth system sciences*, *6*(1), 85–100.

Sun, G., Noormets, A., Chen, J., & McNulty, S. (2008). Evapotranspiration estimates from eddy covariance towers and hydrologic modeling in managed forests in northern wisconsin, usa. *Agricultural and forest Meteorology*, *148*(2), 257–267.

Sun, W., Yang, G., Peng, J., & Du, Q. (2019). Lateral-slice sparse tensor robust principal component analysis for hyperspectral image classification. *IEEE Geoscience and Remote Sensing Letters*, *17*(1), 107–111.

Tan, C.-W., Zhang, P.-P., Zhou, X.-X., Wang, Z.-X., Xu, Z.-Q., Mao, W., ... Yun, F. (2020). Quantitative monitoring of leaf area index in wheat of different plant types by integrating ndvi and beer-lambert law. *Scientific Reports*, *10*(1), 1–10.

Tang, R., Li, Z.-L., Jia, Y., Li, C., Chen, K.-S., Sun, X., & Lou, J. (2013). Evaluating one-and two-source energy balance models in estimating surface evapotranspiration from landsat-derived surface temperature and field measurements. *International Journal of Remote Sensing*, *34*(9-10), 3299–3313.

Tang, R., Li, Z.-L., & Tang, B. (2010). An application of the ts–vi triangle method with enhanced edges determination for evapotranspiration estimation from modis data in arid and semi-arid regions: Implementation and validation. *Remote Sensing of Environment*, *114*(3), 540–551.

Tanim, A. H., Mullick, M. R. A., & Sikdar, M. S. (2021). Evaluation of spatial rainfall products in sparsely gauged region using copula uncertainty modeling with triple collocation. *Journal of Hydrologic Engineering*, *26*(4), 04021004.

Tanner, C. (1960). Energy balance approach to evapotranspiration from crops. *Soil Science Society of America Journal*, *24*(1), 1–9.

Tanner, C. B., & Thurtell, G. W. (1969). *Anemoclinometer measurements of reynolds stress and heat transport in the atmospheric surface layer* (Tech. Rep.). Wisconsin Univ-Madison Dept of Soil Science.

Team, P. (2017). Planet application program interface: In space for life on earth. *San Francisco, CA*, *2017*, 40.

Team, P. (2020). Planet imagery product specifications. *San Francisco, CA*, *2020*.

Team, R. C. (2020). A language and environment for statistical computing [internet]. *R Foundation for Statistical Computing*.

Thom, A. . (1972). Momentum, mass and heat exchange of vegetation. *Quarterly Journal of the Royal Meteorological Society*, *98*(415), 124–134.

Thornthwaite, C. W. (1948). An approach toward a rational classification of climate. *Geographical review*, *38*(1), 55–94.

Timmermans, W. J., Kustas, W. P., Anderson, M. C., & French, A. N. (2007). An intercomparison of the surface energy balance algorithm for land (sebal) and the two-source energy balance (tseb) modeling schemes. *Remote Sensing of Environment*, *108*(4), 369–384.

Todorovic, M. (1999). Single-layer evapotranspiration model with variable canopy resistance. *Journal of Irrigation and Drainage Engineering*, *125*(5), 235–245.

Torgo, L. (1997). Functional models for regression tree leaves. In *Icml* (Vol. 97, pp. 385–393).

Trajkovic, S., Gocic, M., Pongracz, R., & Bartholy, J. (2019). Adjustment of thornthwaite equation for estimating evapotranspiration in vojvodina. *Theoretical and Applied Climatology*, *138*(3), 1231–1240.

Trezza, R., Allen, R. G., & Tasumi, M. (2013). Estimation of actual evapotranspiration along the middle rio grande of new mexico using modis and landsat imagery with the metric model. *Remote Sensing*, *5*(10), 5397–5423.

Trishchenko, A. P., Cihlar, J., & Li, Z. (2002). Effects of spectral response function on surface reflectance and ndvi measured with moderate resolution satellite sensors. *Remote Sensing of Environment*, *81*(1), 1–18.

Trishchenko, A. P., Luo, Y., & Khlopenkov, K. V. (2006). A method for downscaling modis land channels to 250-m spatial resolution using adaptive regression and normalization. In *Remote sensing for environmental monitoring, gis applications, and geology vi* (Vol. 6366, pp. 46–53).

Trout, T. J., & DeJonge, K. C. (2018). Crop water use and crop coefficients of maize in the great plains. *Journal of Irrigation and Drainage Engineering*, *144*(6), 04018009.

Troy, T. J., Kipgen, C., & Pal, I. (2015). The impact of climate extremes and irrigation on us crop yields. *Environmental Research Letters*, *10*(5), 054013.

Tu, T., Su, S.-C., Shyu, H. C., & Huang, P. S. (2001). Efficient intensity-hue-saturation-based image fusion with saturation compensation. *Optical Engineering*, *40*(5), 720–728.

Tubiello, F., Rosenzweig, C., Goldberg, R., Jagtap, S., & Jones, J. (2002). Effects of climate change on us crop production: simulation results using two different gcm scenarios. part i: wheat, potato, maize, and citrus. *Climate research*, *20*(3), 259–270.

Turner, M. G., O'Neill, R. V., Gardner, R. H., & Milne, B. T. (1989). Effects of changing spatial scale on the analysis of landscape pattern. *Landscape ecology*, *3*(3), 153–162.

Twine, T. E., Kustas, W., Norman, J., Cook, D., Houser, P., Meyers, T., ... Wesely, M. (2000). Correcting eddy-covariance flux underestimates over a grassland. *Agricultural and forest meteorology*, *103*(3), 279–300.

Ünlü, M., Kanber, R., & Kapur, B. (2010). Comparison of soybean evapotranspirations measured by weighing lysimeter and bowen ratio-energy balance methods. *African Journal of Biotechnology*, *9*(30), 4700–4713.

USDA-NRCS. (2009). Web soil survey. *URL http://www. websoilsurvey. ncsc. usda. gov-/app/[verified October 29, 2009]*.

Vandermaesen, J., Delalieux, S., Bylemans, D., & Remy, S. (2021). Variable rate irrigation based on uav imagery and real-time sensor data in pear orchards. In *Precision agriculture'21* (pp. 6647–6666). Wageningen Academic Publishers.

Van Der Meer, F. (1995). Spectral unmixing of landsat thematic mapper data. *International Journal of Remote Sensing*, *16*(16), 3189–3194.

Van Dijk, A., Moene, A., De Bruin, H., et al. (2004). The principles of surface flux physics: theory, practice and description of the ecpack library. *Meteorology and Air Quality Group, Wageningen University, Wageningen, the Netherlands*, *99*, 525.

Van Zyl, W., & De Jager, J. d. (1987). Accuracy of the penman-monteith equation adjusted for atmospheric stability. *Agricultural and forest meteorology*, *41*(1-2), 57–64.

Vapnik, V. (1999). *The nature of statistical learning theory*. Springer science & business media.

Varmaghani, A., Eichinger, W. E., & Prueger, J. H. (2021). A meteorological-based crop coefficient model for estimation of daily evapotranspiration. *Hydrological Processes*, *35*(2), e14025.

Verma, S. (1989). Aerodynamic resistances to transfers of heat, mass and momentum.

Vermeulen, S., Zougmore, R., Wollenberg, E., Thornton, P., Nelson, G., Kristjanson, P., ... others (2012). Climate change, agriculture and food security: a global partnership to link research and action for low-income agricultural producers and consumers. *Current Opinion in Environmental Sustainability*, *4*(1), 128–133.

Vermote, E. (2000). Product accuracy/uncertainty: Mod09, surface reflectance; atmospheric correction algorithm product. *http://modarch. gsfc. nasa. gov/MODIS/RESULTS/DATAPROD/*.

Vermote, E., Justice, C., Claverie, M., & Franch, B. (2016). Preliminary analysis of the performance of the landsat 8/oli land surface reflectance product. *Remote Sensing of Environment*, *185*, 46–56.

Vermote, E., Roger, J.-C., Franch, B., & Skakun, S. (2018). Lasrc (land surface reflectance code): Overview, application and validation using modis, viirs, landsat and sentinel 2 data's. In *Igarss 2018-2018 ieee international geoscience and remote sensing symposium* (pp. 8173–8176).

Vermote, E. F., El Saleous, N. Z., & Justice, C. O. (2002). Atmospheric correction of modis data in the visible to middle infrared: first results. *Remote Sensing of Environment*, *83*(1-2), 97–111.

Verstraete, M., & Pinty, B. (1991). The potential contribution of satellite remote sensing to the understanding of arid lands processes. In *Vegetation and climate interactions in semi-arid regions* (pp. 59–72). Springer.

Verstraeten, W. W., Veroustraete, F., & Feyen, J. (2008). Assessment of evapotranspiration and soil moisture content across different scales of observation. *Sensors*, *8*(1), 70–117.

Vickers, D., & Mahrt, L. (1997). Quality control and flux sampling problems for tower and aircraft

data. *Journal of atmospheric and oceanic technology*, *14*(3), 512–526.

Villa, A., Chanussot, J., Benediktsson, J. A., & Jutten, C. (2010). Spectral unmixing for the classification of hyperspectral images at a finer spatial resolution. *IEEE Journal of Selected Topics in Signal Processing*, *5*(3), 521–533.

Vorobiova, N., & Chernov, A. (2017). Curve fitting of modis ndvi time series in the task of early crops identification by satellite images. *Procedia engineering*, *201*, 184–195.

Vose, J. M., Clinton, B. D., Sullivan, N. H., & Bolstad, P. V. (1995). Vertical leaf area distribution, light transmittance, and application of the beer–lambert law in four mature hardwood stands in the southern appalachians. *Canadian Journal of Forest Research*, *25*(6), 1036–1043.

Wada, Y., Wisser, D., Eisner, S., Flörke, M., Gerten, D., Haddeland, I., ... others (2013). Multi-model projections and uncertainties of irrigation water demand under climate change. *Geophysical research letters*, *40*(17), 4626–4632.

Wagle, P., Bhattarai, N., Gowda, P. H., & Kakani, V. G. (2017). Performance of five surface energy balance models for estimating daily evapotranspiration in high biomass sorghum. *ISPRS Journal of Photogrammetry and Remote Sensing*, *128*, 192–203.

Wallace, J. (2000). Increasing agricultural water use efficiency to meet future food production. *Agriculture, ecosystems & environment*, *82*(1-3), 105–119.

Walthert, L., & Schleppi, P. (2018). Equations to compensate for the temperature effect on readings from dielectric decagon mps-2 and mps-6 water potential sensors in soils. *Journal of Plant Nutrition and Soil Science*, *181*(5), 749–759.

Wang, D., Wilson, C., & Shannon, M. (2002). Interpretation of salinity and irrigation effects on soybean canopy reflectance in visible and near-infrared spectrum domain. *International Journal of Remote Sensing*, *23*(5), 811–824.

Wang, J., Schmitz, O., Lu, M., & Karssenberg, D. (2020). Thermal unmixing based downscaling for fine resolution diurnal land surface temperature analysis. *ISPRS Journal of Photogrammetry and Remote Sensing*, *161*, 76–89.

Wang, L., Shi, C., Diao, C., Ji, W., & Yin, D. (2016). A survey of methods incorporating spatial

information in image classification and spectral unmixing. *International Journal of Remote Sensing*, *37*(16), 3870–3910.

Wang, Q., Wu, J., Lei, T., He, B., Wu, Z., Liu, M., ... others (2014). Temporal-spatial characteristics of severe drought events and their impact on agriculture on a global scale. *Quaternary International*, *349*, 10–21.

Wang, T., Melton, F. S., Pôças, I., Johnson, L. F., Thao, T., Post, K., & Cassel-Sharma, F. (2021). Evaluation of crop coefficient and evapotranspiration data for sugar beets from landsat surface reflectances using micrometeorological measurements and weighing lysimetry. *Agricultural Water Management*, *244*, 106533.

Wang, X., Bai, S., Li, Z., Sui, Y., & Tao, J. (2021). The pan and ms image fusion algorithm based on adaptive guided filtering and gradient information regulation. *Information Sciences*, *545*, 381–402.

Wang, Y., Tian, Y., Zhang, Y., El-Saleous, N., Knyazikhin, Y., Vermote, E., & Myneni, R. B. (2001). Investigation of product accuracy as a function of input and model uncertainties: Case study with seawifs and modis lai/fpar algorithm. *Remote Sensing of Environment*, *78*(3), 299–313.

Warhaft, Z. (2000). Passive scalars in turbulent flows. *Annual Review of Fluid Mechanics*, *32*(1), 203–240.

Watanabe, T., Takagi, M., Shimoyama, K., Kawashima, M., Onodera, N., & Inagaki, A. (2021). Coherent eddies transporting passive scalars through the plant canopy revealed by large-eddy simulations using the lattice boltzmann method. *Boundary-Layer Meteorology*, *181*(1), 39–71.

Watson, A. B., & Ahumada, A. J. (1985). Model of human visual-motion sensing. *JOSA A*, *2*(2), 322–342.

Weaver, H. L. (1990). Temperature and humidity flux-variance relations determined by one-dimensional eddy correlation. *Boundary-Layer Meteorology*, *53*(1), 77–91.

Webb, E. K. (1970). Profile relationships: The log-linear range, and extension to strong stability.

Quarterly Journal of the Royal Meteorological Society, *96*(407), 67–90.

Webb, E. K., Pearman, G. I., & Leuning, R. (1980). Correction of flux measurements for density effects due to heat and water vapour transfer. *Quarterly Journal of the Royal Meteorological Society*, *106*(447), 85–100.

Wei, S., Mingzheng, Z., Kunping, J., Dehai, Z., Jianxi, H., & Pengxin, W. (2018). Atmospheric correction method for sentinel-2 satellite imagery. *Acta Optica Sinica*, *38*(1), 0128001.

Wen, X., Si, J., He, Z., Wu, J., Shao, H., & Yu, H. (2015). Support-vector-machine-based models for modeling daily reference evapotranspiration with limited climatic data in extreme arid regions. *Water Resources Management*, *29*(9), 3195–3209.

Wery, J. (2005). Differential effects of soil water deficit on the basic plant functions and their significance to analyse crop responses to water deficit in indeterminate plants. *Australian Journal of Agricultural Research*, *56*(11), 1201–1209.

Wiebe, K., Robinson, S., & Cattaneo, A. (2019). Climate change, agriculture and food security: impacts and the potential for adaptation and mitigation. *Sustainable food and agriculture*, 55–74.

Williams, A., Ternan, J., Fitzjohn, C., De Alba, S., & Perez-Gonzalez, A. (2003). Soil moisture variability and land use in a seasonally arid environment. *Hydrological Processes*, *17*(2), 225–235.

Williams, C. K., & Rasmussen, C. E. (2006). *Gaussian processes for machine learning* (Vol. 2) (No. 3). MIT press Cambridge, MA.

Williams, D., Cable, W., Hultine, K., Hoedjes, J., Yepez, E., Simonneaux, V., ... others (2004). Evapotranspiration components determined by stable isotope, sap flow and eddy covariance techniques. *Agricultural and forest meteorology*, *125*(3-4), 241–258.

Willmott, C. J., Robeson, S. M., & Matsuura, K. (2012). A refined index of model performance. *International Journal of climatology*, *32*(13), 2088–2094.

Wilson, J. (1989). Turbulent transport within the plant canopy. *Estimation of areal evapotranspiration*, *177*, 43–80.

Wilson, K., Goldstein, A., Falge, E., Aubinet, M., Baldocchi, D., Berbigier, P., ... others (2002). Energy balance closure at fluxnet sites. *Agricultural and Forest Meteorology*, *113*(1-4), 223–243.

Wilson, K. B., Hanson, P. J., Mulholland, P. J., Baldocchi, D. D., & Wullschleger, S. D. (2001). A comparison of methods for determining forest evapotranspiration and its components: sap-flow, soil water budget, eddy covariance and catchment water balance. *Agricultural and forest Meteorology*, *106*(2), 153–168.

Wittich, K.-P. (1997). Some simple relationships between land-surface emissivity, greenness and the plant cover fraction for use in satellite remote sensing. *International Journal of Biometeorology*, *41*(2), 58–64.

Wold, S., Esbensen, K., & Geladi, P. (1987). Principal component analysis. chimometrics and intelligent laboratory systems. In *Ieee conference on emerging technologies & factory automation efta* (pp. 704–706).

Wong, T.-T., & Yeh, P.-Y. (2019). Reliable accuracy estimates from k-fold cross validation. *IEEE Transactions on Knowledge and Data Engineering*, *32*(8), 1586–1594.

Woodcock, C. E., & Strahler, A. H. (1987). The factor of scale in remote sensing. *Remote sensing of Environment*, *21*(3), 311–332.

Wright, J. L. (1981). Crop coefficient for estimates of daily crop evapotranspiration. *Proc., American Society of Agricultural Engineers, Irrigation Scheduling Conf.*, 18–26.

Wu, J., Huang, H., Qiu, Y., Wu, H., Tian, J., & Liu, J. (2005). Remote sensing image fusion based on average gradient of wavelet transform. In *Ieee international conference mechatronics and automation, 2005* (Vol. 4, pp. 1817–1821).

Wu, X., Zhang, W., Liu, W., Zuo, Q., Shi, J., Yan, X., ... others (2017). Root-weighted soil water status for plant water deficit index based irrigation scheduling. *Agricultural Water Management*, *189*, 137–147.

Xiao, J., & Moody, A. (2005). A comparison of methods for estimating fractional green vegetation cover within a desert-to-upland transition zone in central new mexico, usa. *Remote sensing*

of environment, *98*(2-3), 237–250.

Xu, L., Chen, N., Zhang, X., Moradkhani, H., Zhang, C., & Hu, C. (2021). In-situ and triple-collocation based evaluations of eight global root zone soil moisture products. *Remote Sensing of Environment*, *254*, 112248.

Xu, T., He, X., Bateni, S. M., Auligne, T., Liu, S., Xu, Z., ... Mao, K. (2019). Mapping regional turbulent heat fluxes via variational assimilation of land surface temperature data from polar orbiting satellites. *Remote Sensing of Environment*, *221*, 444–461.

Yan, H., Shi, H., Hiroki, O., Zhang, C., Xue, Z., Cai, B., & Wang, G. (2015). Modeling bulk canopy resistance from climatic variables for predicting hourly evapotranspiration of maize and buckwheat. *Meteorology and Atmospheric Physics*, *127*, 305–312.

Yan, X., & Su, X. (2009). *Linear regression analysis: theory and computing*. world scientific.

Yang, C., Wu, G., Ding, K., Shi, T., Li, Q., & Wang, J. (2017). Improving land use/land cover classification by integrating pixel unmixing and decision tree methods. *Remote Sensing*, *9*(12), 1222.

Yang, G., Liu, J., Zhao, C., Li, Z., Huang, Y., Yu, H., ... others (2017). Unmanned aerial vehicle remote sensing for field-based crop phenotyping: current status and perspectives. *Frontiers in plant science*, *8*, 1111.

Yang, J., Li, B., & Shiping, L. (2000). A large weighing lysimeter for evapotranspiration and soil-water–groundwater exchange studies. *Hydrological processes*, *14*(10), 1887–1897.

Yang, L., Liu, S., Tsoka, S., & Papageorgiou, L. G. (2017). A regression tree approach using mathematical programming. *Expert Systems with Applications*, *78*, 347–357.

Yang, Y., Han, C., Kang, X., & Han, D. (2007). An overview on pixel-level image fusion in remote sensing. In *2007 ieee international conference on automation and logistics* (pp. 2339–2344).

Yang, Z., Rao, M., Elliott, N., Kindler, S., & Popham, T. (2005). Using ground-based multispectral radiometry to detect stress in wheat caused by greenbug (homoptera: Aphididae) infestation. *Computers and electronics in agriculture*, *47*(2), 121–135.

Yanzhao, Z., & Xin, L. (2018). Progress in the energy closure of eddy covariance systems.

Advances in Earth Science, *33*(9), 898–913.

Yi, Z., Zhao, H., & Jiang, Y. (2018). Continuous daily evapotranspiration estimation at the field-scale over heterogeneous agricultural areas by fusing aster and modis data. *Remote Sensing*, *10*(11), 1694.

Younis, B. A., Speziale, C. G., & Clark, T. T. (2005). A rational model for the turbulent scalar fluxes. *Proceedings of the Royal Society A: Mathematical, Physical and Engineering Sciences*, *461*(2054), 575–594.

Zendehboudi, A., Baseer, M. A., & Saidur, R. (2018). Application of support vector machine models for forecasting solar and wind energy resources: A review. *Journal of cleaner production*, *199*, 272–285.

Zeng, L., Wardlow, B. D., Xiang, D., Hu, S., & Li, D. (2020). A review of vegetation phenological metrics extraction using time-series, multispectral satellite data. *Remote Sensing of Environment*, *237*, 111511.

Zeng, X., Dickinson, R. E., Walker, A., Shaikh, M., DeFries, R. S., & Qi, J. (2000). Derivation and evaluation of global 1-km fractional vegetation cover data for land modeling. *Journal of Applied Meteorology*, *39*(6), 826–839.

Zhang, B., Kang, S., Zhang, L., Du, T., Li, S., & Yang, X. (2007). Estimation of seasonal crop water consumption in a vineyard using bowen ratio-energy balance method. *Hydrological Processes: An International Journal*, *21*(26), 3635–3641.

Zhang, M., Li, S., Yu, F., & Tian, X. (2020). Image fusion employing adaptive spectral-spatial gradient sparse regularization in uav remote sensing. *Signal Processing*, *170*, 107434.

Zhang, Q., Xiao, X., Braswell, B., Linder, E., Baret, F., & Moore III, B. (2005). Estimating light absorption by chlorophyll, leaf and canopy in a deciduous broadleaf forest using modis data and a radiative transfer model. *Remote Sensing of Environment*, *99*(3), 357–371.

Zhang, Y., Han, W., Niu, X., & Li, G. (2019). Maize crop coefficient estimated from uav-measured multispectral vegetation indices. *Sensors*, *19*(23), 5250.

Zhang, Z., Tian, F., Hu, H., & Yang, P. (2014). A comparison of methods for determining field

evapotranspiration: photosynthesis system, sap flow, and eddy covariance. *Hydrology and Earth System Sciences*, *18*(3), 1053–1072.

Zhao, J., Li, C., Yang, T., Tang, Y., Yin, Y., Luan, X., & Sun, S. (2020). Estimation of high spatiotemporal resolution actual evapotranspiration by combining the swh model with the metric model. *Journal of Hydrology*, *586*, 124883.

Zheng, H., Du, P., Chen, J., Xia, J., Li, E., Xu, Z., ... Yokoya, N. (2017). Performance evaluation of downscaling sentinel-2 imagery for land use and land cover classification by spectral-spatial features. *Remote Sensing*, *9*(12), 1274.

Zhong, S., Zhang, K., Bagheri, M., Burken, J. G., Gu, A., Li, B., ... others (2021). Machine learning: new ideas and tools in environmental science and engineering. *Environmental Science & Technology*, *55*(19), 12741–12754.

Zhou, J., Civco, D. L., & Silander, J. (1998). A wavelet transform method to merge landsat tm and spot panchromatic data. *International journal of remote sensing*, *19*(4), 743–757.

Zhou, X., Bi, S., Yang, Y., Tian, F., & Ren, D. (2014). Comparison of et estimations by the three-temperature model, sebal model and eddy covariance observations. *Journal of hydrology*, *519*, 769–776.

Zhu, X., Chen, J., Gao, F., Chen, X., & Masek, J. G. (2010). An enhanced spatial and temporal adaptive reflectance fusion model for complex heterogeneous regions. *Remote Sensing of Environment*, *114*(11), 2610–2623.

Zhuang, Q., Wu, B., Yan, N., Zhu, W., & Xing, Q. (2016). A method for sensible heat flux model parameterization based on radiometric surface temperature and environmental factors without involving the parameter kb- 1. *International journal of applied earth observation and geoinformation*, *47*, 50–59.

Appendix A

Calculation of Variables for the OSEB Algorithm

The r_{ah} term is calculated using Eq. A1 as follows (as in Thom, 1972; Verma, 1989):

$$r_{ah} = \frac{ln\left(\frac{Z_u - d}{Z_{oh}}\right) - \psi_h}{u_* k} \tag{A1}$$

where Z_u is the height of wind speed measurement (m); d is the zero-plane displacement height (m); Z_{oh} is the roughness length for heat transfer (m); ψ_h is the atmospheric stability correction function for heat transfer (dimensionless); k is the Von-Kármán constant and set to 0.41 (Dyer and Hicks, 1970; Dyer, 1974).

The shear or friction velocity (Eq. A2) is calculated as follows (as in Thom, 1972; Verma, 1989):

$$u_* = \frac{Uk}{ln\left(\frac{Z_u - d}{Z_{om}}\right) - \psi_m} \tag{A2}$$

where u_* is the mean shear velocity (m/s), ψ_m is the atmospheric stability correction function for momentum transfer (dimensionless); Z_{om} is the roughness length for momentum transfer (m), and U is the mean horizontal wind speed (m/s).

The ψ_h and ψ_m are equal to zero for quasi-neutral atmospheric conditions. When thermal stratification exists, the Monin-Obukhov stability length (L_{MO}) is considered to correct the estimations of momentum and heat transfer (Monin and Obukhov, 1954). For unstable (L_{MO} < 0) and stable (L_{MO} > 0) atmospheric conditions, Eqs. A3 and A4 present the models for the atmospheric stability corrections for heat transfer (Paulson, 1970; Webb et al., 1970; Businger et al., 1971):

$$\psi_h = \begin{cases} 2 \times ln\left(\frac{1+x_1^2}{2}\right) - 2 \times ln\left(\frac{1+x_1^2}{2}\right) & , \ L_{MO} \leq 0 \\ -5 \times \left(\frac{Z_u - d}{L_{MO}}\right) & , \text{otherwise} \end{cases} \tag{A3}$$

$$x_1 = \left[1 - 16 \times \left(\frac{Z_u - d}{L_{MO}}\right)\right]^{1/4} \tag{A4}$$

where L_{MO} is the Monin-Obukhov stability length (m) and calculated as indicated by Eq. A5 below (Monin and Obukhov, 1954):

$$L_{MO} = -\frac{u_*^3 T_a \rho_a C_{pa}}{gkH} \tag{A5}$$

where g is the gravitational acceleration ($\approx 9.81\ m/s^2$).

For unstable and stable atmospheric conditions, Eq. A6 indicates the models for the atmospheric stability corrections for momentum transfer (Paulson, 1970; Webb et al., 1970; Businger et al., 1971):

$$\psi_m = \begin{cases} 2 \times ln\left(\frac{1+x_1}{2}\right) + ln\left(\frac{1+x_1^2}{2}\right) - 2 \times arctan(x_1) + \frac{\pi}{2} & , \ L_{MO} \leq 0 \\ -5 \times \left(\frac{Z_u - d}{L_{MO}}\right) & , \text{otherwise} \end{cases} \tag{A6}$$

The roughness elements d, Z_{om}, and Z_{oh} are calculated as indicated by Eqs. A7 to A9, respectively (Choudhury and Monteith, 1988; Brutsaert; 1982):

$$Z_{om} = \begin{cases} z_o^{'} + 0.28 \cdot h_c \cdot \sqrt{J} & , \ 0 \leq J \leq 0.20 \\ 0.30 \cdot h_c \cdot \left(1 - \dfrac{d}{h_c}\right) & 0.20 < J \leq 2 \end{cases} \tag{A7}$$

$$d = h_c \cdot \left[ln(1 + J^{1/6}) + 0.03 \cdot ln(1 + J^6) \right] \tag{A8}$$

$$Z_{oh} = 0.10 \cdot Z_{om} \tag{A9}$$

where $z_o^{'}$ is the roughness length of the soil surface ($z_o^{'} \approx 0.01 \ m$) and J is equal to 20% of LAI (m^2/m^2).

The r_p variable for the crop row orientation north-south or east-west is calculated by Eqs. A10 and A11, respectively (Costa-Filho et al., 2021):

$$r_p = \begin{cases} \left(\dfrac{1}{U}\right) \cdot \left(\dfrac{\theta_u}{180^o - \theta_u}\right), & 0^o \leq \theta_u \leq 90^o \\ \left(\dfrac{1}{U}\right) \cdot \left(\dfrac{180^o - \theta_u}{\theta_u}\right), & 90^o < \theta_u \leq 180^o \\ \left(\dfrac{1}{U}\right) \cdot \left(\dfrac{\theta_u - 180^o}{360^o - \theta_u}\right), & 180^o < \theta_u \leq 270^o \\ \left(\dfrac{1}{U}\right) \cdot \left(\dfrac{360^o - \theta_u}{\theta_u - 180^o}\right), & 270^o < \theta_u \leq 360^o \end{cases} \tag{A10}$$

$$r_p = \begin{cases} \left(\frac{1}{U}\right) \cdot \left(\frac{90^o - \theta_u}{90^o + \theta_u}\right), & 0^o \leq \theta_u \leq 90^o \\ \left(\frac{1}{U}\right) \cdot \left(\frac{\theta_u - 90^o}{270^o - \theta_u}\right), & 90^o < \theta_u \leq 180^o \\ \left(\frac{1}{U}\right) \cdot \left(\frac{270^o - \theta_u}{\theta_u - 90^o}\right), & 180^o < \theta_u \leq 270^o \\ \left(\frac{1}{U}\right) \cdot \left(\frac{\theta_u - 270^o}{450^o - \theta_u}\right), & 270^o < \theta_u \leq 360^o \end{cases} \tag{A11}$$

where θ_u is the wind speed direction in degrees.

Appendix B

Calculation of Variables for the TSEB Algorithms

The r_{soil} (s/m) is calculated using Eqs. B1 to B4 (Goudriaan, 1977; Norman et al., 1995; Campbell and Monteith, 2012):

$$r_{soil} = \frac{1}{0.004 + 0.012 \cdot U_{soil}} \tag{B1}$$

$$U_{soil} = U_{canopy} \cdot exp\left[- a_{ext} \cdot \left(1 - \frac{0.05}{h_c} \right) \right] \tag{B2}$$

$$U_{canopy} = \frac{u_*}{k} \cdot ln\left(\frac{h_c - d}{Z_{om}} \right) \tag{B3}$$

$$a_{ext} = 0.20 \cdot (CF \cdot LAI)^{2/3} \cdot h_c^{1/3} \cdot w_c^{-1/3} \tag{B4}$$

where U_{soil} is the mean horizontal wind speed at the ground surface (m/s); U_{canopy} is the mean horizontal wind speed at the top of the canopy (m/s); w_c is the mean leaf width (for maize, 0.09 m); a_{ext} is the wind factor (dimensionless).

The r_x term (s/m) is calculated using Eqs. B5 and B6 below (Norman et al., 1995):

$$r_x = \frac{C'}{LAI} \left(\frac{\Delta}{U_{d+Z_{om}}} \right)^{1/2} \tag{B5}$$

$$U_{d+Z_{om}} = U_{canopy} \cdot exp\left[- a_{ext} \cdot exp\left(1 - \frac{d + Z_{om}}{h_c}\right)\right] \tag{B6}$$

where C' is a weighing coefficient (set to 90 as indicated by Grace, 1981) and $U_{d+Z_{om}}$ is the mean horizontal wind speed at the height equal to $d + Z_{om}$ (m/s).

The r_c term is calculated using Eqs. B7 and B8 (Yan et al., 2015):

$$\frac{r_c}{r_{ah}} = \begin{cases} 3.09 \times \dfrac{r_*}{r_{ah}} + 2.41 \times \sqrt{\dfrac{r_*}{r_{ah}}} + 0.62 & , \; LAI < 2 \\ 2.74 \times \dfrac{r_*}{r_{ah}} - 5.90 \times \sqrt{\dfrac{r_*}{r_{ah}}} + 7.04 & LAI \geq 2 \end{cases} \tag{B7}$$

$$r_* = \rho_a \cdot C_{pa} \cdot \left[\frac{e_s - e_a}{\gamma(R_n - G)}\right] \tag{B8}$$

where r_* is the climatic resistance (s/m).

Appendix C

Remote Sensing Calibration Protocol Code

The Machine-Learning Multispectral Code to Adjust Remote Sensing Data Using IMAGERY Files

Colorado State University

Civil and Environmental Engineering Department

Author: Edson Costa-Filho

Date: 9/12/2022

```
tic
clear; close; clc;
```

a) Menus for choosing the ETa model and remote sensing platform data to be adjusted

```
% Creating a list box with the remote sensing of ETa models that can be chosen by the user

list_model  = {'1) Bausch (1995) Kcr ETa Model','2) Neale et al. (1990) Kcr ETa Model',...
         '3) Trout and DeJonge (2018) Kcr ETa Model','4) Costa-Filho et al. (2021) OSEB ETa Model',...
         '5) Norman et al. (1995) TSEB ETa Model (Parallel)','6) Norman et al. (1995) TSEB ETa Model (Series)'};

name_title = 'ML Regression: Surface Reflectance Code';
prompt_01 = 'Select the preferred Remote Sensing of ETa Model:';

[indx_model,tf_model] = listdlg('Name',name_title,'PromptString',prompt_01,'SelectionMode','single',...
                  'ListString',list_model,'ListSize',[350,90]);

% Creating the buttom menu to choose the platform data to be adjusted based on the RS of ETa model selected
msg_RS = 'Select the platform to be adjusted at its original spatial scale (X m):';

Opt_RS_NealeTrout = ["Landsat-8 or Landsat-9 OLIS/TIRS (30 m spatial resolution)"...
            "Harmonized Planet CubeSat Data (3 m spatial resolution)"...
            "Handheld Multispectral Radiometer (1 m spatial resolution)" "Unmanned Aerial Vehicle (0.03 m spatial resolution)"];
Opt_RS_CostaFilho = ["Landsat-8 or Landsat-9 OLIS/TIRS (30 m spatial resolution)" "Sentinel-2 (10 m spatial resolution)"...
             "Handheld Multispectral Radiometer (1 m spatial resolution)" "Unmanned Aerial Vehicle (0.03 m spatial resolution)"];
Opt_RS_BauschNorman = ["Landsat-8 or Landsat-9 OLIS/TIRS (30 m spatial resolution)" "Sentinel-2 (10 m spatial resolution)"...
            "Harmonized Planet CubeSat (3 m spatial resolution)" "Unmanned Aerial Vehicle (0.03 m spatial resolution)"];


% Selecting the combo RS of ETa model and RS platorm ML regression .mat files to as input to the code

if isempty(indx_model)

    disp('The user selected to cancel the script.')
    return

end

if indx_model == 2 || indx_model == 3

    choice_RS = menu(msg_RS,Opt_RS_NealeTrout);

    if choice_RS == 0

        disp('The user selected to cancel the script.')
        return

    end


    if choice_RS == 1

        FINPUT = 'ML_Kcb_ETa_Neale_Trout_DeJonge_Landsat-8';
        fileToRead1 = cell2mat(string(FINPUT));
        import_matfile(fileToRead1);

    elseif choice_RS == 2

        FINPUT = 'ML_Kcb_ETa_Neale_Trout_DeJonge_CubeSat';
        fileToRead1 = cell2mat(string(FINPUT));
        import_matfile(fileToRead1);

    elseif choice_RS == 3
```

```
        FINPUT = 'ML_Kcb_ETa_Neale_Trout_DeJonge_MSR';
        fileToRead1 = cell2mat(string(FINPUT));
        import_matfile(fileToRead1);

    else

        FINPUT = 'ML_Kcb_ETa_Neale_Trout_DeJonge_UAV';
        fileToRead1 = cell2mat(string(FINPUT));
        import_matfile(fileToRead1);
    end

elseif indx_model == 4
    choice_RS = menu(msg_RS,Opt_RS_CostaFilho);

      if choice_RS == 0

          disp('The user selected to cancel the script.')
          return

     end

     if choice_RS == 1

        FINPUT = 'ML_OSEB_CostaFilho_ETa_Landsat-8';
        fileToRead1 = cell2mat(string(FINPUT));
        import_matfile(fileToRead1);

    elseif choice_RS == 2

        FINPUT = 'ML_OSEB_CostaFilho_ETa_Sentinel-2';
        fileToRead1 = cell2mat(string(FINPUT));
        import_matfile(fileToRead1);

    elseif choice_RS == 3

        FINPUT = 'ML_OSEB_CostaFilho_ETa_MSR';
        fileToRead1 = cell2mat(string(FINPUT));
        import_matfile(fileToRead1);

    else

        FINPUT = 'ML_OSEB_CostaFilho_ETa_UAV';
        fileToRead1 = cell2mat(string(FINPUT));
        import_matfile(fileToRead1);
    end

else
    choice_RS = menu(msg_RS,Opt_RS_BauschNorman);

      if choice_RS == 0

         disp('The user selected to cancel the script.')
         return

     end

     if choice_RS == 1

        FINPUT = 'ML_TSEB_Kcb_Bausch_ETa_Landsat-8';
        fileToRead1 = cell2mat(string(FINPUT));
        import_matfile(fileToRead1);

    elseif choice_RS == 2

        FINPUT = 'ML_TSEB_Kcb_Bausch_ETa_Sentinel-2';
        fileToRead1 = cell2mat(string(FINPUT));
        import_matfile(fileToRead1);

    elseif choice_RS == 3

        FINPUT = 'ML_TSEB_Kcb_Bausch_ETa_CubeSat';
        fileToRead1 = cell2mat(string(FINPUT));
        import_matfile(fileToRead1);

    else
```

```
        FINPUT = 'ML_TSEB_Kcb_Bausch_ETa_UAV';
        fileToRead1 = cell2mat(string(FINPUT));
        import_matfile(fileToRead1);
    end


end


if indx_model >= 2 && indx_model <= 4 && choice_RS == 3

    % Input Parameters

    [num, text, both]=xlsread('ML_Surface_Reflectance_Input_Data.xlsx');

    date = text(3:length(text),1); % Date in mm/dd/yyyy format
    DATE = char(date); % Date in mm/dd/yyyy format
    time = num(1:length(num),1); % ON-SITE time as fraction of hour
    TimeString = datestr(time); % ON-SITE Time as a name
    DOY = num(1:length(num),2); % Day of the Year
    Long = num(1:length(num),3); % Longitude in UTM (m)
    Lat = num(1:length(num),4); % Latitude in UTM (m)
    BLUE_RFL = num(1:length(num),5); % Blue Surface Reflectance (-)
    GREEN_RFL = num(1:length(num),6); % Green Surface Reflectance (-)
    RED_RFL = num(1:length(num),7); % Red Surface Reflectance (-)
    NIR_RFL = num(1:length(num),8); % NIR Surface Reflectance (-)

    SZ = size(BLUE_RFL); % Number of rows and columns of a given image

else

% Input Parameters

% Entering the BLUE surface reflectance imagery file
[file_blue,path_blue] = uigetfile({'*.tif';'*.jp2'},...
                        'Select the BLUE Surface Reflectance Imagery File');
if isequal(file_blue,0)
    disp('The user chose to cancel the script.')
    return
else
   disp(['The user chose the BLUE SR file ', fullfile(path_blue, file_blue)])
end

% Entering the GREEN surface reflectance imagery file
[file_green,path_green] = uigetfile({'*.tif';'*.jp2'},...
                        'Select the GREEN Surface Reflectance Imagery File');
if isequal(file_green,0)
    disp('The user chose to cancel the script.')
    return
else
   disp(['The user chose the GREEN SR file ', fullfile(path_green, file_green)])
end

% Entering the RED surface reflectance imagery file
[file_red,path_red] = uigetfile({'*.tif';'*.jp2'},...
                        'Select the RED Surface Reflectance Imagery File');
if isequal(file_red,0)
    disp('The user chose to cancel the script.')
    return
else
   disp(['The user chose the RED SR file ', fullfile(path_red, file_red)])
end

% Entering the NIR surface reflectance imagery file
[file_nir,path_nir] = uigetfile({'*.tif';'*.jp2'},...
                        'Select the NIR Surface Reflectance Imagery File');
if isequal(file_nir,0)
    disp('The user chose to cancel the script.')
    return
else
   disp(['The user chose the NIR SR file ', fullfile(path_nir, file_nir)])
end

% Reading the imagery file in MATLAB to retrieve geotiff data
```

```
[fileinput,Refmat,bbox] = geotiffread(file_blue);

Long_UTM = [bbox(1,1) bbox(2,1)]; % Longitude in UTM
Lat_UTM = [bbox(1,2) bbox(2,2)]; % Latitude in UTM

% Converting imagery UTM coordinates to decimal degrees from geotiff data (DATUM WGS84)

a_axis = 6378137; % Semi major axis
b_axis = 6356752.31424518; % Semi minor axis
ecc = sqrt(a_axis^2-b_axis^2)/a_axis; % Eccentricity
ecc_2 = sqrt(a_axis^2-b_axis^2)/b_axis; % Second eccentricity
ecc_sq = ecc_2^2; % The second eccentricity to the power of 2
c_radius = a_axis^2/b_axis; % Polar radius of curvature

prompt = {'1. Type the UTM Zone Number from the Imagery (e.g., 1 to 60):',...
    '2. Type the Global Hemisphere (N or S) where the Imagery area is Located (N = North, S = South):',...
    };
dlgtitle = 'Geodata from the Imagery File';
answer = inputdlg(prompt,dlgtitle,[1 100]);
input_data = str2double(answer);

if isempty(input_data)

    disp('The user chose to cancel the script.')

    return

end

fid_GPS = answer(2,1); % Output File Name as a cell array format
filename_GPS = cell2mat(string(fid_GPS)); % Output File Name as a STRING format
Zone_img = input_data(1,1); % UTM zone of the image
Hemis_img = filename_GPS; % Hemisphere of the image

if Hemis_img == 'S'
    Lat_UTM = Lat_UTM-10000000;
end

Mer_Central = 6.*Zone_img-183;
Fi_o = Lat_UTM./(6366197.724*0.9996);
A1 = sin(2.*Fi_o);
A2 = A1.*(cos(Fi_o)).^2;
J2 = Fi_o + A1./2;
J4 = (3.*J2+A2)./4;
J6 = (5.*J4+A2.*(cos(Fi_o)).^2)./3;
Alfa_ftc = 0.75.*ecc_sq;
Beta_ftc = (5/3).*(Alfa_ftc).^2;
Gamma_ftc = (35/27).*(Alfa_ftc).^3;
B_fi = 0.9996.*c_radius.*(Fi_o-(Alfa_ftc.*J2)+(Beta_ftc.*J4)-(Gamma_ftc.*J6));
Ni_o = (c_radius./(1+ecc_sq.*(cos(Fi_o)).^2).^0.50).*0.9996;
Aa = (Long_UTM-500000)./Ni_o;
Bb = (Lat_UTM-B_fi)./Ni_o;
Zeta_ftc = ((ecc_sq.*Aa.^2)./2).*(cos(Fi_o)).^2;
Xi_img = Aa.*(1-Zeta_ftc./3);
Senh_Xi = (exp(Xi_img)-exp(-Xi_img))./2;
ETA_ftc = Bb.*(1-Zeta_ftc)+Fi_o;
Delta_lambda = atan(Senh_Xi./cos(ETA_ftc));
Tau = atan(cos(Delta_lambda).*tan(ETA_ftc));
Fi_rad = Fi_o + (1+ecc_sq.*(cos(Fi_o)).^2-(3/2).*ecc_sq.*sin(Fi_o).*cos(Fi_o).*(Tau-Fi_o)).*(Tau-Fi_o);

Lat_Decimal = (Fi_rad./pi()).*180; % Latitude converted from UTM (m) to decimal degrees
Long_Decimal = (Delta_lambda./pi()).*180+Mer_Central; % Latitude converted from UTM (m) to decimal degrees

% Importing the surface reflectance data as a matrix input (Single format)

BLUE_RFL = double(imread(file_blue)); % Blue Surface Reflectance (-)
GREEN_RFL = double(imread(file_green)); % Green Surface Reflectance (-)
RED_RFL = double(imread(file_red)); % Red Surface Reflectance (-)
NIR_RFL = double(imread(file_nir)); % NIR Surface Reflectance (-)

SZ = size(BLUE_RFL); % Number of rows and columns of a given image

% Creating the georaster summary file to generate imagery

Ref = georasterref('RasterSize',SZ,...
   'LatitudeLimits',[Lat_Decimal(1,1),Lat_Decimal(1,2)],...
```

```
    'LongitudeLimits',[Long_Decimal(1,1),Long_Decimal(1,2)],...
     'RasterInterpretation', 'cells',...
     'ColumnsStartFrom', 'north',...
     'RowsStartFrom', 'west');


% Creating a list box with the variable outputs that can be chosen by the user to create GeoTiFF maps

list_model  = {'1) Adjusted Surface Reflectance','2) Soil and Canopy Surface Reflectance (No Adjustment)',...
         '3) Soil and Canopy Surface Reflectance (Adjusted)','4) Vegetation Indices (Original Data)',...
         '5) Vegetation Indices (Adjusted Data)','6) Light Attenuation Parameters (kp and kv)'};

name_title = 'Output Selection';
prompt_01 = 'Select the desired GeoTiFF maps to be exported:';

[indx_mdl_out,tf_mdl_out] = listdlg('Name',name_title,'PromptString',prompt_01,...
                    'ListString',list_model,'ListSize',[350,90]);

if isempty(indx_mdl_out)

    disp('The user selected to cancel the script.')
    return

end

end
```

b) Decomposing Surface Reflectance into soil (SRs) and canopy (SRc) components

```
% Writing the initial NoData value assigned to the multispectral data

NoData_Value = -9999;

for i = 1:SZ(1,1)

    for j = 1:SZ(1,2)

            if abs(BLUE_RFL(i,j)) == 0

                BLUE_RFL(i,j) = NoData_Value;

            end

             if abs(GREEN_RFL(i,j)) == 0

                GREEN_RFL(i,j) = NoData_Value;

             end

              if abs(RED_RFL(i,j)) == 0

                RED_RFL(i,j) = NoData_Value;

              end

               if abs(NIR_RFL(i,j)) == 0

                NIR_RFL(i,j) = NoData_Value;

               end

    end

end


L = 0.50; % SAVI adjustment factor
N = 1000; % Maximum number of iterations
fc_min = 0; % Mininum value of fractional vegetation cover
fc_max = 0.85; % Maximum value of fractional vegetation cover

a_kp = 0.7848; % Slope of kp
b_kp = -0.0465; % Intercept of kp
```

```
d_NDVI_min = 0.2492; % d(NDVI)/df_c Min
d_NDVI_max = 0.3868; % d(NDVI)/df_c Max

d_BLUE_min = -0.0405; % d(BLUE)/df_c Min
d_BLUE_max = -0.1241; % d(BLUE)/df_c Max

d_GREEN_min = -0.0678; % d(GREEN)/df_c Min
d_GREEN_max = -0.1478; % d(GREEN)/df_c Max

d_RED_min = -0.0903; % d(RED)/df_c Min
d_RED_max = -0.1373; % d(RED)/df_c Max

d_NIR_min = 0.0359; % d(NIR)/df_c Min
d_NIR_max = 0.1813; % d(NIR)/df_c Max

% Variable pre-allocation

NDVI = zeros(SZ(1,1),SZ(1,2));
NDVI_adj = zeros(SZ(1,1),SZ(1,2));
SAVI = zeros(SZ(1,1),SZ(1,2));
SAVI_adj = zeros(SZ(1,1),SZ(1,2));
OSAVI = zeros(SZ(1,1),SZ(1,2));
OSAVI_adj = zeros(SZ(1,1),SZ(1,2));
fc_norman = zeros(SZ(1,1),SZ(1,2));
fc_norman_adj = zeros(SZ(1,1),SZ(1,2));
LAI = zeros(SZ(1,1),SZ(1,2));
LAI_adj = zeros(SZ(1,1),SZ(1,2));
LAI_L = zeros(SZ(1,1),SZ(1,2));
LAI_L_adj = zeros(SZ(1,1),SZ(1,2));
fs_kustas = zeros(SZ(1,1),SZ(1,2));
fs_kustas_adj = zeros(SZ(1,1),SZ(1,2));
CF = zeros(SZ(1,1),SZ(1,2));
CF_adj = zeros(SZ(1,1),SZ(1,2));
fc_kustas_updated = zeros(SZ(1,1),SZ(1,2));
fc_kustas_updated_adj = zeros(SZ(1,1),SZ(1,2));
fc = zeros(SZ(1,1),SZ(1,2));
fc_adj = zeros(SZ(1,1),SZ(1,2));
SRc_BLUE = BLUE_RFL.*200;
SRc_GREEN = GREEN_RFL.*200;
SRc_RED = RED_RFL.*200;
SRc_NIR = NIR_RFL.*200;
SRs_BLUE = zeros(SZ(1,1),SZ(1,2));
SRs_GREEN = zeros(SZ(1,1),SZ(1,2));
SRs_RED = zeros(SZ(1,1),SZ(1,2));
SRs_NIR = zeros(SZ(1,1),SZ(1,2));
d_RED = zeros(SZ(1,1),SZ(1,2));
d_GREEN = zeros(SZ(1,1),SZ(1,2));
d_BLUE = zeros(SZ(1,1),SZ(1,2));
d_NIR = zeros(SZ(1,1),SZ(1,2));
d_NDVI = zeros(SZ(1,1),SZ(1,2));
NDVIs = zeros(SZ(1,1),SZ(1,2));
NDVIc = zeros(SZ(1,1),SZ(1,2));
kv = zeros(SZ(1,1),SZ(1,2));
kp = zeros(SZ(1,1),SZ(1,2));
error_BLUE = ones(SZ(1,1),SZ(1,2));
error_GREEN = ones(SZ(1,1),SZ(1,2));
error_RED = ones(SZ(1,1),SZ(1,2));
error_NIR = ones(SZ(1,1),SZ(1,2));
LHS = zeros(SZ(1,1),SZ(1,2));
SR_BLUE = zeros(SZ(1,1),SZ(1,2));
SR_GREEN = zeros(SZ(1,1),SZ(1,2));
SR_RED = zeros(SZ(1,1),SZ(1,2));
SR_NIR = zeros(SZ(1,1),SZ(1,2));
eta_BLUE = zeros(SZ(1,1),SZ(1,2));
eta_GREEN = zeros(SZ(1,1),SZ(1,2));
eta_RED = zeros(SZ(1,1),SZ(1,2));
eta_NIR = zeros(SZ(1,1),SZ(1,2));
yfit_BLUE_SRc = zeros(SZ(1,1),SZ(1,2));
yfit_BLUE_SRs = zeros(SZ(1,1),SZ(1,2));
yfit_GREEN_SRc = zeros(SZ(1,1),SZ(1,2));
yfit_GREEN_SRs = zeros(SZ(1,1),SZ(1,2));
yfit_RED_SRc = zeros(SZ(1,1),SZ(1,2));
yfit_RED_SRs = zeros(SZ(1,1),SZ(1,2));
yfit_NIR_SRc = zeros(SZ(1,1),SZ(1,2));
yfit_NIR_SRs = zeros(SZ(1,1),SZ(1,2));
yfit_eta_BLUE = zeros(SZ(1,1),SZ(1,2));
```

```
yfit_eta_GREEN = zeros(SZ(1,1),SZ(1,2));
yfit_eta_RED = zeros(SZ(1,1),SZ(1,2));
yfit_eta_NIR = zeros(SZ(1,1),SZ(1,2));
SR_BLUE_adj = zeros(SZ(1,1),SZ(1,2));
SR_GREEN_adj = zeros(SZ(1,1),SZ(1,2));
SR_RED_adj = zeros(SZ(1,1),SZ(1,2));
SR_NIR_adj = zeros(SZ(1,1),SZ(1,2));

for i = 1:SZ(1,1)

    for j = 1:SZ(1,2)

        if BLUE_RFL(i,j) == NoData_Value

        NDVI(i,j) = NoData_Value;
        SAVI(i,j) = NoData_Value;
        OSAVI(i,j) = NoData_Value;
        fc_norman(i,j) = NoData_Value;
        LAI(i,j) = NoData_Value;
        LAI_L(i,j) = NoData_Value;
        fs_kustas(i,j) = NoData_Value;
        CF(i,j) = NoData_Value;
        fc_kustas_updated(i,j) = NoData_Value;
        fc(i,j) = NoData_Value;
        SRs_BLUE(i,j) = NoData_Value;
        SRc_BLUE(i,j) = NoData_Value;
        SRs_GREEN(i,j) = NoData_Value;
        SRc_GREEN(i,j) = NoData_Value;
        SRs_RED(i,j) = NoData_Value;
        SRc_RED(i,j) = NoData_Value;
        SRs_NIR(i,j) = NoData_Value;
        SRc_NIR(i,j) = NoData_Value;
        d_RED(i,j) = NoData_Value;
        d_GREEN(i,j) = NoData_Value;
        d_BLUE(i,j) = NoData_Value;
        d_NIR(i,j) = NoData_Value;
        d_NDVI(i,j) = NoData_Value;
        NDVIs(i,j) = NoData_Value;
        NDVIc(i,j) = NoData_Value;
        kv(i,j) = NoData_Value;
        kp(i,j) = NoData_Value;
        error_BLUE(i,j) = NoData_Value;
        error_GREEN(i,j) = NoData_Value;
        error_RED(i,j) = NoData_Value;
        error_NIR(i,j) = NoData_Value;
        eta_BLUE(i,j) = NoData_Value;
        eta_GREEN(i,j) = NoData_Value;
        eta_RED(i,j) = NoData_Value;
        eta_NIR(i,j) = NoData_Value;
        SR_BLUE(i,j) = NoData_Value;
        SR_GREEN(i,j) = NoData_Value;
        SR_RED(i,j) = NoData_Value;
        SR_NIR(i,j) = NoData_Value;

        else

        NDVI(i,j) = (NIR_RFL(i,j) - RED_RFL(i,j)) / (NIR_RFL(i,j) + RED_RFL(i,j));
        SAVI(i,j) = ((NIR_RFL(i,j) - RED_RFL(i,j)) / (NIR_RFL(i,j) + RED_RFL(i,j) + L)) * (1 + L);

        % Rondeaux et al. (1996)
        OSAVI(i,j) = ((NIR_RFL(i,j) - RED_RFL(i,j)) /...
        (NIR_RFL(i,j) + RED_RFL(i,j) + 0.16))*1.16;

        % LAI (Chávez et al., 2009)
        LAI(i,j) = 0.263 * exp(3.813 * OSAVI(i,j));


        % Calculation of fractional vegetation cover
        % Norman et al. (1995)
        fc_norman(i,j) = 1-exp(-0.5*LAI(i,j));

        % Local LAI calculation (Kustas and Norman, 2000)
        LAI_L(i,j) = LAI(i,j)/fc_norman(i,j);

        % Fractional soil cover (Kustas and Norman, 2000)
        fs_kustas(i,j) = fc_norman(i,j)*exp(-0.5*LAI_L(i,j))...
```

```
                +(1-fc_norman(i,j));

% Clumping factor (Kustas and Normam, 2000)
CF(i,j) = -log(fs_kustas(i,j))/(0.5*LAI(i,j));

% Updated fractional vegetation cover (including clumping
    % factor)
% Kustas and Norman (2000)
fc_kustas_updated(i,j) = 1-exp(-0.5*CF(i,j)*LAI(i,j));

fc(i,j) = fc_kustas_updated(i,j);

% Calculating the first derivative of SR and NDVI data as function of fractional vegetation cover (f_c)

d_NDVI(i,j) = d_NDVI_min - (((fc_min - fc(i,j))/(fc_min - fc_max))...
    *(d_NDVI_min - d_NDVI_max));
d_RED(i,j) = d_RED_min - (((fc_min - fc(i,j))/(fc_min - fc_max))...
    *(d_RED_min - d_RED_max));
d_GREEN(i,j) = d_GREEN_min - (((fc_min - fc(i,j))/(fc_min - fc_max))...
    *(d_GREEN_min - d_GREEN_max));
d_NIR(i,j) = d_NIR_min - (((fc_min - fc(i,j))/(fc_min - fc_max))...
    *(d_NIR_min - d_NIR_max));

d_BLUE(i,j) = d_BLUE_min - (((fc_min - fc(i,j))/(fc_min - fc_max))...
   *(d_BLUE_min - d_BLUE_max));

% Calculating the NDVI values for soil (NDVIs) and canopy (NDVIc)

NDVIs(i,j) = NDVI(i,j) - 2*fc(i,j) * d_NDVI(i,j);
NDVIc(i,j) = NDVI(i,j) + 2*(sqrt(fc(i,j)) - fc(i,j)) * d_NDVI(i,j);

% Calculating the equivalent light extinction (k_v) and the light attenuation parameter (k_p)

kv(i,j) = -(1/LAI(i,j))*log((NDVI(i,j) - NDVIc(i,j))/(NDVIs(i,j) - NDVIc(i,j)));
kp(i,j) = a_kp * kv(i,j) + b_kp;

% Iterating to update SRc and SRs until errors regarding iterated SR are less than 0.1%

while error_BLUE(i,j) > 0.001

SRs_BLUE(i,j) = SRc_BLUE(i,j) - d_BLUE(i,j);

eta_BLUE(i,j) = (SRc_BLUE(i,j)-SRs_BLUE(i,j))/(SRs_BLUE(i,j)-(1/SRc_BLUE(i,j)));

SR_BLUE(i,j) = (SRc_BLUE(i,j)+(eta_BLUE(i,j)*exp(-2*kp(i,j)*LAI(i,j)))/...
                (SRc_BLUE(i,j)))/(1+eta_BLUE(i,j)*exp(-2*kp(i,j)*LAI(i,j)));

error_BLUE(i,j) = abs((BLUE_RFL(i,j) - SR_BLUE(i,j))/BLUE_RFL(i,j));


 if error_BLUE(i,j) > 0

     SRc_BLUE(i,j) = SRc_BLUE(i,j) - fc(i,j)*error_BLUE(i,j)/2*BLUE_RFL(i,j);

 else

     SRc_BLUE(i,j) = SRc_BLUE(i,j) + fc(i,j)*error_BLUE(i,j)/2*BLUE_RFL(i,j);

 end


end

if SRc_BLUE(i,j) < 0 || SRc_BLUE(i,j) == -inf

    SRc_BLUE(i,j) = NaN;

end


while error_GREEN(i,j) > 0.001

SRs_GREEN(i,j) = SRc_GREEN(i,j) - d_GREEN(i,j);

eta_GREEN(i,j) = (SRc_GREEN(i,j)-SRs_GREEN(i,j))/(SRs_GREEN(i,j)-(1/SRc_GREEN(i,j)));
```

```
SR_GREEN(i,j) = (SRc_GREEN(i,j)+(eta_GREEN(i,j)*exp(-2*kp(i,j)*LAI(i,j)))/...
                (SRc_GREEN(i,j)))/(1+eta_GREEN(i,j)*exp(-2*kp(i,j)*LAI(i,j)));

error_GREEN(i,j) = abs((GREEN_RFL(i,j) - SR_GREEN(i,j))/GREEN_RFL(i,j));


 if error_GREEN(i,j) > 0

     SRc_GREEN(i,j) = SRc_GREEN(i,j) - fc(i,j)*error_GREEN(i,j)/2*GREEN_RFL(i,j);

 else

     SRc_GREEN(i,j) = SRc_GREEN(i,j) + fc(i,j)*error_GREEN(i,j)/2*GREEN_RFL(i,j);

 end


end

if SRc_GREEN(i,j) < 0 || SRc_GREEN(i,j) == -inf

    SRc_GREEN(i,j) = NaN;

end

while error_RED(i,j) > 0.001

SRs_RED(i,j) = SRc_RED(i,j) - d_RED(i,j);

eta_RED(i,j) = (SRc_RED(i,j)-SRs_RED(i,j))/(SRs_RED(i,j)-(1/SRc_RED(i,j)));

SR_RED(i,j) = (SRc_RED(i,j)+(eta_RED(i,j)*exp(-2*kp(i,j)*LAI(i,j)))/...
              (SRc_RED(i,j)))/(1+eta_RED(i,j)*exp(-2*kp(i,j)*LAI(i,j)));

error_RED(i,j) = abs((RED_RFL(i,j) - SR_RED(i,j))/RED_RFL(i,j));


 if error_RED(i,j) > 0

     SRc_RED(i,j) = SRc_RED(i,j) - fc(i,j)*error_RED(i,j)/2*RED_RFL(i,j);

 else

     SRc_RED(i,j) = SRc_RED(i,j) + fc(i,j)*error_RED(i,j)/2*RED_RFL(i,j);

 end


end

if SRc_RED(i,j) < 0 || SRc_RED(i,j) == -inf

    SRc_RED(i,j) = NaN;

end


 while error_NIR(i,j) > 0.001

SRs_NIR(i,j) = SRc_NIR(i,j) - d_NIR(i,j);

eta_NIR(i,j) = (SRc_NIR(i,j)-SRs_NIR(i,j))/(SRs_NIR(i,j)-(1/SRc_NIR(i,j)));

SR_NIR(i,j) = (SRc_NIR(i,j)+(eta_NIR(i,j)*exp(-2*kp(i,j)*LAI(i,j)))/...
              (SRc_NIR(i,j)))/(1+eta_NIR(i,j)*exp(-2*kp(i,j)*LAI(i,j)));

error_NIR(i,j) = abs((NIR_RFL(i,j) - SR_NIR(i,j))/NIR_RFL(i,j));


 if error_NIR(i,j) > 0

     SRc_NIR(i,j) = SRc_NIR(i,j) - fc(i,j)*error_NIR(i,j)/2*NIR_RFL(i,j);

 else

     SRc_NIR(i,j) = SRc_NIR(i,j) + fc(i,j)*error_NIR(i,j)/2*NIR_RFL(i,j);
```

```
        end


       end

       if SRc_NIR(i,j) < 0 || SRc_NIR(i,j) == -inf

           SRc_NIR(i,j) = NaN;

       end

       end

   end

end

SRc_BLUE = fillmissing(SRc_BLUE,'pchip');
SRs_BLUE = fillmissing(SRs_BLUE,'pchip');
SRc_GREEN = fillmissing(SRc_GREEN,'pchip');
SRs_GREEN = fillmissing(SRs_GREEN,'pchip');
SRc_RED = fillmissing(SRc_RED,'pchip');
SRs_RED = fillmissing(SRs_RED,'pchip');
SRc_NIR = fillmissing(SRc_NIR,'pchip');
SRs_NIR = fillmissing(SRs_NIR,'pchip');
```

c) Applying the machine-learning regression to adjust the SRc and SRs data

```
% To make predictions on a new predictor column matrix, X, use:
% yfit = c.predictFcn(X) replacing 'c' with the name of the variable that is this struct, e.g. 'trainedModel'.
% X must contain exactly 1 columns because this model was trained using 1 predictors.
% X must contain only predictor columns in exactly the same order and format as your training data.
% Do not include the response column or any columns you did not import into the app.
% For more information, see <a href="matlab:helpview(fullfile(docroot, 'stats', 'stats.map'),...
% ...'appregression_exportmodeltoworkspace')">How to predict using an exported model</a>.

for i = 1:SZ(1,1)

   for j = 1:SZ(1,2)

       if BLUE_RFL(i,j) == NoData_Value

           yfit_BLUE_SRc(i,j) = NoData_Value;
           yfit_BLUE_SRs(i,j) = NoData_Value;
           yfit_GREEN_SRc(i,j) = NoData_Value;
           yfit_GREEN_SRs(i,j) = NoData_Value;
           yfit_RED_SRc(i,j) = NoData_Value;
           yfit_RED_SRs(i,j) = NoData_Value;
           yfit_NIR_SRc(i,j) = NoData_Value;
           yfit_NIR_SRs(i,j) = NoData_Value;


       else

           yfit_BLUE_SRc(i,j) = trainedModel_SRc_BLUE.predictFcn(SRc_BLUE(i,j));

           if yfit_BLUE_SRc(i,j) < 0

               yfit_BLUE_SRc(i,j) = NaN;
           end

           yfit_BLUE_SRs(i,j) = trainedModel_SRs_BLUE.predictFcn(SRs_BLUE(i,j));

           if yfit_BLUE_SRs(i,j) < 0

               yfit_BLUE_SRs(i,j) = NaN;
           end

           yfit_GREEN_SRc(i,j) = trainedModel_SRc_GREEN.predictFcn(SRc_GREEN(i,j));

           if yfit_GREEN_SRc(i,j) < 0

               yfit_GREEN_SRc(i,j) = NaN;
           end
```

```
            yfit_GREEN_SRs(i,j) = trainedModel_SRs_GREEN.predictFcn(SRs_GREEN(i,j));

            if yfit_GREEN_SRs(i,j) < 0

                yfit_GREEN_SRs(i,j) = NaN;
            end

            yfit_RED_SRc(i,j) = trainedModel_SRc_RED.predictFcn(SRc_RED(i,j));

            if yfit_RED_SRc(i,j) < 0

                yfit_RED_SRc(i,j) = NaN;
            end

            yfit_RED_SRs(i,j) = trainedModel_SRs_RED.predictFcn(SRs_RED(i,j));

            if yfit_RED_SRs(i,j) < 0

                yfit_RED_SRs(i,j) = NaN;
            end

            yfit_NIR_SRc(i,j) = trainedModel_SRc_NIR.predictFcn(SRc_NIR(i,j));

            if yfit_NIR_SRc(i,j) < 0

                yfit_NIR_SRc(i,j) = NaN;
            end

            yfit_NIR_SRs(i,j) = trainedModel_SRs_NIR.predictFcn(SRs_NIR(i,j));

             if yfit_NIR_SRs(i,j) < 0

                yfit_NIR_SRs(i,j) = NaN;
            end


        end

    end

end


yfit_BLUE_SRc = fillmissing(yfit_BLUE_SRc,'pchip');
yfit_BLUE_SRs = fillmissing(yfit_BLUE_SRs,'pchip');
yfit_GREEN_SRc = fillmissing(yfit_GREEN_SRc,'pchip');
yfit_GREEN_SRs = fillmissing(yfit_GREEN_SRs,'pchip');
yfit_RED_SRc = fillmissing(yfit_RED_SRc,'pchip');
yfit_RED_SRs = fillmissing(yfit_RED_SRs,'pchip');
yfit_NIR_SRc = fillmissing(yfit_NIR_SRc,'pchip');
yfit_NIR_SRs = fillmissing(yfit_NIR_SRs,'pchip');
```

d) Applying the pixel decomposition model in reverse to obtain adjusted SR data for each RGB and NIR bands

```
    for i = 1:SZ(1,1)

        for j = 1:SZ(1,2)

            if BLUE_RFL(i,j) == NoData_Value

            yfit_eta_BLUE(i,j) = NoData_Value;
            yfit_eta_GREEN(i,j) = NoData_Value;
            yfit_eta_RED(i,j) = NoData_Value;
            yfit_eta_NIR(i,j) = NoData_Value;
            SR_BLUE_adj(i,j) = NoData_Value;
            SR_GREEN_adj(i,j) = NoData_Value;
            SR_RED_adj(i,j) = NoData_Value;
            SR_NIR_adj(i,j) = NoData_Value;

            else

            yfit_eta_BLUE(i,j) = (yfit_BLUE_SRc(i,j)-yfit_BLUE_SRs(i,j))/(yfit_BLUE_SRs(i,j)-(1/yfit_BLUE_SRc(i,j)));
            yfit_eta_GREEN(i,j) = (yfit_GREEN_SRc(i,j)-yfit_GREEN_SRs(i,j))/(yfit_GREEN_SRs(i,j)-(1/yfit_GREEN_SRc(i,j)));
```

```
            yfit_eta_RED(i,j) = (yfit_RED_SRc(i,j)-yfit_RED_SRs(i,j))/(yfit_RED_SRs(i,j)-(1/yfit_RED_SRc(i,j)));
            yfit_eta_NIR(i,j) = (yfit_NIR_SRc(i,j)-yfit_NIR_SRs(i,j))/(yfit_NIR_SRs(i,j)-(1/yfit_NIR_SRc(i,j)));


            SR_BLUE_adj(i,j) = (yfit_BLUE_SRc(i,j)+(yfit_eta_BLUE(i,j)*exp(-2*kp(i,j)*LAI(i,j)))/...
                        (yfit_BLUE_SRc(i,j)))/(1+yfit_eta_BLUE(i,j)*exp(-2*kp(i,j)*LAI(i,j)));

            SR_GREEN_adj(i,j) = (yfit_GREEN_SRc(i,j)+(yfit_eta_GREEN(i,j)*exp(-2*kp(i,j)*LAI(i,j)))/...
                        (yfit_GREEN_SRc(i,j)))/(1+yfit_eta_GREEN(i,j)*exp(-2*kp(i,j)*LAI(i,j)));

            SR_RED_adj(i,j) = (yfit_RED_SRc(i,j)+(yfit_eta_RED(i,j)*exp(-2*kp(i,j)*LAI(i,j)))/...
                        (yfit_RED_SRc(i,j)))/(1+yfit_eta_RED(i,j)*exp(-2*kp(i,j)*LAI(i,j)));

            SR_NIR_adj(i,j) = (yfit_NIR_SRc(i,j)+(yfit_eta_NIR(i,j)*exp(-2*kp(i,j)*LAI(i,j)))/...
                        (yfit_NIR_SRc(i,j)))/(1+yfit_eta_NIR(i,j)*exp(-2*kp(i,j)*LAI(i,j)));

            end

        end
    end
```

e) Calculating the vegetation indices using the adjusted SR data

```
for i = 1:SZ(1,1)

        for j = 1:SZ(1,2)

            if BLUE_RFL(i,j) == NoData_Value

                 NDVI_adj(i,j) = NoData_Value;
                 SAVI_adj(i,j) = NoData_Value;
                 OSAVI_adj(i,j) = NoData_Value;
                 fc_norman_adj(i,j) = NoData_Value;
                 LAI_adj(i,j) = NoData_Value;
                 LAI_L_adj(i,j) = NoData_Value;
                 fs_kustas_adj(i,j) = NoData_Value;
                 CF_adj(i,j) = NoData_Value;
                 fc_kustas_updated_adj(i,j) = NoData_Value;
                 fc_adj(i,j) = NoData_Value;

            else

        NDVI_adj(i,j) = (SR_NIR_adj(i,j) -SR_RED_adj(i,j)) / (SR_NIR_adj(i,j) + SR_RED_adj(i,j));
        SAVI_adj(i,j) = ((SR_NIR_adj(i,j) - SR_RED_adj(i,j)) / (SR_NIR_adj(i,j) + SR_RED_adj(i,j) + L)) * (1 + L);

        % Rondeaux et al. (1996)
        OSAVI_adj(i,j) = ((SR_NIR_adj(i,j) - SR_RED_adj(i,j)) /...
        (SR_NIR_adj(i,j) + SR_RED_adj(i,j) + 0.16))*1.16;

        % LAI (Chávez et al., 2009)
        LAI_adj(i,j) = 0.263 * exp(3.813 * OSAVI_adj(i,j));

        % Calculation of fractional vegetation cover
        % Norman et al. (1995)
        fc_norman_adj(i,j) = 1-exp(-0.5*LAI_adj(i,j));

        % Local LAI calculation (Kustas and Norman, 2000)
        LAI_L_adj(i,j) = LAI_adj(i,j)/fc_norman_adj(i,j);

        % Fractional soil cover (Kustas and Norman, 2000)
        fs_kustas_adj(i,j) = fc_norman_adj(i,j)*exp(-0.5*LAI_L_adj(i,j))...
                    +(1-fc_norman_adj(i,j));

        % Clumping factor (Kustas and Normam, 2000)
        CF_adj(i,j) = -log(fs_kustas_adj(i,j))/(0.5*LAI_adj(i,j));

        % Updated fractional vegetation cover (including clumping
            % factor)
        % Kustas and Norman (2000)

        fc_kustas_updated_adj(i,j) = 1-exp(-0.5*CF_adj(i,j)*LAI_adj(i,j));

        fc_adj(i,j) = fc_kustas_updated_adj(i,j);
```

```
            end

        end

end
```

f) Exporting the adjusted results as .tiff file maps or .csv files

```
if indx_model >= 2 && indx_model <= 4 && choice_RS == 3

% Naming the columns in the .csv file

colNames_SRc_SRs = {'Date','Time','DOY','Longitude','Latitude','SRc_BLUE','SRc_BLUE_adj','SRs_BLUE',...
            'SRs_BLUE_adj','SRc_GREEN','SRc_GREEN_adj',...
            'SRs_GREEN','SRs_GREEN_adj','SRc_RED',...
            'SRc_RED_adj','SRs_RED','SRs_RED_adj',...
            'SRc_NIR','SRc_NIR_adj','SRs_NIR','SRs_NIR_adj'};

colNames_SR = {'Date','Time','DOY','Longitude','Latitude','BLUE_SR','BLUE_SR_adj',...
               'GREEN_SR','GREEN_SR_adj','RED_SR','RED_SR_adj','NIR_SR','NIR_SR_adj'};

colNames_VI_kv_kp = {'Date','Time','DOY','Longitude','Latitude','NDVI','NDVIc','NDVIs','OSAVI','SAVI','f_c','LAI',...
                        'k_v','k_p'};

% Concatenating the table with the results

Export_SRc_SRs_tbl = table(DATE,TimeString,DOY,Long,Lat,SRc_BLUE,yfit_BLUE_SRc,SRs_BLUE,yfit_BLUE_SRs,...
          SRc_GREEN,yfit_GREEN_SRc,SRs_GREEN,yfit_GREEN_SRs,...
          SRc_RED,yfit_RED_SRc,SRs_RED,yfit_RED_SRs,...
          SRc_NIR,yfit_NIR_SRc,SRs_NIR,yfit_NIR_SRs,'VariableNames',colNames_SRc_SRs);

Export_SR_tbl = table(DATE,TimeString,DOY,Long,Lat,BLUE_RFL,SR_BLUE_adj,GREEN_RFL,SR_GREEN_adj,...
          RED_RFL,SR_RED_adj,NIR_RFL,SR_NIR_adj,'VariableNames',colNames_SR);

Export_VI_tbl = table(DATE,TimeString,DOY,Long,Lat,NDVI,NDVIc,NDVIs,OSAVI,...
          SAVI,fc,LAI,kv,kp,'VariableNames',colNames_VI_kv_kp);


% Writing the table as .csv file

writetable(Export_SRc_SRs_tbl,'SRc_SRs_Adjusted_Results.csv','Delimiter',',');
writetable(Export_SR_tbl,'SR_Adjusted_Results.csv','Delimiter',',');
writetable(Export_VI_tbl,'VI_kv_kp_Results.csv','Delimiter',',');


else

% Adjusted surface reflectance imagery (Adjusted SR)

filename1 = 'SR_BLUE_adjusted';
filename2 = 'SR_GREEN_adjusted';
filename3 = 'SR_RED_adjusted';
filename4 = 'SR_NIR_adjusted';

SR_BLUE_adj(SR_BLUE_adj==NoData_Value) = NaN;
SR_GREEN_adj(SR_GREEN_adj==NoData_Value) = NaN;
SR_RED_adj(SR_RED_adj==NoData_Value) = NaN;
SR_NIR_adj(SR_NIR_adj==NoData_Value) = NaN;

if any(ismember(indx_mdl_out,1))

geotiffwrite(filename1,SR_BLUE_adj,Ref);
geotiffwrite(filename2,SR_GREEN_adj,Ref);
geotiffwrite(filename3,SR_RED_adj,Ref);
geotiffwrite(filename4,SR_NIR_adj,Ref);

end

% Decomposed soil and canopy surface reflectance (SRs and SRc)

filename5 = 'SRc_BLUE_no_adjustment';
```

```
filename6 = 'SRc_GREEN_no_adjustment';
filename7 = 'SRc_RED_no_adjustment';
filename8 = 'SRc_NIR_no_adjustment';

SRc_BLUE(SRc_BLUE==NoData_Value) = NaN;
SRc_GREEN(SRc_GREEN==NoData_Value) = NaN;
SRc_RED(SRc_RED==NoData_Value) = NaN;
SRc_NIR(SRc_NIR==NoData_Value) = NaN;

filename9 =  'SRs_BLUE_no_adjustment';
filename10 = 'SRs_GREEN_no_adjustment';
filename11 = 'SRs_RED_no_adjustment';
filename12 = 'SRs_NIR_no_adjustment';

SRs_BLUE(SRs_BLUE==NoData_Value) = NaN;
SRs_GREEN(SRs_GREEN==NoData_Value) = NaN;
SRs_RED(SRs_RED==NoData_Value) = NaN;
SRs_NIR(SRs_NIR==NoData_Value) = NaN;

if any(ismember(indx_mdl_out,2))

    geotiffwrite(filename5,SRc_BLUE,Ref);
    geotiffwrite(filename6,SRc_GREEN,Ref);
    geotiffwrite(filename7,SRc_RED,Ref);
    geotiffwrite(filename8,SRc_NIR,Ref);

    geotiffwrite(filename9,SRs_BLUE,Ref);
    geotiffwrite(filename10,SRs_GREEN,Ref);
    geotiffwrite(filename11,SRs_RED,Ref);
    geotiffwrite(filename12,SRs_NIR,Ref);

end


% Adjusted soil and canopy surface reflectance (adjusted SRs and SRc)

filename13 = 'SRc_BLUE_adjusted';
filename14 = 'SRc_GREEN_adjusted';
filename15 = 'SRc_RED_adjusted';
filename16 = 'SRc_NIR_adjusted';

yfit_BLUE_SRc(yfit_BLUE_SRc==NoData_Value) = NaN;
yfit_GREEN_SRc(yfit_GREEN_SRc==NoData_Value) = NaN;
yfit_RED_SRc(yfit_RED_SRc==NoData_Value) = NaN;
yfit_NIR_SRc(yfit_NIR_SRc==NoData_Value) = NaN;

filename17 =  'SRs_BLUE_adjusted';
filename18 = 'SRs_GREEN_adjusted';
filename19 = 'SRs_RED_adjusted';
filename20 = 'SRs_NIR_adjusted';

yfit_BLUE_SRs(yfit_BLUE_SRs==NoData_Value) = NaN;
yfit_GREEN_SRs(yfit_GREEN_SRs==NoData_Value) = NaN;
yfit_RED_SRs(yfit_RED_SRs==NoData_Value) = NaN;
yfit_NIR_SRs(yfit_NIR_SRs==NoData_Value) = NaN;

if any(ismember(indx_mdl_out,3))

    geotiffwrite(filename13,yfit_BLUE_SRc,Ref);
    geotiffwrite(filename14,yfit_GREEN_SRc,Ref);
    geotiffwrite(filename15,yfit_RED_SRc,Ref);
    geotiffwrite(filename16,yfit_NIR_SRc,Ref);

    geotiffwrite(filename17,yfit_BLUE_SRs,Ref);
    geotiffwrite(filename18,yfit_GREEN_SRs,Ref);
    geotiffwrite(filename19,yfit_RED_SRs,Ref);
    geotiffwrite(filename20,yfit_NIR_SRs,Ref);

end

% Vegetation indices using original SR data

filename21 =  'NDVI';
filename22 = 'OSAVI';
filename23 = 'SAVI';
filename24 = 'LAI';
```

```
filename25 = 'fc';
filename26 = 'NDVIs';
filename27 = 'NDVIc';

NDVI(NDVI==NoData_Value) = NaN;
OSAVI(OSAVI==NoData_Value) = NaN;
SAVI(SAVI==NoData_Value) = NaN;
LAI(LAI==NoData_Value) = NaN;
fc(fc==NoData_Value) = NaN;
NDVIs(NDVIs==NoData_Value) = NaN;
NDVIc(NDVIc==NoData_Value) = NaN;

if any(ismember(indx_mdl_out,4))

    geotiffwrite(filename21,NDVI,Ref);
    geotiffwrite(filename22,OSAVI,Ref);
    geotiffwrite(filename23,SAVI,Ref);
    geotiffwrite(filename24,LAI,Ref);
    geotiffwrite(filename25,fc,Ref);
    geotiffwrite(filename26,NDVIs,Ref);
    geotiffwrite(filename27,NDVIc,Ref);

end

% Vegetation indices using adjusted SR data

filename28 =  'NDVI_adjusted';
filename29 = 'OSAVI_adjusted';
filename30 = 'SAVI_adjusted';
filename31 = 'LAI_adjusted';
filename32 = 'fc_adjusted';

NDVI_adj(NDVI_adj==NoData_Value) = NaN;
OSAVI_adj(OSAVI_adj==NoData_Value) = NaN;
SAVI_adj(SAVI_adj==NoData_Value) = NaN;
LAI_adj(LAI_adj==NoData_Value) = NaN;
fc_adj(fc_adj==NoData_Value) = NaN;

if any(ismember(indx_mdl_out,5))

    geotiffwrite(filename28,NDVI_adj,Ref);
    geotiffwrite(filename29,OSAVI_adj,Ref);
    geotiffwrite(filename30,SAVI_adj,Ref);
    geotiffwrite(filename31,LAI_adj,Ref);
    geotiffwrite(filename32,fc_adj,Ref);

end

% Kp and Kv parameters

filename33 = 'kp';
filename34 = 'kv';

kp(kp==NoData_Value) = NaN;
kv(kv==NoData_Value) = NaN;

if any(ismember(indx_mdl_out,6))

    geotiffwrite(filename33,kp,Ref);
    geotiffwrite(filename34,kv,Ref);

end

end

toc
```

Appendix D

The SI-111 IRT Data Correction Approach

The adjusted T_s data from the SI-111 IRT regarding surface emissivity and background effects is calculated as follows (Eq. D1):

$$T_s^* = \left[\frac{T_{sK}^4 - (1-\epsilon_s)\cdot T_{sky}^4}{\epsilon_s}\right]^{1/4} \tag{D1}$$

where T_s^* is the adjusted T_s data (K); T_{sK} is the nadir-looking unadjusted T_s data (K); T_{sky} is the sky temperature (K).

The T_{sky} variable is calculated as indicated by Eq. D2 below (Evangelisti et al., 2019):

$$T_{sky} = \left(\epsilon_{sky}\cdot T_{aK}^4\right)^{1/4} \tag{D2}$$

where T_{aK} is the local air temperature (K) and ϵ_{sky} is the sky thermal emissivity (dimensionless).

The ϵ_{sky} is calculated as indicated by Eq. D3 below (Berdahl and Martin, 1984):

$$\epsilon_{sky} = 0.711 + 0.56\cdot\left(\frac{T_{dew}}{100}\right) + 0.73\cdot\left(\frac{T_{dew}}{100}\right)^2 \tag{D3}$$

where T_{dew} is the dew point temperature (°C).

The T_{dew} is calculated as in Ham (2005) and presented by Eq. D4:

$$T_{dew} = 240.97 \cdot \frac{ln(\frac{e_a}{0.61121})}{17.502 - ln(\frac{e_a}{0.61121})} \tag{D4}$$

where e_a is the actual vapor pressure (kPa).

Appendix E

Data Collection Instrumentation

Table E1: Summary of primary sensors used at the LIRF research site.

Sensor	Manufacturer	Headquarters	Uncertainty
5TE	Decagon Devices, Inc.	Pullman, WA, USA	$\pm 3\%$ in soils $< 10\ dS/m$.
Mini Trase 6085	Soil Moisture Equipment	Santa Barbara, CA, USA	$\pm 2\%$ full scale for 0 to 100% moisture.
MSR	Cropscan, Inc.	Rochester, MN, USA	RGB: $\pm 2\%$. NIR: $\pm 1\%$. IRT: $\pm 1\%$.
SI-111 IRT	Apogee Instruments	Logan, UT, USA	$\pm 1\%$ ($\pm 0.2\ ^oC$; -10 ^oC to 65 ^oC).
HMP45C Hygrometer	Vaisala	Vantaa, Finland	T_a and RH: $\pm 1\%$.
03101-L Anemometer	RM Young Company	Traverse City, MI, USA	$\pm 1\%$ or ± 0.50 m/s.
NR-Lite	Kipp and Zonen	Delft, the Netherlands	$\pm 3\%$ during daytime.
HFT3-L	Radiation and Energy Balance, Inc.	Bellvue, WA, USA	$\pm 5\%$ on average.
LI-7500DS	LI-COR	Lincoln, NE, USA	Water vapor: $\pm 1\%$; 0 to 60 mmol/mol.
3D Sonic Anemometer	Gill Instruments	Lymington, Hampshire, UK	Wind: $\pm 1.5\%$; Temperature: $\pm 1\%$.
T107	Campbell Scientific, Inc.	Logan, UT, USA	$\pm 2\%$ at 20 ^oC or $\pm 0.4\ ^oC$; -24 ^oC to 48 ^oC.
LI-190R and LI-191R	LI-COR	Lincoln, NE, USA	$\pm 1\%$ for f_c.
LI-200X	LI-COR	Lincoln, NE, USA	$\pm 3\%$ during daytime.
LAI-2200	LI-COR	Lincoln, NE, USA	$\pm 6\%$ for solar noon readings.
TE525 Tipping Bucket	Texas Electronics	Dallas, TX, USA	$\pm 1\%$ for rainfall < 50 mm/hr.

Table E2: Summary of primary sensors used at the IIC research site.

Sensor	Manufacturer	Headquarters	Uncertainty
CS655	Campbell Scientific Inc.	Logan, UT, USA	$\pm 1\%$ in soils $< 10\ dS/m$.
CPN 503 DR	Instrotek, Inc.	Raleigh, NC, USA	$\pm 0.24\%$ at 24% per volume.
MSR	Cropscan, Inc.	Rochester, MN, USA	RGB: $\pm 2\%$. NIR: $\pm 1\%$. IRT: $\pm 1\%$.
SI-111 IRT	Apogee Instruments	Logan, UT, USA	$\pm 1\%$ ($\pm 0.2\ ^oC$; -10 ^oC to 65 ^oC).
HMP45C	Vaisala	Vantaa, Finland	T_a and RH: $\pm 1\%$.
03101-L Anemometer	RM Young Company	Traverse City, MI, USA	$\pm 1\%$ or ± 0.50 m/s.
NR-Lite and CNR01	Kipp and Zonen	Delft, the Netherlands	NR-lite: $\pm 3\%$; CNR01: $\pm 10\%$. Daytime.
HFT3-L	Radiation and Energy Balance, Inc.	Bellvue, WA, USA	$\pm 5\%$ on average.
LI-7500A	LI-COR	Lincoln, NE, USA	Water vapor: $\pm 2\%$; 0 to 60 ppt.
CSAT3 3D Sonic Anemometer	Campbell Scientific, Inc.	Logan, UT, USA	Wind: $\pm 0.3\%$; Temperature: $\pm 0.7\%$.
T107	Campbell Scientific, Inc.	Logan, UT, USA	$\pm 2\%$ at 20 ^oC or $\pm 0.4\ ^oC$; -24 ^oC to 48 ^oC.
LI-190R and LI-191R	LI-COR	Lincoln, NE, USA	$\pm 1\%$ for f_c.
LAI-2200	LI-COR	Lincoln, NE, USA	$\pm 6\%$ for solar noon readings.
TE525 Tipping Bucket	Texas Electronics	Dallas, TX, USA	$\pm 1\%$ for rainfall < 50 mm/hr.

Table E3: Summary of primary sensors used at the AVRC site.

Sensor	Manufacturer	Headquarters	Uncertainty
CS650*	Campbell Scientific Inc.	Logan, UT, USA	$\pm 1\%$ in soils $< 10\ dS/m$.
253-L*	Irrometer	Riverside, CA, USA	$\pm 0.40\%$ on average.
CPN 503 DR	Instrotek, Inc.	Raleigh, NC, USA	$\pm 0.24\%$ at 24% per volume.
MSR16	Cropscan, Inc.	Rochester, MN, USA	RGB: $\pm 2\%$. NIR: $\pm 1\%$. IRT: $\pm 1\%$.
SI-111 IRT	Apogee Instruments	Logan, UT, USA	$\pm 1\%$ ($\pm 0.2\ ^oC$; -10 ^oC to 65 ^oC).
HMP45C	Vaisala	Vantaa, Finland	T_a and RH: $\pm 1\%$.
03101-L Anemometer	RM Young Company	Traverse City, MI, USA	$\pm 1\%$ or ± 0.50 m/s.
Eppley PSP	Eppley Laboratory, Inc.	Newport, RI, USA	$\pm 2\%$ during daytime.
LI-190R and LI-191R	LI-COR	Lincoln, NE, USA	$\pm 1\%$ for f_c.
TE525 Tipping Bucket	Texas Electronics	Dallas, TX, USA	$\pm 1\%$ for rainfall < 50 mm/hr.

* CS650 data in 2021. 253-L data in 2020.